Julius-Maximilians-
UNIVERSITÄT
WÜRZBURG

A radio view of high-energy emitting AGNs

Dissertation zur Erlangung des naturwissenschaftlichen Doktorgrades der Julius-Maximilians-Universität Würzburg

vorgelegt von
Robert Frank Schulz

aus Berlin

Würzburg 2016

Eingereicht am: 22.02.2016
bei der Fakultät für Physik und Astronomie

1. Gutachter: Prof. Dr. Matthias Kadler
2. Gutachter: Prof. Dr. Jörn Wilms
3. Gutachter: .....
der Dissertation

Vorsitzende(r): Prof. Dr. Werner Porod

1. Prüfer: Prof. Dr. Matthias Kadler
2. Prüfer: Prof. Dr. Jörn Wilms
3. Prüfer: Prof. Dr. Raimund Ströhmer
im Promotionskolloquium

Tag des Promotionskolloqiums: 08.07.2016

Doktorurkunde ausgehändigt am: .....

Zusammenfassung

Aktive Galaxienkerne (AGNs) gehören zu den energetischsten Objekten im Universum. Dabei handelt es sich um Galaxien, deren kompaktes Zentrum die Emission der Galaxie über einen Teil oder sogar den kompletten Bereich des elektromagnetischen Spektrums dominiert. Daher werden AGNs intensiv mit Hilfe der Multiwellenlängen-Astronomie studiert. Im Standardmodell der AGNs akkretiert das zentrale *supermassive schwarze Loch* (SMBH) Materie aus der Umgebung und dient damit als Antriebsquelle für die Emission. In der Nähe des stark magnetisierten SMBH können hoch-relativistische Plasmaausflüsse, sogenannte *Jets*, auf beiden Seiten der Scheibe senkrecht dazu entstehen. Diese Jets können sich weit über die Galaxie hinaus ausbreiten. Insgesamt sind nur 10% aller AGNs durch die Jetemission dominiert, da diese auf Grund kleiner Sichtwinkel durch relativistische Effekte verstärkt wird. Dennoch bilden diese AGNs, die auch *Blazare* genannt werden, den Großteil, der von *Fermi*-LAT gefundenen extragalaktischen Objekte im Universum, die γ-Strahlung aussenden. Die Emission der Blazare im niedrigen Energiebereich (vom radio bis UV/X-ray Bereich) wird im Allgemeinen durch Synchrotron-Strahlung der Jets erklärt. Als Ursache der hochenergetischen Emission wird inverse Compton-Streuung von Photonen an den Teilchen des Jet angesehen, wobei mehrere Quellen für die Photonen innerhalb und außerhalb des AGNs sowie auch andere Modelle diskutiert werden. Dies zeigt jedoch, dass die Hochenergieemission stark mit ihrem Entstehungsort im Jet im Zusammenhang stehen kann. Daher ist ein detailliertes Verständnis der Entstehung und Evolution von Jets in AGNs essentiell. Beobachtungen im Radiofrequenzbereich bieten insbesondere mit Hilfe der *Very Long Baseline Interferometrie* (VLBI) den besten Weg um direkt Informationen über die intrinsischen Eigenschaften der Jets bis hinunter zur deren Entstehungsregion zu sammeln.

In der vorliegenden Arbeit konzentriere ich mich auf drei unterschiedliche AGNs, IC 310, PKS 2004−447 und 3C 111, die zwar im γ-Strahlungsbereich aktiv sind, jedoch nicht zur Klasse der Blazare gehören. Ich studiere sie detailliert mit unterschiedlichen radioastronomischen Instrumenten im Kontext ihrer Hochenergieemission und im Vergleich zu den großen Samplen der Langzeitbeobachtungsprogramme MOJAVE (*Monitoring Of Jets in Active galactic nuclei with VLBA Experiments*) und TANAMI (*Tracking Active Galactic Nuclei with Austral Miliarcsecond Interferometry*).

Die leuchtkraftschwache *Radiogalaxie* IC 310 ist ungewöhnlich auf Grund ihrer sehr hellen und variablen Strahlung im TeV-Energiebereich. Ich präsentiere die ersten quasi-simultanen VLBI-Beobachtungen mit dem *Europäischen VLBI Netzwerk* (EVN) zwischen 1.7 GHz und 22.2 GHz sowie Langzeitbeobachtungen von MOJAVE mit dem *Very Long Baseline Array* (VLBA) bei 15.4 GHz. Diese Daten offenbaren einen schwachen einseitigen Radiojet, der von einem hellen und kompakten Kern ausgeht. Der Jet zeigt keine starke zeitliche Entwicklung und Variabilität der Flussdichte. Daher ist dieser nur mode-

rat relativistisch, was ein weiterer Beweis dafür ist, dass die Hochenergieemission nicht direkt mit dem Jet in Verbindung steht. Darüber hinaus, deuten die Daten daraufhin, dass in der Entstehungsregion des Jets starke Magnetfelder vorhanden sind.

In der *Fermi*-ära haben sich *radiolaute narrow-line Seyfert 1* (RL-NLS1) Galaxien zu einer wichtige Klasse an AGNs im γ-Strahlungsbereich entwickelt. Diese Objekte scheinen im Vergleich zu Blazaren eine kleinere Masse des SMBH und eine höhere Akkretionsrate aufzuweisen. Es gibt auch Gemeinsamkeiten mit Blazaren, wie zum Beispiel das Vorhandensein von relativistischen Jets. PKS 2004−447 ist zur Zeit die einzige RL-NLS1 am südlichen Himmel, von der γ-Strahlung detektiert wurde, so dass diese ein faszinierendes Beobachtungsobjekt für TANAMI darstellt. Ich präsentiere das bis jetzt höchst aufgelöste Bild von PKS 2004−447 sowie Langzeitmessungen der Flussdichte bei mehreren Radiofrequenzen. Das VLBI-Bild bei 8.4 GHz zeigt einen einseitigen Jet und eine frühere Beobachtung bei 1.5 GHz offenbart diffuse Emission auf der gegenüberliegenden Seite des Jets. Die projizierte maximale Ausdehnung von PKS 2004−447 wird auf unter 11 kpc geschätzt. Diese Eigenschaften sind konsistent mit RL-NLS1. Das Radiospektrum ist jedoch zur Zeit für die, im γ-Strahlungsbereich detektierten, RL-NLS1 einzigartig, da es ein Maximum unterhalb von 1 GHz zu besitzen scheint und darüber hinaus optisch dünn ist. Dies unterstützt die, in früheren Studien vorgeschlagene, Assoziation zwischen *Compact Steep Spectrum* (CSS) Quellen und RL-NLS1. Beide Klassen werden auch als AGNs in einem jungen Entwicklungsstadium betrachtet.

Die Radiogalaxie 3C 111 gehört zu den schwächeren AGNs im γ-Strahlungsbereich. Im Vergleich zu IC 310 durchlebt diese jedoch starke Ausbrüche im Radiobereich und kommt auf scheinbare Überlichtgeschwindigkeit im Jet auf pc-Skalen. Ich präsentiere drei Beobachtungen mit dem *Globalen mm-VLBI Array* (GMVA), die über ein Jahr verteilt sind und kurz nach dem letzten starken Ausbruch aufgenommen worden sind, sowie Flussdichtemessungen des F-GAMMA Programms. Dank dieser Daten ist es mir möglich die Entwicklung des Jets auf pc-Skalen mit einer Auflösung von bis zu 0.040 pc (projiziert) mit dem Anstieg und dem Abfall des Ausbruchs in Verbindung zu setzen. Eines der faszinierendsten Merkmale des Jets ist eine Krümmung im Jet, die um das Maximum des Ausbruchs aufgetaucht ist. Sie entwickelt sich markant über die Zeit und wird als Instabilität im Jet interpretiert. In der Literatur ist eine Verbindung zwischen der Radio- und γ-Strahlung in 3C 111 vorgeschlagen worden. mm-VLBI Beobachtungen und Flussdichtemessungen im Radiobereich während eines zukünftig ähnlich hohen Radioausbruchs bieten eine exzellente Möglichkeit um die Verbindung zur γ-Strahlung in einer FR II Radiogalaxie zu studieren.

Darüber hinaus, vergleiche ich die γ-Strahlungslautstärke, die dem Verhältnis aus Radio- und γ-Leuchtkraft entspricht, dieser Quellen. IC 310 und 3C 111 liegen an den entgegengesetzten Wertebereichsgrenzen der γ-Strahlungslautstärke des kleinen Samples von Radiogalaxien. Beide Objekte sind über mehr als eine Größenordnung der γ-Strahlungslautstärke von einander getrennt, wobei der Wert von 3C 111 am unteren Ende der Verteilung der Blazare liegt. PKS 2004−447 hat eine ähnliche Lautstärke wie IC 310, jedoch decken alle RL-NLS1 im γ-Strahlungsbereich einen kleineren Wertebereich als Radiogalaxien ab und liegen etwas höher als der Median der Blazare. Für eine detaillierte

statistische Analyse sind die beiden Samples noch zu klein.

Die hier vorliegende Arbeit verdeutlicht anschaulich die Vielfalt der Radioeigenschaften von AGNs im γ-Strahlungsbereich basierend auf drei Quellen, die nicht zur Klasse der in diesem Energiebereich dominierenden Blazare gehören. Im Kontext von Studien mit großen Samples, ermöglichen die Ergebnisse dieser Arbeit einen bedeutenden Einblick in die Eigenschaften von hochenergetischen AGNs.

Abstract

Active galactic nuclei (AGNs) are among the most energetic objects in the Universe. These galaxies that are dominated in part or even throughout the electromagnetic spectrum by emission from their central, compact region. AGNs are extensively studied by multi-wavelength observations. In the standard picture, the main driver of an AGN is a *supermassive black hole* (SMBH) in its centre that is surrounded by an accretion disk. Perpendicular to the disk, in the vicinity of highly magnetized SMBH relativistic outflows of plasma, so-called *jets*, can form on either side that can reach far beyond the host galaxy. Only about 10% of all AGNs are dominated by emission from these jets due to relativistic beaming effects and these so-called *blazars* dominate the extragalactic γ-ray sky. It is commonly accepted that the low-energy emission (radio to UV/X-ray) is due to synchrotron emission from the jet. The high-energy emission is considered to stem from inverse-Compton scattering of photons on the jet particles, but different sources for these photons are discussed (internal or external to the AGN) and other models for the high-energy emission have also been proposed. The nature of the high-energy emission is strongly linked to the location of the emission region in the jet which requires a detailed understanding of the formation and evolution of jets. Radio observations especially using *very long baseline interferometry* (VLBI) provide the best way to gain direct information on the intrinsic properties of jets down to sub-pc scales, close to their formation region.

In this thesis, I focus on the properties of three different AGNs, IC 310, PKS 2004−447, and 3C 111 that belong to the small non-blazar population of γ-ray-loud AGNs. I study them in detail with a variety of radio astronomical instruments with respect to their high-energy emission and in the context of the large monitoring programmes MOAJVE (*Monitoring Of Jets in Active galactic nuclei with VLBA Experiments*) and TANAMI (*Tracking Active Galactic Nuclei with Austral Milliarcsecond Interferometry*).

The low-luminosity *radio galaxy* IC 310 is detected up to the TeV-energies, where it is highly variable and bright like a blazar. I present the first quasi-simultaneous, multi-frequency VLBI campaign conducted with the *European VLBI Network* (EVN) between 1.7 GHz and 22.2 GHz and data from long-term monitoring by MOJAVE with the *Very Long Baseline Array* (VLBA) at 15.4 GHz. The data reveal a faint single-sided jet extending from a bright compact core. The jet does not show strong temporal evolution and it lacks significant flux density variability. Thus it is only moderately relativistic which provides further evidence that the high-energy emission is not directly related to the radio jet. Moreover, the data suggests that the jet formation region close to the SMBH is highly magnetized.

In the *Fermi* era, *radio-loud narrow-line Seyfert 1* (RL-NLS1) galaxies have become an important part of the γ-ray-loud population. They seem to have significantly lower SMBH masses and accrete highly efficiently contrary to other γ-ray loud AGNs. There are

also similarities to blazars such as the existence of highly relativistic jets. PKS 2004−447 is currently the only known γ-ray-loud RL-NLS1 in the southern hemisphere and a prime target for TANAMI. I present the highest-resolution image of the pc-scale jet to date and the first long-term multi-frequency flux density monitoring. The VLBI image at 8.4 GHz exhibits a single-sided jet morphology and an archival VLBI observation at 1.5 GHz reveals additional diffuse emission on the opposite site of the jet. The projected large-scale extent of PKS 2004−447 is estimated to be below 11 kpc. These characteristics are consistent with other γ-ray-loud and -quiet RL-NLS1s. The radio spectrum of PKS 2004−447 is unique among γ-ray-loud RL-NLS1s as it is steep with possible turnover below 1 GHz. This supports a previously suggested association between *compact steep spectrum* (CSS) sources and RL-NLS1. Both classes are considered to represent a young stage in the evolution of AGNs.

The radio galaxy 3C 111 is among the fainter γ-ray sources. In contrast to IC 310, it exhibits strong radio outbursts and apparent superluminal motion on pc scales. I make use of three 86 GHz observations obtained with the *Global mm-VLBI Array* (GMVA) over a period of one year shortly after the peak of one of the strong outbursts and single-dish monitoring by the F-GAMMA programme. The data allow me to relate the pc-scale evolution to the rise and decay of the outburst. One of the most remarkable features is a jet bend that appeared around the peak of the flare, evolves significantly over time and is interpreted as an instability in the jet. A link between the γ-ray emission and radio flares have been proposed in the literature. mm-VLBI and flux density monitoring observations coordinated at the time of a future major outbursts will be ideal to directly probe the proposed γ-ray connection in an FR II galaxy.

I compare the radio-to-γ-ray properties of these sources using the ratio of the γ-ray and radio luminosity, the so-called γ-ray loudness. IC 310 and 3C 111 represent opposite ends of the γ-ray-loudness distribution of the small radio galaxy sub-sample. They are separated by more than an order of magnitude in γ-ray loudness, although 3C 111 is consistent with the lower end of the blazar distribution. PKS 2004−447 has a value similar to IC 310, but the γ-ray-loud RL-NLS1s cover only a smaller range and have values slightly higher than the median of the blazars. Both samples are still small in size preventing a more detailed statistical analysis.

The work presented in this thesis illustrates the diversity of the radio properties of γ-ray loud AGNs based on three sources that do not belong to the dominating class of blazars. In the context of large-sample studies, these results provides important inside into the jet properties of high-energy emitting AGNs.

Contents

Zusammenfassung i

Abstract v

1. Introduction 5

2. Relativistic jets in active galactic nuclei 9
2.1. Classes of AGN . . . 9
2.2. The unification of AGNs . . . 12
2.3. The physics of jets in AGN . . . 14
2.3.1. Emission and absorption . . . 14
2.3.2. The broadband emission . . . 17
2.3.3. Jet formation and evolution . . . 18
2.3.4. Relativistic effects . . . 23
2.4. Radio observations of jets . . . 25
2.4.1. The single-dish . . . 25
2.4.2. From interferometry to very long baseline interferometry . . . 28

3. The pc-scale structures of AGN jets and their high-energy connection 35
3.1. The radio-γ-ray connection in AGN jets . . . 35
3.2. The MOJAVE programme . . . 39
3.3. The TANAMI programme . . . 42
3.3.1. The VLBI array . . . 42
3.3.2. The sample . . . 44
3.3.3. Results from TANAMI . . . 45

4. Radio observations of the TeV emitter IC 310 53
4.1. Presenting IC 310 . . . 53
4.2. Single-dish and VLBI observations . . . 55
4.2.1. Single-dish monitoring . . . 55
4.2.2. EVN observations . . . 55
4.2.3. MOJAVE data . . . 56
4.3. Results . . . 56
4.3.1. The long-term radio spectrum . . . 56
4.3.2. VLBI images . . . 59
4.3.3. Kinematic analysis of the MOJAVE data . . . 61
4.3.4. Spectral index distribution and core shift . . . 64

4.4. Discussion . . . 65
4.4.1. The morphology and kinematic parameters of the jet . . . 65
4.4.2. Implications of the core shift on the magnetic field strength . . . 68
4.4.3. The place of IC 310 in the MOJAVE sample . . . 70
4.5. Summary . . . 71

5. The identity crisis of PKS 2004-447 73
5.1. Presenting PKS 2004-447 . . . 73
5.2. Radio observations . . . 74
5.2.1. TANAMI VLBI, VLBA and VLA observations . . . 74
5.2.2. Flux density monitoring by ATCA . . . 75
5.3. Results . . . 76
5.3.1. ATCA light curve and spectrum . . . 76
5.3.2. The first VLBI image at 8.4 GHz by TANAMI . . . 78
5.3.3. Archival 1.5 GHz VLBA and VLA image . . . 79
5.4. Discussion . . . 82
5.4.1. The spectral evolution . . . 82
5.4.2. The pc to kpc radio morphology . . . 83
5.5. Comparison with other γ-NLS1 galaxies . . . 86
5.5.1. Variability in flux density and spectrum . . . 87
5.5.2. Radio morphology and relativistic jet . . . 88
5.5.3. High-energy emission . . . 89
5.6. Summary . . . 89

6. Resolving the 2007 outburst of 3C 111 with mm-VLBI 93
6.1. Presenting 3C 111 . . . 93
6.2. Single-dish and mm-VLBI observations . . . 94
6.3. The jet of 3C 111 at 86 GHz . . . 95
6.3.1. The sub-pc scale morphology . . . 95
6.3.2. The kinematic of the jet . . . 97
6.4. Discussion . . . 99
6.4.1. Lorentz factor and viewing angle . . . 99
6.4.2. Ejection times and flare evolution . . . 102
6.4.3. The bend of the jet . . . 103
6.4.4. A comparison with previous outbursts and the γ-ray connection . . . 105
6.4.5. Interpretation of C1 and C2 . . . 107
6.5. Summary . . . 108

7. Conclusions and outlook 111

A. The mm-VLBI view of the two-sided jet system of NGC 1052 115
A.1. Zooming into NGC 1052 . . . 115
A.2. The viewing angle of NGC 1052 at 86 GHz . . . 118
A.3. Outlook . . . 119

B. Additional fits to the radio spectrum of PKS 2004−447 121

C. MOJAVE observations of 1H 0323+342 123

D. Model fit components of IC 310 and 3C 111 125

Bibliography 131

List of Figures 143

List of Tables 145

Acknowledgement 147

1. Introduction

The starry sky has fascinated and inspired the human mind for millennia. Its exploration has revealed much more than literally meets the eye thanks to the use of a rich variety of tools. The most prominent example is the optical telescope which in its modern form can be found not only on Earth but also in space.

The beginning of the 20th century marked the emergence of a new branch of astronomy focusing on radio wavelengths thanks to the pioneering work of Karl G. Jansky (Jansky 1933, see also Reber 1988; Sullivan 2009). Observations at radio wavelengths are performed ground-based in a broad wavelength regime (m to sub-mm), though satellites are used as well. These observation can be conduct by day and night and are less dependent on weather conditions in comparison to optical observations. After centuries of astronomical studies solely in the optical regime, radio observations revealed a much different sky and many previously unknown phenomenons in the Universe.

A similar revolution has been the development of detectors suitable for observations in the X-ray and γ-ray-regime. As the Earth's atmosphere is in general opaque to emission at such high energies, satellites have been deployed for astronomical observations. γ-rayastronomy has made a tremendous leap with the launch of the *Fermi Gamma-ray Space Telesope* in 2008 due to its primary instrument, the *Large Area Telescope* hereafter *Fermi*-LAT, that covers the energy range of 100 MeV to > 300 GeV and continuous monitoring of the whole sky every ~ 3 hr (Atwood et al. 2009). Observations in the γ-ray-regime can also be performed indirectly from the ground due to the Cherenkov-effect reaching beyond the GeV-energy regime.

One of the major advantages of radio astronomy is the capability to build large interferometers comprising many individual telescopes that are distributed around the world. Working together as single instrument, these interferometers can reach the best angular resolution in astronomy, down to the sub-mas range.

A beautiful example of the diverse characteristics which only observations in different wavelength regimes reveal, is shown in the classical image of the galactic plane of the Milky Way (Fig. 1.1). The dust and star-dominated optical image (third one from the bottom) changes dramatically with increasing and decreasing wavelength.

Active galactic nuclei (AGNs) are among the most powerful objects that populate the Universe. The exploration of AGNs started in the beginning of the 20th century and has greatly benefited from the development of multi-wavelength astronomy revealing several different classes (see e.g., Shields 1999 for an historical overview). The most powerful AGNs are called *blazars* and are driven by accretion onto the central *supermassive black hole* (SMBH) that leads to the production of highly relativistic outflows, so-called *jets*. The emission from these jets is strongly beamed towards the observer and can dominate the entire electromagnetic spectrum from low radio frequencies to the very high

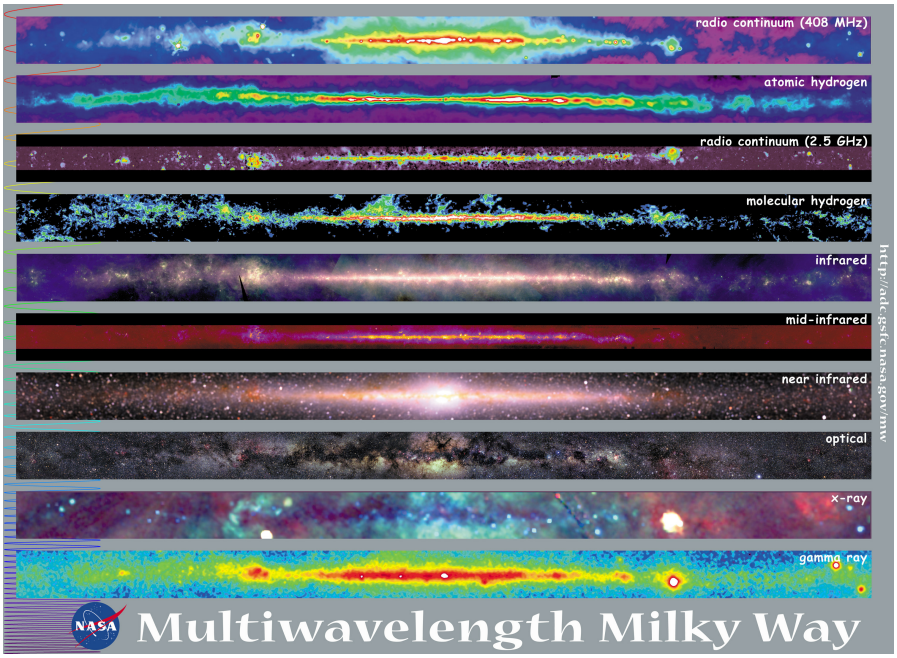

Figure 1.1.: The galactic plane of the Milky Way at different wavelengths from the radio, infra-red, and optical to the X-ray and γ-ray regime (top to bottom). Credit: NASA

γ-rayenergies. However, there are also other powerful AGNs such as *radio galaxies* that exhibit less strongly beamed emission, but still emit up the γ-ray regime. A prominent example is the closest AGN to Earth, the radio galaxy Centaurus A. Figure 1.2 depicts a composite image of Centaurus A showing the dust and stars of the host galaxy thanks to optical and radio (21 cm) observations. It also reveals the powerful jet emission that reaches far beyond the galaxy in the radio and X-ray images. Centaurus A is also a known γ-ray-emitter.

In order to better comprehend the high-energy emission of AGNs, it is vital to gain detailed knowledge of the jet production and evolution. High-angular radio observations provide the only means for most sources to directly obtain information on the properties of these jets down to scales close to the jet formation region in the vicinity of the SMBH. To this purpose, studies of single-sources are as important as of large samples. The former usually permits a more detailed insight due to specifically targeted observations, while the latter allows to perform statistical analysis which improves the understanding of similarities and differences between the classes of AGNs.

This work focuses on selected γ-ray-loud AGNs from the point of view of radio astronomy with a particular emphasis on high-resolution radio observations and discusses their place in the context of large samples. Chapter 2 provides basic information on AGNs and radio astronomical observations of jets. Chapter 3 further elaborates the link between radio and high-energy emission of AGNs and introduces two major monitoring programmes. This is followed by a radio view of three high-energy emitting AGNs, the ac-

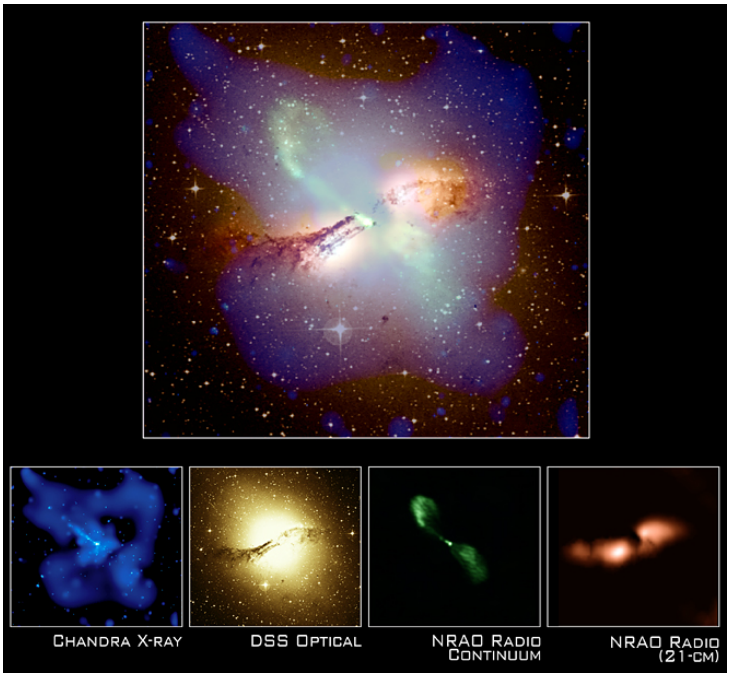

Figure 1.2: Composite image (top) of Centaurus A at different wavelengths with the individual images contributing to the composite image below. Credit: X-ray (NASA/CXC/M. Karovska et al.); Radio 21-cm image (NRAO/VLA/J.Van Gorkom/Schminovich et al.), Radio continuum image (NRAO/VLA/J. Condon et al.); Optical (Digitized Sky Survey U.K. Schmidt Image/STScI)

tive galaxy IC 310 (Chapt. 4), the radio-loud narrow-line Seyfert 1 galaxy PKS 2004−447 (Chapt. 5), and the radio galaxy 3C 111 (Chapt. 6). The main conclusions and outlook based on the research presented here is given in Chapt. 7.

Throughout this work a ΛCDM cosmology is adopted with the following parameters: $H_0 = 70 \mathrm{km\,s^{-1}\,Mpc^{-1}}$, $\Omega_m = 0.3$, $\Lambda = 0.7$ (Freedman et al. 2001).

2. Relativistic jets in active galactic nuclei

The electromagnetic spectrum of AGNs can be totally dominated by thermal and non-thermal emission from the AGN, though the emission does not necessarily have to be localised within the nucleus. As a consequence multi-wavelength studies from the radio to the γ-ray regime are vital for their exploration. This chapter gives a concise overview of the basic properties and classes of AGNs as well as the theoretical understanding of jets in AGNs. The chapter closes with the fundamentals of radio astronomical observations of AGNs.

2.1. Classes of AGN

Historically, the definition of AGN classes were driven primarily by optical and radio observations. This section summarises the different classes that were created and that are most relevant to this study. Excellent overviews are provided by Krolik (1999), Longair (2011), and Beckmann & Shrader (2012).

Blazars

This particular sub-class of AGNs emanates strong continuum emission from the radio to the γ-ray-regime. A further subdivision is made based on the existence of optical emission lines. In case that weak or no lines are present, the blazar is classified as a *BL Lac* object, so named after the AGN BL Lacertae (e.g. Oke & Gunn 1974; Miller & Hawley 1977; Vermeulen et al. 1995). If strong broad emission lines are detected, the blazar is referred to as a *flat-spectrum radio quasar* (FSRQ). Blazars with additional high optical variability are usually classified as *optically violent variables* (OVV).

Blazars are the dominant source of γ-ray emission in the sky as observed by *Fermi*-LAT: The third *Fermi*-LAT source catalog (3FGL, Acero et al. 2015) based on four years of *Fermi*-LAT observations between 100 MeV–300 GeV includes 3033 sources of which $\sim 57\%$ are classified as blazars[1]. The third catalogue of AGNs detected by *Fermi*-LAT (3LAC, Ackermann et al. 2015) at galactic latitudes $|b| > 10^\circ$ shows blazars to be even more dominant. About 98 of the AGNs in the 3LAC Clean sample are considered to be blazars. However, some of these blazars may also have other classifications, such as PMN J1603−4904 which is classified as a BL Lac object, though this has been under

[1] It is worth noting that the 3FGL and its predecessors (Acero et al. 2015) make a distinction between identified and associated γ-ray sources. With respect to AGN only a minority of the γ-ray sources in the 3FGL are identified.

discussion by (Müller et al. 2014a). At TeV energies the dominance of blazars is similarly strong (see e.g., Holder (2012) for a review). According to the catalogue of TeV sources (TeVCat[2], Wakely & Horan 2008) a total of 65[3] AGNs have been detected at TeV energies so far with 94% of them being blazars.

Another classification of blazars is based on the broadband emission from radio to γ-ray energies that exhibits a double hump structure. The position of the synchrotron peak is used to divide blazars into low-frequency, intermediate, and high-frequency synchrotron peaked sources (Subsect. 2.3.1).

The radio emission of blazars is strongly beamed which is why they dominate radio flux density limited samples such as MOJAVE (Lister et al. 2013) and TANAMI (Ojha et al. 2010) (see Chapt. 3). Blazars represent only a minority among the general population of AGNs.

Radio galaxies

These AGNs show strong radio emission over several orders of magnitude in size. The large-scale radio emission can be up to a few Mpc (e.g., Neeser et al. 1995). Based on the radio morphology and surface brightness radio galaxies are divided into Fanaroff-Riley (FR) I and II galaxies (Fanaroff & Riley 1974). FR I radio galaxies have strong two-sided jets which are connected with the radio lobes, while FR IIs usually show a strong one-sided jet extending from a compact central region but two strong radio lobes on opposites sides of the compact centre. FR I and II galaxies populate two regimes in radio power with the dividing line at 178 MHz around $\sim 10^{25}\,\mathrm{W\,Hz^{-1}}$, though this division is not strict.

Based on optical properties, radio galaxies can be separated into *narrow-line radio galaxies* (NLRG) and *broad-line radio galaxies* (BLRG) similar to Seyfert galaxies. The main difference to Seyfert galaxies is the radio loudness, i.e., the ratio of the radio to optical flux (e.g., Kellermann et al. 1989). Radio galaxies usually have a radio loudness larger than 10 which the common value that separates radio-loud and radio-quiet AGNs, though radio quiet does not mean radio silent.

A small number of radio galaxies have also been detected in the γ-ray-regime (Ackermann et al. 2015), such as IC 310 and the FR II galaxy 3C 111, which are both studied in greater detail in Chapt. 4 and Chapt. 6, respectively.

Quasars

Being first identified in the radio and then in the optical regime, the term quasar stands for *quasi-stellar radio source*. The study by Schmidt (1963) demonstrated for the first time that quasars were located at high redshifts. Large surveys have shown them to be the most distant and luminous AGNs. The optical properties are to some extend similar to Seyfert galaxies and both, quasars and Seyfert galaxies, are separated based on their

[2] http://tevcat.uchicago.edu/
[3] Retrieved on 2015-11-01

optical magnitude (Schmidt & Green 1983). The population of quasars can be divided into radio-loud and radio-quiet as well.

Compact steep spectrum & Gigahertz-peaked spectrum objects

Similar to radio galaxies, *compact steep spectrum* (CSS) and *GHz-peaked spectrum* (GPS) objects are classified based on their radio spectrum, which shows an observed turnover either below $\sim$ 1GHz (CSS) or below (GPS). An extensive review is provided by O'Dea (1998). They are relatively compact with a large scale size $\lesssim$ 10 kpc, but they are powerful radio emitters comparable to radio galaxies which suggests that they possibly represent an early stage of AGN evolution (e.g., Kunert-Bajraszewska et al. 2010).

Seyfert galaxies

The most common class of AGNs was the first one to be discovered by Seyfert (1943)[4] based on strong optical emission lines. Khachikian & Weedman (1974) introduced the distinction into Seyfert 1 and 2 galaxies based on the occurrence of broad emission lines in the optical spectrum. Both types show additional narrow emission lines. Differences can also be found in the continuum emission as type-1 galaxies usually have a higher level of continuum emission than type-2 objects that is not related to the host galaxy. Further studies showed that a finer classification seems necessary and this was introduced by Osterbrock (1977). X-ray observations provide another way of distinguishing Seyfert galaxies based on measurements of absorption. Seyfert galaxies are usually radio-quiet, but not all of them are.

Narrow-line Seyfert 1 galaxies

A particular subclass of Seyfert 1 galaxies are narrow-line Seyfert 1 galaxies (NLS1s). The term stems from the fact that the broad emission lines are narrower than in ordinary Seyfert 1 galaxies and was first coined by Osterbrock & Pogge (1985). The criteria for NLS1s are i) a full width at half maximum (FWHM) of the Hβ line below 2000 km s^{-1} and ii) an intensity ratio of the forbidden [O III] λ5007 line and Hβ smaller than 3. Another characteristic of NLS1s is the strong optical [Fe II] emission which shows different correlations and anti-correlations with the properties of the line emission and FWHMs (Grupe 2004; Zhou et al. 2006). Both studies also consider NLS1s to be AGNs in an earlier stage of evolution compared to other Seyfert galaxies. A highly intriguing aspect of NLS1s is that they can be divided into radio-loud and radio-quiet objects as well:

Radio-loud narrow-line Seyfert 1 galaxies (RL-NLS1s) have first systematically been searched for by Komossa et al. (2006). The study found that only 7% of NLS1s are radio-loud. In addition, a small sample of RL-NLS1 have even been detected in the γ-ray-regime (γ-NLS1, e.g., Abdo et al. 2009a,b; Foschini et al. 2015; D'Ammando et al. 2015; Yao et al. 2015) like blazars. Yuan et al. (2008) already reported that RL-NLS1

[4] A brief, but intriguing recount of the discovery of Seyfert galaxies is given by Osterbrock (1999).

share various characteristics with radio-loud AGNs and in particular blazars, though the black-hole masses are usually lower (e.g., Chen et al. 2015). In contrast to radio galaxies, RL-NLS1 are more compact extending only up to 100 kpc but are usually smaller (e.g., Doi et al. 2012; Richards & Lister 2015). Similarities between CSS/GPS sources and RL-NLS1 have also been discussed (e.g., Gallo et al. 2006; Doi et al. 2012). A particular example of a γ-NLS1, PKS 2004−447, is studied in Chapt. 5.

LINER

Low-ionization nuclear emission-line regions (LINERs) are a sub-type of low-luminosity AGN (LLAGN, see Ho 2008 for a review). LLAGN are particular common in the nearby Universe and cover the low end of the luminosity distribution of AGNs not just in the optical, but also in the radio regime. The core luminosity of LINERs is low, but the emission lines are strong and have similar width as Seyfert 2 galaxies. However, it has been suggested that not all LINERs are AGNs (e.g., Heckman & Best (2014) and references therein). A prototypical LINER is NGC 1052 which is briefly discussed in Appendix A.

2.2. The unification of AGNs

The underlying assumptions of the unification models by Lawrence (1987); Antonucci (1993); Urry & Padovani (1995) are that all AGNs are intrinsically the same: The centre of an AGN marks a rotating *supermassive black hole* (SMBH) with a mass between $\sim 10^5\,M_\odot$ and $\sim 10^{10}\,M_\odot$. It is surrounded by an *accretion disk* that rotates around the SMBH. The matter in the accretion disk loses angular momentum and falls into the SMBH, fuelling it. Hot gas above the accretion disk is ionized by the emission of the disk. The resulting emission lines have a high rotational velocity due to the strong gravitational force of the SMBH. They form the so-called *broad line region* (BLR). Further away from the BLR, colder and less dense gas is located that exhibits narrow emission lines and is called the *narrow line region* (NLR). Probably located in the plane of the accretion disk, but further away from it, is a *torus* of dust. In its simplest form, the torus has a donut-like shape and extends in height as far out as the BLR. However, recent X-ray observation indicate that the torus is rather clumpy with regions of different density (e.g., Markowitz et al. 2014). Either the plane of the accretion disk or torus can be considered the symmetry axis of the AGN. Collimated outflows of relativistic plasma, so-called *jets*, are formed in the vicinity of the SMBH and extend in opposite direction perpendicular to the accretion disk. Jets are a prominent feature of radio-loud AGN though it cannot be ruled out that they occur in radio-quiet AGN as well. Figure 2.1 shows a schematic of one side of an AGN (not to scale).

Lawrence (1987), Antonucci (1993), and Urry & Padovani (1995) categorized the population of AGNs using two parameters: the radio power or radio loudness and the presence of broad permitted lines in optical spectra. In order to incorporate LINERs, Tadhunter (2008) added the nuclear luminosity as a third parameter. Differences in the observed

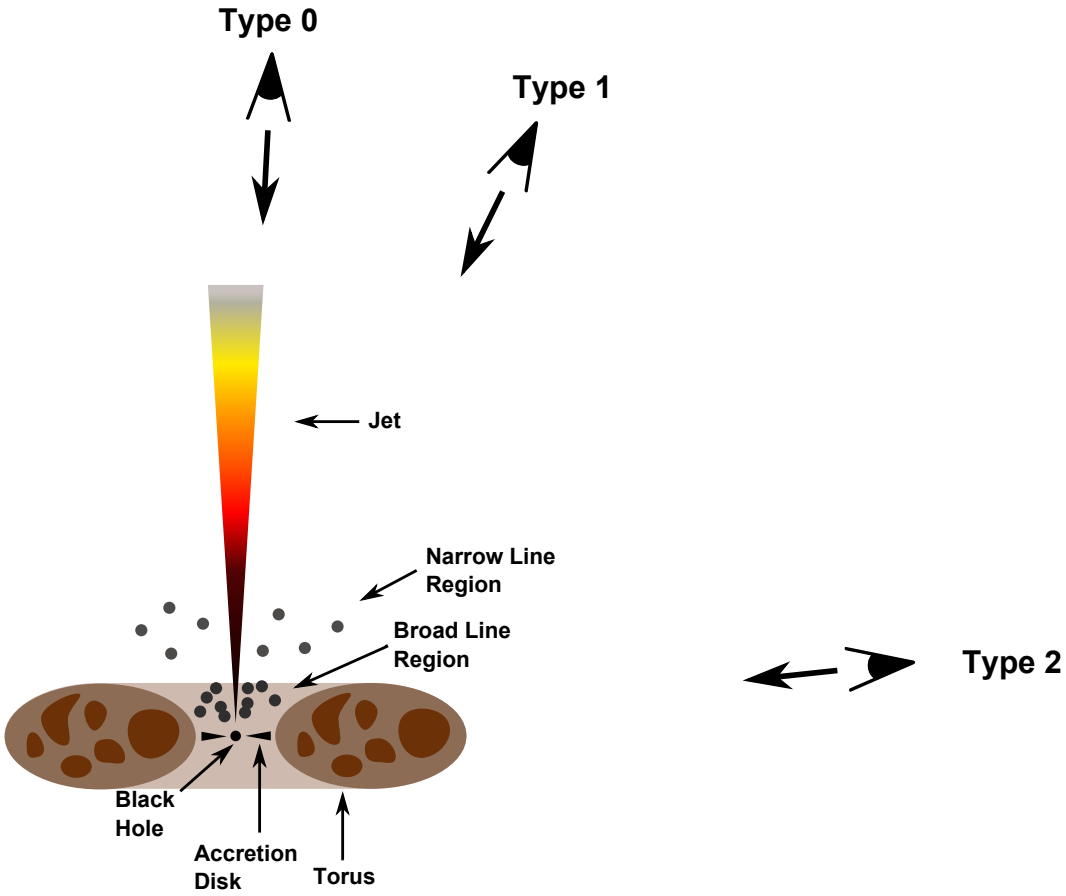

Figure 2.1.: A model of one side of a radio-loud AGN highlighting its main parts following the unification model of AGNs (not to scale). In this model the AGN is symmetric at the plane of the accretion disk. The jet and lobe are absent in case of radio-quiet AGN. Depending on the angle of the observer with the jet axis, different properties of the AGN are visible to the observer.

properties of the AGN would then be related to the viewing angle of the AGN. In type 2 sources (Seyfert 2, NLRG, LINERs, type 2 quasars) the emission from the central region, in particular the BLR, will be obscured by the absorption from the torus. In contrast to this type 1 AGNs (Seyfert 1, BLRG, type 1 quasars) are seen at a smaller angle to the line of sight preventing obscuration due to the torus which makes the BLR visible. The highly beamed emission of blazars (BL Lacs, FSRQs) is explained by very small viewing angles which aligns the jet well with the observer (type 0). Within the radio-loud population BL Lacs and FR I objects are considered to have the same parent population as do FSRQs and FR II, though this has been challenged by Kharb et al. (2010), for example. While orientation-based unification provides a basic model, it cannot account for the dichotomy of radio-loud and radio-quiet sources, the compact, but powerful radio population of CSS/GPS sources as well as the occurrence RL-NLS1. As a consequence the orientation-based unification model has been extended by additional parameters such as the black hole mass, luminosity, the accretion efficiency and the spin of the SMBH (e.g., Falcke & Biermann 1995; Laor 2000; Meier 2002). Other unification schemes do not focus on the radio properties, but instead on the central absorber, intrinsic differences in the AGN population and galaxy evolution especially of radio-quiet AGN in the local Universe (e.g., Heckman & Best 2014; Netzer 2015).

Unification of AGNs has to consider their evolution over time. A particular example is the unification of CSS/GPS sources with the radio-loud population. Bicknell et al. (1997) and O'Dea (1998) consider these sources to be young AGNs and GPS sources to be the progenitors of CSS sources. Kunert-Bajraszewska et al. (2010) further suggested that CSS evolve into FR I or FR II radio galaxy depending on the luminosity and jet system. In case of RL-NLS1, the lower black hole mass, higher accretion rate, the compact radio emission, and the recent detection of significant star formation activity can be interpreted in the context of young AGNs (e.g., Doi et al. 2012; Richards & Lister 2015; Foschini et al. 2015; Berton et al. 2015; Caccianiga et al. 2015). However, the low black hole masses of RL-NLS1 have also been questioned (Calderone et al. 2013; Baldi et al. 2016).

Besides the possibility that the AGN itself evolves over time, it has been shown that the AGN can have a significant impact on the host galaxy. This process is known as *AGN feedback* (see e.g., Fabian 2012 for a review) and covers for example the connection between AGN activity and black hole growth (e.g., Silk & Rees 1998), the quenching of star formation due to AGN activity (e.g., Di Matteo et al. 2005), and the outflow of gas due to the jet (e.g., Morganti et al. 2005). AGN feedback is a way to explain the evolution of the luminosity function of AGN with redshift which peaks for less luminous AGNs at subsequent lower redshifts (e.g, Ueda et al. 2003; Rigby et al. 2011). The activity of AGNs located in galaxy clusters can also have an impact on the intercluster medium in the form of heating (e.g., McNamara & Nulsen 2007).

2.3. The physics of jets in AGN

This section summarises specific physical processes that are relevant for the formation and evolution of jets in AGNs based on Rybicki & Lightman (1979), Longair (2011),

Boettcher et al. (2012), and Beckmann & Shrader (2012) unless otherwise mentioned.

2.3.1. Emission and absorption

The understanding of fundamental radiative processes in AGNs is important in order to model emission and absorption in specific regions of an AGN and the overall *spectral energy distribution* (SED) from the radio to the γ-ray regime. The latter is particular complicated as it includes emission from different parts of the AGNs, such as the jet and the accretion disk, and the interaction of emission through scattering and absorption. Radiative processes can be differentiated into thermal and non-thermal processes based on whether the particle distribution can be described by a Maxwell-Boltzman distribution or not. Especially for blazars, non-thermal processes can dominate the SED.

Bremsstrahlung

Radiation from an accelerated, charged particle such as an electron due to Coulomb interaction with another charged particle, e.g., an ion, is called *Bremsstrahlung* or *free-free emission*. Thermal Bremsstrahlung plays an important role in producing X-ray emission from AGNs, for example. A distribution of electrons with density n_e moving non-relativistically with a Maxwellian velocity distribution with velocity v in a distribution of ions with density n_i and charge Z yields a power per unit volume $\mathrm{d}V$ and bandwidth $\mathrm{d}\omega$ for scattering at small angles and in the low-frequency regime of

$$\frac{\mathrm{d}E}{\mathrm{d}t\,\mathrm{d}V\,\mathrm{d}\omega} \propto n_e n_i Z^2 e^{\frac{-h\nu}{kT}} g_{\mathrm{ff}} \quad , \tag{2.3.1}$$

where g_{ff} is the velocity averaged *Gaunt factor* which accounts for quantummechanical corrections.

The reverse process, i.e., **free-free absorption** (FFA), is relevant in particular for type 2 AGNs in which the central emission is absorbed the dusty torus. The absorbed emission detected by the observer is related to the intrinsic emission via the optical depth τ_{ff} following $S_{\nu,\mathrm{obs}} = S_{\nu,\mathrm{int}} e^{-\tau_{\mathrm{ff}}}$, where S denotes the flux density, i.e., the power emitted per unit area and frequency that is commonly used in radio astronomy with the unit *Jansky* ($1\,\mathrm{Jy} = 10^{-26}\mathrm{W\,m^{-2}\,Hz^{-1}}$). In general, the optical depth τ is determined by the absorption coefficient a integrated over the path length along which absorption occurs: $\tau = \int a\,\mathrm{d}l$. In case of free-free absorption a_{ff} can be calculated to be

$$a_{\mathrm{ff}} \approx 0.0177 T^{-1.5} n_e n_i Z^2 \nu^{-2} g_{\mathrm{ff}}\,\mathrm{cm^{-1}} \quad , \tag{2.3.2}$$

where n_e and n_i are given in units of $\mathrm{cm^{-3}}$. In the astrophysical context, a pure hydrogen plasma having a uniform density is assumed, i.e. $n_e = n_i$ that has a constant temperature along the path (e.g., Levinson et al. 1995; Bicknell et al. 1997). An approximation of g_{ff} is adopted following Bicknell et al. (1997) based on Brown (1987) that is $g_{\mathrm{ff}} \approx$

$11.962 T^{-0.15} \nu^{-0.1}$. This leads to

$$\tau_{\mathrm{ff}} \approx 0.212 L T^{-1.35} \nu^{-2.1} n_{\mathrm{H}}^2 \quad , \tag{2.3.3}$$

where L is the line element. Assuming a spherical absorber as in Kadler et al. (2004b) for example, the column density N_{H} can be calculated if n_{H} is known following $N_H = n_H L$. The value of N_H is commonly used as a measure for absorption.

Synchrotron radiation

One of the major contributions to the emission from AGNs especially for radio-loud AGN is *synchrotron radiation*. A charged particle moving relativistically in a magnetic field undergoes acceleration due to the Lorentz force and thus emits synchrotron radiation

$$\frac{\mathrm{d}\mathbf{v}}{\mathrm{d}t} = \frac{e}{\gamma m_e} (\mathbf{v} \times \mathbf{B}) \quad , \tag{2.3.4}$$

where $\mathbf{v}$ is the velocity of the charged particles, here an electron, and $\mathbf{B}$ the magnetic field. The Lorentz factor γ is defined as $\gamma = (1 - \beta^2)^{-1/2}$ where $\beta = v/c$. Relativistic beaming causes the radiation to be emitted anisotropically in a cone of opening angle $\sim \gamma^{-1}$ if $\gamma \gg 1$.

However, a distribution of charged particles is a more realistic case for which a power-law distribution is commonly assumed, $n(\gamma)\mathrm{d}\gamma = C\gamma^{-p}\mathrm{d}\gamma$ where p is the particle index. It follows that the resulting spectrum can be described by a powerlaw with spectral index $\alpha = (1 - p)/2$

$$S_\nu = S_0 \nu^\alpha \quad . \tag{2.3.5}$$

Here, the common convention of radio astronomy is adapted, in which the sign of the spectral index is not presumed, contrary to high energy astrophysics. Since synchrotron radiation is polarized, its observation can be used to trace the underlying magnetic field distribution.

The synchrotron photons can be absorbed by the electrons that caused their emission. This is called **synchrotron self-absorption** (SSA). This alters the synchrotron spectrum of a source in such a way that a turnover occurs at frequency ν_t that corresponds to an optical depth of $\tau_{\mathrm{SSA}} = 1$. For $\nu < \nu_t$ and $\nu > \nu_t$ the optical depth becomes larger and smaller than one which corresponds to an optically thick and thin medium, respectively. In the former case, the spectrum is independent of the particle index evolving proportional to $\nu^{5/2}$, while in the latter case the spectrum is proportional to v^α with $\alpha < 0$. SSA is of particular importance for the morphology of jets at parsec scales (hereafter pc scales) using VLBI (see Subsect. 2.3.3).

Inverse-Compton scattering

Inverse-Compton (IC) scattering describes the process of a low-frequency photon (e.g., in the optical regime) being up-scattered to higher energies (e.g., to X-ray energies) due

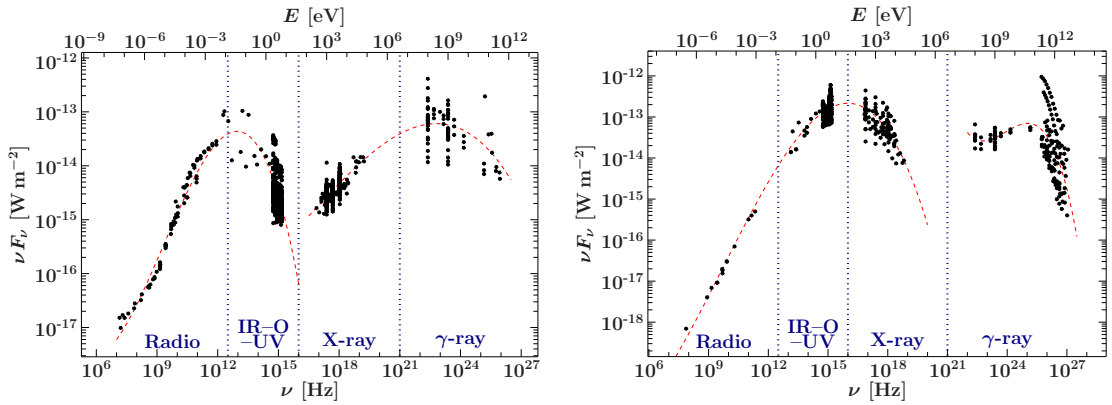

Figure 2.2.: Non-simultaneous SEDs of 3C 279 (left) and PKS 2155−304 (right) obtained from the ASDC SED Builder v3.2 (http://tools.asdc.asi.it/SED/). The red dashed lines are a third degree polynomial fit to the low and high frequency range using the ASDC SED Builder and are for illustration purposes only. The characteristic double-hump structure of blazar SEDs is well visible. The blue dotted lines separate the frequency regimes approximately.
References for 3C 279: Dixon (1970); Kuehr et al. (1981); Moshir & et al. (1990); Wright & Otrupcek (1990); Elvis et al. (1992); White & Becker (1992); Wright et al. (1994); Condon et al. (1998); Hartman et al. (1999); Voges et al. (1999); Giommi et al. (2002); Cohen et al. (2007); Healey et al. (2007); Saxton et al. (2008); Wright et al. (2009); Pittori et al. (2009); Abdo et al. (2010c); Bird et al. (2010); Cusumano et al. (2010b,a); Murphy et al. (2010); Wright et al. (2010); Planck Collaboration et al. (2011); Ajello et al. (2012); Giommi et al. (2012); Nolan et al. (2012); Baumgartner et al. (2013); D'Elia et al. (2013); Evans et al. (2014); Planck Collaboration et al. (2014); Acero et al. (2015)
References for PKS 2155−304: Dixon (1970); Warwick et al. (1981); Piccinotti et al. (1982); Wright & Otrupcek (1990); Elvis et al. (1992); Wright et al. (1994); Condon et al. (1998); Hartman et al. (1999); Voges et al. (1999); Giommi et al. (2002); Mauch et al. (2003); Aharonian et al. (2005a,b); Cohen et al. (2007); Healey et al. (2007); Verrecchia et al. (2007); Aharonian et al. (2009a); Abdo et al. (2010c); Murphy et al. (2010); H.E.S.S. Collaboration et al. (2010); Wright et al. (2010); H.E.S.S. Collaboration et al. (2012); Nolan et al. (2012); Abramowski et al. (2013); Evans et al. (2014); Planck Collaboration et al. (2014); Acero et al. (2015); Biteau & Williams (2015)

to scattering off relativistic electrons (e.g., from the jet). This is possible as the energy gain is proportional to γ^2. In the low-energy regime the energy loss rate is similar to that of synchrotron radiation. The latter depends on the energy density of the magnetic field, while the former depends on the energy density of the radiation field. Hence, inverse-Compton scattering leads to a similar spectral index for a power law distribution of electrons than synchrotron radiation

The efficiency of IC depends on the energy of the incident photon in the rest frame of the electron. If the energy of the photon is significantly lower than the rest mass energy of the electron, the Thomson cross-section is valid and the scattering is elastic. At higher energies of the photon, the Klein-Nishina cross-section has to be considered which limits the efficiency of the IC process.

2.3.2. The broadband emission

The radio to γ-ray SEDs of radio-loud AGNs, especially of blazars, have a distinct double hump structure. Figure 2.2 shows two particularly well sampled SEDs of 3C 454.3 and BL Lac (Abdo et al. 2010a). These SEDs also highlight that variability across the spectrum has to be considered. Various models have been developed to fit the SED of blazars that can generally be divided into leptonic and lepto-hadronic models (see also Boettcher 2010 for a review). All of them have in common that the dominant source of the low-frequency hump, i.e., from the radio up to the UV or X-ray regime, is attributed to synchrotron emission from the jet. The differences in these models is mostly attributed to the explanation of the high-energy peak.

Leptonic models assume that the jet is dominated by leptons, in particular electrons and positrons. If protons are present their contribution is negligible. The high-energy emission is explained by inverse-Compton scattering of photons from the jet or photons external to it. The former is called synchrotron self-Compton (SSC, e.g., Maraschi et al. 1992; Bloom & Marscher 1996). In the latter case, also known as external Compton (EC) process, photons may originate in the accretion disk (e.g., Dermer et al. 1992; Dermer & Schlickeiser 1993), the broad-line region (e.g., Sikora et al. 1994), the dusty torus (e.g., Błażejowski et al. 2000), and the cosmic microwave background (e.g., Tavecchio et al. 2000; Georganopoulos et al. 2006). Hence, the location of the high-energy emission is highly important questions and can be addressed by combined multi-wavelength studies (see Chapt. 3)

Lepto-hadronic models assume that protons are required for the high-energy emission in blazars (e.g., Mannheim & Biermann 1989; Mannheim 1993). At sufficiently high energies proton-proton interaction leads to the production of pions and γ-ray-photons. The pions can further decay into muons and neutrinos. Hence, only hadronic models are capable of producing neutrinos (Mannheim 1995; Stecker 2013) and the search for neutrinos from AGN provides an important tool to test the relevance of hadronic models (see also Sect. 3.3).

In general, SED models require a large amount of parameters which makes it complicated to statistically compare the resulting fits (e.g., Mankuzhiyil et al. 2011; Böttcher et al. 2013). This is further complicated by the assumed geometry of the emission region and the variability of the emission. In the simplest case, the emission region is assumed to be a single-zone in the jet which requires the low- and high-energy emission to be emitted co-spatially. However, single-zone SSC models are usually not sufficient to describe the SED of blazars (e.g., Abdo et al. 2010a; Giommi et al. 2012). One issue is the radio emission that is considered to be produced elsewhere in the jet. In addition, for blazars emitting up to the TeV energies, single zone models often require very high Doppler factors not consistent with data on the jet speed (e.g., Tavecchio et al. 1998; Henri & Saugé 2006). Multi-zone models are designed to overcome these limitations and various models are available, for example two-zone models (e.g., Abdo et al. 2011) or the two-flow model and the spine-sheath model in which the jet consists of an inner and an outer layer with the inner layer being responsible for the beamed emission (e.g., Boutelier et al. 2008; Tavecchio & Ghisellini 2008). The question, where the γ-ray emission is

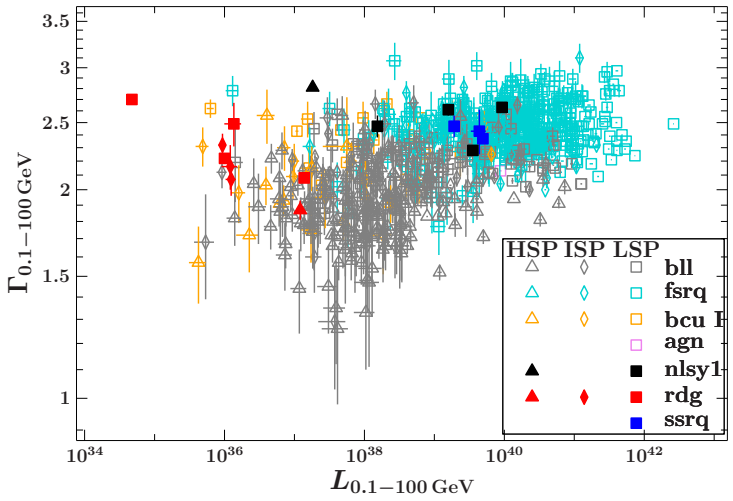

Figure 2.3: Distribution of γ-ray photon index and synchrotron luminosity based on the 3LAC full sample using sources with known redshift (based on data from Ackermann et al. 2015).

produced in the jet, is very important and requires simultaneous multi-wavelength data (see Chapt. 3).

Padovani & Giommi (1995) used the peak synchrotron frequency of BL Lacs to distinguish between high- and low-peaked BL Lac objects. This has been generalised by Abdo et al. (2010a) to include FSRQs. Based on this, blazars can be separated into *low synchrotron peaked* (LSP) objects which have a synchrotron peak frequency $\nu_{\mathrm{peak}}^{\mathrm{syn}} \lesssim 10^{14}\,\mathrm{Hz}$, *intermediate synchrotron peaked* objects with $10^{14}\,\mathrm{Hz} \lesssim \nu_{\mathrm{peak}}^{\mathrm{syn}} \lesssim 10^{15}\,\mathrm{Hz}$, and *high synchrotron peaked* (HSP) objects having $\nu_{\mathrm{peak}}^{\mathrm{syn}} \gtrsim 10^{15}\,\mathrm{Hz}$. Based on a sample of blazar SEDs, Fossati et al. (1998) and Ghisellini et al. (1998) deduced that the more luminous blazars have a lower synchrotron peak frequency and that a higher synchrotron peak frequency coincides with a decrease of the dominance of the high-energy luminosity over the synchrotron luminosity. In this so-called *blazar sequence*, blazars evolve from LSPs to HSPs. The validity of the blazar sequence is still under discussion and modifications have been made to the original scheme (e.g., Padovani 2007; Ghisellini & Tavecchio 2008; Giommi et al. 2012; Finke 2013). The blazar sequence is also related to a separation of the distributions of FSRQs and BL Lacs in terms of the γ-ray photon index and luminosity as shown in Fig. 2.3. It is known as the *blazar divide* and it was suggested that the trend is due to differences in the accretion process (e.g., Ghisellini et al. 2009; Ackermann et al. 2015).

The shape of the SED varies with the type of AGN. For example, quasars can show a peak in the optical regime, the so-called *big blue bump* (e.g., Shields 1978; Wilkes 2004; Shang et al. 2005). In radio-quiet sources emission from the other components of the AGN, such as the torus, the accretion disk and the host galaxy become more important.

2.3.3. Jet formation and evolution

Jets are an integral part of radio-loud AGNs, though they are also hosted in other AGNs. They cover a wide range of spatial scales from sub-pc up to Mpc (e.g., Bridle & Perley

1984; Zensus 1997). Hence, they represent an observational as well as a theoretical challenge. This section focuses predominately on jets up to pc scales.

The launching of a jet

Two scenarios are commonly considered that are capable of forming a relativistic jet. These are the Blandford-Znajek (BZ, Blandford & Znajek 1977) and the Blandford-Payne (BP, Blandford & Payne 1982) processes.

The BZ model requires a rotating SMBH surrounded by an accretion disk. The angular momentum of the SMBH is commonly referred to as its spin a, while the sphere of influence of the SMBH can be expressed by its gravitational radius R_G defined as $R_G = GM_{\rm BH}/c^2$, where G is the gravitational constant and c is the speed of light in vacuum. The accretion disk provides a magnetic field which leads to the formation of a magnetosphere around the rotating SMBH where subsequently a plasma can form. The interaction of the SMBH and the magnetic field alters its configuration and the plasma gets accelerated. Hence, the energy extracted from the SMBH via the BZ process depends on the magnetic field flux and the angular momentum of the SMBH. While the original BZ model was designed for $|a| \ll 1$, Tchekhovskoy et al. (2010) showed that only minor modifications are necessary to correct for highly rotating SMBH. Simulations performed by Tchekhovskoy et al. (2011) revealed that the BZ process can be very efficient in extracting energy from the SMBH in case of highly magnetized accretion disks and a high spin of the SMBH.

The BP model represents another way of producing a relativistic jet (see also Li et al. 1992). The magnetic field lines of the disk have a toroidal component due to the rotation of the disk which allows the extraction of plasma from the accretion disk in form of a relativistic, magnetically driven wind. Figure 2.4 shows the concept of jet launching for magnetised accretion disks which can be achieved either by the BZ or the BP model (Tchekhovskoy et al. 2012). In this picture the formation of a toroidal field and the resulting magnetic pressure provides the initial acceleration of the jet. While the poloidal component dominates close to the black hole, the toroidal component will start to dominate

It is evident from both models alone that the nature of the accretion disk plays an important role. The dominant forces that govern an accretion disk are gravity, pressure, and rotation (see e.g., Abramowicz & Fragile 2013 for a recent review and references therein). The other important factor is the geometry that is usually distinguished into *thin*, *slim*, *thick*, and *advection dominated accretion flow* (ADAF) based on disk height, accretion rate, optical depth, advection dominance, radiation pressure, and accretion efficiency. ADAF disks are of particular interest for low-luminosity AGNs, LINERs and the Galactic centre (e.g., Anderson et al. 2004; Guainazzi et al. 2000; Narayan et al. 1998; Ho 2008; Mościbrodzka et al. 2014). Recent simulations by McKinney et al. (2012) and Tchekhovskoy & McKinney (2012) suggest that thick disks in combination with a high SMBH spin are capable of producing jets via the BZ process in case of highly magnetized disks. According to McKinney et al. (2013), this would have an effect on the alignment of the spin (and jet) axis and the accretion disk. The study showed that for thick disks

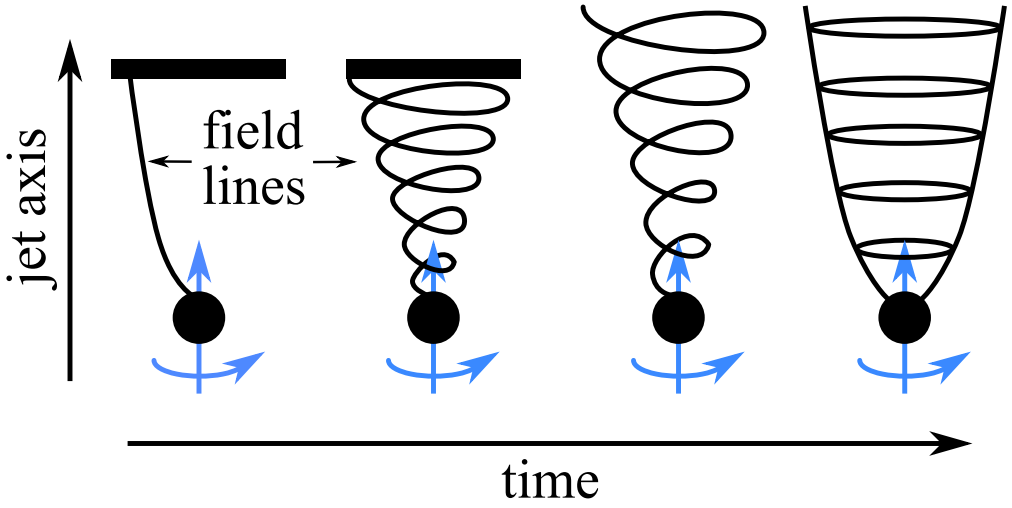

Figure 2.4.: A sketch of the formation of a jet. First, the field lines of a poloidal magnetic field are attached to a perfectly conducting sphere (grey circle, e.g., SMBH or accretion disk) and the ceiling (horizontal line, e.g., ambient medium). Due to the rotation of the sphere toroidal field lines develop that create magnetic pressure. At some point enough pressure is created to accelerate the plasma. Finally, it is possible that the system evolves into a steady state in which the magnetic pressure becomes constant. Based on Tchekhovskoy et al. (2012)

both are initially aligned, but this alignment is altered further away from the SMBH.

Differences in the rotation of the SMBH and the accretion disk changes the efficiency of the system. The case that both rotate in the same direction is called prograde ($a > 1$), while the opposite case is called retrograde ($a < 1$). While studies have shown differences in the efficiency due to prograde and retrograde rotation, it has also been shown that both can be equally efficient (Tchekhovskoy & McKinney 2012 and references therein). The *innermost stable circular orbit* (ISCO[5]), which marks the last stable orbit of a photon, ranges from $1R_{\mathrm{G}}$ to $9R_{\mathrm{G}}$ for the prograde and retrograde case, respectively (see Bardeen et al. 1972; Abramowicz & Fragile 2013). Hence, one way to probe the system observationally is high angular resolution, high frequency radio imaging as is performed by the Event Horizon Telescope (EHT, e.g., Lu et al. 2014; Mościbrodzka et al. 2014). One of the first indirect observations has been performed by Doeleman et al. (2012) with the EHT of M87. The study reported that the distance of the jet launching point to the SMBH is only 5.5 Schwarzchild radii R_{S} ($1R_{\mathrm{S}} = 2R_{\mathrm{G}}$) which indicates a prograde system.

Jet evolution

The pc-scale structure of relativistic jets reveal a range of morphologies in radio images. Blazars usually have a single-sided jet extending from a bright compact region, also

[5] $R_{\mathrm{ISCO}} = R_{\mathrm{G}}(3 + Z_2 - \sqrt{(3 - Z_1)(3 + Z_1 + 2Z_2)})$, where $Z_1 = 1 + (1 - a^2)^{1/3}((1 + a)^{1/3} + (1 - a)^{1/3})$ and $Z_2 = \sqrt{3a^2 + Z_1^2}$

called *core* or they are compact, while radio galaxies show one-sided and two-sided jets. This can be explained by differences in the viewing angle of the jet and Doppler boosting. Although jets often appear to be well collimated, some sources show bends or disruptions in the jet (e.g., Zensus 1997; Kellermann et al. 2004). As blazars are viewed at small angles to the line of sight, any intrinsic change in the position angle of the jet is amplified by the projection effect. Flux density changes in the jet over time show that new plasma is ejected into the jet usually in form of a bright emerging feature. This feature moves downstream and can reach apparent speeds faster than the speed of light for highly relativistic jets, though this is a projection effect (see Sect. 2.3.4). The motion of the plasma is initially considered to be ballistic, but acceleration has been observed in the form of changes in the jet speed and the direction of motion (e.g., Kellermann et al. 2004; Lister et al. 2013; Homan et al. 2015). The emission of jets can be strongly polarised, but it is usually not homogeneously distributed throughout the jet, which indicates changes in the underlying magnetic field (e.g., Jorstad et al. 2005; Hovatta et al. 2012).

From a theoretical point, an idealized jet can be modelled with a conical geometry with a given opening angle with new plasma being ejected into the stream (e.g., Blandford & Königl 1979). If the new plasma has higher density compared to the underlying jet flow, a shock front is created. In the shock-in-jet model for blazars, the shock front passes the acceleration and collimation region which is magnetically dominated. In the kinetically dominated part of the jet, the shock front has gained enough energy for particle acceleration up to the γ-ray-regime which is observable in form of flares (Marscher & Gear 1985; Fromm et al. 2011; Marscher 2009).

Shocks can also be created by differences in the jet pressure with respect to the ambient medium. The jet may expand because it is over-pressured until the situation is reversed which leads to a collimation of the jet. This gives rise to a *recollimation shock* that will lead to a an increase in intensity and polarization (e.g., Gómez et al. 1997; Agudo et al. 2012). Recollimation shocks can become a standing shock in the jet. In case a new shock travels through the jet, for example, due to a new ejection event, this will lead to shock-shock interaction (e.g., Perucho 2013; Fromm et al. 2016).

There are different ways to explain changes in the jet orientation. Close to the black hole where the jet is magnetically driven by a toroidal field, *current-driven instabilities* (CDI) can occur due to differences in the magnetic flux. Further away where the jet is kinetically driven, *Kelvin-Helmholtz instabilities* (KHI) may occur due to differences in the velocity within the plasma. Information on the polarization of the jet is important study instabilities (see e.g., Hardee 2006; Perucho 2012 for reviews, Lobanov & Zensus 2001; Agudo et al. 2012). As mentioned in the previous section, thick accretion disk may also lead to changes in the position angle of the jets, though these changes may occur close to the jet formation region.

The radio spectrum of pc-scale jets is often flat, i.e. $-0.5 \lesssim \alpha \lesssim 0.5$, though it is necessary to distinguish between the often dominating core with a flat spectrum and the jet with a steeper spectrum (e.g., Hovatta et al. 2014). The flat spectrum of the core can be explained by synchrotron self-absorption. Hence, the core marks region where the opacity of the jet plasma is ~ 1 and its position from the SMBH $r_{\rm core}$ will change with

frequency following $r_{\rm core} \propto \nu^{-1/k_r}$ where $k_r \sim 1$ (Königl 1981; Lobanov 1998; Hada et al. 2011; Sokolovsky et al. 2011). Following Lobanov (1998), the core shift also provides a way to estimate the magnetic field at 1 pc from the black hole by calculating the core shift measure $\Omega_{\rm r,\nu}$

$$\Omega_{\rm r,\nu} = 4.85 \times 10^{-9} \frac{\Delta r_{\rm core,\nu_1,\nu_2} D_{\rm L}}{(1+z)^2} \frac{\nu_1 \nu_2}{\nu_2 - \nu_1} [\rm pc\,GHz] \quad , \tag{2.3.6}$$

where $D_{\rm L}$ is the luminosity distance in pc, z the redshift of the source, and the frequencies ν_1 and ν_2 are given in GHz. O'Sullivan & Gabuzda (2009) used $\Omega_{\rm r\nu}$ to estimate the equipartition magnetic field at 1 pc based on Hirotani (2005) assuming a spectral index α of -0.5,

$$B_{\rm 1pc} \simeq 0.025 \left(\frac{\Omega_{\rm r\nu}^3 (1+z)^2}{\delta^2 \psi_{\rm int} \sin^2 \theta_{\rm LOS}} \right) \quad . \tag{2.3.7}$$

However, at high frequencies the core can also be a recollimation shock instead of the $\tau = 1$ region (e.g., Daly & Marscher 1988; Gomez et al. 1995; Marscher 2009; Gómez et al. 2016). The shock-in-jet model suggests that the location of the mm-wavelength core is located at a distance of $10^{4-6}\,R_{\rm S}$, that has been supported by other observations (e.g., Marscher (2006); Agudo et al. (2011); Fromm et al. (2015). The measurements of M 87 mentioned above are supported by core-shift measurements up to 43 GHz yielding a distance of 14–23 $R_{\rm S}$ from the 43 GHz core to the black hole (Hada et al. 2011). The authors conclude that the difference can be explained by spine-sheath structured jet, in which the spine is visible blazars due to the small viewing angle, while for radio galaxies the sheath dominates.

The intensity measured from given source can be related to a black body with brightness temperature $T_{\rm b}$ following $S_\nu = 2kT_{\rm b}\nu^2/c^2$ in the Rayleigh-Jeans limit. Kellermann & Pauliny-Toth (1969) showed that for already small deviations from $T_{\rm b,IC} \sim 10^{12}$ K strong cooling of the synchrotron photons takes place due to IC. This is commonly referred to as the *inverse-Compton limit*. However, the value of $T_{\rm b,IC}$ changes for example for proton jets, non-equipartition jets (e.g., Kellermann 2002). Readhead (1994) considers the limit from equipartition of the magnetic field and particle energy $T_{\rm b,eq} \sim 10^{11}$K to be more reasonable limit (see also Singal 2009).

The kiloparsec-scale (hereafter kpc-scale) jets of radio galaxies terminate due to interaction of the jet plasma with the interstellar or intergalactic medium which can lead to the formation of so-called *radio lobes* or the dissipation of the jet (e.g., Bridle & Perley 1984). Blazar also show a large variety of morphologies on kpc scales and their large scale properties are related to the pc scale jet (Cohen et al. 2007; Kharb et al. 2010). The morphology of the large scale emission is strongly affected by interaction with the ambient medium and Kelvin-Helmholtz instabilities, thus their simulations and the description of the emissivity require rather different parameters than for pc scale jets (e.g., Perucho & Martí 2007; Hardcastle & Krause 2013 and references therein). Since the jet emission covers many order of magnitude in spatial scale, simulations commonly focus

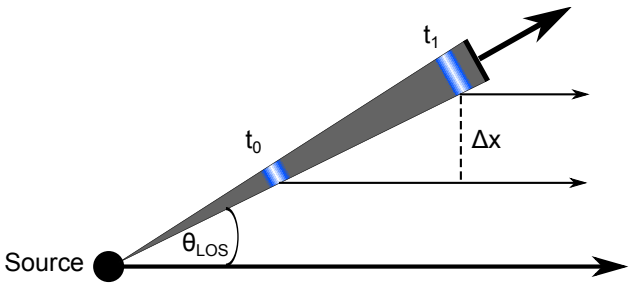

Figure 2.5: The jet of a *Source* is inclined at an angle $\theta_{\rm LOS}$ to the line-of-sight of the *Observer* who is located at a distance D. A feature of the jet travels a projected distance Δx from time t_0 to t_1.

specific parts of the jet.

2.3.4. Relativistic effects

Superluminal motion

One of the most striking effects of the relativistic beaming of jet emission is the motion of features in the jet with apparent velocity $v_{\rm app} > c$, also known as superluminal motion (Rees 1966). It is commonly observed in radio-loud AGNs at various frequencies (e.g., Ghisellini et al. 1993; Zensus 1997; Jorstad et al. 2001b; Kellermann et al. 2004; Lister et al. 2013).

However, this phenomenon is a projection effect of the relativistic motion projected on the plane of the sky. Figure 2.5 illustrates the conditions for superluminal motion. A source is located at distance D from the observer with a jet inclined at an angle $\theta_{\rm LOS}$ to the line-of-sight. A feature in the jet moves with velocity v from time step t_0 to $t_1 = t_0 + \Delta t$ travelling an observed projected distance of Δx in time $\Delta t_{\rm O}$. The apparent velocity $v_{\rm app}$ can be expressed via,

$$v_{\rm app} = \frac{\Delta x}{\Delta t_{\rm O}} = \frac{v \Delta t \sin\theta_{\rm LOS}}{\left(1 - \frac{v}{c}\cos\theta_{\rm LOS}\right)\Delta t} \tag{2.3.8}$$

$$\Rightarrow \beta_{\rm app} = \frac{v_{\rm app}}{c} = \frac{\beta \sin\theta_{\rm LOS}}{1 - \beta\cos\theta_{\rm LOS}} \quad . \tag{2.3.9}$$

Figure 2.6 shows exemplary how $\beta_{\rm app}$ depends on $\theta_{\rm LOS}$ for different intrinsic velocities β. If β approaches c, superluminal motion can be observed for a wide range of inclination angles $\theta_{\rm LOS}$. The minimum β-value which can still reach $\beta_{\rm app} = 1$ is $\beta_{\rm min} = \sqrt{0.5}$. The dashed line in this Figure highlights the maximum apparent velocity $\beta_{\rm app,max}$ which traces the critical angle $\theta_{\rm LOS,crit}$ with $\cos\theta_{\rm LOS,crit} = \beta$ and the Lorentz factor γ with $\beta_{\rm max} = \sqrt{\gamma^2 - 1}$ where $\gamma = 1/\sqrt{1-\beta^2}$. Another way to estimate

VLBI observations of radio jets measure structural changes in the jet in angular units, e.g., mas per year. In order to convert the angular velocity μ into $v_{\rm app}$ the redshift z of the source has to be taken into account due to the expanding nature of the Universe (see

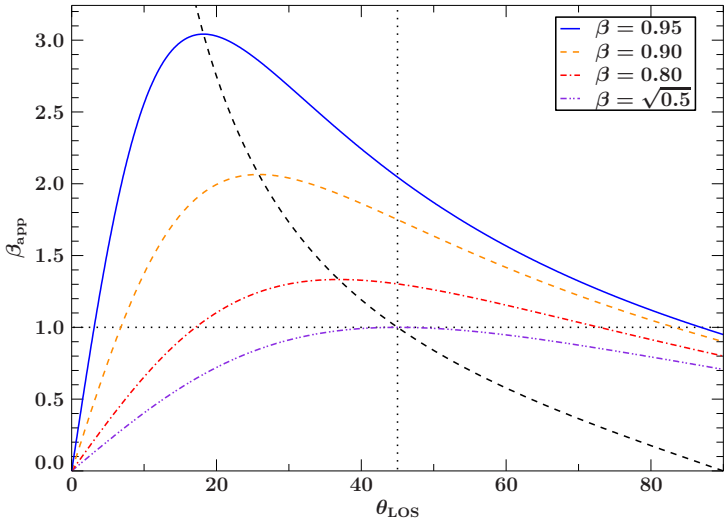

Figure 2.6: The apparent velocity $\beta_{\rm app}$ with respect to $\theta_{\rm LOS}$ for different intrinsic jet velocities. The dashed lines shows the shift of the maximum $\beta_{\rm app}$ for a given β. The dotted lines intersect with the maximum of $\beta = \sqrt{0.5}$, which is the lowest possible value of β which can reach $\beta_{\rm app} = 1$.

e.g., Chodorowski 2005 for discussion),

$$v_{\rm app} = \frac{\mu D_{\rm L}}{c(1+z)} \quad , \tag{2.3.10}$$

where $D_{\rm L}$ denotes the luminosity distance. Hence, the additional (1+z)-factor becomes increasingly important for z>0.01.

In consequence, unless the source is oriented very close to the plane of the sky the observer will always measure an apparent motion. This gives rise to the inversion problem discussed in the next following.

The inversion problem

The emission from highly relativistic jets observed at a small angle to the line of sight is relativistically boosted (e.g., Urry & Padovani 1995)

$$L_{\rm obs} = \delta^n L_0 \quad , \tag{2.3.11}$$

where $L_{\rm obs}$ is the observed luminosity, L_0 the intrinsic luminosity, $\delta = (\gamma(1-\beta\cos\theta_{\rm LOS}))^{-1}$ the Doppler factor and $n = p - \alpha$ depends on the spectral index α. The parameter p depends on the geometry of the observed emission region, i.e. an isolated feature ($p = 3$) and a smooth jet ($p = 2$).

As a result, without knowledge of β and $\theta_{\rm LOS}$, it is not possible to calculate L_0 and γ uniquely. Vice versa, if either L_0 or δ are unknown, $\beta_{\rm app}$ and $L_{\rm obs}$ cannot be determined. This is known as the *inversion problem* and it has been extensively studied by Cohen et al. (2007). The study showed that, however, statistical arguments can be for a sample of sources with $\gamma \gg 1$.

The inclination angle of the jet

Under the assumption that the two jets in AGN are intrinsically symmetric, the intrinsic flux density of both jest is the same. Hence, the ratio of the emission of the approaching S_J and the receding S_cJ jet, i.e. the jet and counter jet, is the related to β and θ as

$$R = \frac{S_\mathrm{J}}{S_\mathrm{cJ}} = \left(\frac{1+\beta\cos\theta_\mathrm{LOS}}{1-\beta\cos\theta_\mathrm{LOS}}\right)^n \tag{2.3.12}$$

While S_J and S_cJ can be measured from radio imaging, β remains unknown. This problem can be solved if β_app is known. As both, R and β_app, depend on β and θ_LOS, the combination can be used to trace the parameter range of β and θ_LOS. Examples are given in Sect. 3.3 and Subsect. 4.4.1. Based on this constraints on δ can be calculated.

In the absence of such information, a limit on δ and θ_LOS can also be inferred from variability in the light curve (e.g., Lähteenmäki & Valtaoja 1999; Hovatta et al. 2009; Fromm et al. 2013).

2.4. Radio observations of jets

Observations of AGNs are performed throughout the entire electromagnetic spectrum with ground- and space-based instruments. As shown in the previous sections of this chapter, synchrotron emission dominates the low-energy regime of AGNs. This section summaries the principles of radio astronomy with a particular focus on interferometry related to the data presented in this work. It is primarily based on Taylor et al. (1999), Thompson et al. (2001), and Wilson (2011). As different instruments were used for the observations of IC 310, PKS 2004−447, and 3C 111specific details on the data reduction are given in the corresponding chapters.

Radio astronomy covers the wavelength (frequency) regime $\gtrsim \mathcal{O}(10^2)\,\mu$m ($\lesssim \mathcal{O}(10^0)$ THz). However, Earth's atmosphere is not fully opaque over the complete frequency regime. At wavelengths $\gtrsim \mathcal{O}(10^0)$ m ($\lesssim \mathcal{O}(10^2)$ MHz) the ionosphere starts to affect observations, while at wavelengths $\lesssim \mathcal{O}(10^0)$ cm ($\gtrsim \mathcal{O}(10^1)$ GHz), the mm/sub-mm regime, it is the troposphere that causes disturbances due to water vapour and molecules (e.g., Carilli et al. 1999; Erickson 1999; Wilson 2011).

2.4.1. The single-dish

A fundamental difference in the design of radio telescopes is related to the desired frequency range. At frequencies above a few hundred MHz a reflector is commonly used to focus the incident electromagnetic emission onto a receiver or sub-reflector. Depending on the wavelength, the reflector or *dish* can be mesh-like or solid (see Fig. 2.7b–d), while at lower frequencies a simpler design of dipoles for example are sufficient to receive the emission (see Fig. 2.7a). However, the transition is not sharp. Other differences in the design are related to the optical system, i.e. the location of the receiver and the mount of the telescope.

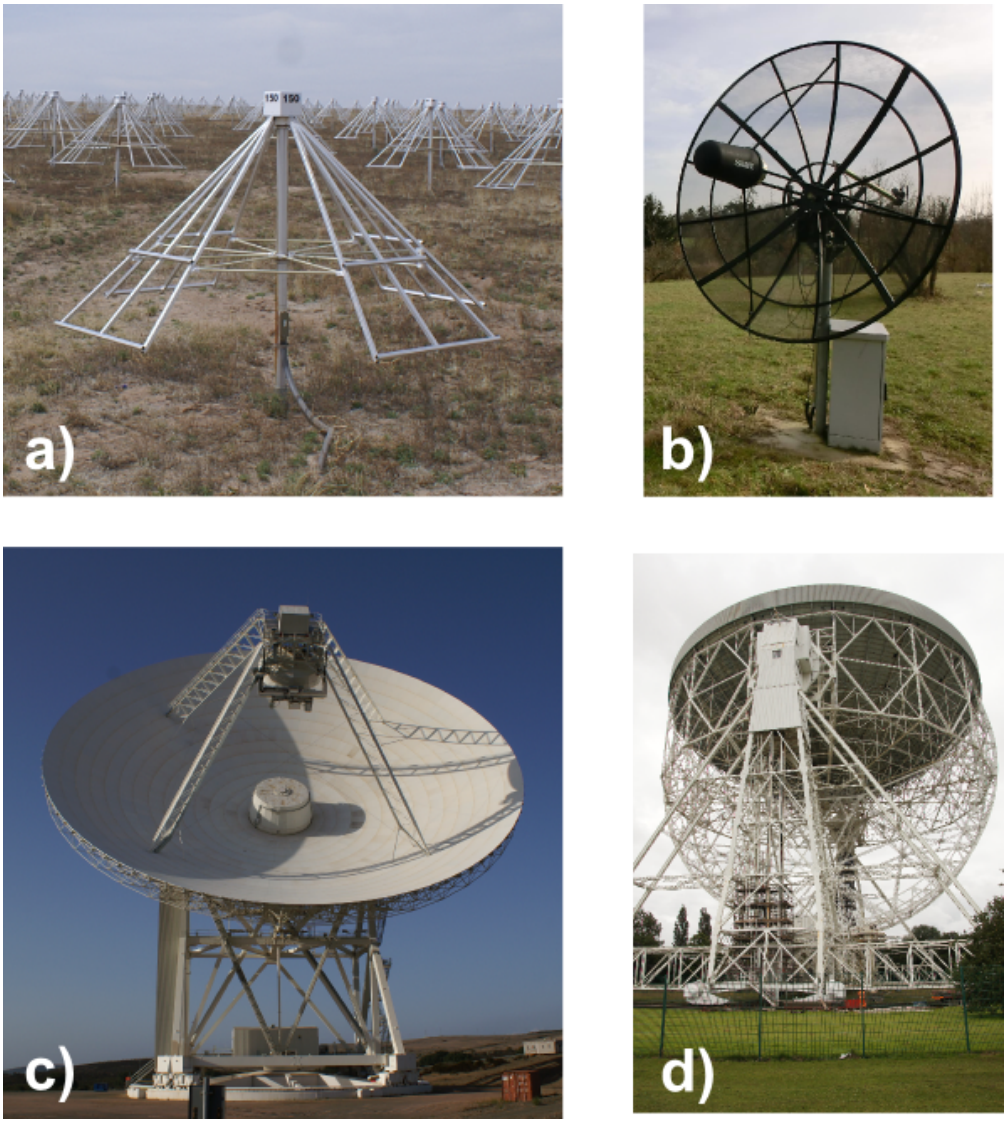

Figure 2.7.: Gallery of selected radio telescopes: (a) antenna of the Long Wavelength Array (LWA, New Mexico, USA), (b) Small Radio Telescope (Bamberg, Germany), (c) Sardinia radio telescope (Sardinia, Italy), (d) Lovell Telescope (Jodrell Banks, England).

The power received by a radio telescope is a convolution of the brightness distribution $B(\nu, \theta, \phi)$ of the source and the reception pattern $\Theta(\nu, \theta, \phi)$ of the telescope accounting for the effective area $A_e(\nu)$ and integrating over the frequency and solid angle

$$P = \int A_e(\nu) \int \Theta(\nu, \theta, \phi) B(\nu, \theta, \phi) \mathrm{d}\nu \mathrm{d}\Omega \quad . \tag{2.4.1}$$

Thus, the performance of the aperture of a radio telescope with respect to the reception of radiation depends on A_e and $\Theta(\nu, \theta, \phi)$. The latter can be interpreted as a result of the interference pattern of waves on the reflector. It can be described as a *beam* with a dominant *main lobe*, the so-called *primary beam*, and various smaller side lobes. The beam is optimized so that the emission from the source is received by the main lobe and unwanted signals due to the side lobes are minimized. The *full-width at half maximum* (FWHM), also called the *half power beamwidth*, of the main lobe determines the angular resolution or *field of view* of the telescope and depends on the wavelength and diameter D of the dish as

$$\mathrm{FWHM} = k \frac{\lambda}{D} \quad , \tag{2.4.2}$$

where k is in first-order approximation unity and depends on the geometry of the aperture.

A_e is related to the geometric area A_g of the telescope via the aperture efficiency η as $A_e = \eta A_g$. The product of A_e and the beam solid angle, i.e. the beam integrated over solid angle, is equal to the wavelength squared. This relation shows that a trade-off between sensitivity and field of view is necessary. For a given frequency, a large effective area will lead to a better sensitivity at the cost of a decrease in the field of view. A similar quantity to the beam solid angle is the *gain*[6], i.e., the solid angle of a sphere divided by the beam solid angle. As the shape of the aperture changes with zenith angle, so-called *gain curves* are measured and used for calibration.

An equally important part of the performance of a telescope is the receiver that processes the radiation collected by the telescope. It is common practice to measure the output in terms of an *antenna temperature* T_A. It corresponds to the temperature of a resistor that is equivalent to the measured flux density in the Rayleigh-Jeans approximation

$$S = \frac{k\nu^2}{c^2} T\Omega \quad . \tag{2.4.3}$$

However, T_A contains not only the signal from the source, but additional contributions collectively referred to as the *system temperature* T_sys. Hence, another requirement of calibrating a radio telescope is to measure T_sys that is frequency dependent.

Another way of describing the performance of a radio telescope with respect to the system temperature, aperture efficiency and the surface area of a telescope is the *system*

[6]This should not be confused with the gain of the receiver, for example.

equivalent flux density (SEFD)

$$SEFD = \frac{T_{\rm sys}}{\eta A} 2\, k_{\rm B} \quad , \tag{2.4.4}$$

where the factor 2 stems from the fact that in case of an un-polarized source only half of the emission is measured by a single channel receiver. Larger telescopes usually have lower SEFDs which is important for heterogeneous interferometers (see next section). Equation 2.4.4 also demonstrates that a high $T_{\rm sys}$ at a particular observing frequency can increase the SEFD.

Practical considerations limit the size of a radio telescope and thus its angular resolution. The largest[7] fully steerable radio telescopes have been built up to a diameter of 100 m in Germany (100-m Effelsberg telescope, Wielebinski et al. 2011) and the USA (Green Bank Telescope, Prestage et al. 2009). However, even these large telescopes are only capable of reaching a resolution of a few tens of arcsec at the highest frequencies of about 90 GHz. Hence, in terms of AGN single-dish observations are often used to measure flux density light curves, line spectra and multi-frequency radio spectra. When interpreting radio spectra it is important to keep in mind the dependence of the FWHM on the frequency. If the observed source is sufficiently extended beyond the primary beam, it is possible that extended emission is missed by the telescope leading to a steepening of the spectrum.

In this thesis, data obtained with the 100 m Effelsberg telescope (Bad Münstereifel, Germany) and the Owens Valley Radio Observatory (California, USA, Richards et al. 2011) are used.

2.4.2. From interferometry to very long baseline interferometry

In a nutshell, the basic principle of interferometry is to measure the spatial coherence of incident emission at two or more primary antenna elements[8]. According to the van Cittert-Zernike theorem the Fourier transformation of the coherence function yields the intensity distribution of the source.

Interferometry in theory

A few assumptions are necessary to derive the basic equations that link the intensity distribution and the coherence function:

i) Emission that stems from different locations within the source is incoherent. Hence, the coherence functions differs only from zero, if the emission detected by the

[7] The largest radio telescope in the world is currently the Arecibo radio telescope (http://www.naic.edu/index_scientific.php in Puerto Rico with a diameter of about 300 m. It will be surpassed by the FAST radio telescope in China with a diameter of about 500 m (Nan et al. 2011). However, these type of radio telescopes are only capable of changing the location of the receiver and thereby alter the orientation of the beam on the sky in a limited range.

[8] Actually, the first interferometric observation was performed with the sea-cliff interferometer (McCready et al. 1947) that consisted of only a single receiving element (see also Sullivan 1991).

antenna element has the same origin.

ii) The space between the observer and the source is empty. Hence, the emission travels freely to the observer. The atmosphere of Earth is a particular good example that violates this assumption. However, this and other effects are usually dealt with during data reduction.

iii) The distance between the source and the observer is large enough that the far-field approximation can be applied, i.e., the incident wave fronts are planar. This has to be reconsidered, for example, in the case of observations of objects within the solar system.

iv) The angular size of the intensity distribution is small. This makes it possible to consider the intensity distribution of the source to lie within a plane tangential to the celestial sphere. For very extended sources or large field of views, this may not be the case any more.

The third assumption implies that the time delay τ_g of signal received at two stations separated by $\mathbf{b}$ from a source at $\mathbf{s}$ is simply $\tau_\mathrm{g} = \mathbf{b} \cdot \mathbf{s}/c$, the so-called *geometric delay*. It can be corrected before correlation to some extend by inserting an *instrumental delay*.

It is convenient to define a coordinates system, in which $\mathbf{s}$ with the components (l, m, n) is given relative to the *phase tracking center*[9] $\mathbf{s_0}$ as $\mathbf{s} = \mathbf{s_0} + \sigma$. The components of the baseline vector $\mathbf{b}$ are (u, v, w), where w is oriented in direction of $\mathbf{s_0}$ and is normal to the plane formed by u to the North and v to the East. The latter is also referred to as the (u, v)*-plane*. Because of the fourth assumption, the three dimensional case reduces to two-dimensions and the coherence function in the form of the *complex visibility* $V(u, v)$ is given by

$$V(u,v) = \int\int A(l,m) I(l,m) e^{-2\pi\imath(ul+vm)} \mathrm{d}l\mathrm{d}m \tag{2.4.5}$$

where $A(l, m)I(l, m)$ is the *modified brightness distribution*. $A(l, m)$ accounts for the beam of the primary antenna element and has to be considered in the end to retrieve the actual intensity distribution. However, in the following it is only referred to $I(l, m)$ for simplicity. $V(u, v)$ is commonly expressed in terms of an amplitude and phase[10]

Fourier transformation states that the inverse of equation 2.4.5 is

$$I(l,m) = \int\int V(u,v) e^{2\pi\imath(ul+vm)} \mathrm{d}u\mathrm{d}v \quad . \tag{2.4.6}$$

and this represents the case for the observer. However, an interferometer consists of a limited number of telescopes. Thus, it samples only a certain amount of spatial frequencies

[9] There are actually two more centers in radio interferometry, i.e. a *pointing center* and a *delay center*.
[10] However, it is stored as a complex number with a real and imaginary part.

in the (u, v)-plane and a sampling function $S(u, v)$ has to be introduced

$$I_D(l, m) = \int\int S(u, v)V(u, v)e^{2\pi\imath(ul+vm)}\mathrm{d}u\mathrm{d}v = B(l, m) * I(l, m) \tag{2.4.7}$$

where the last term stems from the fact that a convolution of two functions correspond to the product of the Fourier transform of the functions. $B(l, m)$ represents the point spread function of the interferometry, commonly called the *dirty beam* in radio astronomy and $I_D(l, m)$ the *dirty image*. The goal in data reduction is to use deconvolution methods to extract $I(l, m)$, which is also referred to as *imaging*. The quality of the image reconstruction depends predominantly on the sampling of $S(u, v)$. It can be improved by using the rotation of the Earth, because the (u, v)-coordinates depend on the zenith angle of the source with respect to the array. This process is called *Earth rotation synthesis*.

The minimum and maximum of the (u, v)-coverage also defines the maximum size and the resolution of the image, respectively. Similar to a single dish (equation 2.4.2), the resolution can be estimated using equation 2.4.2 if the longest baseline of the array is considered as the equivalent diameter of a synthesised dish.

Another important aspect of an interferometer, besides the resolution, is the sensitivity. It is necessary to differentiate the *baseline sensitivity* $\Delta S_{i,j}$, where i, j denote the baseline and the *image sensitivity* ΔI. A reasonable approximation for the former is given by

$$\Delta S_{i,j} = \frac{1}{\eta}\frac{SEFD_i \times SEFD_j}{\sqrt{2\Delta\nu\tau}} \quad , \tag{2.4.8}$$

where τ is the integration time and η and efficiency factor. Following Walker (1989), an estimate of ΔI can be obtained for single polarization from

$$\Delta I = \frac{1}{\eta\sqrt{\Delta\nu T_{\mathrm{obs}}}}\frac{1}{\sqrt{\sum_{i,i,i<j}\frac{1}{SEFD_i \times SEFD_j}}} \quad , \tag{2.4.9}$$

where T_{obs} is the observing time. equation 2.4.8 shows that even a baseline with a (small) telescope with a high SEFD value can reach sufficient sensitivity if it is paired with a (large) telescope with a low SEFD. This is also tremendously helpful for the whole array (equation 2.4.9), especially in case of heterogeneous arrays. A reasonably good image sensitivity can still be achieved by an array with several telescopes with high SEFDs, if it is also include a few telescopes with a low SEFD. Even though the high-SEFD telescopes may not detect the source on their baselines, it could still be detected on baselines with low-SEFD telescopes making the observation feasible.

Interferometry in practice

The data received by each station are combined in the *correlator* that performs the autocorrelation of the signals. This step needs significant amount of computational resources. First, the number of baselines scales with $N(N-1)/2$. Second, the number of visibilities depend on the observation time and the amount of initial time and frequency

averaging. Third, the incoming signal is commonly measured at not just one but several frequency bands with a bandwidth that is small compared to the observing frequency. These *intermediate frequencies* (IF) are shifted in small steps with respect to the observing frequency[11]. In addition, it is possible to perform observations with up to four polarisations, i.e. in terms of circular polarisation[12] left and right (LL, RR) and the cross-terms (LR, RL), which are later used to calculate the stokes parameters I, Q, U, and V.

Before deconvolution can be attempted, the data quality has to be inspected and if necessary data have to be flagged. In addition, the amplitudes have to be calibrated by applying measurements of the system temperatures for each telescope and the gain curve. At high frequencies, weather information are required to account for changes in the opacity of the atmosphere, in particular the troposphere. It also affects the phase, because the coherence time decreases at higher frequency. At lower frequencies, these effects are caused by the ionosphere. Another step is the bandpass calibration that is necessary due to changes over the finite bandwidth of the system.

In case of realistic data reduction, the integral in equation 2.4.7 includes additional functions which provide a weighting of the visibilities: *Natural weighting* treats every visibility equally. This results in the best signal-to-noise ratio (SNR). However, most interferometers have a higher sampling density at smaller baselines. Hence, it will lead to a down-weighting of the longest baselines. In contrast to this, in *uniform weighting* the visibilities are weighted according to their number density within a given region of the (u, v)-domain. While this decreases the SNR, it provides a higher angular resolution. A combination of both is *robust weighting*. In addition, it may be useful to weight a certain part of the visibility distribution in general. This is called *tapering* and it is often used as a Gaussian function. It provide the means to down-weight longer baselines in order to gain sensitivity for diffuse large scale emission.

Different deconvolution methods have been developed that are mostly based either on CLEAN (Högbom 1974) or MEM (e.g., Cornwell & Evans 1985). The former is a iterative process of building a model for $I_D(l, m)$, while the latter searches for a model that maximizes the entropy of the solution. A relatively new set of methods for deconvolution is based on compressed sensing (e.g., Wenger et al. 2010; Li et al. 2011). In the following, the focus lies on CLEAN, because it was used for all images presented in this work. In principle CLEAN works as follows.

1. Identify the brightest pixel in the image or within a user specified window. The use of windows improves the performance of CLEAN.
2. Subtract a delta component with flux density defined by a given gain factor (usually 2%–3% of the peak flux) multiplied by the dirty beam from the dirty image.
3. Go back to step 1 if significant flux density is left.

[11] Modern receivers can cover a broad frequency band with respect to the center frequency, e.g., the high-band of LOFAR covers 120 MHz to 160 MHz. The data are sometimes frequency averaged after the correlation during data reduction to reduce the computing time (e.g., de Gasperin et al. 2012).

[12] Some instruments such as ALMA use linear polarisation receivers (e.g., Marti-Vidal et al. 2014)

4. Approximate the dirty beam by an elliptical Gaussian distribution, the so-called CLEAN-beam, and convolve it with the CLEAN-model from steps 1 to 3. Finally, add the residuals to the image.

The resulting image from this procedure can sometimes be improved through *self-calibration* (e.g., Cornwell & Wilkinson 1981), i.e. the derived model is used to improve the calibration of the data. Naturally, this requires a high SNR and a sufficiently good initial model of the data. Self-calibration is based on the closure relations for amplitude and phase that do not depend on errors from individual stations. The *closure phase* is the sum of the phase of three telescopes, while the *closure amplitude* is the ratio of the amplitude of four stations. A major disadvantage of phase self-calibration the loss of absolute position information. The combination of imaging and self-calibration is also known as *hybrid imaging* and the process can be described in principle by the following steps.

1. Create a model of the brightness distribution iteratively using CLEAN and phase self-calibration.
2. Determine a constant gain for the amplitudes by performing amplitude self-calibration over the full time range. It is possible, but not necessary to also do phase self-calibration.
3. Rebuild the model as in step 1.
4. Now, perform amplitude self-calibration to calculate a gain that is constant over a fraction of the observing time.
5. Repeat steps 3 and 4 by successively lowering the time range for amplitude self-calibration until in the last step every visibility is self-calibrated
6. Perform a final CLEAN-step with a small gain and phase self-calibration over the full image.

CLEAN produces a model of the brightness distribution using δ-components. However, such a detailed model is not always feasible during analysis, for example in terms of a kinematic analysis of an AGN jet based on the identification of various features in the jet over a given period of time or if the brightness temperature of a jet feature is estimated. Here, a simpler approach still yields good results. Based on the self-calibrated image, the CLEAN-model is replaced by a limited number of two-dimensional Gaussian functions which are fit directly to the visibilities. This procedure is called *model fitting*.

Equation 2.4.9 provides a way to gain an estimate of the image sensitivity. However, the equation cannot account for observational and technical difficulties, but it is still sufficient for planning an observation. In practice, the image sensitivity is calculated based on the final CLEAN-image. In this thesis, the method by Böck (2012) is adopted that fits a Gaussian distribution to a source-free region of the CLEAN-image. In order to differentiate from the theoretical approximation, the actual image sensitivity is denoted as σ.

A variety of connected-element interferometers exists that cover the tens or hundreds of MHz regime, e.g., the *Murchison Widefield Array* (WA, Tingay et al. 2013), the *Long Wavelength Array* (LWA, Ellingson et al. 2009), and *Low Frequency Array* (LOFAR, van Haarlem et al. 2013), up to hundreds of GHz, e.g., the *Atacama Large Millimeter/submillimeter Array* (ALMA, Wootten & Thompson 2009) and the *Submillimeter Array* (SMA, Ho et al. 2004). In this work, data from the *Very Large Array* (VLA, Perley et al. 2011) and *Australia Telescope Compact Array* (ATCA, Wilson et al. 2011) are presented.

The most widely used software packages for reducing interferometric data are `AIPS`[13] (Greisen 2003), `CASA`[14] (McMullin et al. 2007), and `MIRIAD`[15] (Sault et al. 1995). However, only `AIPS` is capable of performing the specialised tasks necessary for VLBI data as described in the next section. Hence, it was used for all calibration steps prior to imaging. The remaining calibration procedures as well as model fitting were performed with the software package `DIFMAP`.

What makes VLBI special

The most distinct feature of VLBI is the missing real-time link between the telescopes of the array. This requires that each station has its own clock for time referencing, but it also allows a distribution of the telescopes around the world. Hence, VLBI arrays can have baselines above 10^4 km on Earth or even longer if a satellite is part of the array. The array can have a very heterogeneous design, consisting of telescopes of different size and characteristics that belong to individual institutes and are only used for VLBI for a limited amount of their observing time. In fact, most VLBI arrays work this way, with notable exceptions being e.g., the *Very Long Baseline Array* (VLBA, Napier 1994) and the *Korean VLBI-Network* (KVN, Lee et al. 2014).

Usually, each telescope needs to record the data on disks that have to be shipped to the correlator, which presents a considerable logistical effort. However, the use of high-speed internet connections as for example offered by the *European VLBI Network* (EVN, Venturi 2010), makes it possible to directly transfer the data to the correlator, though such *eVLBI*[16] observations are not yet standard.

A significant issue directly affects the calibration of the data: the atmosphere at each station is uncorrelated leading to a decrease in the quality of the phase measurements. Additionally, different clocks at different stations will also introduce errors. The correlator model can only corrected these problems to some degree. As a result, the phase will show a slope over time and frequency, also known as the *fringe rate* and *fringe delay* that hast to be corrected for. It may also lead to an offset between IFs. A way to correct these effects is provided by the method of *fringe fitting* (e.g., Schwab & Cotton 1983; Cotton 1995) that is applied in two steps

- *The manual phase calibration* is a fringe fit on a single scan that removes the fringe

[13] http://www.aips.nrao.edu/index.shtml
[14] http://casa.nrao.edu/
[15] http://www.atnf.csiro.au/computing/software/miriad/
[16] http://www.evlbi.org/

rate and delay within an IF. The fringe rate of the reference antenna will be set to zero. The solutions from the fit are applied to the whole data. For global arrays in which not all telescope observe the source simultaneously, it may be necessary to perform multiple manual phase calibration on parts of the array which are linked through different reference antennas.

- *The global fringe fit* searches for delays and rates over all the IFs for each telescope and each scan. This should correct any residual offset between the IFs and zero phase.

The step of fringe fitting can be applied before and after amplitude calibration, but it is usually done before the bandbass calibration. It represents a calibration procedure distinct to VLBI. A critical issue especially of the manual phase calibration is a sufficiently high SNR of the target. This cannot be guaranteed since the majority of AGNs are relatively weak sources. To this purpose, a strong source is observed alternately that serves as a calibrator. The solutions found by the manual phase calibration for the calibrator are then applied to the target source.

Hybrid imaging is widely used in VLBI. Hence, the absolute position information of the source is in general not available. In terms of jets in AGNs, this has a profound impact as it hinders a measurement of the distance of the jet to the black hole, for example. However, there are methods such as phase referencing which provide means to regain this information.

For the majority of the VLBI data presented in this thesis, the hybrid-imaged data were model fitted with circular or elliptical Gaussian components in `DIFMAP`. Since the size of these components vary, it is common practice to normalize the total flux of the component S_{comp} by its size and express the result in terms of a *brightness temperature* T_{B}. Replacing Ω in equation 2.4.3 with the FWHM of an elliptical Gaussian, this yields (e.g., Kovalev et al. 2005)

$$T_{\mathrm{B}} = \frac{2\ln 2}{\pi k}\frac{S_{\mathrm{comp}}(1+z)c^2}{\nu^2 a_{\mathrm{maj}} a_{\mathrm{min}}} \quad , \tag{2.4.10}$$

where a_{maj} and a_{min} are the major and minor FWHM of the component. It is possible that the fit of a_{maj} and a_{min} becomes very small, even zero. Even in these cases, an upper limit on the size a_{lim} and thereby a lower limit on T_{b} can be obtained following Lobanov (2005)

$$a_{\mathrm{lim}} = 2^{2-\xi/2} b_{\phi} \sqrt{\frac{\ln 2}{\pi} \ln\left(\frac{SNR}{SNR-1}\right)} \quad , \tag{2.4.11}$$

where b_{phi} is the size of the CLEAN-beam in direction of the position angle ϕ and ξ is 2 for uniform weighting and 0 for natural weighting. The signal-to-noise SNR of the component is calculated from the ratio of its peak flux density and the noise level from the image based on the Gaussian components, because it usually has a higher noise level than the CLEAN-image and it is thus more conservative. Since a_{lim} depends on the SNR, it can be smaller than the size of the beam. A different approach to over-resolution

was presented by Martí-Vidal et al. (2012). Recently, Lobanov (2015) demonstrated that it is possible to determine T_b directly from the visibility data.

A disadvantage of `DIFMAP` is that it does not provide a way to estimate the uncertainties of the model fit components. A first-order approximation is given by Fomalont (1999) based on the SNR of the component, which was adapted by Lee et al. (2008), but the uncertainties may be larger. A more sophisticated approach, where the uncertainties are directly determined from the fit to the visibilities, was recently presented by Martí-Vidal et al. (2014). Großberger (2014) developed a method to perform model fitting for multiple observations at the same time and calculate the uncertainties using χ^2-statistics. It is made possible by linking `DIFMAP` to *Interactive Spectral Interpretation System* (ISIS, Houck & Denicola 2000) that performs the actual minimization of χ^2. However, the computing time for these calculations increase quickly with the number of model fit components and thus free parameters, which is why it was only used in specific cases. Further details on the model fitting are given in the corresponding chapters. In general, no phase self-calibration was used for the model fitting in `DIFMAP`.

While connected interferometers reach angular resolutions down to hundreds of mas at the highest frequencies, VLBI provide resolutions down to tens of μas (e.g., Krichbaum et al. (2008); Tilanus et al. (2014)). This allows the study for example of jets in AGNs on sub-pc scales. The data presented in this work were obtained with the VLBA, EVN, the Global mm-VLBI array (GMVA, Krichbaum et al. 2008) and a heterogeneous array of austral telescopes used by the TANAMI programme (Kadler et al. 2015).

3. The pc-scale structures of AGN jets and their high-energy connection

VLBI observations provide the only means for the majority of AGNs to probe the pc-scale jets and directly gain information on the inclination angle of the jet to the line-of-sight as well as intrinsic jet properties such as the Doppler factor. These studies are vital for a better understanding of the high-energy emission observed in AGNs. Long-term observations and if possible a large sample to perform statistical analyses are required. This chapter will further elaborate the link between radio and high-energy emission in AGNs focusing in particular on the γ-ray emission. Sect. 3.2 and 3.3 introduce two major monitoring programmes with a special emphasis on recent results that I obtained as part of the TANAMI collaboration.

3.1. The radio-γ-ray connection in AGN jets

The first sample studies of the radio and γ-ray connection in AGNs were made possible due the all-sky survey of the *Energetic Gamma Ray Experiment Telescope* (EGRET) on board the *Compton Gamma-Ray Observatory* (*CGRO*) between 1991 and 1995 (e.g., Hartman et al. 1999 and references therein). These established that the prominent class of γ-ray sources are blazars (e.g., Reich et al. 1993; Hartman et al. 1999; Sowards-Emmerd et al. 2003, 2004). The continuous monitoring of the γ-ray sky by *Fermi*-LAT since 2008 provided a significant boost thanks to improved data sampling, sensitivity and source detection that also lead to an increase in the detection of non-blazars, such as radio and Seyfert galaxies (Massaro et al. 2016 and references therein). EGRET-based studies of the radio and γ-ray luminosities were able to show a strong correlation for AGNs due to various limiting factors. This changed, however, with the *Fermi*-LAT and a statistically significant correlation was found for all blazars and also for BL Lacs and FSRQs separately (e.g., Ackermann et al. 2011 and references therein).

Comparison of AGN populations

A prominent question is whether γ-ray-loud and -quiet AGNs are significantly different from each other intrinsically. VLBI observations of γ-ray-detected AGNs showed that they are usually compact, exhibit high brightness temperatures and often superluminal apparent speeds. Although these are not entirely unique characteristics of γ-ray-loud AGNs, they provide evidence that Doppler boosting plays a crucial role as required by theoretical models (e.g., von Montigny et al. 1995; Impey 1996; Moellenbrock et al. 1996; Jorstad et al. 2001b; Kovalev et al. 2009; Müller 2014; Böck et al. 2016). Piner et al. (2007)

reported no statistical difference for example in the proper motion of EGRET-detected and non-detected sources. However, other studies on EGRET- and later *Fermi*-LAT-detected sources concluded that γ-ray-quiet AGNs exhibit lower apparent speeds than γ-ray-loud ones (Kellermann et al. 2004; Lister et al. 2009b; Piner et al. 2012). In general, BL Lac objects seem to have lower Doppler factors than FSRQs, which is explained by a selection bias with less BL Lacs detected at higher redshifts (e.g., Giroletti et al. 2004b; Kellermann et al. 2004; Hovatta et al. 2009; Lister et al. 2013). Intriguingly, BL Lac objects dominate at TeV-energies (e.g., Holder 2012 and TeVCat) showing often low (compared to FSRQs) to no apparent motion and low radio emission consistent with low to moderate Doppler boosting (e.g., Giroletti et al. 2004a; Piner & Edwards 2004; Piner et al. 2007; Lister et al. 2015 and references therein). While this can be interpreted in terms of the blazar sequence, it challenges theoretical models (see Chapt. 2).

All other types of AGNs that are detected by *Fermi*-LAT are radio-loud and most of them have jets, but their numbers are limited (Massaro et al. 2016 and references therein). γ-ray-loud radio galaxies show both, sub- and superluminal motion. The few detected radio galaxies at TeV energies all exhibit subluminal motion on the smallest scales. However, in two γ-NLS1 superluminal motion has been suggested (D'Ammando et al. 2013b; Karamanavis 2015).

A link between radio flux density variability and detectability by *Fermi*-LAT seems to exist for FSRQs, but it is not evident for BL Lacs which could be due to differences in the underlying process that produces the γ-ray emission (Richards et al. 2014 and references therein). Furthermore, instrumental bias has to be considered for *Fermi*-LAT as the detection depends on the shape and peak of the high-energy spectrum (Lister et al. 2015).

The location of the γ-ray emission region

Multi-wavelength observations are essential to shed light on the nature of the γ-ray emission for which various models have been suggested such as SSC, IC and EC (see Sect. 2.3). This issue is closely related to the origin of the γ-ray emission with respect to the jet, for example in the shock-in-jet model Marscher (2009). It requires simultaneous high-resolution VLBI observations and flux density measurements in combination with γ-ray monitoring as well as monitoring in the optical to X-ray regimes, if possible.

Radio flares coincide with the appearance of new features of the VLBI jet (e.g., Marscher & Gear 1985; Valtaoja et al. 1999; Savolainen et al. 2002) and this link seems to extend to the γ-ray regime. Jorstad et al. (2001b,a) reported a correlation between γ-ray flares and the appearance of new features in the pc-scale jet of EGRET-detected blazars. New plasma seemed to be ejected from the core before or close to a γ-ray-flare, suggesting that both emanate from the same shock region. A comparison of the high-frequency radio and γ-ray light curves indicate a time delay between flares in both energy regimes with the rise of the radio flare coinciding with the γ-ray flare (Lähteenmäki & Valtaoja 2003; León-Tavares et al. 2011). Recently, Fuhrmann et al. (2014) performed a detailed cross-correlation analysis of stacked radio and γ-ray light curves showing that the radio flare down to mm-wavelengths lags behind the γ-ray flare which is interpreted in

terms of an origin of the γ-ray emission upstream of the mm-core. However, the authors remarked that further single-source correlations have to be conducted. The upstream location of the origin of the γ-ray emission is also favoured by Max-Moerbeck et al. (2014) using 15 GHz monitoring by OVRO, but the authors also stress the difficulty of cross-correlation. Ramakrishnan et al. (2015) performed cross-correlations of *Fermi*-LAT and 37 GHz light curves for a sample of 55 AGNs. The study found a large range of positive delays between the high-energy and low-energy outburst, though most of the flares indicated co-spatial origin. However, in two cases the radio outburst preceded the γ-ray flare. In addition, Fuhrmann et al. (2014) suggested that BLR photons are responsible of the γ-ray emission which is supported by other studies such as Casadio et al. (2015a) on the radio galaxy 3C 120 and Rani et al. (2013) for the FSRQ 3C 273. However, Casadio et al. (2015b), for example proposed that SSC is a possibility in CTA102 as well. In addition, Meyer et al. (2012) favours EC for high-powered blazars. Several other studies have linked the occurrence of γ-ray-flares with the appearance of new components in the pc-scale jet, e.g., Marscher et al. (2010); Agudo et al. (2011); Schinzel et al. (2012); Karamanavis et al. (2016). As an example, Marscher et al. (2010) reported that a single new feature ejected into the pc-scale jet of PKS 1510-089 could be the cause for several optical and γ-ray-flares. However, not all γ-ray-flares can be associated with new VLBI components (e.g., Jorstad et al. 2001a; Casadio et al. 2015b,a) and cross-correlation techniques do not always find correlated high- and low-energy events (Ramakrishnan et al. 2015). The significance of the link between the radio and γ-ray activity as a tool to determine the γ-ray emission region has been questioned by Nalewajko et al. (2014).

An example for the difficult link between flares in both energy regimes is depicted in Fig. 3.1 that shows the radio-to-γ-ray light curve of CTA 102 based on data from Casadio et al. (2015b). The γ-ray flare in late 2012 is accompanied by an increase in radio flux density and high activity in other wavelength regimes. VLBI data of the sources reveal the appearance of a new component that moves with superluminal apparent speeds. However, the two other, smaller γ-ray-flares in 2011 and 2013 do not seem to have a multi-wavelength counterpart.

It is important to point out that the origin of the γ-ray emission from AGN is not exclusive to the pc-scale jet. Due to the spatial resolution of the LAT on board of *Fermi* this can only be studied well in close and extended sources. The most prominent example is Centaurus A. Abdo et al. (2010d) and Abdo et al. (2010e) studied the γ-ray emission from the central few kpc and the large radio lobes at a few hundred kpc. The former was interpreted as synchrotron self-Compton from a slow sheath in the jet, while the latter was attributed to inverse-Compton of CMB and EBL photons. According to Massaro et al. (2016) γ-ray emission from lobes could also be a scenario for FR II radio galaxies with strong contributions from the radio lobes such as 3C 111.

Unidentified γ-ray sources

A significant number (33%) of γ-ray sources in the 3FGL have no associations and it remains a challenge to find multi-wavelength counterparts. In this context, the term unidentified refers to γ-ray sources that have neither an identified nor an associated

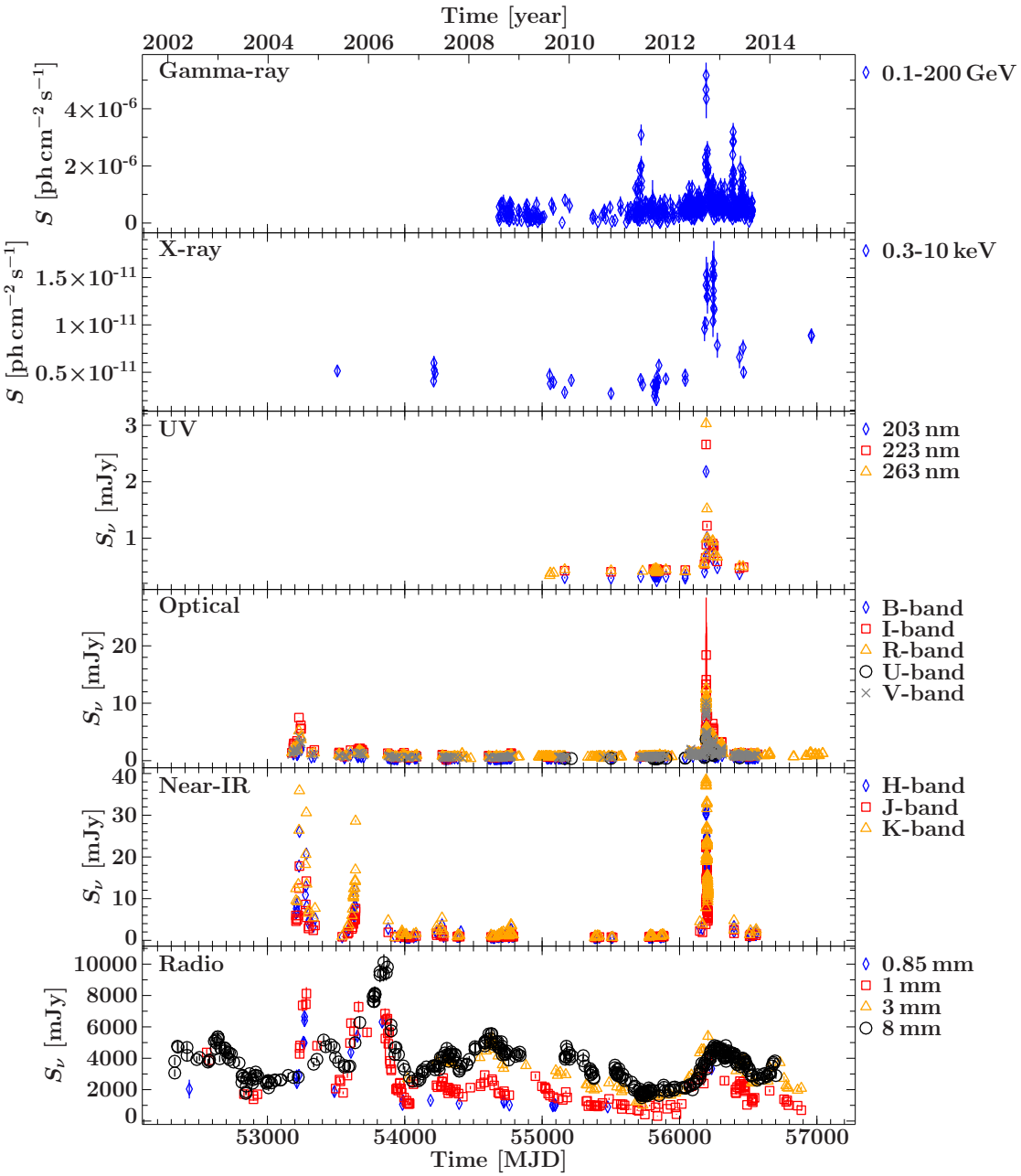

Figure 3.1.: Multiwavelength light curves of CTA 102 from the γ-ray, X-ray, optical, near-infrared to the radio millimeter regime (top to bottom). Note, the activity in the radio prior to the outburst without any counterparts at other wavelengths. Based on data from Casadio et al. (2015b)

source, although identification and association have technically different meanings in the context of *Fermi*-LAT (e.g., Acero et al. 2015). Different methods have been applied to find further associations using the full electromagnetic spectrum and statistical approaches (e.g., Acero et al. 2013; Massaro et al. 2013b,a; Schinzel et al. 2015, see also Massaro et al. 2016 for a review). Most of the unidentified γ-ray sources are distributed in the galactic plane, which exhibits a significant amount of diffuse γ-ray-emission and it is expected that the majority is explained by AGNs.

About 20% of unidentified γ-ray sources are localised in so-called *empty fields*, where no radio counterpart has been found in the error ellipse of *Fermi*-LAT (Schinzel et al. 2015). In case that these sources are AGNs, non-thermal emission is expected at different wavelengths which requires multi-wavelength observations. However, since most of the empty fields are located within the Galactic plane cm-wavelength radio observations may be hindered by scattering Taylor & Cordes (1993) and free-free absorption of matter inside the Galactic plane. A pilot project is currently under way that uses ALMA at mm-wavelengths for observations of fields where a X-ray source detected by *Swift* coincides with the *Fermi*-LAT sources and construct SEDs if counterparts are found (PI: C. Müller, R. Schulz). The effects of the galactic foreground are expected to be less strong at low wavelengths due to the frequency dependence of free-free absorption and scattering.

The radio-to-X-ray connection

A connection between the X-ray and radio properties blazars is also evident from the fact that the radio spectrum of blazars can often be described by a simple power-law (Kadler 2005 and references therein). In addition, a correlation has been reported for 3C 120 and 3C 111 between the activity of the VLBI jet and dips in the X-ray light curve Marscher et al. (2002); Chatterjee et al. (2011).

X-ray jets have been observed in AGNs though their origin is interpreted in a different way for FR I and II radio galaxies (Sambruna et al. 2004; Marshall et al. 2005 and references therein). In case of FR I the X-ray emission is considered to be due to synchrotron self-Compton, while in FR II it is due to inverse-Compton. However, this may not be true in all cases. Hogan et al. (2011) suggested a link between the detection of an X-ray jet with the strength of the extended emission of the AGN, which in turn has shown to be correlated with the apparent speed of the pc-scale jet by Kharb et al. (2010). This would allow the use of radio properties as a trigger for the detection of an X-ray jet.

3.2. The MOJAVE programme

The programme *Monitoring of Jets in Active Galactic Nuclei with VLBA Experiments* (MOJAVE, e.g., Lister & Homan 2005; Lister et al. 2009a, 2013) observes a sample of 259 AGNs above a declination of $-30°$ with the VLBA at 15 GHz. It was initially designed to study a radio flux density limited sample of AGN jets, but it has been expanded to low radio luminosity and γ-ray-detected AGN. According to Lister et al. (2013) the MOJAVE sample can be divided into three sub-samples:

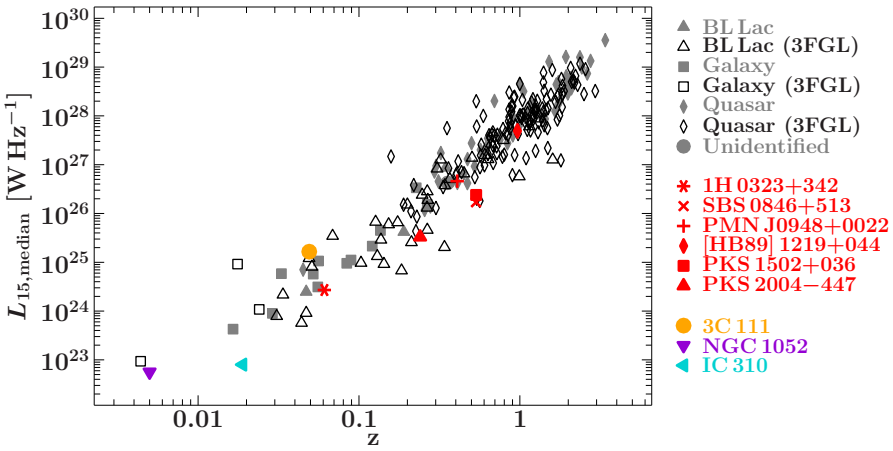

Figure 3.2.: The median 15 GHz VLBA luminosity distribution of the MOJAVE sources with known redshift. The gray, filled and black symbols represent the γ-quiet and -loud (2FGL selected) sources, respectively. Sources of specific interest to this work are highlighted in colour.

(i) The **Radio-selected MOJAVE 1.5 Jy Sample** is a complete sample of sources above $-30°$ declination which have a VLBA flux density at 15 GHz of $\geq 1.5\,Jy$ at least once between 1994.0 and 2010.0. In contrast to the earlier definition of the sample (Lister et al. 2009a) sources in the Galactic plane, i.e. $|b| \leq 10°$ are included as well. 94% of the 186 AGN of this sample are blazars (78% FSRQs, 16% BL Lacs).

(ii) The **γ-ray-selected 1FM Sample** is based on the first *Fermi*-LAT catalogue (Abdo et al. 2010b). It includes all γ-ray sources above $-30°$ declination and outside the galactic plane ($|b| > 10°$) which have γ-ray flux above 100 MeV of $\geq 3 \times 10^{-11}$erg cm^{-2} s^{-1} in the first 11 months of *Fermi*-LAToperations. Except for two γ-ray sources with no counterpart, the sample is complete.

(iii) The **Low-Luminosity Compact AGN Sample** contains 43 sources above $-30°$ declination with a 8 GHz VLBA flux density above 0.35 Jy and a redshift ≤ 0.3. In contrast to the two other sub-samples the low-luminosity sample is not complete.

Figure 3.2 shows the luminosity-redshift distribution of the MOJAVE sample presented in Lister et al. (2013) for all sources with known redshift as given in this study. They represent about 91% of the MOJAVE sample. The median radio luminosity at 15 GHz was calculated from the total image flux densities in Lister et al. (2009a) and Lister et al. (2013) using a spectral index of 0 for the K-correction. Figure 3.2 also highlights the γ-ray detected sources from MOJAVE. Lister et al. (2013) provided the associations with γ-ray sources from the second *Fermi*-LAT catalogue (2FGL, Nolan et al. 2012). As the third *Fermi*-LAT catalogue (3FGL, Acero et al. 2015) is available, the associations in Lister et al. (2013) were cross-checked with the 3FGL. Except for one source 4C +06.69 (MOJAVE designator 2145+067) all 2FGL sources were listed in the 3FGL as well. A search for new sources was not conducted.

The plot also highlights the γ-NLS1 sources which are observed by MOJAVE and PKS 2004−447 was added to this plot based on results from TANAMI (Schulz et al. 2016, see also the next section and Chapt. 5). IC 310, 3C 111, and NGC 1052 are also part of MOJAVE. As they are of special interest to this work (Chapters 4, Chapt. 6, and A) they have been highlighted in colour as well. 3C 111 is listed again in the 3FGL after being included only in the 1FGL, but it is not part of the third LAT AGN catalogue due to its location at a galactic latitude below 10° (3LAC, Ackermann et al. 2015). Of the highlighted sources only for 3C 111, NGC 1052, and [HB89] 1219+044 the structural evolution has been studied by Lister et al. (2009a) and Lister et al. (2013). However, there are kinematic studies available for 1H 0323+342 (Wajima et al. 2014; Karamanavis 2015; Furhmann et al. 2016, RAA submitted) and SBS 0846+513 (D'Ammando et al. 2013b). The analysis of MOJAVE data on IC 310 which is presented in Chapt. 4 represents the first kinematic study of this source.

Most of the BL Lac objects of the MOJAVE sample are γ-ray detected (Lister et al. 2011, 2013). Lister et al. (2011) found that the γ-ray-loudness, i.e., the ratio of the γ-ray to radio luminosity varies over four orders of magnitude. The γ-ray and median 15 GHz VLBA luminosities are shown in Fig. 3.3 with the γ-ray luminosity calculated following Lister et al. (2011). The γ-ray data were taken from the 3FGL using the same associations as for Fig. 3.2. The dashed lines highlight the logarithm of the γ-ray loudness from 0 to 4, i.e., from 10^0 to 10^4. The distribution of sources is consistent with Lister et al. (2011), though the figure shows more γ-ray-loud sources as the association was based on Lister et al. (2013). The γ-NLS1s all seem to fall within a γ-ray-loudness of 10^2 and 10^3 and the galaxies are located an order of magnitude below except for IC 310 (see also Chapt. 4). BL Lacs and quasars have similar median γ-ray-loudness values of ~ 270 and ~ 220, respectively. The two non-blazar γ-ray-loud classes exhibit larger differences with ~ 450 or ~ 520 (γ-NLS1) depending on whether PKS 2004−447 was considered or not and ~ 90 (radio galaxies). Lister et al. (2011) fit the luminosity distribution and obtained $L_{0.1-100\,\mathrm{GeV}} \propto L^{0.92\pm0.05}_{\mathrm{MOJAVE,median}}$. A linear regression fit to the data shown in Fig. 3.3 without errors and excluding PKS 2004−447 yields $L_{0.1-100\,\mathrm{GeV}} \propto L^{0.89\pm0.03}_{\mathrm{MOJAVE,median}}$ consistent with Lister et al. (2011).

In addition, BL Lac objects seem to show certain trends not visible for FSRQs: HSP BL Lacs have brightness temperatures below the average value of the sample and weaker polarization of the VLBI core Lister et al. (2011). The radio modulation index based on 15 GHz OVRO monitoring (Richards et al. 2011) is lower for HSP BL Lacs compared to other BL Lac objects and FSRQs. Lister et al. (2011) conclude that HSP BL Lacs have lower Doppler factors than LSP BL Lacs in line with previous studies, though both seem to stem from the same parent population. Moreover, the study concludes that the linear trend in the properties of BL Lacs does not favour the scenario that the high-energy peak is due to inverse-Compton from external photons.

An important factor in comparing γ-ray-loud and quiet samples is related to instrumental bias. This has been studied by Lister et al. (2015) using the population of γ-ray detected sources within the 1.5 Jy sample based on the 3FGL. The study finds that 23% of the sources were not detected and concludes that the energy regime covered by

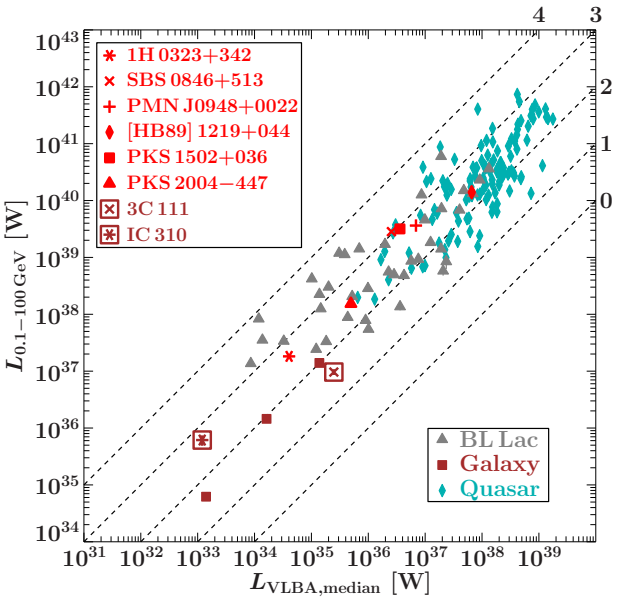

Figure 3.3: The 0.1–100 GeV γ-ray and median 15 GHz VLBA luminosity distribution of the MOJAVE sample. This plot was adapted from Lister et al. (2011) using the 3FGL data of the γ-ray-detected MOJAVE sources. However, the γ-ray associations are based on Lister et al. (2013) who used the 2FGL. Highlighted are the γ-NLS1 which are part of MOJAVE, PKS 2004−447, 3C 111, and IC 310. The letter three are also part of MOJAVE. The dashed lines indicate the γ-ray-loudness with respect to the 15 GHz VLBA luminosity in logarithmic steps from 0 to 4, i.e. from 10^0 to 10^4. Sources of specific interest to this work are highlighted in colour the top left legend.

Fermi-LAT is one of the reasons: Sources with low synchrotron peak will also have their high-energy peak at lower energies, possibly outside the *Fermi*-LAT energy range. In addition, the Doppler factor estimated from the radio flux density variability or the apparent speed can be a proxy for detection of γ-ray activity by *Fermi*-LAT. Both, high variability and high apparent speeds indicate high Doppler factors of the radio emission and this is a signature of γ-ray-loud AGNs. However, the authors also point out that Richards et al. (2014) reported a decrease in variability with increasing synchrotron peak frequency.

3.3. The TANAMI programme

The multi-wavelength study of a large sample of AGNs is by design one of the main drivers of the programme *Tracking Active Galactic Nuclei with Austral Milliarcsecond Interferometry* (TANAMI). To this purpose, it utilizes a variety of instruments in the radio, optical, X-ray, and γ-ray-regime to observe a radio and γ-ray-selected sample of more than 90 sources with declination <-30°. Unless otherwise mentioned, the details of the TANAMI programme presented here are based on Ojha et al. (2010); Böck (2012); Müller et al. (2014a); Kadler et al. (2015).

The scientific goals of TANAMI can be summarized as follows:

Multifrequency VLBI monitoring

TANAMI monitors its sample with (quasi)-simultaneous 8.4 GHz and 22.3 GHz VLBI observations (see below for details on the array) in order to perform kinematic and spectral index studies of the pc scale jet (e.g., Müller et al. 2011, 2014b). The multi-

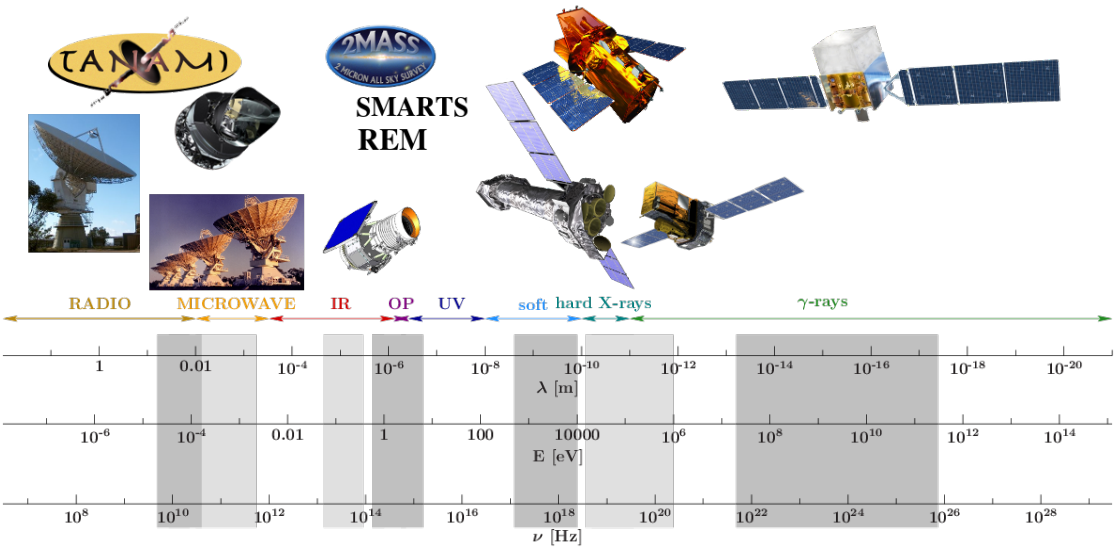

Figure 3.4.: The instruments used as part of the TANAMI programme and their frequency, wavelength, and energy coverage. The gray-shaded regions highlight the covered frequency ranges. (Credit: F. Krauss, C. Müller)

frequency high-resolution radio data provide important information on the jet properties such as inclination angle and Doppler factor.

Simultaneous spectral energy distributions

Fermi-LAT provides a constant monitoring of the γ-ray-sky. The combination with additional data from radio, optical, and X-ray observations (Fig. 3.4) allows the construction of (quasi)-simultaneous broad-band spectral energy distributions (e.g., Müller et al. 2014a; Krauß et al. 2014). This is vital to study the changes in the SEDs of the AGNs with time over the complete electromagnetic spectrum, i.e. in the flaring, quiescent or intermediate state (Krauß et al. 2013). It will also provide a vast catalogue of (quasi-)simultaneous SEDs (Krauß et al. 2016).

Multimessenger astronomy

The prospect of studying neutrinos from AGNs is another key stone of TANAMI since its beginnings. The focus of TANAMI on the southern sky is favourable for neutrino detectors such as IceCube, ANTARES and KM3Net. Hence, TANAMI is well suited to combine multi-wavelength information of AGNs with neutrino signals (Krauß et al. 2014; ANTARES Collaboration et al. 2015).

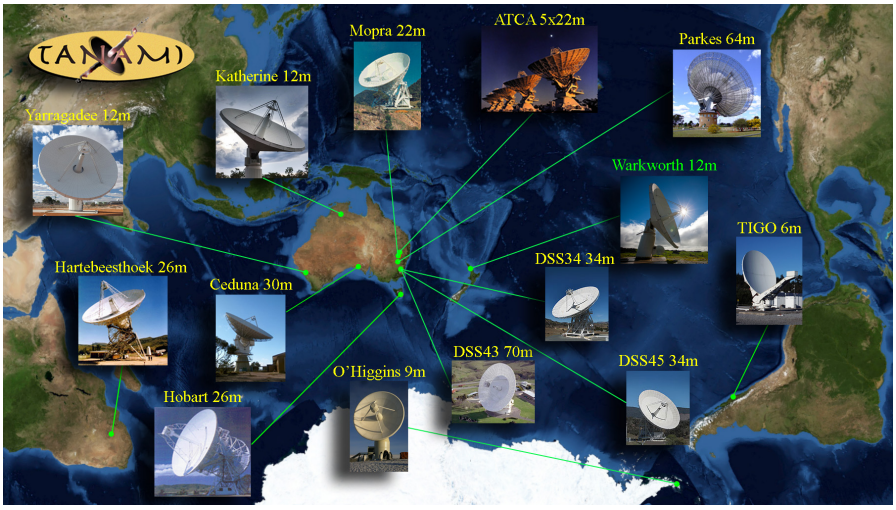

Figure 3.5.: Map of the radio telescopes used for the VLBI array in TANAMI and their location (Credit: M. Kadler, J. Wilms)

3.3.1. The VLBI array

TANAMI utilizes a heterogeneous array of radio telescopes (Fig. 3.5): The centrepiece is a network of VLBI stations (Preston et al. 1989) which comprises the five antennas of the *Long Baseline Array* (LBA), a station at Hartbeesthoek (South Africa), and two telescopes operated by the NASA Deep Space Network at Tidbinbilla. Two additional German telescopes operated by the Bundesamt für Kartographie und Geodäsie are used through the International VLBI Service. These are GARS at O'Higgins (Antarctica) and TIGO which has recently moved from Conception (Chile) to La Plata (Argentina). The (u, v)-coverage was recently improved through the inclusion of the two antennas of the Australian AuScope geodetic VLBI array (Lovell et al. 2013) at Katherine (Northern Territory) and Yarragadee (Western Australia), and two more telescopes (Johnston et al. 2007; Tzioumis et al. 2010), one at Warkworth (New Zealand) and the Australian SKA Pathfinder (ASKAP) station in Western Australia (Australia). Most of the transoceanic telescopes are not equipped with 22 GHz receivers. Hence, the (u, v)-coverage and resolution of TANAMI VLBI data are better at 8.4 GHz. A complete list of the telescopes is given in Table 3.3

The shortest baselines of $\sim$100–300 km are usually provided by Parkes, Mopra and ATCA, while the longest baselines (up to 10000 km) are reached with TIGO, O'Higgins, and Hartbeesthoek. The most sensitive antennas are ATCA, Parkes and DSS43/DSS45. Since the baseline sensitivity is predominantly determined by the antenna with the best sensitivity, i.e., lowest SEFD, TIGO and O'Higgins can still provide data even though they are relatively small and have a low sensitivity on their on. TANAMI observations can reach a sensitivity as low as 0.1 mJy/beam and a resolution down to 0.5 mas (e.g., Ojha et al. 2010; Müller et al. 2014b; Müller et al. in prep)

In practice, each VLBI session consists of 24 hrs observation of $\sim$ 20 sources. Each

Table 3.1.: The TANAMI sample

	BL Lacs[a]	Quasars[a]	Galaxies[a]	Unidentified[a]	total
γ-ray-loud[b]	16	42	5	8	71
γ-ray-quiet[b]	0	6	11	2	19
total	16	48	16	10	90

Note: [a]based on Böck et al. A&A accepted; Müller et al. in prep.; PKS 2004−447 was included in the γ-ray-loud Galaxies [b]Based on the 3FGL associations from Acero et al. (2015)

source is scanned for on average 10 min over a range of hour angles to ensure optimal (u, v)-coverage. The data is correlated on the DiFX correlator (Deller et al. 2007, 2011) at Curtin University in Perth, Western Australia. Details on the a-priori calibration, imaging and self-calibration specific to TANAMI are summarized in Ojha et al. (2010) (see also Sect. 2.4).

3.3.2. The sample

The sources of the TANAMI sample are located at declination $< -30°$. They were selected originally in two ways (Ojha et al. 2010 and references therein):

(i) A **Radio flux density limited** sample was selected under the condition of a 5 GHz flux density above 2 Jy and a flat radio spectrum between 2.7 GHz and 5.0 GHz

(ii) A **γ-ray selected** sample in preparation of *Fermi*-LAT observations which included all known γ-ray-detected AGNs by EGRET.

In addition, sources of special interest were included. Hence, the original TANAMI sample in Ojha et al. (2010) comprises 44 AGNs. With the beginning of operations of *Fermi*-LAT new γ-ray-detected AGNs were included, but also γ-ray-quiet sources were added to the sample based on their radio properties. Similar to MOJAVE, the TANAMI sample is biased towards the brightest radio and γ-ray-sources on the southern sky. The sample has grown to about 90 sources (Müller 2014; Böck et al. 2016; Müller et al. in prep.).

Table 3.1 lists the distribution of the optical classification of the AGNs in the TANAMI sample. For about 21 sources (23%) no redshift information is available. This fraction is higher than in the MOJAVE sample, though it is most likely a result of the availability of better spectroscopic data for the northern sources. In addition, some TANAMI sources are located within the galactic plane making it difficult to ascertain redshift information. The majority of sources are quasars similar to the MOJAVE sample and most of them are γ-ray-loud.

3.3.3. Results from TANAMI

Numerous studies have been performed with TANAMI data. Therefore, the following is a summary of recent results that I obtained or contributed to using radio data of TANAMI

sources.

AGN as possible neutrino sources

A major breakthrough in neutrino astronomy was the detection of extragalactic neutrinos up to PeV-energies with the IceCube neutrino detector (Aartsen et al. 2013; IceCube Collaboration 2013). Two of these events (EC14 and EC20) are located on the southern hemisphere. Krauß et al. (2014) analysed the AGNs of the TANAMI sample which coincided with the position of the neutrino events. Due to the large positional uncertainties of 13.°2 and 10.°7, respectively, of the two events three AGNs per event location were found in the TANAMI sample. Based on the X-ray to γ-ray SED of Krauß et al. (2014) were able to estimate the expected number of neutrinos from these sources. This suggests that the AGNs were capable of producing the neutrinos observed by IceCube, a conclusion that is supported by a follow-up study with the ANTARES neutrino detector (ANTARES Collaboration et al. 2015).

All of the analysed AGNs were quasars except for one BL Lac object (PMN J1717−3342). 8.4 GHz VLBI images by TANAMI revealed different pc-scale morphologies. A single-sided jet structure was found in the four sources PKS B0235−618, PKS B0308−611, PMN J1717−3342, and PMN J1802−3940. They all have a dominating bright compact VLBI core with brightness temperatures of $\sim 10^{11}$ K. One source, Swift J1656.3−3302, was only a single-baseline experiment though no detailed structural information could be obtained. The TANAMI VLBI image of PKS B0302−623 showed a symmetric radio morphology with compact core surrounded by halo-like emission with the brightness temperature of the core around 10^{11} K. The brightness temperatures indicated that the radio emission is beamed as expected from blazars.

Another PeV-neutrino event (IC35) was reported by IceCube based on three years of observations Aartsen et al. (2014). A search of AGN from the TANAMI sample located within the area of positional uncertainty of the event revealed 20 sources (Kadler et al. 2016). The study performed the same analysis as in Krauß et al. (2014) which revealed that one single source, PKS B1424-418, was bright enough to explain the neutrino flux. PKS B1424-418 showed a very strong increase of γ-ray activity over a period of one year coinciding with the detection of the neutrino event. In addition, it also showed the strongest increase of radio emission observed from a TANAMI source within 6 years of observations. The increase of flux density was located primarily in the compact core and took place over time frame of $\sim$ 16 months, though this may have been shorter as it is subjected to the cadence of VLBI observations. This is also reflected by an increase in brightness temperature from 4.2×10^{11} K to 13×10^{11} K within a region of projected size of 3 pc.

The inclination angle of the pc-scale jet of Centaurus A

Centaurus A is the closest AGN to Earth located at a distance of 3.8 Mpc (Harris et al. 2010). Due to its close proximity its emission can be spatially resolved with instruments in various parts of the entire electromagnetic spectrum (e.g., Kraft et al. 2002; Abdo

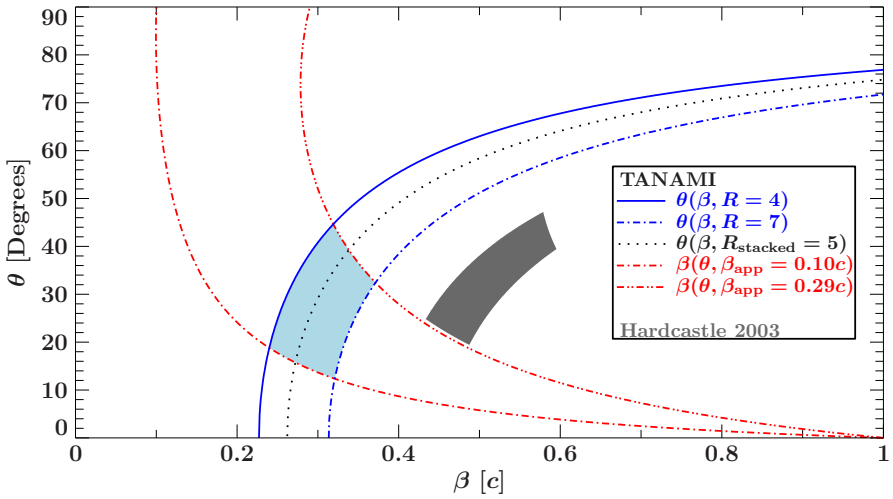

Figure 3.6.: Inclination angle θ and intrinsic speed β of Centaurus A from measurements of the jet-to-counter jet ratio R and apparent speed $\beta_{\rm app}$. The blue-shaded area highlights the allowed parameter space for θ and β. The grey-shaded area stems from the measurements of Hardcastle et al. (2003). Credit Müller et al. 2014b, A&A, 569, A115, reproduced with permission © ESO.

et al. 2010d,e; Müller et al. 2011; Feain et al. 2011). TANAMI VLBI observations at 8.4 GHz provide ultra-high spatial resolution down to 18 mpc (Müller et al. 2011, 2014b) revealing a double-sided jet with multiple emission features. Müller et al. (2014b) studied the structural changes in the pc-scale jet of Centaurus A with seven 8.4 GHz observations over $\sim$ 4.5 yrs revealing a subluminal apparent speeds increasing downstream of the jet which is interpreted in the context of a spine-sheath model as a possible explanation.

The measurements of the speed and jet-to-counter jet ratios of Centaurus A also provided the means of constraining the inclination angle of the jet to the line of sight $\theta_{\rm LOS}$ and the intrinsic jet speed β (see also Sect. 2.3.4). The result is shown in Fig. 3.6. The blue-shaded area depicts the allowed range of parameters for $\theta_{\rm LOS}$ and β which are $12^\circ \lesssim \theta_{\rm LOS} \lesssim 45^\circ$ and $0.24 \lesssim \beta \lesssim 0.37$, respectively. It is important to note that not all parameter combinations are permitted due to the shape of the blue-shaded area. Intriguingly, this analysis also shows that in order to explain the measurements on projected scales of hundreds of pc by Hardcastle et al. (2003), a significant increase in β is necessary while $\theta_{\rm LOS}$ does not change by much. This provides evidence for ongoing acceleration further downstream of the jet.

Arcsecond polarization and spectral index properties of TANAMI sources

The ATCA 20 GHz (AT20G) survey is a blind survey at 20 GHz below a declination of 0° with additional 4.8 GHz and 8.6 GHz observations (Murphy et al. 2010). The 4.8 GHz and 8.6 GHz observations were always simultaneous and the 20 GHz measurements were usually quasi-simultaneous to the lower frequency measurements. A significant fraction of sources in the TANAMI sample have been observed by the AT20G survey.

Table 3.2.: Fractional polarization of the TANAMI sample from AT20G observations

ν [GHz] (1)	N^{a} (2)	$m_{\mathrm{median}}{}^{b}$ [%] (3)	$m_{\mathrm{median}}{}^{c}$ [%] (4)
5	37 (23)	3.46 ± 0.13	2.3
8	37 (23)	2.80 ± 0.05	2.3
20	34 (28)	2.97 ± 0.06	2.5

Note: Columns: (1) frequency of AT20G observations; (2) number of sources with measured polarization and the number of sources with upper limits in brackets with the mean and median calculated by disregarding the upper limits; (3) mean fractional polarization in percent at frequency ν with standard error; (4) median fractional polarization in percent at frequency ν

Chhetri et al. (2013) used 6-km-baseline observations from the AT20G survey to estimate the compactness of the sources which the authors defined as the *6-km visibility*, i.e., the scalar ratio of the long baseline to the short baseline visibility amplitude. The study determined that sources with a ratio above 0.86 can be considered compacted based on a statistical analysis of the 6-km visibility sample. 65 TANAMI sources overlap with this sample and except for two sources, PKS 0244−470 and PKS 0625−354, all are classified as compact. Both sources are BL Lac objects with an FR I-like large-scale structure (Böck et al. 2016). Centaurus A, Centaurus B, PKS 2152−699, PKS 0521−365 and PKS 0518−458 (Pictor A) also have a compact 6-km visibility though they are flagged as extended, which suggests that most of the 20 GHz emission stems from a compact region (see also Burke-Spolaor et al. 2009).

Notable characteristics of the AT20G data for the TANAMI sources are the usually quasi-simultaneous observations at the three frequencies with a median of only 13 days and the measurements of polarization. Table 3.2 lists the mean and median polarization of the TANAMI sample from AT20G measurements. It also shows that about 40% of the sources with polarization information have only upper limits. While the median fractional polarization of the three frequencies is consistent, the mean indicate a small decrease with increasing frequency. However, this could be the result of the very high fractional polarization of $\sim$ 28.8% at 4.6 GHz by PKS 1333-337, while otherwise the polarization at all three frequencies goes as high as $\sim$ 10%. The median fractional polarization listed in Table 3.2 is consistent with an analysis of a flux-limited ($S_{20} > 500$ mJy) extragalactic AT20G sub-sample by Massardi et al. (2013), though a study of sources with $S_{20} > 250$ mJy suggested increasing fractional polarization from 4.8 GHz to 20 GHz by 17% (Massardi et al. 2011). An adequate comparison is the MOJAVE sample for which Lister & Homan (2005) reported average and median fractional polarization of (2.43 ± 0.19)% and 1.9%, respectively, at 15 GHz based on VLBA observations of 131 sources. These results are comparable, though similar to the AT20G measurements they represent an average over multiple emission zones in the jet. Individual jet features of the MOJAVE sources show much higher polarization up to 30% (Lister & Homan 2005; Hovatta et al. 2014).

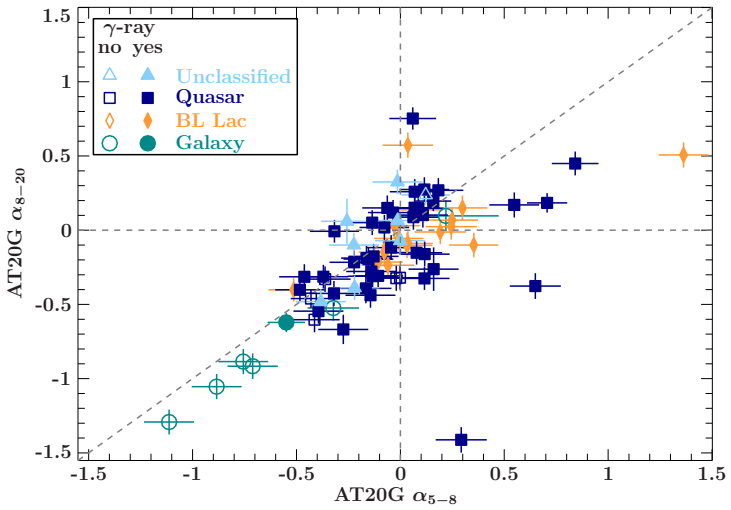

Figure 3.7: Spectral index between 4.8 GHz and 8.6 GHz and between 8.6 GHz and 20 GHz of TANAMI sources based on AT20G data. The diagonal line indicates a consistent power-law over all three frequencies, while deviations indicate changes in the spectral index. The horizontal and vertical dashed lines indicate how the spectral index changes. The γ-ray associations are based on the 3FGL.

The multi-frequency data provide the means of testing whether a simple power-law is sufficient to explain the radio spectrum. To this purpose spectral indices were calculated for the 4.8–8.6 GHz and 8.6–20 GHz bands with the results shown in Fig. 3.7. Most of the TANAMI sources have flat spectra, i.e. $-0.5 \lesssim \alpha \lesssim 0.5$ and are located along the diagonal of the diagram which means that their radio spectrum can be described well by a single power-law. Consistently steep spectral indices are only found in radio galaxies. PMN J1326−5256 and [HB89] 2052−474 are the most prominent exceptions from this case: The AT20G radio spectrum of the BL Lac object PMN J1326−5256 seems to change from inverted to flat. The steepening spectrum towards 20 GHz of [HB89] 2052−474 may be the result of variability as it represents a rare example for a large time delay of over two years between the 20 GHz and the low frequency observations. The same spectral analysis was performed on the complete extragalactic AT20G sub-sample by Massardi et al. (2011) who concluded that the dominance of flat radio spectra is a selection effect due to flux density limitation. This is also the case of the MOJAVE sample (e.g., Hovatta et al. 2014).

The γ-ray loudness of the TANAMI sample

In Sect. 3.2 the γ-ray-loudness of the MOJAVE sample was discussed in terms of the ratio of the γ-ray- and median 15 GHz VLBA luminosity. Although the TANAMI sample is smaller than MOJAVE it is possible to perform a similar study using the median 8.4 GHz VLBI luminosity. The γ-ray loudness has been previously studied by Böck et al. (2016) and Müller (2014) using data from the 1FGL. The former performed a similar analysis to the one presented here, while the latter studied the γ-ray loudness with respect to the redshift distribution, brightness temperature and jet morphology. Both studies used the flux density from a single observation. Here, I used γ-ray data from the recently released 3FGL and determine the median of the 8.4 GHz flux density from the total flux density of all available images in the TANAMI archive. Hence, a small number of additional

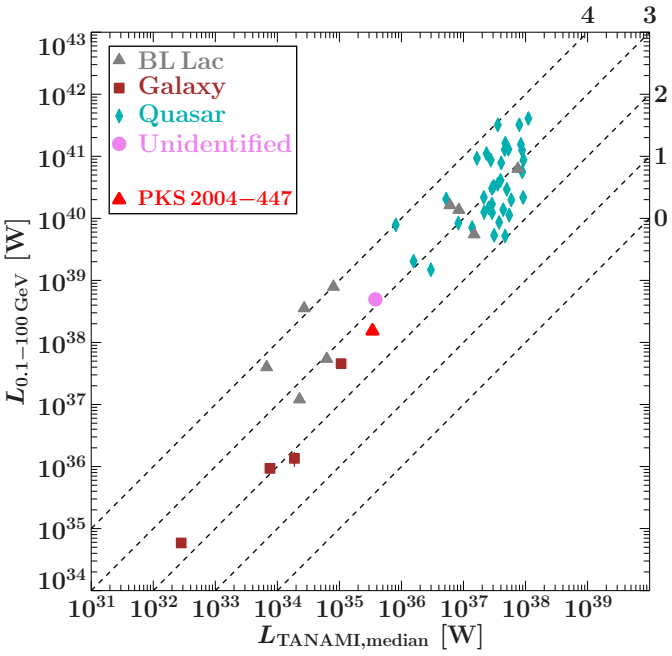

Figure 3.8: 0.1–100 GeV γ-ray and median 8.4 GHz VLBI radio luminosity distribution of the TANAMI sample for sources with known redshift as presented in Müller (2014); Böck et al. (2016). However, the γ-ray associations and data were taken from the 3FGL. PKS 2004−447 is highlighted as the only γ-NLS1 in the TANAMI sample. The dashed lines represent the γ-ray-loudness with respect to 8.4 GHz VLBI luminosity logarithmically from 0 to 4, i.e., from 10^1 to 10^4.

γ-ray sources were included, while the sources with upper limits in the γ-ray regime in Böck et al. (2016) were not considered. The γ-ray and radio luminosity were calculated by accounting for the K-correction of the γ-ray data using the photon index and in case of the radio data a flat spectral index of $\alpha = 0$ as in Sect. 3.2. In addition, only sources with known redshift in Böck et al. (2016) were considered.

Fig. 3.8 shows the resulting distribution of the radio and γ-ray luminosities and similarities to MOJAVE are visible. As already shown in Böck et al. (2016) most of the high-luminosity sources are quasars with BL Lacs and radio galaxies populating the lower luminosity regime. Fig. 3.8 indicates no sources with a γ-ray-loudness between 1 and 10 similar to Fig. 3.3 for the MOJAVE sample. In addition only one source seems to be located within a γ-ray loudness range of 10 to 100 and the overall distribution of BL Lacs and quasars is not as broad. Consistent with MOJAVE the γ-ray loudness of the TANAMI sample goes as high as 10^4, but more quasars are found in the range of 10^3–10^4 even though the number of sources is lower for TANAMI. The median values of the BL Lacs and quasars are ~ 1600 and ~ 1000, respectively. This may be a selection effect as TANAMI includes the brightest AGNs on the southern sky. It is also possible that the radio emission is less strongly beamed at the lower frequencies of TANAMI compared to MOJAVE, which would suggest inverted spectra. Further investigations are required.

Böck et al. (2016) reported a scaling of the γ-ray and radio luminosity of $L_\gamma \propto L_\mathrm{r}^{0.87\pm0.04}$ which is consistent within the uncertainties with the fit by Lister et al. (2011) and in Sect. 3.2. Performing a linear regression fit to the logarithm of the γ-ray and median radio luminosity as shown in Fig. 3.8 without the uncertainties on the γ-ray luminosity yields $L_{0.1-100\,\mathrm{GeV}} \propto L_{\mathrm{TANAMI,median}}^{1.02\pm0.05}$. This is slightly higher than the result from Böck

et al. (2016), though it may be due to the different γ-ray and radio data used. However, the result is consistent with Lister et al. (2011) but again slightly higher than the fit obtained in Sect. 3.2 using the 3FGL data.

Table 3.3.: The TANAMI array

Station	Location[a]	Diameter [m]	SEFD[b] [Jy]/[Jy]	8.4 GHz/22 GHz[c]
(1)	(2)	(3)	(4)	(5)
ATCA[a]	Narrabi, NSW, AU	5×22	39/106	✓/✓
Parkes[a]	Parkes, NSW, AU	64	43/810	✓/✓
Mopra[a]	Coonabarabran, NSW, AU	22	430/675	✓/✓
Ceduna[a]	Ceduna, SA, AU	30	600/2500	✓/✓
Hobart[a]	Mt. Pleasant, TAS, AU	26	560/1800	✓/✓
DSS43[b]	Tidbinbilla, ACT, AU	70	25/60	✓/✓
DSS45[b]	Tidbinbilla, ACT, AU	34	87/-	✓/-
Hartbeesthoek	Hartbeesthoek, ZA	26	340/-	✓/-
O'Higgins[c]	O'Higgins, AQ	9	1500/-	✓/-
TIGO[c]	Conception, CL / La Plata, AR	6	12000/-	✓/-
Warkworth	Auckland, NZ	12	3500/-	✓/-
ASKAP	WA, AU	12	3500/-	✓/-
Katherine	NT, AU	12	3500/-	✓/-
Yarragadee	WA, AU	12	3500/-	✓/-

Note: Columns: (1) station name; (2) location of the telescope; (3) diameter of the telescope; (4) SEFD of the telescope at 8.4/22 GHz, taken from the LBA Sensitivity calculator http://www.atnf.csiro.au/vlbi/calculator/ (obtained on 2015-11-16); (5) capability of observing at 8.4 GHz and 22.3 GHz.
Country codes (following ISO 3166, https://www.iso.org/obp/ui/#search, obtained 2015-11-16): AU: Australia, ZA: South Africa, AQ: Antarctica, CL: Chile, AR: Argentina, NZ: New Zealand; Australian territory codes: NSW: New South Wales; SA: South Australia, ACT: Australia Capital Territory, WA: Western Australia, NT: Northern Territory. [a]These telescope form the LBA
[b]Operated by the NASA Deep Space Network
[c]Operated by the Bundesamt für Karthographie und Geodäsie

4. Radio observations of the TeV emitter IC 310

The TeV population of AGNs are dominated by BL Lac objects, though quasars and a small number of radio galaxies have also been detected at such high energies. However, only about 65 sources have been discovered so far. Therefore, radio observations especially with VLBI are vital to gain insight into the physical parameters of their jets.

One of the more peculiar AGNs at TeV energies is the radio galaxy IC 310. In this chapter, I present an extensive VLBI campaign of IC 310 based on the first quasi-simultaneous multi-frequency observations with the EVN and long-term monitoring by MOJAVE. These observations are part of a larger multi-wavelength campaign (Glawion 2014). Selected results from the EVN observations have been presented in the collaborative work of Aleksić et al. (2014b) and Schulz et al. (2014). The complete radio study will be published in Schulz et al. in prep.

4.1. Presenting IC 310

IC 310 is located at a distance of $z = 0.018940$ (Bernardi et al. 2002) in the Perseus cluster of galaxies (Ryle & Windram 1968) with a mass of the SMBH of about $3 \times 10^8 M_\odot$ (Aleksić et al. 2014b). At this distance 1 mas correspond to about 0.38 pc. On kpc-scales, a narrow and straight radio jet extends to the south-west. The angular length of the jet decreases from about 720″ at a few hundred MHz to about 240″ at 10.6 GHz most likely due to the optically thin spectrum of the synchrotron emission of the jet (Miley 1973; Gisler & Miley 1979; Mack et al. 1993; Condon et al. 1998; Lal & Rao 2005). Figure 4.1 shows the kpc-scale jet of IC 310 at 1.4 GHz image obtained with the VLA as part of the NVSS (Condon et al. 1998).

Based on the kpc-scale morphology within the galaxy cluster, IC 310 has been initially classified in the radio regime as a head-tail radio galaxy (Miley 1973; Mack et al. 1993; Sijbring & de Bruyn 1998). However, an analysis of snap-shot VLBA observations of the pc-scale jet at 8.4 GHz by Kadler et al. (2012), revealed a single-sided jet extending from a dominant compact core similar to blazars with a viewing angle of $\theta_{\rm LOS} \lesssim 38°$. The study also showed that the position angle of the jet is well aligned from pc to kpc scales. Single-dish measurements with the 100 m Effelsberg telescope between 2.7 GHz and 15 GHz confirmed that the low-frequency emission is dominated by the large-scale jet with its optically thin spectrum. Kadler et al. (2012) concluded that IC 310 represents an example of an AGN with characteristics of blazars and radio galaxies.

Optical and X-ray observations by Owen et al. (1996) and Rector et al. (1999) indicated

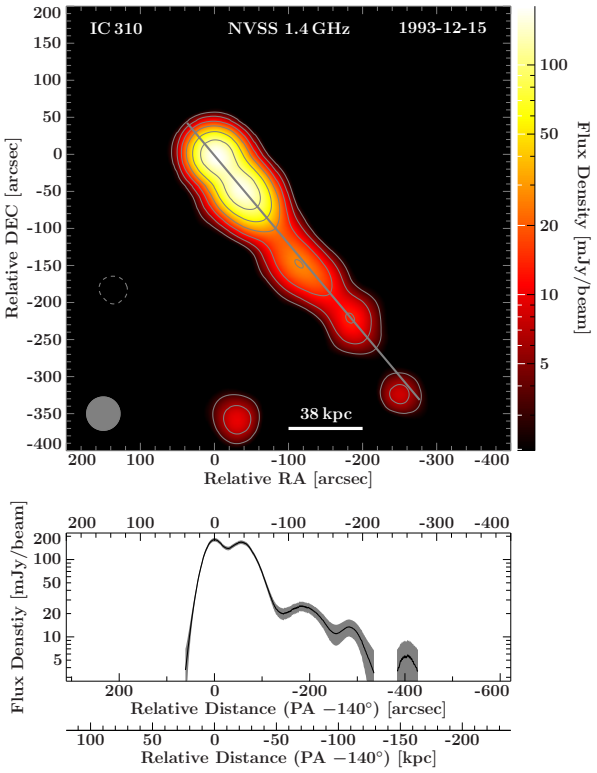

Figure 4.1: NVSS image (top panel) of IC 310 at 1.4 GHz (Condon et al. 1998) with the surface brightness along the position angle of the jet of $\sim$ 140° (bottom panel) as indicated by the gray solid line. The contour lines start at three times the noise level of 0.65 mJy beam^{-1} and increase logarithmically by a factor of 2. The grey ellipse correspond to FWHM of the beam (45″). The shaded regions in the bottom panel correspond to the uncertainty of the flux density and considers the noise distribution following Müller et al. (2011).

that the nucleus of IC 310 is consistent with a low-luminous BL Lac object. X-ray imaging revealed that most of the X-ray emission stems from the nucleus and is not related to the large-scale jet (Sato et al. 2005; Dunn et al. 2010).

Like the centre of the Perseus cluster, 3C 84, IC 310 has been detected in the GeV and TeV energy range. First, *Fermi*-LAT detected IC 310 above 30 GeV (Neronov et al. 2010). Not shortly afterwards, Aleksić et al. (2010) reported the detection by MAGIC above 300 GeV with photon index of about -2 between 2 GeV and 7 TeV based on the combination of *Fermi*-LAT and MAGIC data.

The detection at very high energies is not the only intriguing characteristic of IC 310. At these energies, the source has been shown to be highly variable. Aleksić et al. (2014c) detected variability above 300 GeV on time scales of days and up to a factor of $\sim$ 7 without significant spectral variability between 120 GeV and 8 TeV. As discussed by the authors, variability on these time scales is also known from the radio galaxy M 87.

Extremely short variability on time scales of about 4.8 min in the rest frame of the source was observed by Aleksić et al. (2014b). The study suggested that a gap in the magnetosphere of the rotating SMBH represents the most likely cause of the variability at these energies. The jet as a possible origin amongst others was excluded due to the limited amount of Doppler boosting available. This was based on a lower limit on the viewing angle of 10° that limits the large scale size of the source to a few Mpc consistent with the largest sizes measured so far for radio galaxies (Neeser et al. 1995) and an upper limit that I derived from a 5.0 GHz VLBI from the EVN observation presented in this

chapter of $\lesssim 20°$.

4.2. Single-dish and VLBI observations

4.2.1. Single-dish monitoring

IC 310 was observed multiple times simultaneously at several frequencies with the 100 m Effelsberg telescope between 2011 and 2013. Long-term monitoring of IC 310 was performed with the 40 m telescope of the OVRO telescope at 15 GHz. The Effelsberg and OVRO data were provided fully calibrated by Dr. U. Bach (MPIfR) and Dr. T. Hovatta (Metsähovi Radio Observatory), respectively. The data were also discussed in Glawion (2014).

4.2.2. EVN observations

The EVN conducted four observations of IC 310 quasi-simultaneously between 2012-10-21 and 2012-11-07 at 1.7 GHz, 5.0 GHz, 8.4 GHz, and 22.3 GHz. Correlation of the data and a pipeline calibration were performed at JIVE. However, in order to improve the data quality a manual calibration was performed.

The basic steps of the calibration performed in `AIPS` are described in Subsect. 2.4.2. The total flux density of IC 310 is only about 100 mJy which is too weak for fringes on all baselines, in particular at 22.3 GHz. Hence, a bright and close calibrator, 3C 84, was used during the observations. Even though most of the flux density of 3C 84 stems from a compact region, the source is extended for VLBI observations at all frequencies. Hence, at 1.7 GHz, 5.0 GHz and 8.4 GHz 3C 84 was calibrated and imaged first alone and the resulting model was used as an input for the global fringe fit. However, the result of the fringe fit was only marginally different from the fringe fit without a model for the calibrator. Therefore, this step was omitted for the calibration of the 22.2 GHz data.

A further complication in the calibration arose from missing T_{sys} and gain curve information due to technical problems for the stations Bd, Zc, and Jb. This issue was solved differently at 22.2 GHz compared to the lower frequency data. For the latter, the calibration in AIPS was performed and the data were imaged and self-calibrated in `DIFMAP` without the problematic stations. This provided a CLEAN-model that was used to determine constant amplitude correction factors for the three stations in `DIFMAP`. These factors were applied to the FT entry for the respective telescope in the ANTAB table. The new ANTAB table was loaded into AIPS and the amplitude calibration was repeated. Afterwards, the new data were imaged and self-calibrated.

At 22.2 GHz opacity effects have to be considered for the amplitude calibration in `AIPS`. However, even after performing the appropriate calibration steps, the amplitudes of the IC 310 and the calibrator 3C 84 were significantly too low. As is shown in Sect. 4.3, the single-dish measurements by Effelsberg are consistent with the total flux density on VLBI scales. Effelsberg measured (115 ± 14) mJy for IC 310 at 23.1 GHz on 2012-11-19 that is close enough in time and frequency to be considered simultaneous to the EVN

observations. Hence, this value was set as the flux density of IC 310 in `AIPS` for the amplitude calibration.

As the coherence time decreases with increasing frequency, it was possible to use a higher averaging time at the lower frequencies. The observing times of the EVN observations increase with frequency, thus fewer steps of amplitude self-calibration were necessary at the lower frequencies. Because the data at 22.3 GHz was very noise in terms of the visibility phase, STARTMOD was used prior to averaging which performs a phase self-calibration for a point source model. This resulted in less noisy phases after averaging than without STARTMOD.

Table 6.1 lists the parameters of the imaged and self-calibrated data. Given the difficulty of the amplitude calibration, an uncertainty of 10% of the flux density at 1.7 GHz, 5.0 GHz, and 8.4 GHz and 15% at 22.3 GHz is assumed. For comparison, the MOJAVE programme adopts an uncertainty of 5% of the total flux density (Lister et al. 2013), Based on the hybrid imaged data, two-dimensional Gaussian functions were fitted to the visibility data, i.e., elliptical and circular Gaussian functions for the core and jet, respectively. The parameters of the components are given in Table D.2. The uncertainties of the components were calculated following Lee et al. (2008).

4.2.3. MOJAVE data

The MOJAVE programme provides fully calibrated and hybrid imaged data of IC 310[1] at 15 GHz obtained with the VLBA. Table 6.1 lists the corresponding image parameters. Following Lister et al. (2013), the uncertainty of the total flux density is considered to be 5%. The data were model fitted similar to the EVN data including the estimates of the uncertainties.

The MOJAVE observation on 2013-08-10 shows significantly lower data quality and image fidelity than the other observations that is caused by very low data sampling. While this still provides a reasonable measurement of the total flux density, the resolution is insufficient to resolve the jet. Hence, this observation is not considered in the kinematic analysis.

4.3. Results

4.3.1. The long-term radio spectrum

The radio spectrum of IC 310 is shown in Fig. 4.2. It includes the measurements by Effelsberg as mentioned in Subsect. 4.2.1 and Kadler et al. (2012), OVRO, VLBA (MOJAVE and Kadler et al. 2012), EVN and archival data. The latter extend down to about 200 MHz.

The VLBI data from Kadler et al. (2012), the MOJAVE programme and the EVN observations show a flat spectrum that is very likely due to the dominant VLBI core. In

[1] http://www.physics.purdue.edu/astro/MOJAVE/sourcepages/0313+411.shtml

Table 4.1.: EVN and MOJAVE observations and image parameters

Date	ν	Array Configuration	S_{tot}	S_{peak}	σ_{noise}	Beam
[yyyy-mm-dd]	[GHz]		[mJy]	[mJy/beam]	[mJy/beam]	[mas×mas, °]
(1)	(2)	(3)	(4)	(5)	(6)	(7)
2012-10-21	1.7	Ef Wb Jb On Mc Nt Tr Sv[a] Zc Bd Ur Sh	100 ± 10	78	0.033	$15.4 \times 4.0, 7.6$
2012-10-29	5.0	Ef Wb Jb On Mc Nt Tr Ys Sv[a] Zc Bd Ur Sh	110 ± 10	77	0.027	$5.0 \times 1.2, -8.5$
2012-11-01	8.4	Ef Wb On Mc Nt Ys Sv Zc[b] Bd Ur Sh[b] Ro	100 ± 10	70	0.037	$2.6 \times 0.8, -16.7$
2012-11-07	22.2	Ef Jb On Nt[b] Ys Mh Sv Zc Ur Sh Ro[c]	97 ± 14	106	0.32	$0.97 \times 0.29, 6.4$
2012-03-04	15.4	VLBA	107 ± 5	96	0.32	$1.52 \times 0.84, 27.4$
2012-09-27	15.4	VLBA	90 ± 5	80	0.19	$1.28 \times 0.83, 31.4$
2012-12-10	15.4	VLBA	95 ± 5	73	0.17	$0.98 \times 0.82, 3.5$
2013-05-05	15.4	VLBA	94 ± 5	78	0.30	$1.19 \times 1.05, -0.5$
2013-08-12	15.4	VLBA	105 ± 5	100	0.85	$2.79 \times 0.77, 29.2$
2013-12-15	15.4	VLBA	104 ± 5	77	0.07	$1.00 \times 0.71, 5.7$
2014-05-12	15.4	VLBA	100 ± 5	70	0.09	$1.05 \times 0.61, 1.4$
2015-07-20	15.4	VLBA	100 ± 5	70	0.12	$0.81 \times 0.58, -8.2$

Note: Columns: (1) date of observation; (2) frequency of observation; (3) VLBI array used for observation; (4) total flux density of the image; (5) peak flux density of the image; (6) noise level of the image; (7) CLEAN-beam of the image.
EVN: Ef Effelsberg, Wb Westerbork, Jb Jodrell Banks, Mc Medicina, Nt Noto, Tr Torun, Sv Svetlo, Zc Zelenchk, Bd Badary, Ur Urumqi, Sh Shanghai, Mh Metsähovi
[a]Did not observe, due to repairs
[b]Only RCP data
[c]Did not observe, due to technical problems

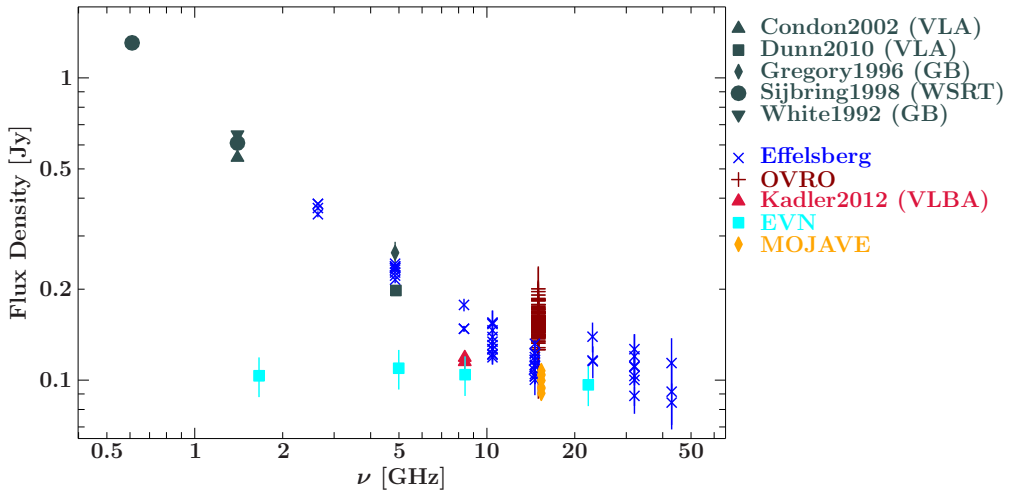

Figure 4.2.: Radio Spectrum of IC 310 based on Effelsberg observations (including data from Kadler et al. 2012), OVRO monitoring, VLBA observations from Kadler et al. (2012) and the MOJAVE programme, EVN observations and archival data (Condon et al. 2002; Dunn et al. 2010; Gregory et al. 1996; Sijbring & de Bruyn 1998; White & Becker 1992).

addition, the MOJAVE data do not show any significant variability with respect to the total flux density and they are consistent with the measurements by Effelsberg.

The data by Effelsberg show that the radio spectrum of IC 310 is steep $\lesssim 10$ GHz and flattens at higher frequencies with limited variability (see also Glawion 2014). This indicates that Effelsberg picks up predominantly the emission from the pc-scale jet at frequencies > 10 GHz. Kadler et al. (2012) reported that already at 8.4 GHz about 80% of the flux density measured by Effelsberg stems from scales below 1 mas. The archival data shown in Fig. 4.2 fit well into the steep spectrum of Effelsberg at which the synchrotron emission from the large scale dominate.

However, caution has to be exercised when interpreting the radio spectrum of IC 310. The data obtained by OVRO at 15 GHz lies above measurements by Effelsberg at 14.6 GHz. In order to further investigate the discrepancy, the OVRO measurements closest in time to the Effelsberg observations are compared with each other. The time delay ranges from within one day to up to 40 days. A simultaneous observation (within one day) occurred on 56348.8 (Effelsberg) and 56349.2 (OVRO) in MJD corresponding to 2013-02-25 and 2013-02-26, respectively. It yields a difference in flux density of about 30%. Looking only at data that were obtained within two days results in a range of differences of 16%–38%. This is significant for single-dish observations. The most probable cause of this is related to the FWHM of the primary beam of Effelsberg and OVRO that are $50''$[2] and $157''$ Richards et al. (2011). Thus, it is possible that OVRO picks up more of the extended emission of the jet than Effelsberg. Although Fig. 4.1 was obtained at 1.4 GHz, it shows that strong emission from the jet extends about $100''$ from the first peak that can still be significant at 15 GHz.

[2] https://eff100mwiki.mpifr-bonn.mpg.de/doku.php?id=information_for_astronomers:rx_list

In the 6 cm band (4.85 GHz) the primary beam of Effelsberg and OVRO at 15 GHz are of similar size. Calculating the spectral index for the observation closest in time, i.e. within two days, yields a flat spectral index of about -0.3. This suggests that the steepness of the radio spectrum is instrumentally biased and there seems to be extended jet emission even at 15 GHz.

4.3.2. VLBI images

The total intensity images based on the multi-frequency EVN observations are shown in Fig. 4.3. The dynamic range, i.e. the ratio of the peak flux density to the noise level, ranges from ~ 1900 to ~ 2900 at the lower three frequencies and about 330 at 22.2 GHz. The images between 1.7 GHz and 8.4 GHz reveal a one-sided jet extending from a bright and dominant core which is consistent with the 8.4 GHz VLBA images from Kadler et al. (2012). At the highest frequency only a bright compact VLBI core is visible. Although there are weak features to the east and west of the core in the residual map that can be emphasized during hybrid imaging, these are considered not to be reliable due to the level of noise in the data at this frequency.

The Gaussian components fitted to the visibility data allow the measurement of the brightness temperature of the core, that is considered to be the component at the upstream end of the jet. The values are relatively consistent across the lower three frequencies with $(1.2\text{–}2.1)\times10^{10}$ K. At 22.2 GHz the total flux density is contained within a region of < 0.06 mas (< 0.02 pc projected). The core contains on average 76% of the total flux density below 22.2 GHz.

Eight observations were performed by MOJAVE between 2012 and 2015 revealing a similar jet morphology. A stacked image based on the MOJAVE data is depicted in Fig. 4.4. It was created by convolving all observations with the enclosing beam, i.e. the size of the elliptical is chosen to include all other beams following Böck (2012). The observation on 2013-08-05 was omitted (see Subsect. 4.2.3). Afterwards, the images were added and averaged. The stacked image shows that the decrease in the brightness distribution is slightly extended along the jet, but still occurs rapidly.

It is important to point out that the jet is not equally well detected in all observations. The core component at 15 GHz contains between 65% and 94%. However, the size of this component varies as it depends on the coverage at the longest baselines. This will lead to changes in the size of the core. Hence, a *core region* is defined that includes all components within 0.8 mas of the core component. This leads to a slightly different range for the core dominance of 75% to 94%, though these changes are not significant within the uncertainties of the flux density calibration. Since the jet is relatively weak, i.e. most of the jet components have a flux density below 10 mJy, its detection depends heavily on the sensitivity. This is supported by the fact that the jet is observed best on 2013-12-15 and 2014-05-12 which reached the best sensitivity.

The position angle of the jet is estimated based on the Gaussian model fit components of the EVN and MOJAVE observations (column 3 in Table D.2 and column 4 in Table D.1). The core component was always ignored. Table 4.2 lists the weighted mean and variance with the weight determined from the flux density of the component and

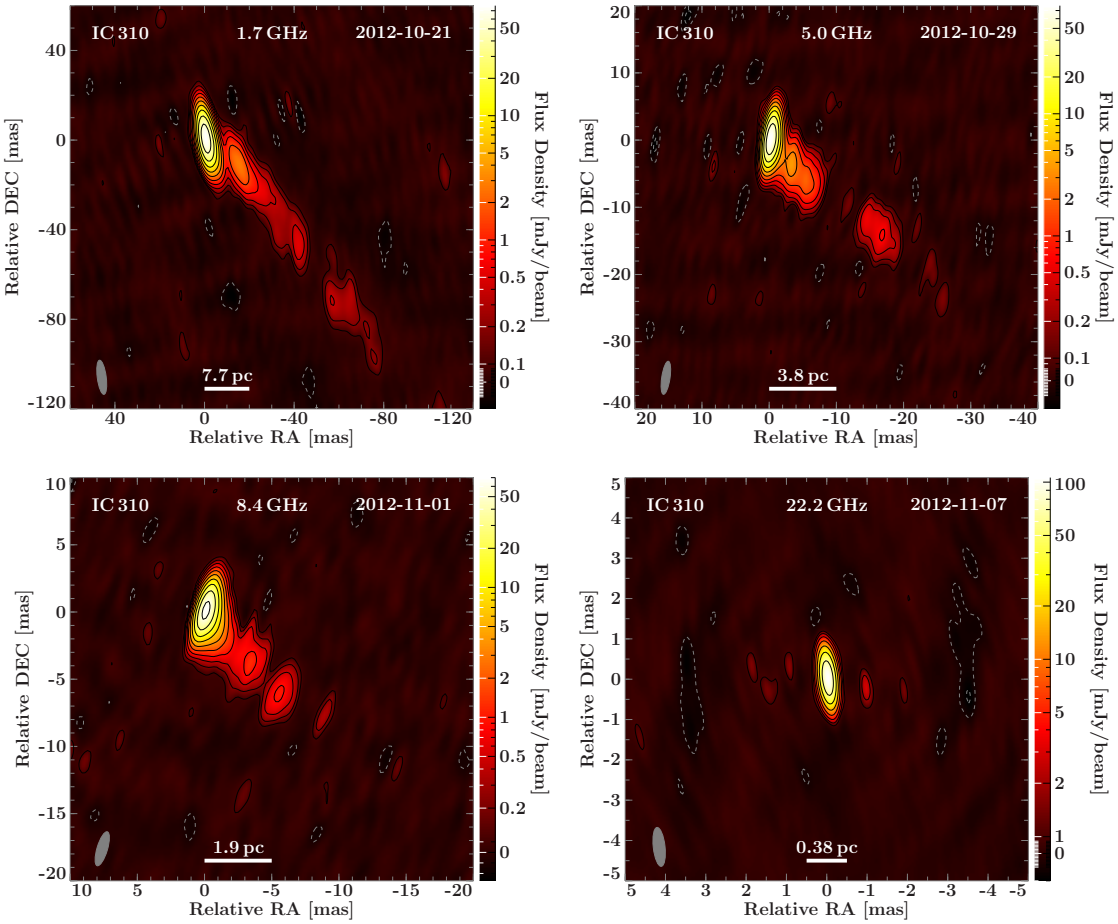

Figure 4.3.: Multi-frequency EVN images of IC 310 from the top left to the bottom right: 1.7 GHz, 5.0 GHz, 8.4 GHz, 22.2 GHz. The grey ellipse in the bottom, left corner represents the CLEAN-beam. The contour lines starts at three times the noise level and increase logarithmically by a factor of two. The image parameters are given in Table 6.1.

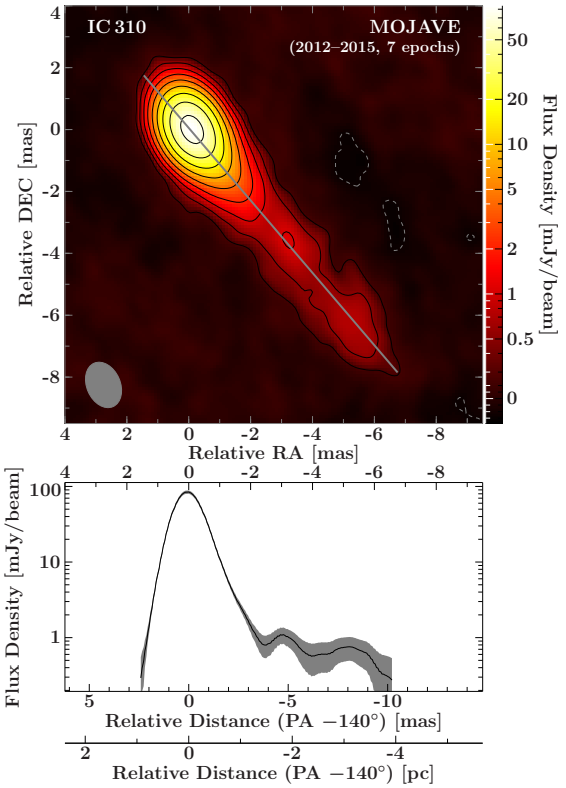

Figure 4.4: Stacked and averaged image of the MOJAVE observations of IC 310 (top panel) and the brightness along a the position angle of the jet at about $\sim -140°$ (bottom panel). The MOJAVE images are convolved with a common beam of 1.53 mas × 1.08 mas, PA 24°. The contour lines start at three times the noise level of the stacked image (0.09 mJy beam^{-1}) and increase logarithmically by a factor of two. The shaded region in the bottom panel accounts for the uncertainty of the flux density and includes the noise level of the image.

the median of the position angle. The mean and median position angles at 15 GHz are $(-138 \pm 6)°$ and -139. The EVN observation indicate small difference in the position angle, but based on the available data these cannot be considered significant. It is possible that they are affected by systematic effects of the individual observation since only one observation per frequency is available in comparison to the MOJAVE data.

4.3.3. Kinematic analysis of the MOJAVE data

The MOJAVE data provide the opportunity to study the temporal evolution of the jet of IC 310 in detail for the first time. In the first step, the position of the Gaussian components are aligned to the core component. Next, components at different epochs are associated with each other by comparing the evolution of the underlying brightness distribution. To this purpose a plot of the time evolution of the MOJAVE images is created as shown in Fig. 4.5. The figure also highlights the kinematic components based on the association process which are labelled with a "J" plus an integer that increases for components that appear later. The core is simply labelled "Core".

The position of the components was fitted in two dimensions using linear regression

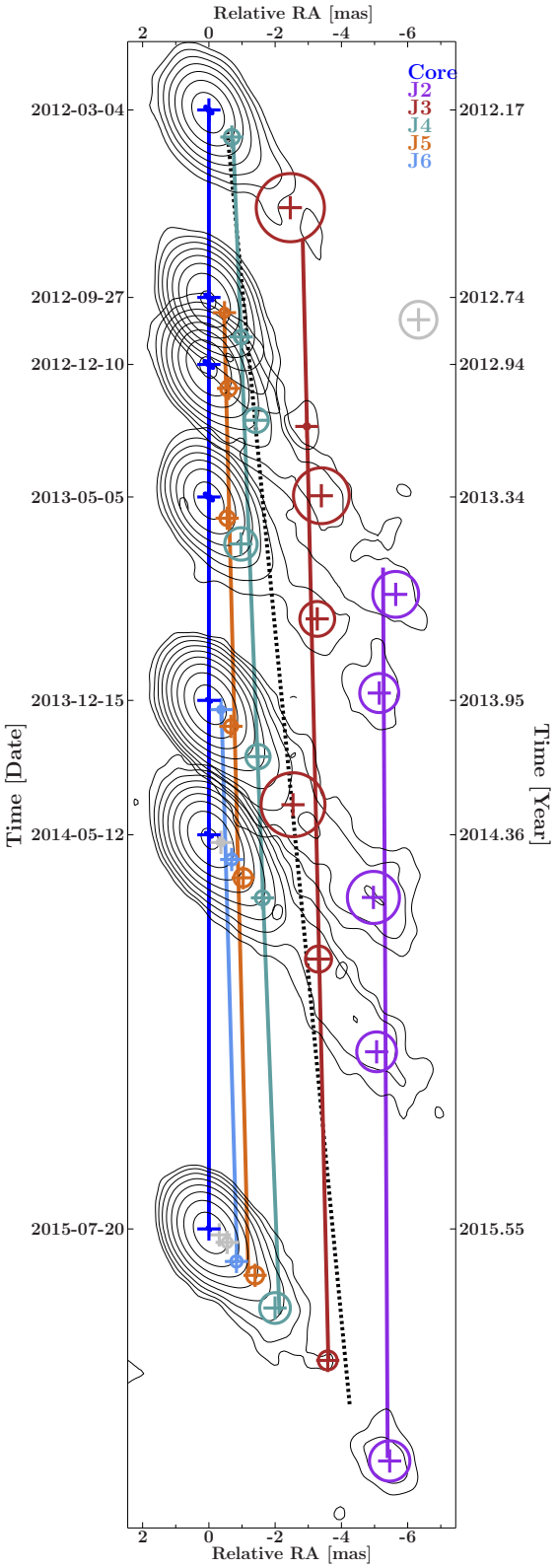

Figure 4.5: The time evolution of the MOJAVE images. The contour lines show on the CLEAN-images after convolution with the same common beam as in Fig. 4.4. The lowest contour line is set at three times the noise level of the individual image and higher contour lines scale logarithmically with a factor of 2. Crosses mark the position of the Gaussian components and the size of the circle or ellipse correspond to the size of the component. Those that were associated for the kinematic analysis are highlighted in colour and the solid lines represent the two-dimensional kinematic fit to the position of the components. The dashed line indicate the fastest component of an alternative model for comparison.

Table 4.2.: Position angle measurements from EVN and MOJAVE

Date [yyyy-mm-dd] (1)	ν [GHz] (2)	$\phi_{\mathrm{jet,wm}}$ [a] [°] (3)	$\phi_{\mathrm{jet,median}}$ [a] [°] (4)
2012-10-21	1.7	-135 ± 7	-139
2012-10-29	5.0	-134 ± 10	-130
2012-11-01	8.4	-137 ± 7	-138
2012-03-04	15.0	-138 ± 3	-139
2012-09-27	15.0	-139 ± 5	-140
2012-12-10	15.0	-140 ± 1	-139
2013-05-05	15.0	-141 ± 3	-139
2013-12-15	15.0	-138 ± 6	-140
2014-05-12	15.0	-137 ± 8	-140
2015-07-20	15.0	-134 ± 9	-138

Note: Columns: (1) date of observation; (2) frequency of observation; (3) weighted mean position angle of the jet from Gaussian model fit components with the error corresponding to the weighted variance; (4) median position angle of the jet from Gaussian model fit components.

and assuming ballistic motion:

$$x = (t - t_{\mathrm{mid}})v_x + x_0 \tag{4.3.1}$$

$$y = (t - t_{\mathrm{mid}})v_y + y_0 \quad , \tag{4.3.2}$$

where v_x and v_y are the angular velocity and $t_{\mathrm{mid}} = (t_{\mathrm{max}} - t_{\mathrm{min}})/2$ the mid point of observation. According to Lister et al. (2009a) measurement of the angular velocity requires components with at least five consecutive associations, ten in case of acceleration. Thus, latter cannot be discussed based on the given data. Except for J6 all components have at least five associations. Hence, the velocity of J6 is considered to be an estimate only. The apparent angular speed and the apparent speed are calculated from the fit and listed in Table 4.3. The distance of the components over time are shown in Fig. 4.6, where the lines are calculated from the fit.

Figure 4.4 indicate that there are two regions of slightly elevated brightness in the jet. These provide the best indicators for the time evolution as the jet lacks any other distinct features. These regions are tracked by components J2 and J3, but due to the low brightness of the jet the reliability of the position of these features is difficult to assess. Several other components emerging from the core region are identified. All of kinematic components show subluminal apparent motion.

The lack of strong and distinct features of the jet as for example seen in 3C 111 (see Chapt. 6) makes it difficult to find associations across the observations. Hence, other associations are considered, including faster kinematic models. These cannot be entirely discarded and the fastest reasonable kinematic component is indicated by the dashed line in Fig. 4.5 and Fig. 4.6 with $\beta_{\mathrm{app}} = 2.25 \pm 0.06$. However, these models are not capable

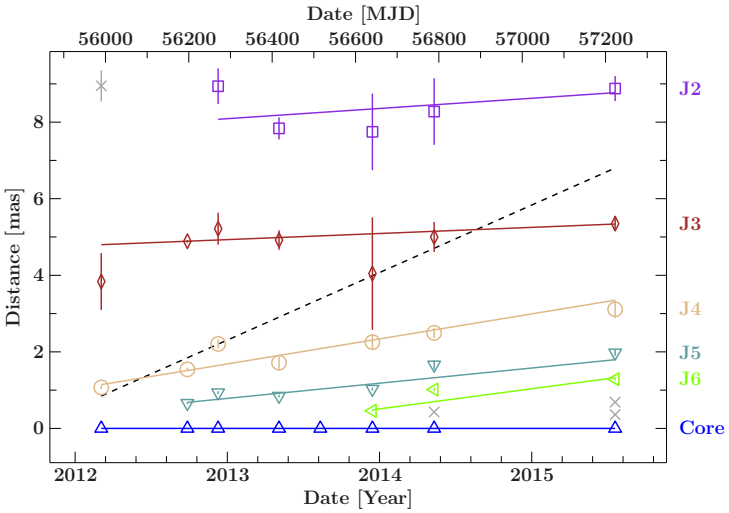

Figure 4.6: Distance of the MOJAVE components with time aligned to the core. The kinematic components are highlight in colour and the solid line indicate the kinematic fit. The dashed, black line corresponds to the fastest component of an alternative model for comparison.

Table 4.3.: Velocity, speed and ejection time of IC 310at 15 GHz

ID	N	$v_{\mathrm{app,x}}$ [mas yr^{-1}]	$v_{\mathrm{app,y}}$ [mas yr^{-1}]	$v_{\mathrm{app,est}}$ [mas yr^{-1}]	$\beta_{\mathrm{app,est}}$	$t_{0,\mathrm{est}}$ [yr]
(1)	(2)	(3)	(4)	(5)	(6)	(7)
J1	5	-0.1 ± 0.2	-0.30 ± 0.09	0.31 ± 0.09	0.4 ± 0.1	1980 ± 20
J2	7	-0.23 ± 0.06	-0.02 ± 0.03	0.23 ± 0.06	0.29 ± 0.08	1980 ± 10
J3	7	-0.42 ± 0.04	-0.50 ± 0.02	0.65 ± 0.03	0.83 ± 0.04	2010.4 ± 0.2
J4	6	-0.26 ± 0.02	-0.30 ± 0.01	0.40 ± 0.02	0.51 ± 0.02	2011.0 ± 0.2
J5	3	-0.30 ± 0.02	-0.45 ± 0.01	0.54 ± 0.02	0.68 ± 0.02	2013.0 ± 0.1

Note: Columns: (1) Label of the kinematic component; (2) number of associated Gaussian components; (3,4) estimated apparent angular velocity of the components; (5) estimated apparent angular speed of the components; (6) estimated apparent speed of the components; (7) estimated ejection time of the components

of maximizing the number of associations compared to the one presented here. The same applies for models with slower component speeds, which in addition are not capable of accounting for the newly appearing components (see also Sect. 4.4).

4.3.4. Spectral index distribution and core shift

Since the EVN observations are quasi-simultaneous, it is possible to study the spectral index distribution of the jet. As mentioned in Subsect. 2.3.3 the position of the VLBI core, i.e., the region of $\tau = 1$, changes with frequency. Therefore, it is necessary to determine the shift of the core in order to align the images properly. Because of the loss of absolute position information, other methods have to be used to determine this shift. One way is to use cross-correlation techniques of the optically thin jet emission at two frequencies (e.g., Pushkarev et al. 2012; O'Sullivan & Gabuzda 2009). Another approach that is

used here, is to identify a feature of the optically thin jet that appears at in this case two adjacent frequencies (e.g., Kovalev et al. 2008; Sokolovsky et al. 2011; Müller et al. 2011). The position of this feature is determined from Gaussian model fit components at the two frequencies. As was done in the kinematic analysis, all components are first aligned to the position of the core. Now, it is possible to determine the core shift from the difference of the position of the chosen components from both frequencies.

In order to properly find a common feature in the jet without being biased by the higher resolution of the higher frequency image, both images are first convolved with a common beam. Due to the change in jet size with frequency, it was only possible to identify a common feature in two adjacent frequencies. Because no jet was detected at 22.2 GHz, this observation is omitted in this analysis.

For the alignment of the 1.7 GHz and 5.0 GHz images, the components $C1_{1.7}$ and $C1_{5.0}$ in Table D.2 are used. This results in core shift of $\Delta x_{5.0,1.7} = (-1.16 \pm 0.36)$ mas and $\Delta y_{5.0,1.7} = (-2.22 \pm 0.36)$ mas which corresponds to $\Delta r_{5.0,1.7} = (2.50 \pm 0.36)$ mas and $\phi_{5.0,1.7} = (-152.5 \pm 8.4)^\circ$ in polar coordinates. In order to properly shift the images for the spectral index maps, the size of the pixel are reduced to 0.2 mas which is slightly lower than the pixel size at 5.0 GHz (0.3 mas). Given the uncertainties a smaller pixel size is not necessary. The decreased pixel size was only used for the deconvolution with the common beam. The resulting spectral index map is shown in Fig. 4.7 (left panel). Since the images are shifted, the offset of the core component from the phase centre has to be accounted for. The image confirms the flat to inverted spectrum at the location of the core and reveals a mostly optically thin jet. The spectral index from the components used for alignment is about -1.

In order to align the images at 5.0 GHz and 8.4 GHz the components $C2_{5.0}$ and $C2_{8.4}$ in Table D.2 are chosen. The positional difference of these components yield a core shift of $\Delta x_{8.4,5.0} = (-0.31 \pm 0.20)$ mas and $\Delta y_{8.4,5.0} = (0.15 \pm 0.20)$ mas ($\Delta r_{8.4,5.0} = (0.34 \pm 0.20)$ mas, $\phi_{8.4,5.0} = (-65 \pm 34)^\circ$). The right panel of Fig. 4.7 shows the spectral index map for which a pixel size of 0.05 mas. The pixel size of the original image at 8.4 GHz image is 0.2 mas. Except for a small area downstream of the jet, the spectral index is of the jet is $\lesssim -1$. The increased spectral index at the edges of the jet could be the result of imperfect alignment, although these areas correspond to the weakest parts of the jet and are thus less reliable. The components used for the alignment result in a consistent spectral index of ~ -0.8.

Although it is not possible to measure the core shift from 1.7 GHz to 8.4 GHz, the sum of the two core shifts can be calculated to be $\Delta x_{8.4,1.7} = (-1.46 \pm 0.42)$ mas and $\Delta y_{8.4,1.7} = (-2.07 \pm 0.42)$ mas ($\Delta r_{8.4,1.7} = (2.54 \pm 0.42)$ mas, $\phi_{8.4,5.0} = (-144.8 \pm 9.4)^\circ$). The position angle of the core shift vector over the full frequency range $\phi_{8.4,1.7}$ is consistent with the position angle of the jet as is $\phi_{5.0,1.7}$ though $\phi_{8.4,5.0}$ deviates slightly.

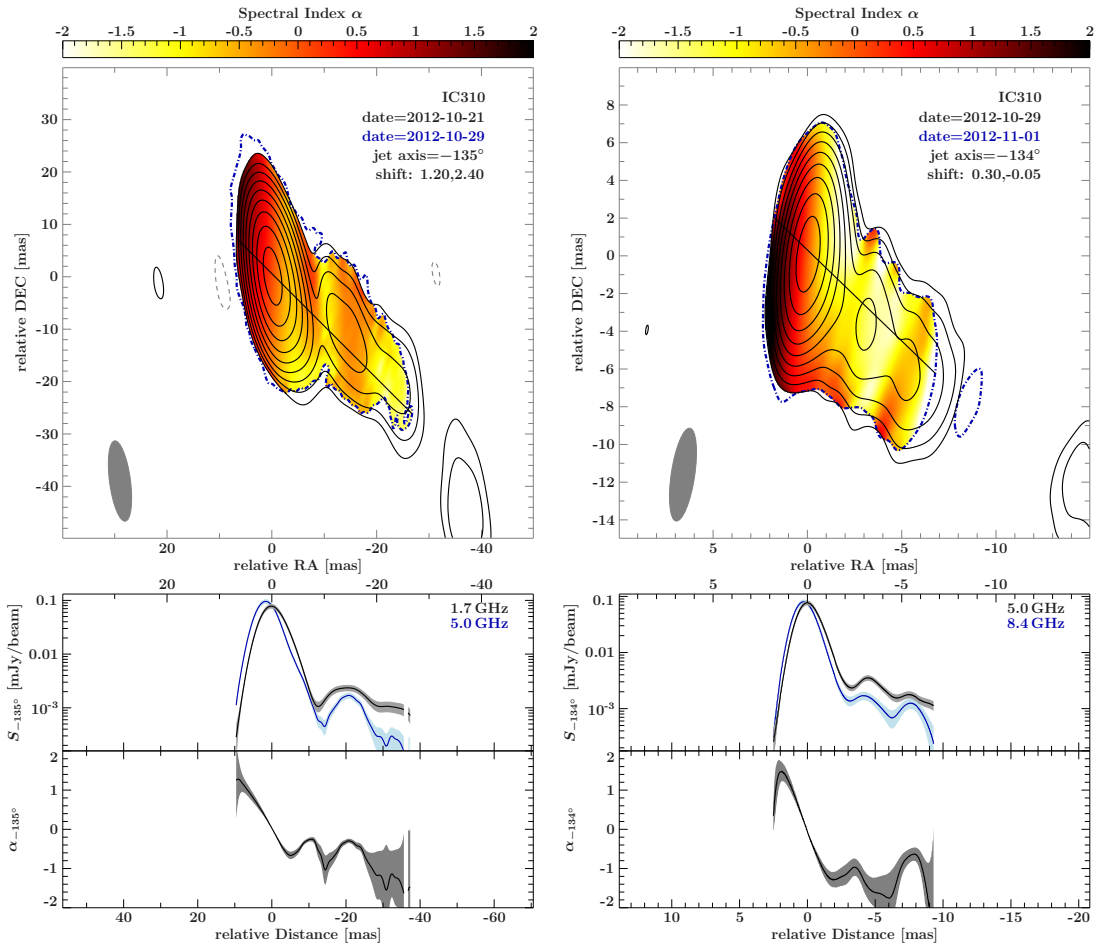

Figure 4.7.: Spectral index maps of IC 310 between 1.7 GHz and 5.0 GHz (left panel) and between 5.0 GHz and 8.4 GHz (right panel). The straight solid line in the upper panels indicate the average ridge line from the position angle of the jet at the lower frequency (see Table 4.2). The black and blue contour lines correspond the lower and higher frequency jet, respectively, though for the higher frequency jet only lowest contour line is shown for simplicity. In general, the contour lines start at five times the noise level of the respective image. The middle panels indicate the jet brightness along the ridge line at the two frequencies and the bottom panels shows the corresponding spectral index maps. The grey shaded areas in the middle and bottom panels reflect the uncertainty based on the noise and uncertainty of the amplitude calibration. Note, that the given shifts include the offset core components from the phase centre.

4.4. Discussion

4.4.1. The morphology and kinematic parameters of the jet

Kadler et al. (2012) showed that the position angle of the jet is stable from a few mas to hundreds of arcsec, though this was based on only two VLBA snap-shot observations. The long-term MOJAVE and multi-frequency EVN observations in Subsect. 4.3.2 confirm the stability of the position angle of the jet that seems to hold over about five orders of magnitude in size

As discussed in Subsect. 2.3.4, the viewing of the jet to the line of sight $\theta_{\rm LOS}$ and the intrinsic speed β have to be determined in order to calculate the Doppler factor δ. However, the combination of a measured $\beta_{\rm app}$ (see Subsect. 4.3.3) and the jet-to-counter jet ratio R allows to constrain the parameter space of β and $\theta_{\rm LOS}$.

R is particular difficult to estimate in a single-sided jet, because only an upper limit on the jet-to-counter jet ratio can be given by taking the flux density of the counter jet to be three times the noise level, for example. A strong upper limit can be estimated from the peak flux density of the jet in the image with the highest SNR. This is provided by the EVN image at 5.0 GHz and leads to $R \approx 950$. The peak flux density stems from the core region, which is a blend of many emission regions ($p = 2$) and it is approximated by a flat spectrum ($\alpha = 0$). In the limit of $\beta \to 1$, this yields $\theta_{\rm LOS} \lesssim 20^\circ$ which is the value used in Aleksić et al. (2014b). A lower limit of $\theta_{\rm LOS} = 10^\circ$ is adopted from Aleksić et al. (2014b), which would imply $\beta \gtrsim 0.95$.

Figure 4.8 shows the result of combining R and $\beta_{\rm app}$, for which the maximum value of $\beta_{\rm app}$ was chosen following Cohen et al. (2007). It is evident from this figure that there is no significant overlap between the parameter space set by $R = 950$ (blue, solid line) and the kinematic model (red lines), even if the maximum $\beta_{\rm app}$ of the faster, but less reasonable model is considered (grey lines) due to $\theta_{\rm LOS} \gtrsim 10^\circ$. This suggests, that the upper limit of $R = 950$ is too high, which can be due to the blending of multiple emission regions inside the core including emission from the counter jet. It also excludes values of β above ~ 0.95 and thereby, high Lorentz and Doppler factors. However, it is important to point out that it does not exclude the possibility of $\theta_{\rm LOS} = 20^\circ$ or lower, because smaller values on R lead to a higher upper limit on $\theta_{\rm LOS}$. It is also possible that the pattern speed estimated from R is not equal to the bulk speed determined from the kinematic analysis Giroletti et al. (2004a).

A more conservative estimate of $R \approx 46$ is taken from the first feature after the core at 5.0 GHz, which provides the lowest upper limit obtainable from the jet due to the best noise level. Lower values of R are unrealistic. Since this feature is part of the jet stream and not completely isolated and the peak brightness has to be used rather than the flux density, it is reasonable to use $p = 2$. As shown in Fig. 4.7 (right panel), the spectral index in this region is ~ -1. This leads to the dashed, blue line in Fig. 4.8. The combination with the maximum value of $\beta_{\rm app}$ yields the grey, shaded region in this figure that corresponds to the parameter space of $0.66 \lesssim \beta \lesssim 0.84$ and $10^\circ \lesssim \theta_{\rm LOS} \lesssim 34^\circ$. However, certain combinations of parameters are not permitted due to the shape of the gray, shaded region, e.g., $\theta_{\rm LOS} \sim 10^\circ$ and $\beta = 0.66$ instead of $\theta_{\rm LOS} \sim 10^\circ$ and $\beta \approx 0.84$.

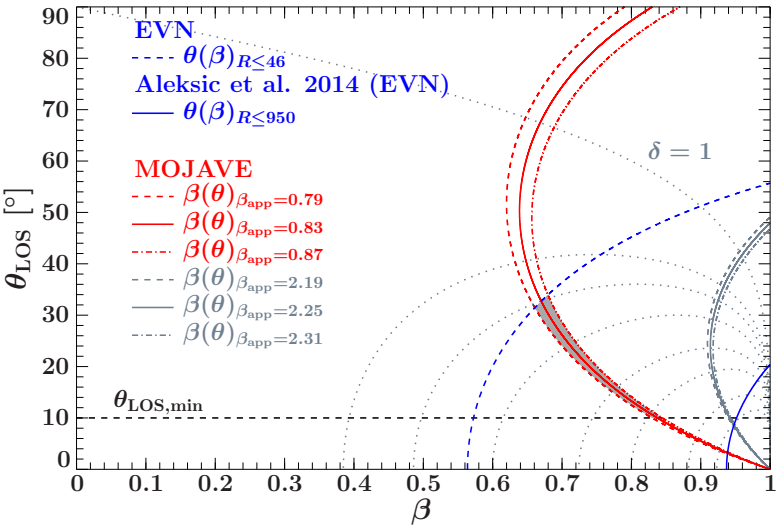

Figure 4.8.: $\theta_{\rm LOS}$ and β based on the limit on R (blue lines) and the maximum $\beta_{\rm app}$ (red and grey lines), respectively. The red lines are based on the kinematic model from Subsect. 4.3.3, while the grey lines stem from the less likely faster model. The black, dashed line marks the lower limit on $\theta_{\rm LOS}$ from Aleksić et al. (2014b). Note, that there are no intersections of the grey lines and $\theta(\beta)_{R=950}$ suggesting that this upper limit is too strong on β, though it does not exclude the range of $\theta_{\rm LOS}$, because this is covered by the more conservative upper limit from $R = 46$. The grey-shaded area highlights the parameter space of β and $\theta_{\rm LOS}$ based on the kinematic model (red lines). The grey, dotted contour lines show the increasing value of δ in steps of {1, 1.5, 1.7, 2, 2.5, 3, 4, 5} with outer most contour line corresponding to $\delta = 1$

Two opposite cases for the jet parameters are given in Table 4.4 for simplicity, leading to $1.4 \lesssim \gamma \lesssim 1.8$ and $1.7 \lesssim \delta \lesssim 3.1$. These results suggest that the jet of IC 310 is only moderately beamed. In addition, they support the conclusion in Aleksić et al. (2014b) that the highly variable flare at TeV energies cannot be explained by the jet as much larger values of δ would be necessary.

The kinematic model presented in Subsect. 4.3.3 indicates that the jet in IC 310 does not show superluminal motion, i.e. $\beta_{\rm app} < 1$, though it cannot be entirely excluded. This is not unusual for BL Lac sources at TeV energies (e.g., Piner et al. 2008, 2010; Lico et al. 2012; Aleksić et al. 2013), but there are TeV sources with $\beta_{\rm app} > 1$ in the MOJAVE sample (BL Lacs and quasars, see Subsect. 4.4.3), for example. The radio galaxies M 87, Centaurus A, and NGC 1275 that are all detected at TeV energies do not show superluminal motion as well (Lister et al. 2013). However, in terms of M 87, superluminal motion on scales of a few mas (e.g., Acciari et al. 2009) and especially in the so-called HST-1 region at a distance of $\sim 0\farcs8$ (Biretta et al. 1999) have been reported. The Doppler factors and viewing angles derived for IC 310 are similar to values from the innermost regions of the jets of these radio galaxies (Kovalev et al. 2007; Müller et al. 2014a; Aleksić et al. 2014a; Hada et al. 2016), but also with BL Lac objects (e.g., Giroletti et al. 2004b; Lico et al. 2012). A topic of extensive studies remains the site of the VHE emission in the three TeV detected radio galaxies (Aharonian et al. 2009b; Abdo et al.

Table 4.4.: The parameters of the jet of IC 310 based on the two extreme values of the parameter space in Fig. 4.8

$\theta_{\rm LOS}$ [°]	β	γ	δ
(1)	(2)	(3)	(4)
~ 10	~ 0.84	~ 1.8	~ 3.1
~ 34	~ 0.68	~ 1.4	~ 1.7

Note: Columns: (1) viewing angle of the jet; (2) intrinsic jet speed; (3,4) Lorentz and Doppler factor of the jet.

2010d; Harris et al. 2011; Abramowski et al. 2012; Hada et al. 2015). The discrepancies of δ implied by the high-energy emission and by the radio jet has led to the development various models that commonly incorporate substructure within the jet, e.g., the two-flow model (e.g., Boutelier et al. 2008), the spine-sheath model (e.g., Ghisellini et al. 2005), mini jets (e.g., Giannios et al. 2009) and decelerating jets (e.g., Georganopoulos & Kazanas 2003). However, these models currently cannot explain the short TeV variability of 4.8 min in IC 310 (Aleksić et al. 2014b).

4.4.2. Implications of the core shift on the magnetic field strength

Several extensive studies have been performed to measure the core shift in jets of AGNs and generally support the theoretical prediction that the shift is proportional to ν^{-1} (Lobanov 1998; O'Sullivan & Gabuzda 2009; Sokolovsky et al. 2011; Hada et al. 2011). Due to the limited frequency coverage, it is not feasible to study the frequency dependent change of the core shift in IC 310. Therefore, the following analysis assumes that the core shift of IC 310 follows the ν^{-1}-dependency. The EVN and MOJAVE observations have shown that the jet of IC 310 is detected relatively well up to 15 GHz, suggesting that such a detailed study would be possible with more frequencies.

The uncertainties of the core shift are rather large compared to other studies (Kovalev et al. 2008; Sokolovsky et al. 2011; Pushkarev et al. 2012) even though all three used slightly different methods to estimate the uncertainties. For example, Sokolovsky et al. (2011) estimated uncertainties between 0.04 mas and 0.07 mas depending on the frequency, but compared these to uncertainties based on Lee et al. (2008) and found that the latter leads to 3–40 times higher values. This would still be below the values calculated for IC 310, but it could be a result of the low surface brightness of the jet, because the uncertainties by Lee et al. (2008) are based on the SNR of a component.

Pushkarev et al. (2012) reported that the relative difference of the position angles of the core shift vector and the jet $|\phi_{\nu_1,\nu_2} - \phi_{\rm jet}|$ is below 45°for about 80% of the sources in the MOJAVE sample. In this study, all shifts were given with respect to 15.4 GHz. Hence, it is only reasonable to compare the values of $\phi_{8.4,5.0}$ and $\phi_{8.4,1.7}$, though the latter is not a direct measurement. The former shows a larger deviation, while the latter fits well. This is in line with the conclusion of Pushkarev et al. (2012) that the position angles

show larger deviations for lower core shift values. Sokolovsky et al. (2011) measured a median core shift of the studied sample between 15.4 GHz and 8.4 GHz of about 0.06 mas and between 15.4 GHz and 1.7 GHz of about 1.7 mas. This is lower than $\Delta r_{8.4,1.7}$ for IC 310 even without adding 0.06 mas, but it is still consistent within the error with the maximum value reported by Sokolovsky et al. (2011).

Under the assumption that the kinematic properties of the jet of IC 310 at 15 GHz are similar at other frequencies, it is possible to combine the results with the core shift measurements to gain insight into the magnetic field strengths of the jet following Lobanov (1998) and O'Sullivan & Gabuzda (2009) (see Subsect. 2.3.3). First of all, the core shift measure $\Omega_{r,\nu}$ (equation 2.3.6) has to be calculated with the assumption that the core shift is proportional to ν^{-1} in IC 310. This yields $\Omega_{r,8.4,5.0} = (1.6 \pm 1.0)\,\mathrm{pc\,GHz}$ and $\Omega_{r,5.0,1.7} = (2.4 \pm 0.4)\,\mathrm{pc\,GHz}$ with the error based on the uncertainty of the core shift.

In order to estimate the magnetic field at 1 pc from the black hole using equation 2.3.7, the intrinsic half-opening angle $\psi_{\mathrm{int}} = \psi_{\mathrm{app}} \sin\theta_{\mathrm{LOS}}$ is determined based on the apparent half-opening angle ψ_{app}. To this purpose, all 15 GHz components at a distance beyond 0.8 mas from the core to avoid confusion with the central region are considered. This yields an upper limit of ψ_{app} because of the remaining distance to the SMBH. ψ_{app} is calculated from the FWHM of the circular component a_{maj} and the distance r as

$$\psi_{\mathrm{app}} = \arctan\left(\frac{a_{\mathrm{maj}}}{2r}\right) \quad . \tag{4.4.1}$$

This results in a median value of $\psi_{\mathrm{app}} \lesssim 7.7°$ that yields $\psi_{\mathrm{int}} \lesssim 1.3°$ for $\theta_{\mathrm{LOS}} \approx 10°$ and $\psi_{\mathrm{int}} \lesssim 4.3°$ for $\theta_{\mathrm{LOS}} \approx 34°$ from Subsect. 4.4.1. The range of ψ_{int} is consistent with the distribution within the MOJAVE sample (Pushkarev et al. 2009). Equation equation 2.3.7 assumes that $\alpha = -0.5$ which is also reasonable for IC 310 given the spectral index distribution shown in Fig. 4.7. Since Table 4.4 lists a minimum and maximum value for δ, both are used as an input parameter and the resulting magnetic field strengths are calculated for $\Omega_{r,8.4,5.0}$ and $\Omega_{r,5.0,1.7}$ (see Table 4.5). The estimates of $B_{1\,\mathrm{pc}}$ are consistent with O'Sullivan & Gabuzda (2009), but at the lower end of the MOJAVE sample (Pushkarev et al. 2012). Since ψ_{int} is a lower limit, $B_{1\,\mathrm{pc}}$ corresponds as an upper limit. In addition, Pushkarev et al. (2012) used the critical angle approximation to estimate θ_{LOS} and the sample of the study is dominated by blazars.

Following Lobanov (1998) and O'Sullivan & Gabuzda (2009), the de-projected distance of the radio core from the jet base r_{core} at frequency ν in GHz can be calculated under the given assumptions as

$$r_{\mathrm{core}} = \frac{\Omega_{\mathrm{r},\nu_2,\nu_1}}{\nu \sin\theta_{\mathrm{LOS}}} \quad . \tag{4.4.2}$$

The resulting range of r_{core} (Table 4.5) is at the lower end compared to blazars, for which $10^{4-6}\,R_{\mathrm{S}}$ are considered for the distance of the mm-VLBI core at 43 GHz or 86 GHz (e.g., Marscher 2006; Agudo et al. 2011; Fromm et al. 2015). An extrapolation of r_{core} down to 43 GHz assuming the ν^{-1}-dependence yield $\sim (0.2\text{–}1.1) \times 10^4\,R_{\mathrm{S}}$. However, it is above measurements of M 87 which are between 14–23 R_{S} at 43 GHz or 50–80 R_{S} at 8.4 GHz (Hada et al. 2011). This further shows that IC 310 shares characteristics with blazars.

Table 4.5.: Estimates of the magnetic fields strengths

ν_2, ν_1 [GHz, GHz] (1)	Ω_{r,ν_2,ν_1} [pc GHz] (2)	$\psi_{\rm int}$ [°] (3)	δ (4)	$B_{1\,\rm pc}$ [G] (5)	$B_{1\,\rm R_S}$[a] [10^3 G] (6)	$r_{\rm core}$[b] [pc] ([10^4 $R_{\rm S}$]) (7)	$B_{\rm core}$[a] [G] (8)
5.0, 1.7	2.4 ± 0.4	$\lesssim 1.3$	3.1	$\gtrsim 0.17$	$\gtrsim 5.9$	~ 2.8 (~ 9.6)	$\gtrsim 0.06$
5.0, 1.7	2.4 ± 0.4	$\lesssim 4.3$	1.7	$\gtrsim 0.095$	$\gtrsim 3.3$	~ 0.86 (~ 3.0)	$\gtrsim 0.11$
8.4, 5.0	1.6 ± 1.0	$\lesssim 1.3$	3.1	$\gtrsim 0.13$	$\gtrsim 4.4$	~ 1.1 (~ 3.8)	$\gtrsim 0.11$
8.4, 5.0	1.6 ± 1.0	$\lesssim 4.3$	1.7	$\gtrsim 0.071$	$\gtrsim 2.5$	~ 0.34 (~ 1.2)	$\gtrsim 0.21$

Note: Columns: (1) frequencies for which the core shift was calculated; (2) core shift measure; (3) intrinsic half-opening angle; (4) doppler factor; (5) magnetic field at 1 pc; (7) magnetic field at $1\,R_{\rm S}$ extrapolated assuming $B \propto r^{-1}$; (8) de-projected distance of the core at ν_2 to the jet base.

For a predominantly toroidal field, the magnetic field scales with the distance to the black hole as $B \propto r^{-1}$. This can be used to extrapolate the magnetic field at the location of the core $B_{\rm core}$ and to the vicinity of the black hole at $1\,R_{\rm S}$, for example ($B_{1\,R_{\rm S}}$, e.g., Sokolovsky et al. (2011); Baczko et al. (2016)). The parameter space of IC 310 yields values of $B_{1\,R_{\rm S}} \gtrsim 2.5 \times 10^3$ G. These values are a few times below the estimates of Sokolovsky et al. (2011) which are based on an extrapolation to $1\,R_{\rm G}$ though, but the difference is not significant due to the uncertainty in the position of the core in IC 310 and the viewing angle. However, it is still within the range derived for the LINER NGC 1052 (Baczko et al. 2016, see also Appendix A).

4.4.3. The place of IC 310 in the MOJAVE sample

A comparison of the kinematic results of IC 310 and the MOJAVE sample is depicted in Fig. 4.9. The median 15 GHz luminosity is calculated as explained in Sect. 3.2. The TeV-detected sources of the MOJAVE sample are highlighted based on Lister et al. (2013) and are dominate by BL Lac objects as is the case for the general population of TeV sources. The two TeV-detected radio galaxies besides IC 310 are M 87 and NGC 1275. According to Lister et al. (2013) the low-luminosity AGN sample, which is dominated by radio galaxies and BL Lac objects, is not statistically complete, but can be considered representative. The radio galaxy with the lowest value of $L_{15,\rm VLBA,median}$ is NGC 1052.

The maximum apparent speed of IC 310 according to Table 4.3 fits relatively well within the distribution of the other AGNs in luminosity range that do not show superluminal motion. This is another indicator that makes the kinematic model leading to the much faster maximum apparent speed of 2.2 c discussed in Subsect. 4.3.3 less likely. However, a statistical analysis is not feasible due to the limited number of sources.

Figure 3.3 in Sect. 3.2 shows the γ-rayloudness of the MOJAVE sample. IC 310 has a γ-rayloudness of about 510 which is the highest value for the small radio galaxy sub-sample. This fits well to the suggestion by Aleksić et al. (2014c) that IC 310 is the brightest radio galaxy in the TeV regime. The median γ-rayloudness of the radio galax-

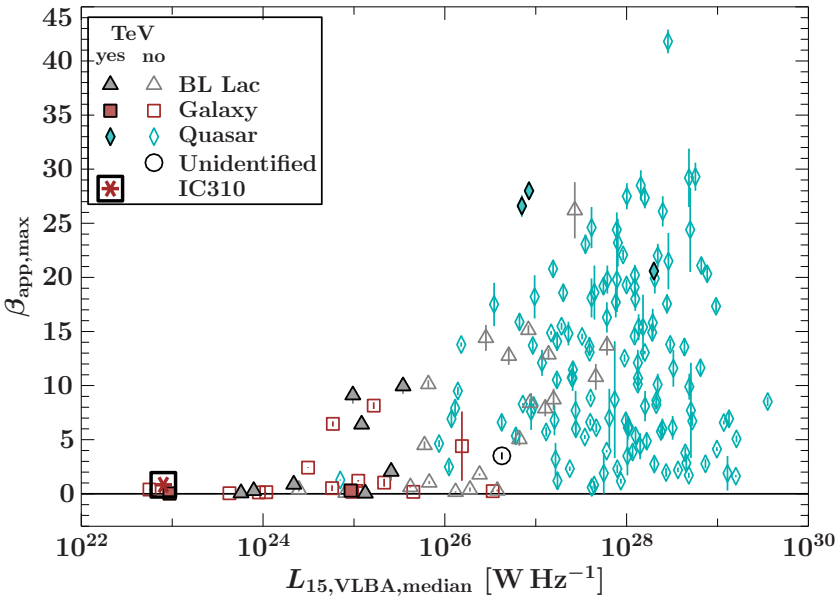

Figure 4.9: Distribution of the maximum β_{app} and the median 15 GHz luminosity of the MOJAVE sample based on Lister et al. (2013) (see also Sect. 3.2) highlighting TeV-detected and non-detected sources. IC 310 is marked by the asterisk surrounded by a black square.

ies is $\sim$ 90 (including IC 310) and ranges over about one order of magnitude due to IC 310. It is also about a factor of two above the median of the quasar and bl lacs. Interestingly, the γ-rayloudness of IC 310 is similar to the median value of the γ-NLS1s. The limited number of γ-ray-detected radio galaxies makes it difficult to ascertain whether the γ-rayloudness of IC 310 is unusually high for the population. However, BL Lacs and quasars cover almost three orders of magnitude in γ-rayloudness and thus, it is possible that radio galaxies also show a similar scatter that could be related to differences in the high-energy emission processes (e.g., Meyer et al. 2011, 2012).

4.5. Summary

In this chapter, an extensive VLBI campaign of the radio jet of IC 310 which is a highly variable TeV emitter has been presented. Four quasi-simultaneous EVN observations were conducted at 1.7 GHz, 5.0 GHz, 8.4 GHz and 22.2 GHz in addition to eight 15.4 GHz VLBA observations by the MOJAVE programme over three years. The data reveal a single-sided, faint jet extending from a bright, dominant, and compact VLBI core in the images below 22.2 GHz. Due to the limited sensitivity at 22.3 GHz, only the core is detected at this frequency. The total flux density of the VLBI images are consistent with a flat radio spectrum and does not exhibit significant variability. This is also seen in single-dish flux density measurements above $\sim$ 10 GHz, while the optically thin synchrotron emission of the large scale jet dominates at lower frequencies. The EVN and MOJAVE observations indicate that the position angle is stable over time on pc-scales and it is consistent with the large scale jet on scales of hundreds of kpc.

The MOJAVE data at 15 GHz vary in sensitivity that most likely hinders the detection of the jet in some observations. The favoured kinematic model indicates apparent motion

of $\sim 0.2\,c$–$\sim 0.9\,c$. In combination with upper limits on the jet-to-counter jet ratio from the higher sensitive EVN observation at 5.0 GHz, this suggests only moderate Doppler factors between 1.7 and 3.1 and low Lorentz factors in the range of 1.4–1.8. These results confirm that the jet of IC 310 cannot account for the high variability observed at TeV-energies. The upper limit on the viewing angle is slightly higher than the estimate by Aleksić et al. (2014b), but does not exclude it. The MOJAVE data indicate an upper limit on the intrinsic half-opening angle of the jet at 15 GHz $\lesssim 4.3°$ depending on the viewing angle. These results and the core shift measurements from the EVN observations below 22.2 GHz lead to an estimate of the magnetic field strengths at 1 pc $\gtrsim 0.07$ G which are consistent with the lower end of the MOJAVE sample. Extrapolating the magnetic field down to the jet launching region near the SMBH assuming a purely toroidal field yield a value of $\gtrsim 2.5 \times 10^3$ G.

IC 310 stands out within the MOJAVE sample.. Its 15 GHz luminosity is at the lower end and about an order of magnitude below the lowest luminosity blazar. It has the highest value γ-ray-loudness among the limited sample of radio galaxies and is about an order of magnitude above the lowest value in the sample. This indicates that there is significant scattering among the radio galaxies, though on smaller scales than estimated for the blazars which vary over almost three orders of magnitude. The apparent motion of IC 310 fits the distribution of the low-luminosity sub-sample of MOJAVE.

The lack of superluminal motion is not unusual for TeV-detected radio galaxies and BL Lac objects a in light of the variability at very high energies on scales of minutes. Further high-sensitivity monitoring is necessary to confirm the kinematics of the jet. Further radio observations above 15 GHz are difficult due to the low flux density and decrease in sensitivity with increasing frequency, but the 22.2 GHz data suggest that the size of the emission region is below 0.02 pc projected (0.1 pc de-projected). Improved low-frequency sampling would provide tighter constraints on the core shift and thereby on the distance of the core to the black hole. The results presented in this chapter underline that similar to other γ-ray-detected radio galaxies, IC 310 exhibits blazar-like properties.

5. The identity crisis of PKS 2004-447

The detection of γ-ray emission in radio-loud narrow-line Seyfert 1 (γ-NLS1) galaxies provided intriguing new insight into the γ-ray-loud population of AGNs sharing some properties with blazars, while differing in others (see Chapt. 2). The sample of γ-NLS1s remains an exclusive group of γ-ray-loud AGNs, but it is growing. Nevertheless, many sources still require detailed studies in particular in the radio regime.

This chapter focuses on the γ-NLS1 galaxy PKS 2004−447 currently detected in the southern sky and that makes it an ideal target for the TANAMI programme. I obtained the results presented in this chapter within the framework of TANAMI. They are feature for the most part in the upcoming publication in *Astronomy & Astrophyics* Schulz et al. (2016) and they have also contributed to Kreikenbohm et al. (2016). Hence, this chapter is largely based on Schulz et al. (2016).

5.1. Presenting PKS 2004-447

PKS 2004−447 is located at a redshift of $z = 0.24$ (Drinkwater et al. 1997) corresponding to ~ 1.2 Gpc and was among the first radio-loud narrow-line Seyfert 1 (RL-NLS1) galaxies to be detected in the γ-rays by *Fermi*-LAT (Abdo et al. 2009b). However, its classification as a NLS1 galaxy has been under discussion in the literature. Oshlack et al. (2001) classified PKS 2004−447 as a RL-NLS1 candidate for the first time, although the weak optical Fe II emission are unusual for a NLS1 galaxy. This issue has been picked up e.g., by Zhou et al. (2003), Gallo et al. (2006), Komossa et al. (2006), and Yuan et al. (2008), but so far it remains unresolved and the source continues to be classified as a NLS1. Due to the weak Fe II emission Komossa et al. (2006) suggested that it may also be classified as a narrow-line radio galaxy.

In the radio Oshlack et al. (2001) reported that the radio luminosity and spectrum fits into the class of CSS sources with a spectral index of $\alpha_r = -0.67$ between ~ 2 GHz and ~ 10 GHz. In addition, long term variability was reported at low frequencies by Oshlack et al. (2001), while Gallo et al. (2006) measured unusual short term variability at 6.65 GHz on times scales of a few days for which they favoured interstellar scintillation rather than intrinsic variability as an explanation. Gallo et al. (2006) also measured the radio spectrum of PKS 2004−447 simultaneously between 1.4 and 17.9 GHz with ATCA and reported a spectral index of ~ -0.52 (see also Subsect. 5.4.1). Due to its flat spectrum in the low-GHz regime PKS 2004−447 has been considered as a flat-spectrum radio source. As such it was included in the CRATES sample (Healey et al. 2007) and the study of flat-spectrum RL-NLS1 by Foschini et al. (2015). However, the CSS-like nature of PKS 2004−447 is unusual within the γ-NLS1-sample (Angelakis et al. 2015).

PKS 2004−447 also stands out in terms of its radio-loudness (Kellermann et al. 1989), i.e., the ratio of the radio (usually at 1.4 GHz or 5.0 GHz) to optical flux. However, different values have been reported: Oshlack et al. (2001) determined a radio-loudness at 5.0 GHz of 1710–6320 depending on the optical flux, whereas Gallo et al. (2006) measured 3800 based on simultaneous optical and radio data. Recently, Foschini (2011) listed a value of 6358 at 1.4 GHz.

Using the velocity of the Hβ line and the empirical relation between the radio of the broad line region and the optical luminosity at 510 nm, Oshlack et al. (2001) estimated a black hole mass of $\sim 5 \times 10^6\,M_\odot$. Recently, this has been questioned by the study of Baldi et al. (2016) which reported a value of $6 \times 10^8 M_\odot$.

At X-ray energies PKS 2004−447 shows a possible soft-excess in the *XMM-Newton* spectrum of 2004 below 1 keV (Gallo et al. 2006). However, an analysis of the same and new (from 2012) *XMM-Newton* data by Kreikenbohm et al. (2016) did not confirm such an excess in the new data, but the study did not rule it out for the old observation as well. Kreikenbohm et al. (2016) suggested that this could be due to different states of activity as the flux was significantly higher in 2004 than in 2012. Based on the *XMM-Newton* data and *Swift* monitoring by Kreikenbohm et al. (2016) found moderate flux and spectral variability with a time scale of the flux variability of months and years. As mentioned in Sect. 2.1 the soft excess is not unusual for NLS1 and CSS sources.

Following its detection in the γ-ray-regime by Abdo et al. (2009b), PKS 2004−447 has been listed in every *Fermi*-LAT source catalogue from the 1FGL to the 3FGL. The 3FGL lists 3FGL J2007.8-4429 as the associated γ-ray counterpart of PKS 2004−447. It has a γ-ray flux of $(8.0 \pm 1.0) \times 10^{-9}$W m^{-2} and a photon index of -2.47 ± 0.09 between 0.1 GeV to 100 GeV. The photon index is consistent with the distribution of the other four γ-NLS1 listed in the 3FGL, which vary between ~ -2.2 and ~ -2.8. The γ-ray flux is a factor of two to five lower than the other four γ-NLS1. However, three γ-NLS1 are not included in the 3FGL. Paliya et al. (2013) reported flux variability between 0.1 GeV and 300 GeV, though the source was detected only two times with a binning of 30 days over a period of 1.2 years.

Since the sample of γ-NLS1s is rather small, it is not possible perform statistical analysis in any wavelength regime. So far, the optical properties are unusual for a NLS1, while the radio properties seem to be consistent with a CSS source and a RL-NLS1. The γ-ray detection suggests that a highly relativistic jet (e.g. Abdo et al. 2009a,b) is at work in PKS 2004−447, which has to be confirmed by high-resolution radio observations of the jet.

5.2. Radio observations

5.2.1. TANAMI VLBI, VLBA and VLA observations

After the detection PKS 2004−447 by *Fermi*-LATit was added to the TANAMI sample. The first VLBI observation by TANAMI was performed on 2010-10-29 at 8.4 GHz. Th DiFX correlator (Deller et al. 2007, 2011) at Curtin University in Perth (Western

Table 5.1.: Summary of interferometric observations of PKS 2004−447

Date [YYYY-MM-DD] (1)	Freq. [GHz] (2)	Array[a] (4)	$S_{\rm peak}$ [mJy beam^{-1}] (5)	$\sigma_{\rm RMS}$ [mJy beam^{-1}] (6)	$S_{\rm total}$ [mJy] (7)	Beam [mas,mas,°] (8)
2010-10-29	8.4	TANAMI	195 ± 39	0.079	294 ± 59	$2.83 \times 0.62, -2.7$
2010-10-29[a]	8.4	TANAMI	249 ± 50	0.064	301 ± 60	$5.61 \times 4.42, -63$
1998-10-12	1.5	VLBA	213 ± 21	0.41	605 ± 61	$14.1 \times 4.16, -9.0$
1998-10-13	1.5	VLA	726 ± 73	0.16	730 ± 73	$11500 \times 3000, -1.7$

Note: [a]Tapered image obtained with a Gaussian taper with a value of 0.1 at a radius 60 Mλ
Columns: (1) Date of observation; (2) frequency of the observation; (3) Array configuration; (4) size of the Gaussian taper with a value of 0.1; (5) peak flux density of the image; (6) noise level of the image; (7) total flux density of the image; (8) CLEAN-beam of the image (major, minor axis and position angle).
Configuration of the TANAMI: PKS: Parkes (64 m), AT: ATCA (5×22 m), MP: Mopra (22 m), HO: Hobart (26 m), CD: Ceduna (30 m), HH: Hartebeesthoek (26 m); VLBA 8×25m (no Hancock and Brewster), including phased VLA antenna Y27, no data available from Hancock and Brewster; VLA in B configuration with 27×25 m stations.

Australia) correlated the data. Further calibration and hybrid imaging was performed following Ojha et al. (2010) (see Sect. 2.4 for a general description). Hence, a conservative uncertainty of 20% is adopted for the amplitude calibration of the TANAMI data. Natural weighting was used for imaging. In addition to the full-resolution image, a low-resolution image was created by applying a Gaussian taper of 0.1 at 60 Mλ to check for diffuse large-scale emission.

In addition, the only archival VLBA observation (project code: BD0050) was analysed as well. It was conducted in combination with the phased VLA at 1.5 GHz on 1998-10-12 . Given the low declination of PKS 2004−447 only eight out of ten VLBA stations provided data. A-priori calibration was performed by E. Ros (MPIfR) in `AIPS`. The data were imaged and self-calibrated in `DIFMAP` with uniform weighting as outlined in Sect. 2.4 In order to estimate the uncertainty of the amplitude calibration the process of hybrid imaging was repeated several times. This yields 10% for a conservative uncertainty estimate. In comparison the MOJAVE program, which observes with the VLBA at 15 GHz, uses an uncertainty of 5% (Lister & Homan 2005). However, due to the very low declination of PKS 2004−447 the here assumed higher uncertainty is more reasonable.

The VLA participated in 'B' configuration as a phased array. The unphased VLA data were extracted from the archive and calibrate by E. Ros (MPIfR) independently. The aim of this was to check for missing flux in the VLBA image.

The image parameters that were obtained from the different interferometry observations are given in Table 5.1.

5.2.2. Flux density monitoring by ATCA

The Australia Telescope Compact Array (ATCA) has been monitoring PKS 2004−447 as part of the regular flux density measurements of TANAMI sources (C1730 programme, Stevens et al. 2012) since 2011-05-17. The monitoring covers frequencies between 5.5 GHz and 40 GHz using a bandwidth of 2 GHz. PKS 1934−638 has been used as a flux density calibrator. J. Stevens (CSIRO) provided the calibrated data for PKS 2004−447 as well as additional data from the ATCA Calibrator Database[1]. This extends the frequency range down to 1.7 GHz and up to 45 GHz.

As the data from the ATCA monitoring programmes is not imaged other methods were used by J. Stevens to check for extended structure, i.e. the defect and the closure phases. The defect uses the scalar-averaged flux density $S_{\rm sca}$ and the vector-averaged flux density $S_{\rm vca}$. It is defined as $(S_{\rm sca}/S_{\rm vca} - 1) \times 100\%$. Since vector averaging uses the phase information it is less sensitive to flux density away from the phase centre as scalar averaging, which will cover all of the flux density within the field of view. As described in Sect. 2.4 the closure phase is the sum of the phase from three telescopes in the array. It will be zero within the noise if the source is unresolved and the data is well calibrated. If the source is resolved the closure phase will be non-zero.

Hence, if no other source lies within the field of view except for the unresolved source in the phase centre, both the closure phase and the defect will be zero. "Confusing structure", i.e., flux density away from the phase centre, may occur if there is a significant defect, but it is weak in brightness and thus the closure phase is still close to zero. Those structures have a frequency dependent effect on the calibration and can make the radio spectrum slightly steeper. At frequencies above 17 GHz, PKS 2004−447 shows a moderate defect and very low closure phases. Hence, the sources is unresolved for ATCA at lower frequencies, i.e., $\lesssim 9.0$ GHz. The maximum baseline of ATCA at 9.0 GHz (4 cm-band) and 17.0 GHz (15 mm-band) is $\sim 150\mathrm{k}\lambda$ and $\sim 300\mathrm{k}\lambda$. This limits the maximum extend to be between $1\farcs7$ and $0\farcs9$. However, based on the performed calibration, the influence of the "confusing structure" on the spectrum is considered to be negligible.

5.3. Results

5.3.1. ATCA light curve and spectrum

Figure 5.1 shows the radio light curve (top panel) and spectrum (bottom panel) obtained from the ATCA monitoring of PKS 2004−447 between 2010-02-13 and 2014-03-26. This represents the first simultaneous multi-frequency monitoring of this source.

Table 5.2 lists the spectral index from fits to specific spectral ranges (see also Subsect. 5.4.1). The fits assume a power law of the spectrum $S_\nu = k\nu^\alpha$, where k is the proportionality constant and α is the spectral index. Linear regression was used to obtain α via $\log S_\nu = \log k + \alpha \log(\nu/\mathrm{GHz})$ taking into account the uncertainty of the flux density measurements. The power law fits seem to describe the data well, except perhaps

[1] http://www.narrabri.atnf.csiro.au/calibrators

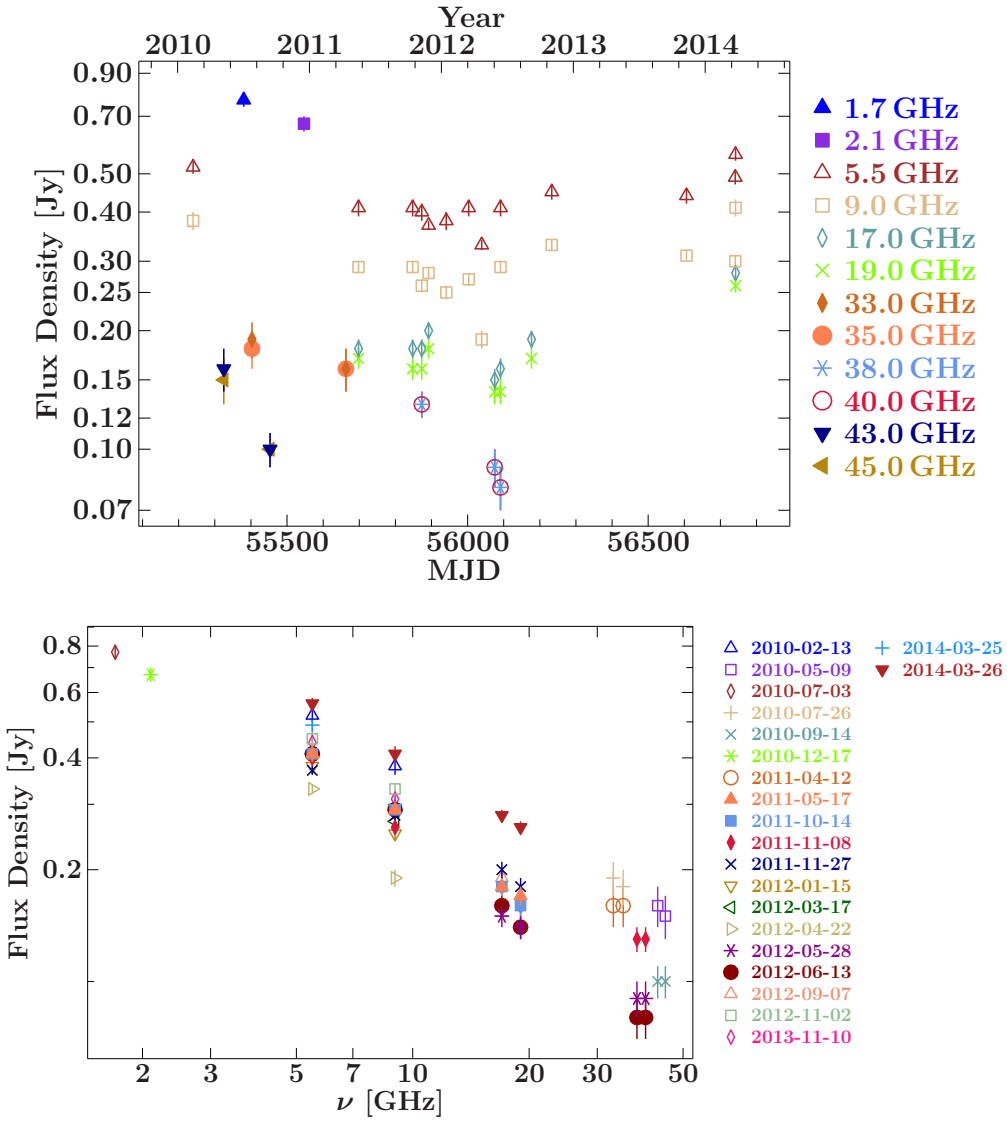

Figure 5.1.: *Top:* ATCA radio light curve of PKS 2004−447 based on all available frequencies. Filled symbols represent the data with more than two data points which are used for the spectral fits (see Table 5.2). *Bottom:* Radio spectrum between 1.7 GHz and 45 GHz from 2010-02-13 to 2014-03-26. Filled symbols represent data for which spectral index fits were performed.

Table 5.2.: Spectral indices for different frequency ranges of the ATCA data

Date	$\alpha_{5.5-40}$	$\alpha_{5.5-19}$	α_{17-40}
(1)	(2)	(3)	(4)
2004-04-12[a]		-0.56 ± 0.03	
2011-05-17		-0.72 ± 0.05	
2011-10-14		-0.75 ± 0.05	
2011-11-08	-0.57 ± 0.03	-0.71 ± 0.05	-0.36 ± 0.09
2011-11-27		-0.56 ± 0.04	
2012-05-28			-0.61 ± 0.12
2012-06-13	-0.86 ± 0.04	-0.86 ± 0.06	-0.82 ± 0.13
2014-03-26		-0.62 ± 0.04	

Note: Columns: (1) Date of observations; (2) Spectral index between 5.5 GHz and 40 GHz; (3) Spectral index between 4.8 GHz and 18 GHz for Gallo et al. (2006) and 5.5–19 GHz for the TANAMI ATCA data; (4) Spectral index between 17 GHz and 40 GHz.
[a]Data taken from Gallo et al. (2006).

on 2011-11-08. Here, the spectral index below and above 19 GHz seem to deviate which suggests a flattening of the spectrum at higher frequency. At this time the flux above 19 GHz increased compared to earlier observations (see also Subsect. 5.4.1).

The spectrum seems to vary moderately above 5 GHz with α ranging from ~ -0.5 to ~ -0.9. In two cases, simultaneous data for the full frequency range of 5.5–40 GHz were available (i.e., 2011-11-08, 2012-06-13). While the fits for the different spectral ranges are consistent within the uncertainties for the data from 2012-06-13, this is not the case for 2011-11-08. This may be due to the elevated flux density at 38 GHz and 40 GHz at this time compared to latter observations. There seems to be no counterpart for this higher activity at lower frequency. In addition, a second period of high activity seems be around 2014-03-06 at 5.5 GHz and 9.0 GHz. However, the sparse sampling of the light curve prevent a more detailed analysis of the evolution of the high activity states.

In order to quantify the variability in the light curve in more detail, the variability index V_ν at frequency ν is used following Hovatta et al. (2008),

$$V_\nu = \frac{(S_{\nu,\max} - \sigma_{\nu,\max}) - (S_{\nu,\min} + \sigma_{\nu,\min})}{(S_{\nu,\max} - \sigma_{\nu,\max}) + (S_{\nu,\min} + \sigma_{\nu,\min})} \quad , \tag{5.3.1}$$

where $S_{\nu,\max}$ and $S_{\nu,\min}$ are the maximum and minimum flux density at frequency ν and $\sigma_{\nu,\max}$ and $\sigma_{\nu,\min}$ the corresponding uncertainties. This represents a basic indicator as it takes into account only the minimum and maximum value at the given frequency. Hence, it is very sensitive to outliers and it can yield negative values if there is almost no variability in the light curve. Other indicators would be for example the fractional variability index by Vaughan et al. (2003) or the modulation index by Richards et al. (2011) (see this study for more detailed discussion). However, due to the low sampling of the date, V_ν will be used as a simple approach. V_ν was calculated for frequencies between

Table 5.3.: Variability Index V_ν between 5.5 GHz and 19 GHz

ν [GHz] (1)	V_ν (2)	N^a (3)	Δt^b [days] (4)
5.5	0.22	13	1502
9.0	0.34	13	1502
17.0	0.27	8	1044
19.0	0.28	8	1044

Note: Columns: (1) frequency; (2) variability index; (3) number of measurements; (4) time between first and last observation

5.5 GHz and 19.0 GHz, for which the most data were obtained (see Table 5.3). It seems that PKS 2004−447 is moderately and similarly variable on all of these frequency.

5.3.2. The first VLBI image at 8.4 GHz by TANAMI

The first VLBI image at 8.4 GHz obtained by TANAMI is shown in Fig. 5.2. The morphology resembles a single sided jet extending from a bright, dominating VLBI core, which is located at the origin of the map. The jet is partially resolved in the full-resolution image (top panel), though its emission is highly diffuse beyond ~ 10 mas from the centre. A region of enhanced emission or 'hot spot' can be seen ~ 45 mas from the core to the north-west. This jet and the 'hot spot' are much better visible in the tapered image (bottom panel).

A total flux density of (294 ± 59) mJy is measured in the untapered image, consistent with the tapered image. The dynamic range at 8.4 GHz $\mathrm{DR}_{8.4}$, i.e., the ratio of the peak flux density to the rms noise level is about ~ 2400.

After deleting only the `CLEAN`-components within 1 mas of the core region, an elliptical Gaussian component was fitted to the visibility data. This allows a further analyse of the VLBI core. The fit was performed in `ISIS` with a direct link to `DIFMAP`, which allows an error calculation of the fit parameters based on χ^2-statistics (Großberger 2014). Table 5.4 lists the results of the fit with the errors corresponding to 1σ uncertainties. The compact component contains a flux density of $(229.8^{+0.4}_{-0.2_{\mathrm{stat}}} \pm 35_{\mathrm{sys}})$ Jy, which represents about 80% of the total flux density in the image. The brightness temperature T_b was calculated following equation 2.4.10. This yields a value for the core of $T_b = (5.7 \pm 1.4) \times 10^{10}$ K, where the 1σ error is dominated by the uncertainty of the axis ratio of the component. This T_b-value is consistent with the equipartition limit of $\sim 5 \times 10^{10}$ K by Readhead (1994). However, it is well below the inverse-Compton limit of 10^{12} K by Kellermann & Pauliny-Toth (1969).

Performing a similar analysis to the 'hot spot' yields a brightness temperature of $\sim 10^7$ K for this region. The error calculation was not performed here, because only an estimated is required here.

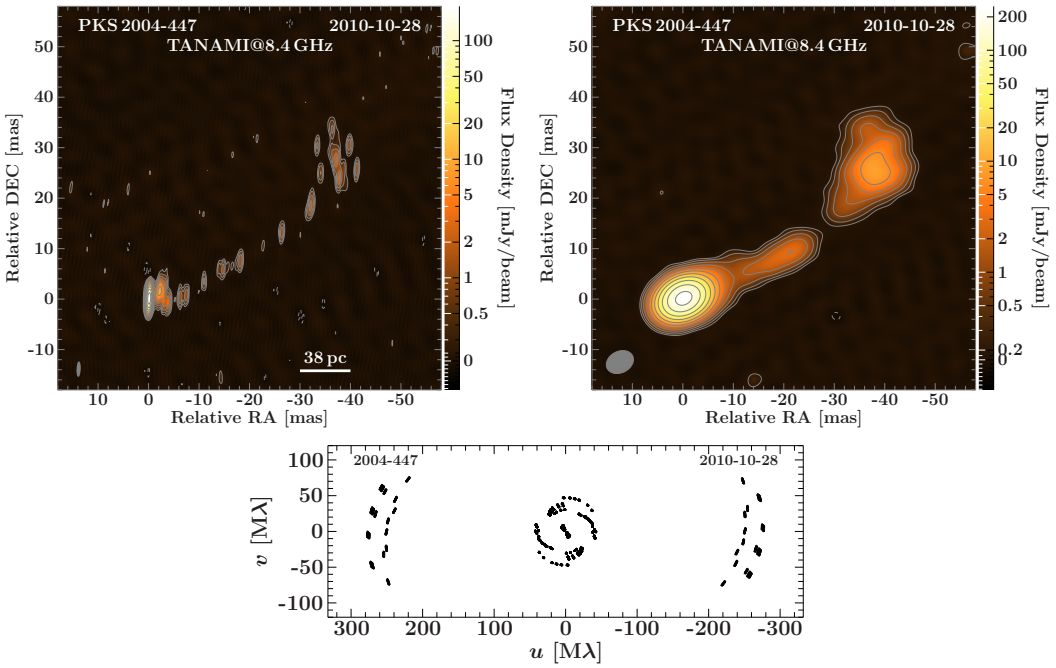

Figure 5.2.: Left: TANAMI image of PKS 2004−447 at 8.4 GHz with full resolution. The white scale bar indicates a corresponding projected length in pc. Right: TANAMI image of PKS 2004−447 obtained with the Gaussian taper. The first contour line of each image is set to three times the rms of the image and higher-level contour lines increase logarithmically by a factor of two. The grey, dashed contour lines represent negative flux density and scale in the same way. The CLEAN-beam is highlighted by the grey ellipse in the bottom left corner. Bottom: (u, v)-coverage corresponding to the TANAMI observation.

5.3.3. Archival 1.5 GHz VLBA and VLA image

The images of the archival VLBA+VLA observation at 1.5 GHz on 1998-10-12 are shown in Fig. 5.3. The dynamic range of the VLBA image (top panel) is $\mathrm{DR}_{1.5} \sim 500$, which is slightly lower than the TANAMI image. This is most likely a result of the sparse sampling in the (u, v)-domain due to the low declination of the source for the VLBA. The VLBA image has a total flux density of (605 ± 61). It also reveals a one-sided jet extending from a bright compact core. However, the jet is much more prominent at this lower frequency. This may be the result of higher activity in the jet or the steep spectral index of the optically thin synchrotron emission or a combination of both. Similar to the TANAMI image, the VLBA image depicts enhanced emission on the north-western end of the jet similar to the TANAMI image. This region again has a brightness temperature of $\sim 10^7$ K. In addition, it shows substantial diffuse emission on the eastern side. Hence, the total extend of PKS 2004−447 at 1.5 GHz is about 140 mas.

Applying the analysis of Subsect. 5.3.2 to the VLBI core at 1.5 GHz yields a component with a flux density of $(248.8 \pm 0.4_{\mathrm{stat}} \pm 25_{\mathrm{sys}})$ mJy. This represents about 40% of the total flux density. The core has a brightness temperature of $(3.4 \pm 0.3) \times 10^{10}$ K at this

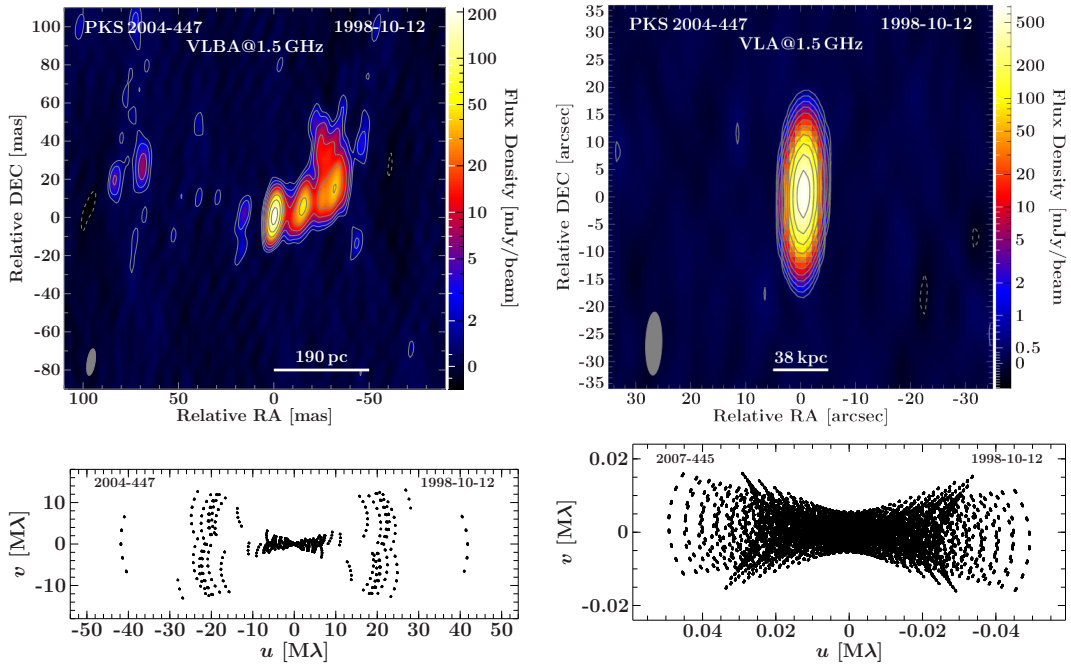

Figure 5.3.: VLBA (top left) and VLA (top right) image of PKS 2004−447 at 1.5 GHz with the image parameters given in Tab. Table 5.1. The contour lines begin at three times the noise level and increase logarithmically by a factor of 2. Negative flux density is represented by grey, dashed contour lines. The CLEAN-beam is shown by the grey ellipse in the bottom left corner. The white scale bar indicates a corresponding projected length in pc (top left) and kpc (top right), respectively. The (u, v)-coverage corresponding to the VLBA and VLA observations are depicted in the bottom left and right images, respectively.

frequency.

The total flux density of the VLA image (bottom panel in Fig. 5.3) is consistent with the VLBA image within the uncertainties. Nevertheless, the total flux density in both images also suggests that about $\sim 80\%$ of the total flux density of the source is located within ~ 140 mas, which corresponds to a projected size of ~ 530 pc in east-west direction. The flat visibility distribution of the VLA data suggests that no extended emission is picked up by the VLA above a detection limit of three times the noise level, i.e., $0.48\,\mathrm{mJy\,beam^{-1}}$. This is confirmed by a fit of an elliptical Gaussian component which is unresolved. After subtracting the model from the visibility data, the residuals do not show any significant emission which is not modelled by the component. Hence, the beam of the VLA observation provides a direct upper limit on the size of the source in east-west direction of less than 11 kpc.

Table 5.4.: Parameters of the core component of the TANAMI and VLBA images

ν	$S_{\rm core}$	$a_{\rm maj}$	ratio	$\theta_{\rm PA}$	$T_{\rm b}$
[GHz]	[mJy]	[mas]	[mas]	[°]	[10^{10} K]
(1)	(2)	(3)	(4)	(5)	(6)
8.4	$229.8^{+0.4}_{-0.2_{\rm stat}} \pm 35_{\rm sys}$	0.3651 ± 0.0016	$0.64^{+0.15}_{-0.14}$	88 ± 3	5.7 ± 1.4
1.5	$248.8 \pm 0.4_{\rm stat} \pm 25_{\rm sys}$	$2.93^{+0.14}_{-0.12}$	0.63 ± 0.04	31^{+8}_{-7}	3.4 ± 0.3

Note: Columns: (1) frequency of the TANAMI (8.4 GHz) and the VLBA (1.5 GHz) image; (2) flux density of the core component with systematic and statistical error from the fit; (3) major axis of the component with the statistical error from the fit; (4) axis ratio, i.e. ratio = $a_{\rm min}/a_{\rm maj}$ with statistical error; (5) position angle of $a_{\rm maj}$; (6) brightness temperature. The statistical errors are given in 1σ interval.

5.4. Discussion

5.4.1. The spectral evolution

The persistent steep spectrum of PKS 2004−447 above 5 GHz over four years of monitoring as discussed in Subsect. 5.3.1 is consistent with archival radio observations by Oshlack et al. (2001) and Gallo et al. (2006) in 2001 and 2004, respectively: Oshlack et al. (2001) reported a spectral index of −0.67 based on simultaneous observations between 2.7 GHz and 5 GHz. Gallo et al. (2006) performed simultaneous ATCA observations between 1.4 GHz and 17.9 GHz, which yielded a spectral index of −0.52 over the full frequency range.

Fig. 5.4 shows the ATCA data from the TANAMI programme presented in the previous section together with most of the available archival data in the literature. It is worth noting that PKS 2004−447 has been observed as part of the ALMA Calibrator survey at frequencies above 90 GHz. The new ATCA data from TANAMI are highlighted by colour and correspond to the observations for which spectral fits were obtained (see Table 5.2). In addition, the data by Gallo et al. (2006) are highlighted by colour as well. For better comparison of the spectral index from the new ATCA data and Gallo et al. (2006) a common, overlapping spectral range was defined, i.e., 4.8 GHz and 19 GHz. The data in this frequency range was fitted separately (see column three in Table 5.2). This yields a slightly different spectral index for the data by Gallo et al. (2006) for the limited frequency range of $\alpha_{4.8-18} = -0.56 \pm 0.03$. A similar spectral index is observed on 2011-11-27. Combining the spectral indices from all fits in this frequency range yield a weighted mean of $\alpha_{\rm wm} = -0.68 \pm 0.10$ and a median of $\alpha_{\rm median} \approx -0.72$. The weighted mean is consistent Oshlack et al. (2001) and the new data confirm the CSS-like spectrum of PKS 2004−447 originally suggested by Gallo et al. (2006).

As mentioned in the previous section the radio spectrum flattens above 17 GHz on 2011-11-08, because of the increased flux density at 38 GHz and 40 GHz. On 2011-09-17 the X-ray light curve of PKS 2004−447 shows increased activity (Kreikenbohm et al. 2016). Moreover, the X-ray spectrum of PKS 2004−447 is sufficiently described by a

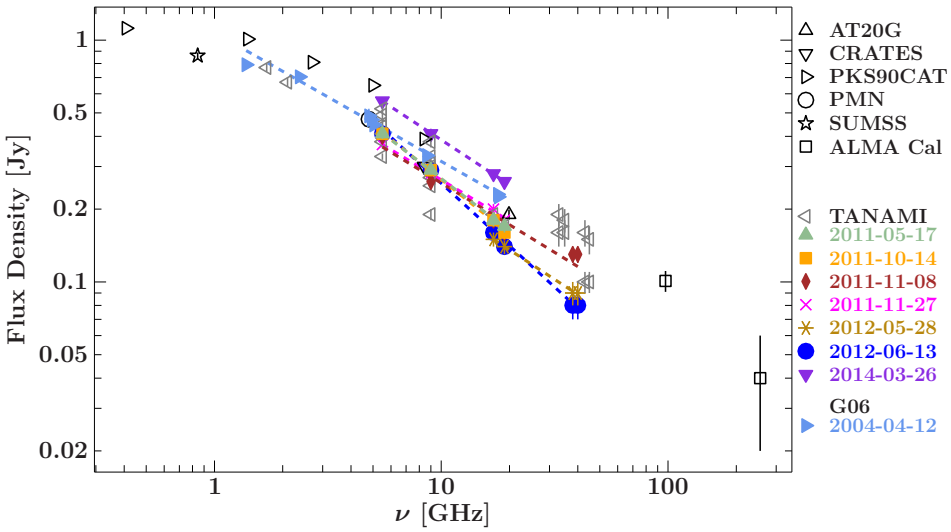

Figure 5.4.: Spectrum of ATCA monitoring between 1.7 GHz and 45 GHz from 2010 Feb 13 to 2014 Mar 26 from Schulz et al. (2016). The coloured symbols and dashed lines show data for which the spectral index was fitted, including the archival data from Gallo et al. (2006) (light-blue, right-oriented triangles). Non-simultaneous archival data from various catalogues are shown in grey: AT20G (asterisk, Murphy et al. 2010; Chhetri et al. 2013), CRATES (bottom-oriented triangles, Healey et al. 2007, PKS90CAT (right-oriented triangles, Wright & Otrupcek 1990), PMN (circles, Griffith & Wright 1994; Wright et al. 1994), SUMSS (stars, Mauch et al. 2013), and ALMA calibrator database (ALMA Cal, rectangles, Fomalont et al. 2014). Based on Schulz et al. (2016).

single power law, which suggest that the X-ray emission stems predominantly from the jet. While this coincidence is intriguing, the sparse sampling of the radio and X-ray light curve does not allow for detailed correlation analysis.

Although the study by Gallo et al. (2006) suggested PKS 2004−447 to be a CSS source, it has been classified as a flat-spectrum source in previous studies based on non-simultaneous data below 5 GHz (e.g., Oshlack et al. 2001; Healey et al. 2007; Foschini et al. 2015). In fact, the combined spectrum in Fig. 5.4 suggests a flattening at lower frequencies. To further characterize this, the spectral index between 1.4 GHz and 2.4 GHz was calculated using the data from Gallo et al. (2006). This yields $\alpha_{1.4-2.4} = -0.21 \pm 0.08$, which is significantly flatter than above 2.4 GHz. Although the radio data do not show the complete turnover in the spectrum, a fit to the averaged radio spectrum and to the ATCA data was performed (Appendix B). This shows that the turnover in the spectrum is most likely below 2 GHz, which is still consistent with turnover frequencies for CSS sources, although at turnover frequencies > 1 GHz GPS sources are dominating (O'Dea 1998).

In order to compare the luminosity at 5 GHz of PKS 2004−447 with the sample by O'Dea (1998), the flux density of the ATCA data with spectral fits between 5.5 GHz and 19 GHz is extrapolated to 5 GHz. The luminosities are calculated following e.g., Ghisellini et al. (2009) accounting for the K-correction using the fitted radio spectral indices. From

this, the weighted mean luminosity is determined to be $L_{5,\mathrm{wm}} = (7.4 \pm 1.1) \times 10^{25} \mathrm{W\,Hz^{-1}}$. The result is consistent with the lower end of the luminosity distribution in the CSS/GPS sample by O'Dea (1998). These results provide further evidence that PKS 2004−447 is perhaps a CSS source as proposed by Gallo et al. (2006).

5.4.2. The pc to kpc radio morphology

Recently, Orienti et al. (2015) published an analysis of the same archival VLBA data at 1.5 GHz. This study does not report on the diffuse emission on the eastern side, which is seen in this analysis. However, the image by Orienti et al. (2015) has a smaller field of view showing only the core and jet. A core-jet structure is not unknown for CSS sources, though it is more common in GPS sources (e.g., O'Dea 1998; Fanti et al. 2001 and references therein). However, only a few CSS/GPS sources with core-jet structures are known in general.

The high brightness temperatures of $> 10^{10}$ K at 1.5 GHz and 8.4 GHz provides evidence of relativistic beaming of the jet emission. The non-simultaneous spectral index of the core emission at both frequencies is relatively flat ($\alpha_{\mathrm{Core},1.5-8.4} \approx -0.04$), while the total flux density provides a steeper spectral index of $\alpha_{\mathrm{VLBI}} \sim -0.4$. Since the observations are non-simultaneously it is not possible to ascertain why the α_{VLBI} is flatter compared to the spectral indices from the ATCA observations.

The angle of the jet to the line of sight θ_{LOS} is calculated following equation 2.3.12 for a continuous jet for two cases:

(i) the diffuse emission on the eastern side in the VLBI image at 1.5 GHz can be attributed to the counter-jet, in which case the emission on the north-western side is completely attributed to the jet (except for the core). The flux density is determined by summing up the `CLEAN`-components in the corresponding regions. This yields $S_{\mathrm{J}} \approx 310$ mJy and $S_{\mathrm{cJ}} = 59$ mJy, respectively. As no simultaneous spectral index could be determined for the jet, $\alpha_{\mathrm{jet}} \sim -1$ is assumed based on Hovatta et al. (2014), who studied the spectral index distribution in a sample of blazar jets based on simultaneous data. As β is unknown, an upper limit can only be obtained for θ with $\beta \to 1$ resulting in $\theta_{\mathrm{LOS},1.5} \lesssim 74^{\circ}$ at 1.5 GHz.

(ii) The second case considers the TANAMI image at 8.4 GHz, where the counter-jet is not detected. Here, five times the rms noise level is assumed as a detection limit of the counter-jet (i.e., $S_{\mathrm{cJ}} \approx 0.1 \mathrm{mJy\,beam^{-1}}$). For the jet, the peak flux density per beam of the first feature west to the core is measured to be $S_{\mathrm{J}} \approx 9.5 \mathrm{\,mJy\,beam^{-1}}$. Using This results in $\theta_{\mathrm{LOS},8.4} \lesssim 50^{\circ}$ with the same value of α_{jet}.

This lower upper limit can be explained naturally by the higher R-value compared to the first case. If the jet velocity is known, it would be possible to determine whether there is a change in jet angle. Since equation 2.3.12 contains two unknown parameters, it is only possible to determine a lower limit on β assuming $\theta_{\mathrm{LOS}} \to 0^{\circ}$. This yields $\beta_{1.5} \gtrsim 0.27$ and $\beta_{8.4} \gtrsim 0.67$ for the first and second case, respectively. Differences in the results from both frequencies may be well explained by the different scales from which the emission was measured.

The observation of such a 'hot spot' as seen on the western side at a distance of ~ 45 mas is not unknown for CSS/GPS sources (Dallacasa et al. 2002a,b). The diffuse emission to the north of the 'hot spot' from the core can be seen in both images on the western side. This emission has a different position angle with respect to the jet. It may indicate a backflow of the jet plasma after interaction with the ambient medium. Similarly, the diffuse emission on the eastern side at 1.5 GHz may also be due to interaction of the counter-jet with the ambient medium. The non-detection of the eastern emission at 8.4 GHz suggests a steep spectrum with $\alpha \lesssim -1.9$ assuming $5\sigma_{\rm rms}$ as a detection, and if the non-simultaneity can be neglected. If the eastern emission cannot be attributed to the counter-jet, this would change the estimates of $\theta_{\rm LOS}$ and β at 1.5 GHz.

The VLA image presented in the right panel of Fig. 5.3 provides the only direct limit on the large scale projected size $l_{\rm ps}$ of PKS 2004−447. However, if PKS 2004−447 is a CSS source than its radio spectrum provides an indirect way to estimate $l_{\rm ps}$. O'Dea & Baum (1997) studied a sample of CSS and GPS sources and found a correlation between the $l_{\rm pc}$ and the turnover frequency ν_m in the rest frame of the source in the radio spectrum which follows a power law of $\nu_m \propto l_{\rm ps}^{-0.65}$. The data on PKS 2004−447 allow the study of several indirect estimates of the projected linear size:

(i) The radio spectrum in Fig. 5.4 suggest that the turnover extends as far down as 408 MHz. This frequency can be used as the currently best known lowest possible turnover frequency. The observing frequency $\nu_{\rm m,obs} = 408$ MHz corresponds to a rest frame frequency $\nu_m \approx 500$ MHz. This yields $l_{\rm ps} \sim 2$ kpc. Considering the fits made in Subsect. 5.4.1, using this frequency likely underestimates ν_m and thereby overestimates $l_{\rm ps}$.

(ii) It is also possible to estimate $l_{\rm ps}$ using ATCA data from the ATCA Calibrator database. As explained in Subsect. 5.2.2, PKS 2004−447 is unresolved for ATCA in the wavelength band of 4 c,. Here, the visibility data distribution is flat out ot a (u, v)-radius of $d_{\rm max} \approx 150\,{\rm k}\lambda$. Using $\sin\phi \approx 1.22\lambda/d_{\rm max}$, this yields an angular size of $\phi \lesssim 1\farcs7$, which corresponds to $l_{\rm ps} \lesssim 6.4$ kpc. Hence, the relationship by O'Dea & Baum (1997) provide a lower limit on the turnover frequency of $\nu_{\rm m} \gtrsim 240$ MHz and $\nu_{m,obs} \gtrsim 200$ MHz in the rest and observer frame, respectively.

(iii) A statistical constrain on the $l_{\rm ps}$ can be obtained from the ATCA 20 GHz (AT20G) survey (Murphy et al. 2010; Chhetri et al. 2013). Chhetri et al. (2013) studied the compactness of the AT20G sample based on the ratio of the visibilities at the shortest and longest (u, v)-spacing, which the authors label 6 km-visibility. The study reports that sources with a 6 km-visibility higher than 0.86 can be considered compact down to a scale of $0\farcs15$. PKS 2004−447 has a 6 km-visibility of 1.00 ± 0.03. Hence, the angular size limit corresponds to $l_{\rm ps} \lesssim 0.63$ kpc. Interestingly, the angular size matches the largest extent in the VLBA image at 1.5 GHz (~ 140 mas $\approx 530\,pc$) very well. However, as explained in Subsect. 5.2.2, ATCA usually resolve the source at such high frequencies. Hence, the limit from Chhetri et al. (2013) cannot be used as an upper limit on the overall size. The compactness may simply indicate that a substantial amount of flux density is located within $l_{\rm ps} \lesssim 0.63$ kpc

and the extended emission was not picked up by the observations in Chhetri et al. (2013).

The strongest limit on the linear size and turnover frequency stems from case (ii) and is consistent with sizes of CSS sources (O'Dea 1998; Kunert-Bajraszewska et al. 2010). However, since these estimates are based on indirect measurements, the conservative but directly determined upper limit of 11 kpc from the VLA data is used in the following, though it cannot be ruled out that extended emission below the sensitivity threshold of the VLA image exists. Using 9.0 GHz VLA observations of three RL-NLS1 which achieved a sensitivity between 0.021 mJy/beam and 0.05 mJy/beam, Richards & Lister (2015) reported the first detection of extended emission of these sources. The study proposes that high sensitivity observations with the VLA are necessary to detect such emission. The large scale size determined by Richards & Lister (2015) would be resolvable by the beam of the 1.5 GHz VLA observation of PKS 2004−447, which argues in favour of the non-detection due to insufficient sensitivity. However, extrapolating the detection limit of 0.48 mJy/beam at 1.5 GHz down to 9.0 GHz using a steep synchrotron spectrum of ~ -0.7 results in a flux density of 0.14 mJy/beam, which is approximately 14 times the lowest sensitivity in Richards & Lister (2015). Although no image analysis can be done for the ATCA observation, the sensitivity at 9.0 GHz is approximately 0.07 mJy/beam. As this is comparable with Richards & Lister (2015) and the ATCA data do not resolve PKS 2004−447, it is less likely that extended emission is missed at 1.5 GHz by the VLA. Only high-sensitivity similar to the VLA or better and high-resolution observations ($\sim 1''$) at low radio frequencies ($\lesssim 1.5$ GHz) can be used to put the tightest constrains on the large scale extend of PKS 2004−447 as the steep synchrotron spectrum would make the extended emission more prominent at such frequencies. Hence, the VLA limit is adopted here.

This limit results in a turnover frequency of $\nu_{\mathrm{m,obs}} \gtrsim 140$ MHz, though the actual value of the turnover frequency is most likely at higher frequencies. However, such low frequencies are currently not accessible for PKS 2004−447. Kunert-Bajraszewska et al. (2010) studied a sample of CSS, GPS and low-luminous compact (LLC) objects in terms of their 1.4 GHz luminosity and linear size. Based on the flux density measurement at 1.38 GHz by Gallo et al. (2006) and using $\alpha_{1.38--2.7}$ from Subsect. 5.4.1, this yields $L_{1.38} \approx 1.2 \times 10^{26}\,\mathrm{W\,Hz^{-1}}$, which corresponds to the lower end of the luminosity distribution of the CSS sample by Kunert-Bajraszewska et al. (2010). Intriguingly, even the lowest estimate on the linear size of PKS 2004−447 is consistent with the CSS-sample in this study. Moreover, it also agrees with the lower end of the distribution of LLC objects. However, this is not unusual as a selection criteria of $L_{1.4} \leq 10^{26}\,\mathrm{W\,Hz^{-1}}$ was used among others for the LLC sample.

The results from the radio observations presented here confirms the CSS-like nature of PKS 2004−447 as suggested by Gallo et al. (2006). It has been discussed in the literature that CSS/GPS sources represent a young evolutionary stage of AGN or perhaps their jets are not strong enough to produce larger radio emission (e.g., O'Dea 1998; Stanghellini 2003; Kunert-Bajraszewska et al. 2010 and references therein). More recent studies such as Fanti et al. (2011) and Randall et al. (2011) favour the paradigm of them being young.

A connection to RL-NLS1 has been discussed by Komossa et al. (2006); Doi et al. (2012); Caccianiga et al. (2014); Komossa et al. (2015); Gu et al. (2015). In fact both paradigms have been considered by various studies (e.g., Abdo et al. (2009b); Foschini et al. (2015); Berton et al. (2015)). There has also been evidence of star forming in RL-NLS1, which would agree well with the young-age scenario (Caccianiga et al. 2015). If PKS 2004−447 is indeed a CSS source, than it would belong to an even more exclusive sample: Only one other CSS source (3C 286) is currently listed in the 3LAC (Ackermann et al. 2015). A similar unusual γ-ray source is PMN J1603−4904 as reported by Müller et al. (2014a). On the one hand its radio spectrum is moderately steep, on the other hand it has a very symmetric mas-scale morphology similar to compact symmetric objects. Such sources have been discussed as being young radio sources (e.g., Wilkinson et al. 1994; An et al. 2012).

5.5. Comparison with other γ-NLS1 galaxies

As described in Chapt. 2, the sample of γ-NLS1 consists of about eight sources at the moment. PKS 2004−447 remains the only one on the southern hemisphere. In the following, the results of PKS 2004−447 will be compared to the sample γ-NLS1 (see also Table 5.5). Table 5.5 lists the radio-loudness at 1.4 GHz $RL_{1.4}$ though ∼ 5 GHz is often used as well in the literature (e.g. Zhou et al. (2003); Doi et al. (2006); Zhou et al. (2007); Yuan et al. (2008)). Different values have been reported for $RL_{1.4}$ for the sources listed in Table 5.5. For example, Oshlack et al. (2001) reported $RL_{4.85}$ between 1710 and 6320 depending on the analysis of the optical data, while Gallo et al. (2006) estimated $RL_{4.9} \approx 3800$. Foschini (2011) reported at 1.4 GHz $RL_{1.4}$ to be 6358. In the case of PMN J0948+0022, Zhou et al. (2003) determined $RL_{4.85} \approx 1982$, while Doi et al. (2012) reported $RL_5 \approx 537$. In order to be consistent Table 5.5 provides the values of $RL_{1.4}$ for the γ-NLS1s by Foschini (2011). Here, PKS 2004−447 is the radio-loudest γ-NLS1. The only exception is the very recent γ-NLS1 [HB89] 1219+044, which is not part of the sample in Foschini (2011) and for which only RL_5 was available in the literature (Yao et al. 2015).

5.5.1. Variability in flux density and spectrum

The flux density variability of PKS 2004−447 (see Subsect. 5.4.1) is comparable to other γ-NLS1 (e.g., Zhou et al. 2007; D'Ammando et al. 2013a,b; Angelakis et al. 2015). Angelakis et al. (2015) presented the longest and best sampled multi-frequency radio monitoring of the four prominent northern γ-NLS1s between 2.64 GHz and 142.33 GHz: 1H 0323+342, SBS 0846+513, PMN J0948+0022, and PKS 1502+036. The best sampled light curves were obtained for PMN J0948+0022, showing the radio spectrum to be inverted for most of the time. A similar radio spectrum was obtained for SBS 0846+513, but the least amount of data were taken for this source. In contrast, 1H 0323+342 has a flat radio spectrum in most of the observations and PKS 1502+036 varies between GHz-peaked (consistent with D'Ammando et al. 2013a) and flat. Based on the

data by Angelakis et al. (2015), the variability index V was calculated at 4.85 GHz and 8.35 GHz for comparison with PKS 2004−447. Table 5.5 lists the results and shows that PMN J0948+0022 has the highest variability consistent with the analysis by Foschini et al. (2012) and Angelakis et al. (2015). 1H 0323+342 and PKS 1502+036 have similar V-values with PKS 2004−447, though significantly more data are available for the two northern sources. While Table 5.5 lists only $V_{4.85}$ and $V_{8.35}$ for the four northern sources V_ν was also calculated for the other frequencies. However, the amount of data available varies strongly and usually decreases with higher frequency. Nevertheless, it is interesting to note that at 23 GHz and 32 GHz 1H 0323+342 has the highest variability indices among the four sources. Hovatta et al. (2008) compiled V_ν for a sample of blazars at multiple frequencies, including 4.8 GHz and 8 GHz. Although the light curves in Hovatta et al. (2008) were obtained over a longer time range, a comparison shows that the γ-NLS1s are consistent with the lowest end of the distributions of $V_{4.8}$ and V_8. The exception is PMN J0948+0022, which is consistent with the median for quasars and BL Lacs. In addition to the variations in the flux density variability, Angelakis et al. (2015) also reported a delay of the radio flares with frequency for 1H 0323+342 and PMN J0948+0022, but not for PKS 1502+036. The former behaviour is known from blazars and radio galaxies such as 3C 111 (e.g. Chatterjee et al. 2011). Also similar to blazars, the variability of the γ-NLS1s usually increases with higher radio frequencies (Angelakis et al. 2015).

Angelakis et al. (2015) concluded that despite the differences in the radio spectrum, the spectra matches those obtained for blazars by the F-GAMMA programme (Angelakis et al. 2012): PKS 1502+036 could be matched with type 5b. Although not provided by Angelakis et al. (2015), a simple visual comparison of the spectra of the other sources in Angelakis et al. (2015) with Angelakis et al. (2012) suggests that 1H 0323+342 and PMN J0948+0022 could be similar to type 2 and type 1b, respectively. Due to the sampling such a comparison is not practical for SBS 0846+513. The similarity with blazars is consistent with the previous study by Yuan et al. (2008), which suggested a general link between RL-NLS1s and blazars. It is intriguing that PKS 2004−447 shows a completely different spectrum from the other γ-NLS1s and does not fit the classification by Angelakis et al. (2012). It may however not be necessary to question the classification of PKS 2004−447 as a NLS1 from a radio point of view to explain this difference. Komossa et al. (2015) reported that the RL-NLS1 RX J2314.9+2243 which also shows a steep radio spectrum may be a γ-ray source though the detection is only tentative. Moreover, Berton et al. (2015) compared a sample of steep-spectrum and flat-spectrum RL-NLS1. Their results suggest that both stem from the same parent population[2] and that the difference in the radio spectrum may be attributed to a larger angle of the jet to the line of sight. This is consistent with PKS 2004−447 and as such, it would make it the first steep-spectrum RL-NLS1 detected at γ-ray energies.

[2]The study also indicates that flat-spectrum RL-NLS1s and disk-hosted broad-line radio galaxy share the same parent population.

5.5.2. Radio morphology and relativistic jet

The dominating pc-scale morphology of blazars is a single-sided jet which has its origin in a bright, often dominating VLBI core (see e.g., Ojha et al. 2010; Lister et al. 2013 and references therein). Such a morphology is also seen in γ-NLS1 at pc scales (e.g., Doi et al. 2006; D'Ammando et al. 2013a,b; Wajima et al. 2014). This is in stark contrast to the kpc-scale morphology, where the projected linear size is usually smaller in RL-NLS1 in general compared to other radio-loud AGN (e.g., Yuan et al. 2008; Doi et al. 2012; Richards & Lister 2015). In case of the γ-NLS1listed in Table 5.5, the extent of the large scale structure has only been directly measured for four sources, i.e. 1H 0323+342, PMN J0948+0022, [HB89] 1219+044, and FBQS J1644+2619.

While the γ-ray detection provides strong evidence for a relativistic jets harboured in γ-NLS1, the pc-scale jet morphology and its properties does this in the radio as well. The one-sidedness of the jet is often explained by relativistic beaming, which at low inclination angles of the jet to the line of sight and sufficiently high Doppler factors lead to the measurement of apparent superluminal motion (e.g., Lister et al. 2013 and references therein). However, not much information is available for γ-NLS1. D'Ammando et al. (2013b) estimated superluminal motion of $\beta_{\rm app} = 9.3 \pm 0.6$ in SBS 0846+513 based on three observations, though five observations are usually necessary for a robust measurements (e.g., Kellermann et al. 2004). Recently, a maximums apparent jet speed of $\beta_{\rm app} = 6.92 \pm 0.29$ has been reported for 1H 0323+342 (Furhmann et al. 2016, RAA submitted; see also Appendix C). Intriguingly, the recently detected γ-NLS1 [HB89] 1219+044 has a maximum apparent speed of only 0.82c according to Lister et al. (2013). This suggests a range of Doppler factors for the jets in γ-NLS1.

Another strong indicator of relativistic beaming in radio jets is the brightness temperature from the VLBI core $T_{\rm B}$. Based on available VLBI data at 15 GHz and 8 GHz, $T_{\rm B}$ was computed (Doi et al. 2012; Lister et al. 2013; Foschini et al. 2015). In case of [HB89] 1219+044, the $T_{\rm B}$ value was directly taken from Pushkarev & Kovalev (2012). The results show that except for PKS 2004−447 $T_{\rm B}$ is above the equipartition limit. In case of SBS 0846+513, PMN J0948+0022, and [HB89] 1219+044 $T_{\rm B}$ exceeds even the inverse-Compton limit. These results are consistent with blazars (e.g., Kovalev et al. 2005) and show a wide range of $T_{\rm B}$-values over two orders of magnitude.It $T_{\rm B}$ is inverse-proportional to the Doppler factor assuming an brightness temperature from equipartition (e.g., Readhead 1994), this also suggests different Doppler factors. The Doppler factor may also be computed from the variability brightness temperatures $T_{\rm B,var}$ from the radio light curves (e.g., Lähteenmäki & Valtaoja 1999). Since the Doppler factor is less sensitive to changes in $T_{\rm B,var}$, it provides a more conservative estimate. Nevertheless, a range of $T_{\rm B,var}$-values have been measured for γ-NLS1 (e.g., Angelakis et al. 2015).

5.5.3. High-energy emission

All of the γ-NLS1 listed in Table 5.5 have also been observed at X-ray energies on multiple occasions (e.g., Foschini et al. 2015; Kreikenbohm et al. 2016; Yao et al. 2015). However, the amount of multi-epoch observations varies and most of the data were ob-

tained by Swift (Foschini et al. 2015). The spectrum can often be sufficiently described as a simple power law, except for PMN J0948+0022 and [HB89] 1219+044, which show an excess in the soft X-ray band (e.g., Kreikenbohm et al. 2016; Yao et al. 2015 and references therein). A detailed analysis of the X-ray spectrum using archival and new XMM-Newton and Swift observations of PKS 2004−447 by Kreikenbohm et al. (2016) did not find a significant soft excess in the X-ray regime as suggested by Gallo et al. (2006)[3]. As summarised in Kreikenbohm et al. (2016), most of the γ-NLS1 show flux and spectral variability. In order to compare the variability in the X-ray and radio regime, the variability index V_X was calculated based on data in the literature. The negative value for PKS 1502+036 is most likely a result of the very low cadence of X-ray observations for this source, which do not vary. However, the amount of data for 1H 0323+342, SBS 0846+513, PMN J0948+0022, and PKS 2004−447 is sufficient for a comparison of V_X and V_ν. Once again, PMN J0948+0022 has the highest variability index. Moreover, V_X for SBS 0846+513 and PKS 2004−447 suggests higher variability in the X-ray regime, while the variability is similar at X-rays and radio energies for 1H 0323+342 and PMN J0948+0022.

The power law index between 1.1 and 2.0 for the γ-NLS1 listed in Table 5.5 fits into the range covered by FSRQs and BL Lacs Foschini et al. (2015); Kreikenbohm et al. (2016); Yao et al. (2015). However, Foschini et al. (2015) pointed out that the distribution of X-ray and γ-rayluminosities is more consistent with FSRQs, whereas Kreikenbohm et al. (2016) suggested that the γ-NLS1 overlap well with BL Lacs.

Figure 3.3 shows the γ-ray loudness of the MOJAVE sample. The red data highlight the γ-NLS1 population. The 15 GHz luminosity of PKS 2004−447 is extrapolated from the 8.4 GHz TANAMI flux density using the median spectral index. Although only a limited number of sources is available, the γ-NLS1match the luminosity distribution of the BL Lac population. The γ-ray loudness is distributed between $\sim 10^1$ and $\sim 10^2$. This range is comparable to IC 310, but otherwise above the radio galaxies. Although PKS 2004−447 shows some distinct differences in the radio properties, the γ-ray loudness is only marginally smaller than for 1H 0323+342. With the detection of more γ-NLS1 in the γ-ray-regime statistically analysis may become possible. Currently, PKS 2004−447 is the only γ-NLS1 in the TANAMI sample and its value is consistent with the distribution in the MOJAVE sample (see Fig. 3.8), though the BL Lacs and quasars have slightly higher values compared to the MOJAVE sample.

5.6. Summary

γ-NLS1 represent an intriguing target to study the high-energy emission in AGN different from blazars. Hence, it is vital to learn more about them and study the relativistic jets they harbour. This chapter has presented a detailed analysis of the radio properties of the only γ-NLS1 on the southern hemisphere as part of the TANAMI monitoring programme. The first ever image of PKS 2004−447 at 8.4 GHz reveals a bright, dominating VLBI core

[3]This is consistent with an analysis by Orienti et al. (2015)

Table 5.5.: Properties of γ-NLS1

Source	z	$T_{b,15}$ [10^{11} K]	$T_{b,8}$ [10^{11} K]	$l_{\rm ps}$ [kpc]	spectrum	variability	$V_{4.85/5.5}$	$V_{8.35/9.0}$	V_X	$\rm RL_{1.4}/RL_5$
(I)	(II)	(III)	(IV)	(V)	(VI)	(VII)	$(VIII)$	(IX)	(X)	(XI)
1H 0323+342	0.061	7.3 ± 2.7 (6.2)	-	24	steep, flat	F/S	0.30	0.32	0.37	318/-
SBS 0846+513	0.584	36 ± 27 (7.5)	-	<2.2	flat, inverted	F/S	0.13	0.14	0.42	4496/-
PMN J0948+0022	0.585	64 ± 15 (44)	4.0 ± 1.3 (1.7)	104	flat, inverted	F/S	0.55	0.65	0.50	846/-
[HB89] 1219+044	0.966	119 ± 95 (96)	43	~ 80	flat	F/-	-	-	-	-/1700
PKS 1502+036	0.409	3.9 ± 1.1 (3.0)	-	<25	GHz-peaked, flat	F/S	0.27	0.30	-0.4	3364/-
FBQS J1644+2619	0.145	-	6.3	60	-	-	-	-	-	396/-
PKS 2004−447	0.24	-	0.4 ± 0.1	<11	CSS-like, steep	F/S	0.22	0.33	0.45	6358/-

Note: Hyphens indicate that no data were available

Columns: (I) Source name; (II) redshift from NED; (III) mean T_b at 15 GHz based on reference (1) except for [HB89] 1219+044(2), brackets refer to the median; (IV) mean T_b at $\sim$8 GHz based on (1) and median in brackets for PMN J0948+0022, 1H 0323+342 from (3), FBQS J1644+2619 from (4), [HB89] 1219+044 from (5); (V) projected linear size from VLA observations, for SBS 0846+513 and PKS 1502+036 the major axis the beam of the highest resolution VLA image from (6) and (7), respectively, for 1H 0323+342, PMN J0948+0022, and FBQS J1644+2619(4), for [HB89] 1219+044(8); (VI) radio spectrum, for 1H 0323+342 (3, 9), SBS 0846+513 (6, 9, 10), PMN J0948+0022 (11, 9), PKS 1502+036 (7, 9), FBQS J1644+2619 (4); (VII) F: flux variability, S: spectral variability from simultaneous data; $(VIII, IX)$ variability index for 1H 0323+342, SBS 0846+513, PMN J0948+0022 and PKS 1502+036 at 4.85 and 8.35 GHz from (9), PKS 2004−447 at 5.5 and 9.0 GHz; (X) variability index at X-ray energies 0.3–10 keV for 1H 0323+342 (1), SBS 0846+513 (10), PMN J0948+0022 (1), and PKS 1502+036 (7), 0.5–10 keV for PKS 2004−447 (12), for PKS 1502+036 negative value due to consistent flux measurements within the uncertainties; (XI) radio loudness at 1.4 GHz and 5.0 GHz, for [HB89] 1219+044(13), otherwise (14)

References: (1) Foschini et al. (2015), (2) Lister et al. (2013), (3) Wajima et al. (2014), (4) Doi et al. (2012), (5) Pushkarev & Kovalev (2012), (6) D'Ammando et al. (2012), (7) D'Ammando et al. (2013a), (8) Kharb et al. (2010), (9) Angelakis et al. (2015), (10) D'Ammando et al. (2013b), (11) D'Ammando et al. (2014), (12) Kreikenbohm et al. (2016), (13) Yao et al. (2015), (14) Foschini (2011)

from which a single sided jet extends to the north-west. The comparison with the only other VLBI image at 1.5 GHz shows both images to be morphological consistent except for diffuse emission on the eastern sided only detected at the lower-frequency image. The high-brightness temperature VLBI core at 8.4 GHz of $\sim 6 \times 10^{10}$ K, which is consistent with equipartition suggest at least a moderately relativistic jet. A conservative upper limit on the large-scale size was determined at 1.5 GHz to be 11 kpc, though about 80% of the total flux density stems from a region of projected ~ 530 pc in diameter. Moreover, the first long-term flux density measurements simultaneously at multiple frequencies suggests confirms the steep spectrum above 5 GHz to be consistent over several years, while the data suggests a turnover below 2 GHz. These findings provide further strong evidence that PKS 2004−447 fits the classification of a CSS source, which was suggested in earlier studies.

The exclusive sample of γ-NLS1 has grown steadily over the recent years. While the sample is still small, it shows a range of characteristics as well as similarities, e.g., γ-NLS1 share the single-sided jet morphology on pc scales. A comparison of the variability index in the radio and X-ray regime shows a different strength in variability for some sources and similar variability for others, though more data is necessary for the majority of the sources in the sample to confirm it. The VLBI core brightness temperatures range over two orders of magnitude and exceed in some cases even the inverse-Compton limit. γ-NLS1 exhibit striking differences in the radio spectrum. At the moment, the CSS-like spectrum of PKS 2004−447 is unique within this sample. It is also extremely rare among all γ-ray-detected AGN in the 3LAC catalogue. However, the γ-ray-loudness PKS 2004−447 is consistent with the other γ-NLS1 with sample overlapping with the BL Lac population and the lower end of the quasar population of the MOJAVE sample.

It is important to keep in mind that the NLS1-classification of PKS 2004−447 is still not for certain. The radio data presented here and the X-ray data discussed in Kreikenbohm et al. (2016) are not suitable to answer this question. Improved optical observations are needed to study the strength of the Fe II emission in more detail. In terms of its radio properties it shares characteristics of blazars and CSS sources similar to RL-NLS1.

PKS 2004−447 will be further monitored by TANAMI, including high-resolution VLBI images and flux density measurements. This will make it possible to study changes in the jet over time and it will provide a database for a more detailed study of the variability in the radio regime. The characterisation of the turnover in the radio spectrum represents a key element in the study of PKS 2004−447. However, this requires measurements at frequencies below 400 MHz. This will make PKS 2004−447 an exciting target for precursors to the Square Kilometre Array, such as the MWA and the GMRT (e.g., Wayth et al. 2015; Nityananda 2009).

6. Resolving the 2007 outburst of 3C 111 with mm-VLBI

As discussed in Sect. 3.1, several studies have shown a strong connection between the appearance of new features in the pc-scale jet, radio outbursts and γ-ray flares. However, usually only a single VLBI component is identified.

This raises the question whether such components could be resolved with sufficiently high angular resolution. One of the best ways to achieve this is VLBI at 3 mm-wavelengths with the Global mm-VLBI Array (GMVA). Not only does it provide one of the highest angular resolution currently achievable with VLBI, but a radio outburst appears usually earlier at mm wavelengths than at cm wavelengths, due to the propagation of the flare through the jet stream and the frequency dependence of synchrotron self-absorption. In addition, mm-wavelength emission tends to be less contaminated by the optically thin synchrotron emission from the jet.

A highly exciting source to perform such a study is 3C 111. This chapter presents results from three GMVA observations following a major radio outburst in 2007 leading to the appearance of multiple components. It is based on initial results presented in Schulz (2012) and Schulz et al. (2013), but presents an improved calibration and analysis of the GMVA data. The results of this chapter will published in Schulz et al. in prep.

6.1. Presenting 3C 111

3C 111 is a broad-line radio galaxy located at a redshift of 0.049 (Véron-Cetty & Véron 2010). At this distance 1 mas corresponds to about 0.96 pc in projected linear scale. The source shows a classical FR II morphology on kpc-scales with a bright compact central region, a one-sided jet extending to the north-west and two bright lobes at opposited sites of the compact region (Linfield & Perley 1984). The morphology has been interpreted in terms of an alignment of the jet towards the observers in the north-west direction. On pc scales 3C 111 shows a one-sided jet extending at a position angle consistent with the large-scale jet to the north-west from a bright compact core with the jet exhibiting superluminal motion up to $\sim 8\,c$ (e.g., Götz et al. 1987; Preuss et al. 1988; Kellermann et al. 2004; Jorstad et al. 2005; Kadler et al. 2008; Lister et al. 2013).

In the X-ray regime, Chatterjee et al. (2011) interpreted the coincidence of dips in the X-ray light curve with the radio activity as a disk-jet connection as in the radio galaxy 3C 120. On kpc-scales, Hogan et al. (2011) observed an X-ray jet aligned with the radio jet.

Variable γ-ray emission is also a characteristic of 3C 111 which it has in common with

blazars albeit at a lower scale. 3C 111 has been detected in the γ-ray regime already with EGRET which made it the first FR II radio galaxy observed at such high energies (Hartman et al. 1999). It has been part of the 1FGL and 3FGL but not of the 2FGL and it belongs to the low-latitude sample of the 3LAC. It is one of only three FR II type radio galaxies detected at γ-ray energies in the 3FGL Massaro et al. (2016). Grandi et al. (2012) associated a radio flare with a γ-ray detection by *Fermi*-LAT, elevated optical emission and activity in the pc-scale jet.

In the radio regime, several outbursts have been observed. Three particular strong ones in February 1975, January 1996, and August 2007 with a flux density above 10 Jy at 90 GHz (Wills 1975; Alef et al. 1998; Trippe et al. 2011). Intermediate outbursts up to $\sim 7\,c$ (at 90 GHz) seem to occur on shorter time scales than larger ones (Trippe et al. 2011). Not much information is available on the impact of the first outburst on the jet. The event in 1996 led to the ejection of a bright feature into the jet, which shaped its evolution for about a decade at 15 GHz (Kadler et al. 2008) leading to several trailing components. At 43 GHz this feature has been shown to be significantly polarised (Jorstad et al. 2005). Intermediate outburst have also been identified with the appearances of new components in the jet (Kadler et al. 2008; Chatterjee et al. 2011; Großberger 2014). The latest major outburst in 2007 was associated at 43 GHz with a single new feature causing a slightly bended jet structure (Chatterjee et al. 2011). At 15 GHz, a complex evolution of the jet was observed as a result of the outburst (Großberger 2014; Beuchert et al. in prep.). Global mm-VLBI Array observations have been obtained in the aftermath of the 2007 outburst to resolve the impact on the jet structure at highest angular resolution.

6.2. Single-dish and mm-VLBI observations

Single-dish flux density monitoring at 86 GHz was provided by F-GAMMA team that observed a sample of γ-ray-loud AGNs at cm and mm wavelengths (e.g., Angelakis et al. 2012).

The basic steps of the calibration and imaging procedure of the GMVA data are outlined in Sect. 2.4 and can also be found in detailed in Schulz (2012). A problem which was encountered in Schulz (2012) was missing flux density in the first two GMVA observations after comparison with single-dish measurements. The upper panel of Fig. 6.1 shows the F-GAMMA light curve at 86 GHz and the VLBI flux density from Schulz (2012). The lower panel shows the ratio of single-dish to VLBI flux density. Apparently, the flux density in the first two GMVA observations after calibration and imaging are significantly lower than the expected value from the single-dish observations. There are two possible explanations for this behaviour:

First, there may be significant extended flux resolved out by the VLBI observations. However, comparing the VLBI flux density at from the 43 GHz VLBA-BU-Blazar programme[1] and the F-GAMMA data at the same frequency shows good agreement of the data. In addition, if unresolved emission is not picked up by the GMVA images this will

[1] https://www.bu.edu/blazars/VLBAproject.html

lead to a constant offset which is not the case here. The single-dish and VLBI flux density at 15 GHz agree already very well during flares as these are dominated by compact emission from the (sub-)pc-scale jet (see Großberger 2014). Hence, this case is unlikely to be the reason for the missing flux density.

The second possible cause is related to the amplitude calibration. Difficulties in measuring the system temperatures, the gain curve of the telescope and in obtaining the weather information at this high frequency can significantly affect the amplitude calibration before imaging and self-calibration were performed. This issue can lead to different offsets for different observations and it is considered to be most likely the cause of the missing flux density.

An *ad-hoc* way to correct this was adapted from Hodgson (2014):

1. determine a correction factor from the ratio of single-dish to VLBI flux density (lower panel in Fig. 6.1).
2. Scale the flux density of the CLEAN-components corresponding to the image by the correction factor.
3. Load the data as it were prior to imaging and self-calibration and import the model of the scaled CLEAN-components.
4. Scale the visibility amplitudes by a constant factor, e.g., via *gscale true* in `DIFMAP`.
5. Image and self-calibrate the new data.

In contrast to Hodgson (2014), the closest single-dish measurement was used to calculate the correction factor and this yields 1.5 ± 0.2 (2007-10-15) and 2.1 ± 0.2 (2008-05-11). The uncertainty in flux density after this procedure is determined from the uncertainty of the correction factor and the initial amplitude calibration. The latter has been estimated to be about 15%. These steps were performed to produce the images presented in this chapter which were also used for model fitting of the data. The exception is the image of the third GMVA observation for which an amplitude correction was not necessary. Hence, the data of this observation are taken from Schulz (2012). All GMVA images presented here were created with natural weighting to obtain the best image SNR. The image parameters are listed in table Table 6.1.

The amplitude corrected data were model fitted with circular Gaussian components in order to describe the main features of the brightness distribution. Since no changes were made for the third image, the model from Schulz (2012) was used. The parameters of the model fit components are listed in Table D.3. Due to high SNR of the observations, the estimated uncertainties based on Lee et al. (2008) is usually below the systematic value from the amplitude calibration. The uncertainty of the position of the component is taken to be $0.5 a_{\mathrm{maj}}$. It leads to larger values than following Lee et al. (2008), but since only three observations are available for the kinematic analysis, this approach introduces a larger scatter of the data. The same estimate of the uncertainty has also been used by Müller et al. (2014b). The size of the components was compared to the resolution limit as explained in Subsect. 2.4.2.

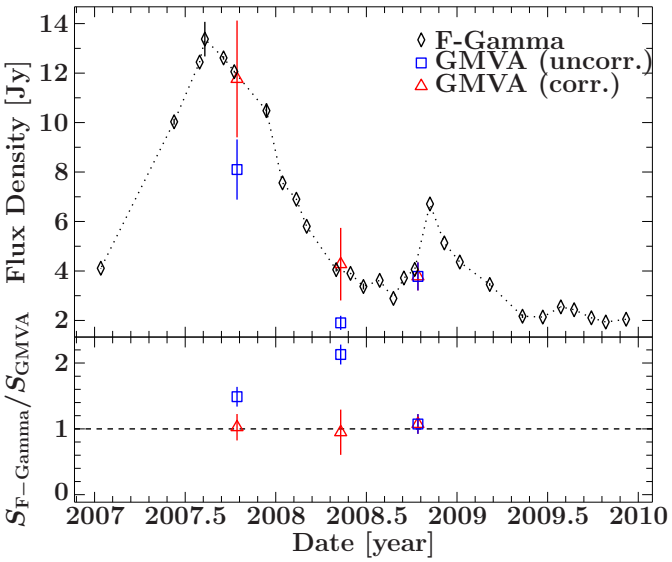

Figure 6.1: *Top:* 86 GHz light curve of 3C 111 obtained with the F-GAMMA programme (black diamonds) and the VLBI flux density from the GMVA observations before (blue, squares) and after (red triangles) performing the amplitude correction. The dashed line does not represent a fit to the data. *Bottom:* Ratio of the F-GAMMA flux density closest in time with the GMVA observation to the GMVA flux density.

Table 6.1.: Properties of the GMVA observations of 3C 111 at 86 GHz

Date [YYYY-MM-DD] (1)	σ_{noise} [mJy beam^{-1}] (2)	S_{peak} [Jy beam^{-1}] (3)	S_{total} [Jy] (4)	S_{SD} [Jy] (5)	Beam [μas$\times\mu$as, °] (6)
2007-10-15	0.32	2.41 ± 0.36	11.8 ± 1.8	12.06 ± 0.22	$148 \times 45, -11$
2008-05-11	0.16	0.93 ± 0.14	4.27 ± 0.64	4.06 ± 0.16	$152 \times 59, -16$
2008-10-14	0.13	1.87 ± 0.28	3.78 ± 0.57	4.06 ± 0.21	$167 \times 67, -18$

Note: Columns: (1) Date of observation; (2) Noise level of the image; (3) Peak flux density of the image; (4) Total flux density of the image; (5) Flux density of the F-GAMMA observation closest in time to the GMVA observation, i.e. 2007-10-09, 2008-05-02, 2008-10-07; (6) The CLEAN-beam of the image given by the major, minor axis and the position angle of the beam measured from the north eastwards.

Additionally, selected VLBA data at 43 GHz were taken from the VLBA-BU-Blazar programme that offers fully calibrated and imaged data. These were model fitted in Schulz (2012). The 43 GHz data used here were previously discussed by Chatterjee et al. (2011).

6.3. The jet of 3C 111 at 86 GHz

6.3.1. The sub-pc scale morphology

Fig. 6.2 shows the natural weighted images of the three GMVA observations with the same noise level and colour scale. This provides a direct comparison of the evolution of the jet morphology with time. In addition, Fig. 6.2 highlights the (u, v)-coverage of each GMVA observation. Even though the coverage decreases slightly over the course of the

observing campaign, it is still excellent especially in direction of the position angle of the jet, where the (u, v)-coverage has its largest extend. Therefore, the minor axis of the CLEAN-beam is well aligned with the position angle and it provides the best resolution along the jet down to ~ 0.045 mas which corresponds to ~ 0.043 pc.

The jet extends to the north-east from the brightest feature, though a small extension to the west is also detected. This is considered to be the most upstream feature of the jet (see Subsect. 6.4.5). One of the most remarkable feature in the jet is a bend at a distance of around 0.4 mas from the origin of the map. Over the course of seven months, i.e., from the first to the second observations, the size of the bend increases, but it seems to be moving outwards radially. At the same time the overall brightness of the jet decreases. In the third observation, the bend is not visible any more, but instead a feature of diffuse emission larger in size than rest of the jet is visible downstream. The last two images also show a weak, diffuse feature at a distance of about 4 mas–5 mas, but due the large distance and the lack of emission in-between, it is not considered to be reliable. Hence, the largest extend of the jet is measured in the last observation with about ~ 1.8 mas or ~ 1.7 pc.

The changes in the brightness of the jet corresponds well to the evolution of the radio light curve. As shown in Fig. 6.1 the first observation occurred only about two months after the peak of the F-GAMMA light curve, when a significant amount of flux density is still a significant localised upstream of the jet. As shown in Fig. 6.3 and Table D.3 the brightest feature of the jet comprises two Gaussian components (C2a,b) with another compact component (C1) to the west. All three components contribute about 48% to the total flux density of the image even though the components cover a compact region of about 0.1 mas or 0.096 pc in linear scale. In the next observation only one Gaussian component is necessary to model fit the brightest feature of the jet (C2) and the component C1 covers the feature to the west. The fraction of the flux density in this compact region to the total flux density decreases slightly to about 37%. At the same time the overall flux density decreases. However, in the last observation the compact region marked by C2a,b, again comprising two model fit components, and C1 dominate the overall flux density with $\sim$ 74%. The light curve shows that the observation occurred at a rising slope towards a smaller outburst at the end of 2008. This suggests that the increase is localised within the compact region, while the jet cools down due to the lack of new plasma.

The components C2 and C1 also exhibit the highest brightness temperatures of the jet covering $10^{10.54-11.50}$K. The median is consistent with the equipartition limit by Readhead (1994) of $\sim 10^{11}$ K.

6.3.2. The kinematic of the jet

A robust kinematic analysis using the standards of the MOJAVE programme requires kinematic components with at least five model fit components (Lister et al. 2009a). In particular, the measurement of the ejection time benefits from an even higher number of components. Hence, only estimates can be obtained for the velocity and ejection time of a kinematic component at best.

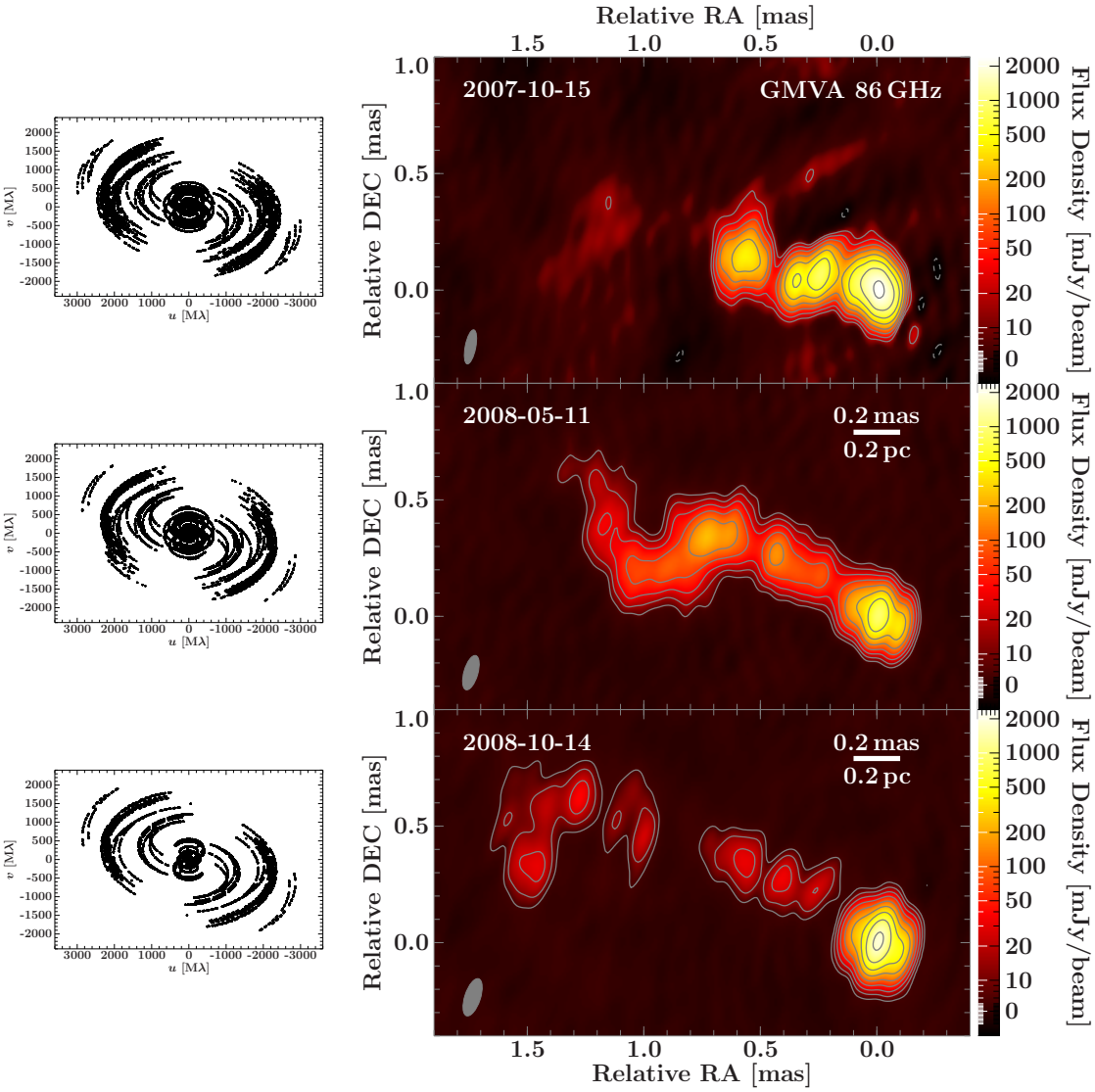

Figure 6.2.: Images of the GMVA observations of 3C 111 with a common noise level for which the last observations was used as a reference and a common colour scale. The (u, v)-coverage of the observations are shown in the smaller panels left to the images.

In case of 3C 111, a jet speed of $1\,\mathrm{mas\,yr^{-1}}$ corresponds to about $3.3\,c$ and jet speeds up to $\sim 6\,c$ have been measured at lower frequencies (Jorstad et al. 2005; Kadler et al. 2008; Chatterjee et al. 2011). If the jet moves at a similar high speed at 86 GHz, this will lead to a displacement of the components of about 0.18 mas per month. In fact, the changes in jet morphology over time in Fig. 6.2 already indicates a significant evolution. This makes it difficult to associate the model fit components.

In order to facilitate the association, the selected 43 GHz images from the VLBA-BU-Blazar programme are used. Figure 6.3 shows the time evolution of these images in combination with the GMVA images. Like the latter, the 43 GHz images are aligned to the most upstream component as fitted in Schulz (2012). The combination of 43 GHz and 86 GHz data shows that features described by the components at 86 GHz are also seen at 43 GHz. The labels of the associated components reflect the morphology of the jet, i.e. a C1 and C2 correspond to the two components upstream of the jet in the compact region (see Subsect. 6.3.1), while components that belong to the jet are assigned a "J" plus an integer that increases upstream and over time. The association seems to work best for components J2 and J3, but also the other components seem to be reasonably well identified. Similar to the case C2a,b in the first and second observation, the kinematic component J2 comprises two model fit components that are considered to mark the same region due to their proximity and the lack of such components in later observations.

The velocity of each kinematic component is determined from a linear regression fit of the position over time following equation 4.3.2. Based on these fits, the apparent speed $\beta_{\mathrm{app}} = \sqrt{\beta_{\mathrm{app,x}}^2 + \beta_{\mathrm{app,y}}^2}$ is calculated and the results are given in Table 6.2. The ejection time T_0 of the component is calculated from the linear regression fit to the distance of the components over time. This is a reasonable simplification due to the limited amount of observations available.

As can be seen in Fig. 6.3, the evolution of the bend is described by two components, J2 and J3. Both move at similar speeds, though the ejection time differs marginally. Overall, all jet speeds are consistent within the uncertainty with the exception of C2 that is interpreted as a stationary feature. Based on the jet speed, it is now possible to calculate the critical viewing angle $\theta_{\mathrm{LOS,crit}}$ and the minimum Lorentz factor γ_{min} as described in Sect. 2.3.4. Using the maximum value of β_{app} following Cohen et al. (2007), this yields $\theta_{\mathrm{LOS,crit,86}} \sim 13^\circ$ and $\gamma_{\mathrm{min,86}} \sim 4.6$.

6.4. Discussion

6.4.1. Lorentz factor and viewing angle

Several studies of the evolution of the pc-scale jet have been performed at 15 GHz (Kadler et al. 2008; Lister et al. 2009a, 2013; Großberger 2014) and 43 GHz (Jorstad et al. 2005; Chatterjee et al. 2011). There is a broad distribution of apparent speeds ranging from $\sim 2\,c$ up to $\sim 8\,c$ at 15 GHz and up to $\sim 6\,c$ at 43 GHz. The estimated apparent speeds of the jet components at 86 GHz, listed in Table 6.2, do not reflect this broad distribution. This is most likely due to the limited amount of observations and especially the short

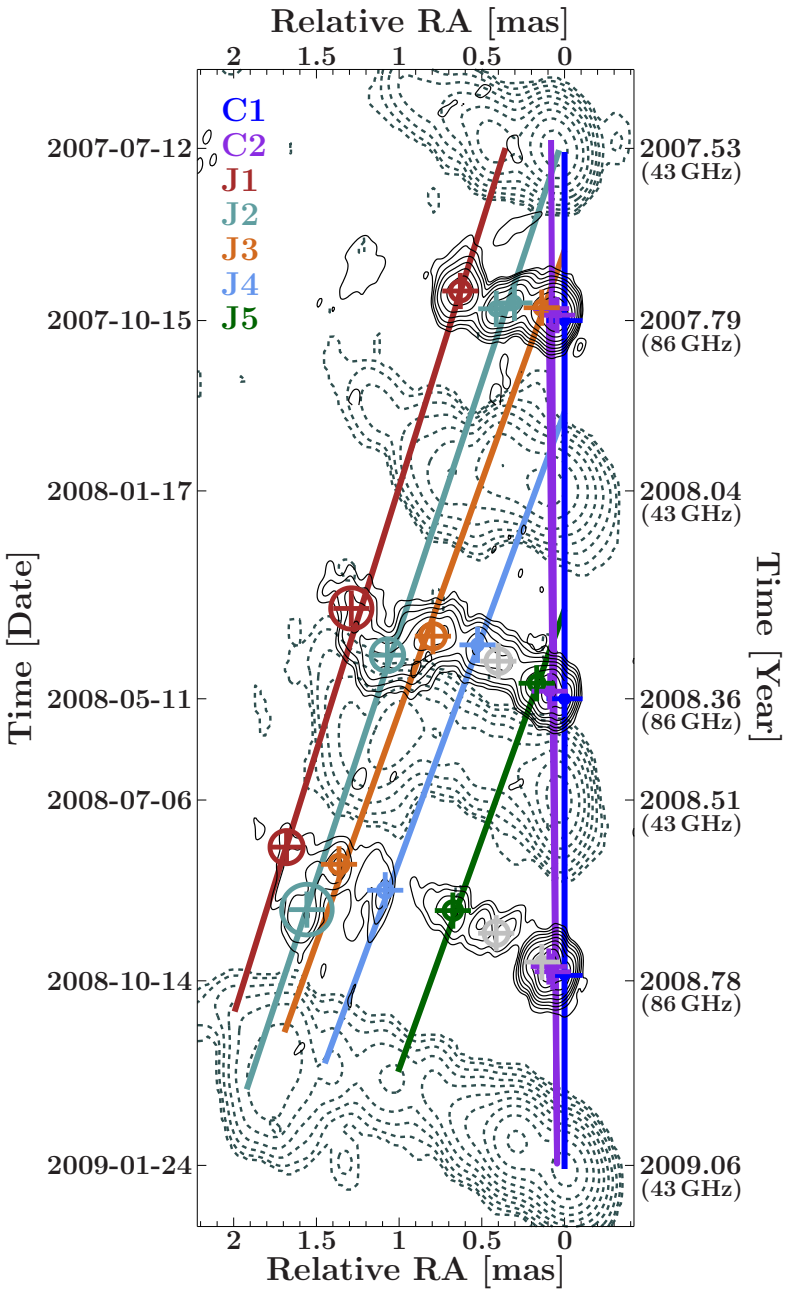

Figure 6.3.: The GMVA images (black contour lines) spaced according to their time separation with the Gaussian model fit components. The coloured components are used in the kinematic analysis and solid lines are calculated from the kinematic fit in both coordinates. The GMVA images were convolved with a common beam of 0.167 mas × 0.067 mas, PA −18°. The gray, dashed contour lines show the selected VLBA images at 43 GHz that were used to constrain the association of the GMVA components. The contour lines at both frequencies start at three times the noise level of each image and increase logarithmically by a factor of 2. The images are aligned to the most upstream component.

Table 6.2.: Estimates of the velocity, speed and ejection time of the components at 86 GHz

ID	$v_{\mathrm{app,x}}$ [mas yr^{-1}]	$v_{\mathrm{app,y}}$ [mas yr^{-1}]	$v_{\mathrm{app,est}}$ [mas yr^{-1}]	$\beta_{\mathrm{app,est}}$	$t_{0,\mathrm{est}}$ [yr]
(1)	(2)	(3)	(4)	(5)	(6)
C2	0.0 ± 0.02	-0.004 ± 0.009	-0.03 ± 0.02	-0.09 ± 0.06	
J1	1.1 ± 0.1	0.60 ± 0.06	1.2 ± 0.1	4.0 ± 0.3	2007.2 ± 0.2
J2	1.2 ± 0.2	0.31 ± 0.06	1.3 ± 0.1	4.2 ± 0.4	2007.5 ± 0.1
J3	1.22 ± 0.07	0.59 ± 0.03	1.36 ± 0.06	4.5 ± 0.2	2007.67 ± 0.04
J4	1.3 ± 0.1	0.44 ± 0.06	1.4 ± 0.1	4.5 ± 0.4	2007.90 ± 0.06
J5	1.2 ± 0.2	0.70 ± 0.08	1.4 ± 0.1	4.5 ± 0.5	2008.22 ± 0.05

Note: Columns: (1) Label of the component; (2,3) estimated apparent angular velocity of the components; (4) estimated apparent angular speed of the components; (5) estimated apparent speed of the components; (6) estimated ejection time of the components

time frame of 1 yr of the observing campaign.

Lister et al. (2013) reported a maximum value of the β_{app} at 15 GHz of (8.15 ± 0.31). This yields $\theta_{\mathrm{LOS,crit,15}} \sim 7.0^\circ$ and $\delta_{\mathrm{crit,15}} = \gamma_{\mathrm{min,15}} \sim 8.2$ at 15 GHz. At 43 GHz the maximum of $(6.37 \pm 0.29)\,c$ was determined by Chatterjee et al. (2011) that corresponds to $\theta_{\mathrm{LOS,crit,43}} \sim 8.9^\circ$ and $\gamma_{\mathrm{min,43}} \sim 6.4$. Jorstad et al. (2005) used the flux density variability of the components to determine θ_{LOS}, δ and γ. The maximum γ from variability is measured to be 6.6 consistent with Chatterjee et al. (2011) and $\gamma_{\mathrm{min,86}}$, but below $\gamma_{\mathrm{min,15}}$ and the average value of γ from variability of 4.4 ± 1.3 is even closer to $\gamma_{\mathrm{min,86}}$.

Due to the one-sidedness of the pc-scale jet, it is difficult to estimate the viewing angle. Kadler et al. (2008) suggested that $\theta_{\mathrm{LOS}} \leq 21^\circ$ based on the jet-to-counter jet ratio for which the noise level of the image defined the upper limit of the flux density of the counter jet. The study found that this value is inconsistent with the estimate of Lewis et al. (2005) of $\theta_{\mathrm{LOS}} \gtrsim 21^\circ$ that was ascertained by putting a limit on the total de-projected size of 3C 111. Jorstad et al. (2005) reported an average value of $(18.1 \pm 5.0)^\circ$ based on variability which would still be consistent with Lewis et al. (2005). Another estimate of $\sim 8.1^\circ$ was obtained by Hogan et al. (2011) based on the X-ray jet of 3C 111 on kpc scales assuming no deceleration from pc to kpc scales. Intriguingly, this value is fairly consistent with $\theta_{\mathrm{LOS,crit,15}}$ and $\theta_{\mathrm{LOS,crit,43}}$. As noted already by Kadler et al. (2008), a change in jet angle seems unlikely as the average position angle of the jet shows that it is well aligned from pc to kpc scales and at such angles small changes in the viewing angle would be amplified in projection. Nevertheless, it cannot be excluded. Assuming that the viewing angle of the pc scale jet ranges between $\sim 7^\circ$ and $\sim 20^\circ$ leads to a scaling factor between ~ 8 and ~ 3 from projected to de-projected scales.

It is not very likely that differences in the jet speed between frequencies is a result of different scales within the jet. Pushkarev et al. (2012) reported a decrease of the core shift from 8.1 GHz to 12.1 GHz with the reference set to 15.4 GHz of ~ 0.3 mas to ~ 0.1 mas. In addition, the bend of the jet is well visible at both, 43 GHz and 86 GHz, which suggests that similar scales are being probed. Another possibility is related to the

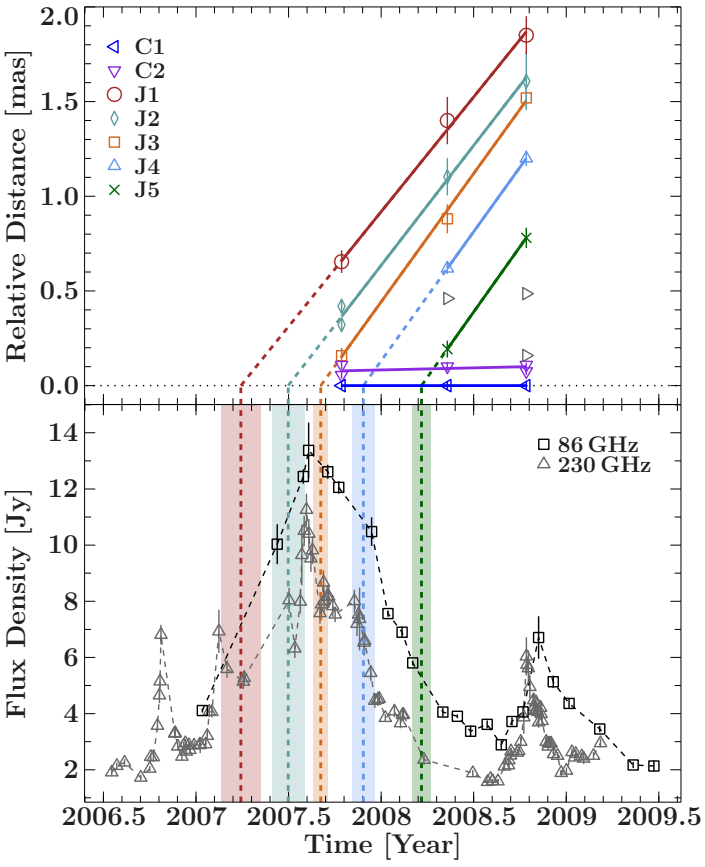

Figure 6.4: Top panel: Distance of the component with respect to C1 over time with the components used in the kinematic analysis emphasized by colour. The solid lines are calculated from the vector fit of the position of the components. The dashed lines represent the extrapolation backwards to the ejection time estimated in the distance-time domain. Bottom panel: 86 GHz (F-GAMMA, black squares) and 230 GHz (SMA, grey triangles, Chatterjee et al. 2011) light curve of 3C 111 between 2006.5 and 2009.5. The dashed lines correspond to the estimated ejection date with the uncertainty highlighted by the shaded region.

jet activity, so that new material ejected into the jet stream could have different Lorentz factors. It is possible to keep the angle to the line of sight constant by increasing γ (see Fig. 2.6). However, this is further complicated by the evolution of the jet due to instabilities as for example discussed by Kadler et al. (2008).

6.4.2. Ejection times and flare evolution

The estimated ejection time of the jet components J1 to J5 listed in Table 6.2 can be compared with the evolution of the F-GAMMA light curve. This is shown in Fig. 6.4. In addition to the 86 GHz light curve, the SMA light curve at 230 GHz is included based on data from Chatterjee et al. (2011). The higher frequency data show a more complex evolution of the large outburst with two smaller peaks at the end of 2006 and the beginning of 2007, respectively. A comparison between the peaks of the radio light curves in mid 2007 and in the end of 2008 shows only a small time delay. As shown in Chatterjee et al. (2011) and Großberger (2014) this delay increases with decreasing frequency. This behaviour is not unusual for blazars (e.g., Fuhrmann et al. 2014).

The shaded regions in Fig. 6.4 correspond to the uncertainty of the ejection time. Due to the limited number of observations, the ejection times are only indicative. As stated

earlier, the 43 GHz used in this work were previously analysed by Chatterjee et al. (2011) as part of a monitoring campaign over 5.4 years. However, only the brightest components were tracked in this study, while all 86 GHz components are considered for the kinematic analysis if associations are possible. A comparison with the associations at 86 GHz shows reasonable agreement except for component K5 in Chatterjee et al. (2011). In contrast to Chatterjee et al. (2011), the bend of the jet is separated into multiple components which makes a more detailed analysis possible.

The ejection times of the components J2 and J3 are fairly consistent with K6 in Chatterjee et al. (2011) and seem to be strongly related to the peak of the outburst. Even the ejection time of K5 is only marginally below J1, since K5 is slightly slower than J1. This leads to K5 being ejected before the minor outburst and not afterwards like J1. However, the difference is small given the data sampling at 86 GHz.

The complex evolution of the jet at 86 GHz with the ejection of multiple components is also seen at 15 GHz by Großberger (2014) leading to consistent ejection times at both frequencies (see Table 4.3 in Großberger 2014) even though the outburst occurred at the beginning of 2008 at 15 GHz. In particular, component B70a at 15 GHz could be related to J2, though the position angle is about $\sim 70°$ and not around $\sim 75°$ as in the case of J2. A possible explanation could be the different scales on which the components were studied. Großberger (2014) suggested that B70a and B64a have the same origin which the study supported with comparison with the 43 GHz analysis in Schulz (2012). The ejection time of B64a is consistent within the uncertainties of J3 suggesting that both B64a and B70a could have their origin J3 and J2, respectively. The components also have fairly similar jet speeds. However, J3 and B63a also have consistent ejection times, but B63a is faster than J3. Hence, a clear association of B64a and B70a with J3 and J2 is not possible. Similar to the evolution at mm-wavelengths, the 15 GHz jet feature related to the major outburst evolves into a complex emission region (Großberger 2014, Beuchert et al. in prep).

6.4.3. The bend of the jet

The bend or kink described by components J1, J2 and J3 is reminiscent of an instability that grows over time. As mentioned in Subsect. 2.3.3 such a kink can be created by current-driven instabilities (CDI) or Kelvin-Helmholtz instabilities (KHI). Following Perucho et al. (2012) for example, the amplitude A of such an instability can be described by

$$A = A_0 e^{(x_{\mathrm{int}} - x_{\mathrm{int},0})/\lambda_i} \tag{6.4.1}$$

where A_0 is the amplitude at $x_{\mathrm{int},0}$, $x_{\mathrm{int}(,0)}$ de-projected distances and λ_i the growth length. In order to avoid the need to de-project both image coordinates, the system is rotated by $90° - \phi_{\mathrm{jet}}$, where ϕ_{jet} is the position angle of the jet (see Fig. 6.5). Here, the median position angle of the components was calculated to be $\sim 65°$ and used for ϕ_{jet}. In the rotated system A is given by the difference of the y-coordinates of J2 and J3, i.e. $A = \Delta y = y_{\mathrm{J2}} - y_{\mathrm{J3}}$ and the x-coordinate corresponds to the projected distance x_{obs} that

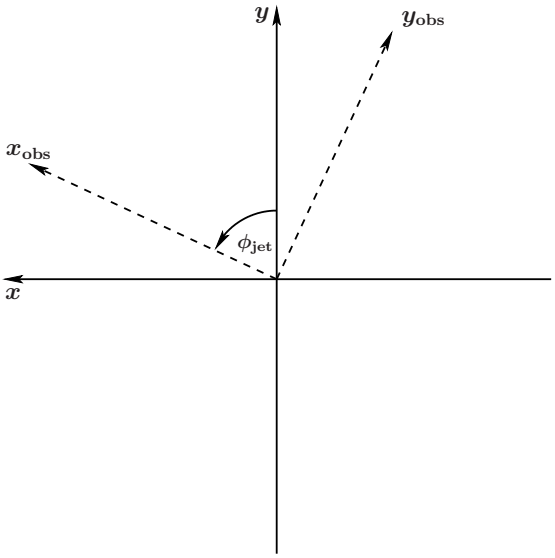

Figure 6.5: The two coordinate systems relevant for the analysis of the bend. The dashed lines mark the coordinate system of the source, i.e. $x_{\rm obs}$ and $y_{\rm obs}$ are oriented along and perpendicular to the jet axis. x and y mark the rotated coordinate system of the jet.

is related to the intrinsic distance as $x_{\rm int} = x_{\rm obs} \sin\theta_{\rm LOS}$ in equation 6.4.1. The distance of the instability is taken to be the x-coordinate of J2. As shown in Subsect. 6.4.1, $\theta_{\rm LOS}$ of the pc-scale jet is not exactly known, thus a lower and upper limit of $\sim 8°$ and $\sim 21°$ and an average value of $\sim 15°$ is used in the following.

Figure 6.6 shows the superposition of the components J2 and J3 along the jet axis and the linear regression fit to the positions. In order to avoid small, systematic variations from observation to observation, the latter is used in the following.

First, the growth length is estimate, which requires two measurements of the amplitude and distance of the instability (A, $x_{\rm int}$). Because of the fact that in the last observations the bend is not visible any more, the first two instances are chosen, i.e., (~ 0.078 mas,$\sim$ 1.4 mas) and (~ 0.23 mas,~ 4.1 mas). This yields $\lambda_{\rm i,15} \sim 2.6$ mas, $\lambda_{\rm i,8} \sim 4.8$ mas, and $\lambda_{\rm i,21} \sim 4.8$ mas depending on $\theta_{\rm LOS}$.

Having $\lambda_{\rm i}$, A_0 is calculated for $x = 0$, i.e. the position of C1 to be $A_0 \sim 0.046$ mas. In the first GMVA observation the minor axis of the CLEAN-beam is similar to this value of A_0. Unfortunately, the amplitude of the instability is orientated rather in the direction of the major axis. Nevertheless, this implies that instability could have been observed relatively early in the jet at 86 GHz especially if additional north-south baselines would have been available, e.g., through the inclusion of ALMA.

A highly interesting question is the initial location of the instability depending on A_0 which is practically the reverse scenario as before. In the most extreme case, the size of the jet base provides a minimum value for A_0. However, such a value has only been measured in M 87 at 230 GHz by Doeleman et al. (2012). Even though, $\theta_{\rm LOS}$ for M 87 has been estimate to be 15°–45°(e.g., Ly et al. 2007; Acciari et al. 2009) consistent at the lower end with 3C 111, Hada et al. (2011) showed that the location of the SMBH from the 43 GHz core is 14 $R_{\rm S}$–23 $R_{\rm S}$. This is in contrast to estimates for blazars of $10^{4-6} R_{\rm S}$ (e.g., Marscher 2006, 2009; Agudo et al. 2011; Fromm et al. 2015), though these sources usually

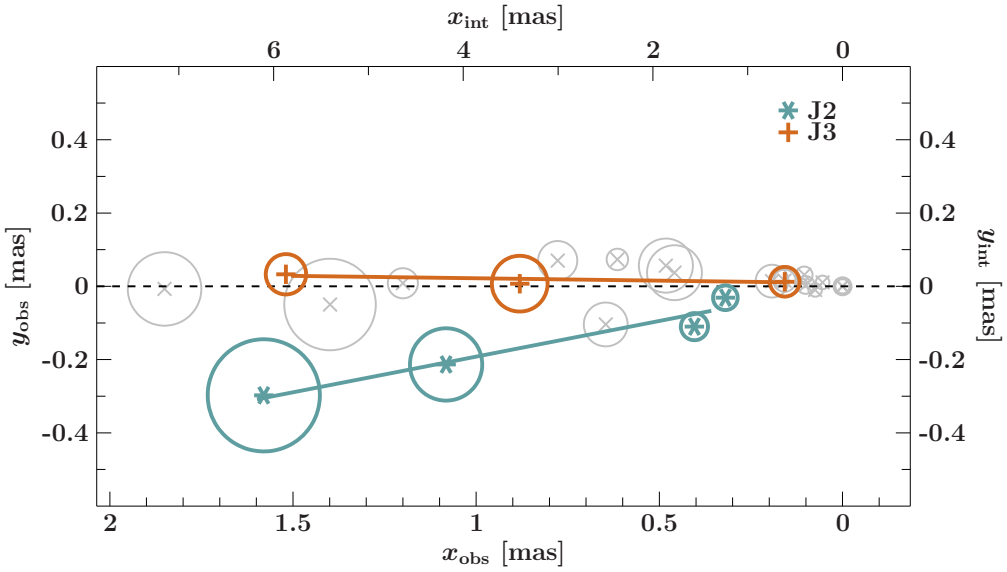

Figure 6.6.: The position of the model fit components rotated so that the position angle of the jet ($\sim 65°$) is orientated along the x-axis. The components are aligned to C1. The intrinsic coordinates are calculated using $\theta_{\rm LOS} = 15°$. Highlighted in colour are the components J2 and J3 and the solid lines correspond to the kinematic fits. Note, in the chosen coordinate system $y_{\rm obs} = y_{\rm int}$.

have smaller values of $\theta_{\rm LOS}$. Additionally, Chatterjee et al. (2011) reported a projected distance between 0.1 pc–0.3 pc of the corona as the production site of the X-ray emission, and the VLBI core at 43 GHz based on variability. In terms of the upper limit and $\theta_{\rm LOS} = 15°$, this corresponds to an intrinsic distance of about 1.2 pc or $5 \times 10^4 R_{\rm S}$.

Figure 6.7 shows how A_0 and x_0 scales for different values of $\theta_{\rm LOS}$ and on projected scales. Assuming that the size of the jet base of M 87 is valid for 3C 111, this results in $x_{\rm int,15} \sim -14\,pc \approx -7.4 \times 10^5 R_{\rm S}$ (horizontal, dashed line). While this still fits within the range of $10^{4-6} R_{\rm S}$ for blazars, it is about a factor of 10 above the value estimated by Chatterjee et al. (2011) assuming no core shift between 43 GHz and 86 GHz. If a core shift is taken into account, it will make the distance to the corona at 86 GHz even smaller.

Two fundamental assumptions in this analysis are that J2 and J3 evolve ballistic, i.e. that the acceleration occurs on negligibly small scales and that the growth of the amplitude can be fully described by equation 6.4.1. Both assumptions may not be the correct. Taking the distance estimated by Chatterjee et al. (2011) as $x_{\rm proj,0} = -0.3$ pc, would yield $A_0 \sim 0.03\,pc \approx 1.2 \times 10^3 R_{\rm S}$. This would imply that initial size of the instability is already large. This would imply that the initial size of the instability is already large or acceleration occurs during the initial growth of the amplitude.

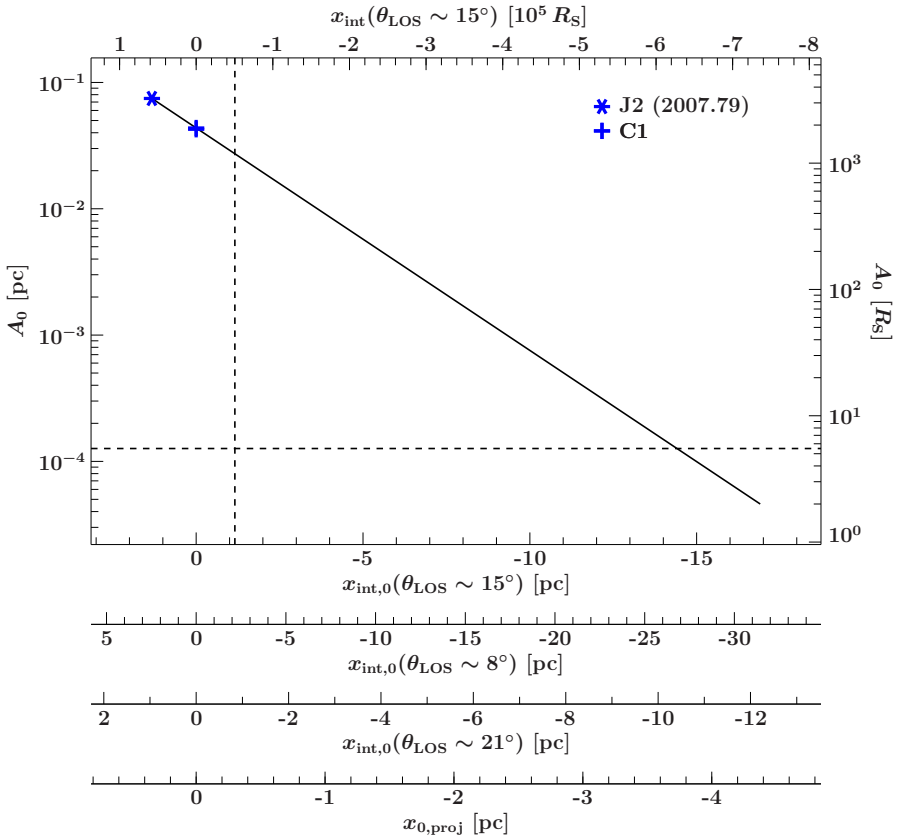

Figure 6.7.: The dependence of the initial amplitude A_0 on x_0. The horizontal, dashed line marks the size of the jet base measured by Doeleman et al. (2012) in M 87. The vertical dashed line refers to maximum distance of the 43 GHz core to the corona from Chatterjee et al. (2011) assuming that the core shift is negligible, otherwise the this value would be smaller. The reference point used for this extrapolation is J2 in the first GMVA observation. The multiple x-axes are given for the intrinsic distance along the jet using the different estimates of $\theta_{\rm LOS}$, except for the bottom x-axis that reflects the projected distance.

6.4.4. A comparison with previous outbursts and the γ-ray connection

As mentioned in Sect. 6.1, two other outburst of 3C 111 above 10 Jy have been detected. The most information are available for the one in 1996. Hence, it is best suited for a comparison with the one in 2007. According to Alef et al. (1998), the high flux density was measured in 1996 January at 90 GHz, but no information on the evolution of the light curve are available. Hence, it is difficult to ascertain whether the peak occurred before or after.

The long-term light curve at mm-wavelengths between 1997 and 2010 indicates at least three smaller outbursts up to about 7 Jy at 3 mm. One of these smaller outbursts occurred in 1997, about a year after the measurement reported by Alef et al. (1998). Intriguingly, this looks very familiar when compared to the 2007 outbursts. Figure Fig. 6.4 shows a

small outburst little over a year after the peak at the end of 2008.

As seen Fig. 6.3 and in later images by Chatterjee et al. (2011), the bend evolves into a large complex emission region that moves radially outward. Jorstad et al. (2005) observed a large, diffuse feature at a distance of about 2 mas from the core at 43 GHz in at the end of 1998 March. The study interpreted this feature as the relic of the outburst. At 15 GHz where the jet can be traced as far out as 10 mas from the VLBI core, Kadler et al. (2008) reported that the a complex evolution of the jet including the development of trailing components set in as a result of the outburst related plasma moving through the jet. It affected the jet for over a decade.

Polarization information of the pc-scale jet are only scarcely available for the outburst in 1996. Kharb et al. (2003) presented two 43 GHz images which revealed a feature possibly related to the 1996 outburst to be polarized. This would be consistent with the images in Jorstad et al. (2005) in which the relic feature is also polarized. Polarization at 15 GHz was only available from 2002 on for Kadler et al. (2008). Nevertheless, the images suggest weak polarization where the outburst related feature should be. Due to the long-term MOJAVE monitoring polarization is available for the 2007 outburst from the beginning. The complex emission region which appeared because of the outburst according to Großberger (2014) shows a strong evolution in the degree of polarization over time (Beuchert et al. in prep.).

In conclusion, there are several indications that the outbursts in 1996 and 2007 are similar which leads to the question about the difference between the larger and smaller outburst and their connection. The different flaring activity makes 3C 111 an ideal target to study the duty cycle of activity in an AGN and its relation to pc-scale jet. Flux density measurements at mm-wavelengths are best suited for this kind of study as they are least contaminated by the large scale synchrotron emission and dominate by the pc-scale jet.

The fact that 3C 111 is not contained in all *Fermi*-LAT source catalogues is most likely due to variable γ-ray emission. While the *Fermi*-LAT was not yet available in 2007, Grandi et al. (2012) analysed *Fermi*-LAT data during the time of the smaller outburst at the end of 2008. The study reports a weak detection by *Fermi*-LAT in 2008 October/November with a TS-value of 9.7 using a two-month binning and otherwise upper limits. Note, that the *Fermi*-LAT source catalogues have a detection value of TS = 25. Grandi et al. (2012) interpreted the two events as linked. This would suggest that a future outburst of similar scale than in 2007 could also lead to higher γ-ray emission than reported by Grandi et al. (2012). However, there is also the possibility that not all radio outbursts lead to a significant increase γ-ray emission as mentioned in Sect. 3.1.

Based on the γ-ray-flux from the 3FGL and the median 15 GHz total flux density from the MOJAVE programme (see Sect. 3.2), 3C 111 has a γ-rayloudness of ~ 38. As shown in Fig. 3.3, this is at the lower end of the γ-ray-loudness distribution within the MOJAVE sample, but it is not unusual. The γ-ray-loudness range of 10 to 100 is also populated by quasars and BL Lacs at higher radio and γ-ray luminosities. In terms of the radio galaxies, only IC 310 has a γ-ray-loudness above 100, but the sample contains only 5 sources.

6.4.5. Interpretation of C1 and C2

VLBI observations below 86 GHz commonly attribute the most upstream component to be the core of the jet in 3C 111 that also coincides with the brightest feature of the jet (e.g., Jordán et al. 2005; Kadler et al. 2008). This is case in the majority of AGNs with one-sided jets (e.g., Kovalev et al. (2005)).

As shown in Fig. 6.2 and Fig. 6.3 the 86 GHz data reveal a component, C1, to the west of the brightest feature, C2. A similar feature was reported by Grandi et al. (2012) using slightly super-resolved 43 GHz data from the VLBA-BU-Blazar programme, which the authors suggest to be a feature of the counter jet due to it being stationary. However, there are arguments against this interpretation.

One argument is related to the implications on θ_{LOS}. If C2 and C1 reflect the cores of the jet and counter jet, the ratio of the flux density $R \sim 2.8$ can be used to calculate θ_{LOS} following equation 2.3.12. The combination with the results from kinematic analysis in Subsect. 6.3.2 shows that there is no range of θ_{LOS} and β that yield R and β_{app}. Only a substantial change in θ_{LOS} in the direction of the observer immediately after C2 would be able to correct this discrepancy. However, this is contrast to the steady decrease in brightness downstream of C2 and the stable position angle of the jet.

Another issue stems from the Doppler boosting and de-boosting of the jet and counter jet emission. As stated in Subsect. 2.3.4 the radio emission of the core is Doppler boosted by a factor of $\delta^{3+\alpha}$ with respect to the intrinsic flux. An additional $\delta^{3+\alpha}$ is necessary to get the emission of the core of the counter jet assuming intrinsic symmetry of both jets. In case of a flat radio spectrum of the core, i.e., $\alpha = 0$, $\delta \sim 1.2$ is necessary to account for the calculated value of R from C2 and C1. This is well below the critical Doppler factor calculated in Subsect. 6.4.1 and the variability Doppler factor from Jorstad et al. (2005).

Based on these arguments, the scenario of C1 being the first feature of the jet. Additional evidence for this interpretation would be a time delay of the flux density of C2 and C1 with respect to the overall flux density of the source due to the speed of the jet plasma. However, the data sampling is not good enough to perform such a study. The existence of a stationary feature has already been reported by Jorstad et al. (2005), though east of the core as the brightest feature of the jet.

As indicated in Subsect. 2.3.3, the most upstream feature of the VLBI jet does not necessarily has to be region of $\tau = 1$, but could also correspond to recollimation shocks. These shocks can become prominent at mm-wavelengths, while at lower frequencies the $\tau = 1$-region dominates (e.g., Marscher 2006).

6.5. Summary

This chapter presents three 86 GHz GMVA observations of unprecedented quality of the γ-ray-loud, FR II radio galaxy 3C 111 over a period of one year following a major outburst above 10 Jy in mid 2007. A kinematic analysis is performed for which selected VLBI images at 43 GHz from the VLBA-BU-Blazar programme were used in order to

facilitate the associations of components. Because of this, it is possible to estimate the apparent speed of different features in the jet and their ejection time for comparison with a light curve at 86 GHz from the F-GAMMA programme.

The VLBI images reveal the one-sided jet system with a resolution down to $\sim 50\mu$as and a dynamic range of (5.8–14) $\times 10^3$. The first GMVA observation occurred only about two months after the peak in the 3 mm light curve when the source was still at high level of flux density and shows that almost 50% of the total flux density is located within a region of about 0.1 mas (~ 0.096 pc projected size). The jet morphology evolves dramatically over the year and depict the emergence of an instability leading to the formation of a bend that is very likely related to the peak of the outburst. Due to the excellent resolution of the GMVA data, the bend is well resolved and traceable. It seems to move radially outwards along the position angle of the jet and forms a complex, diffuse emission region in the last observations.

The single-dish flux density measurements show that the outburst covered a time range of at least two years and included a few smaller outbursts, some which can be associated tentatively with ejection of a new component at 86 GHz consistent with the literature. The kinematic analysis suggest that the components move with apparent speeds between ~ 4.0 c and ~ 4.5 c. The lack of a broad distribution of $\beta_{\rm app}$ as known from lower frequency monitoring is most likely due to the limited amount of GMVA observations over short period of time. The maximum $\beta_{\rm app}$ correspond to a $\gamma_{\rm min} \sim 4.6$ and $\theta_{\rm LOS,crit} \sim 13^\circ$.

The GMVA images reveal an additional feature to the west of the brightest feature that is considered to be part of the jet and not the detection of a counter jet. Both features have brightness temperatures exceeding 10^{11} K at times and these are located within a region of about 0.1 mas. Since the brightest feature is stationary, a possible interpretation would be in the framework of recollimation shocks. However, further mm-VLBI observations are necessary.

Since it was suggested in the literature that a correlation between the γ-ray and radio activity as known from blazars exists, it is possible that the 2007 radio outburst would have lead to increased γ-ray emission. 3C 111 is not part of all *Fermi*-LAT source catalogue which also suggests that γ-ray emission is variable. Because of the long evolution of the radio outburst in 2007, a similar event in the future would be an ideal case to study the radio-γ-ray-connection in this radio galaxy in detail. There are several indications that the event in 2007 is similar to a radio outburst in 1996 that also peaked above 10 Jy at 3 mm. Hence, 3C 111 will undergo a radio outburst of similar scale in the future. In case of such an event, GMVA observations would be ideal to study the impact on the pc-scale jet and the inclusion of ALMA would be provide a significant boost in resolution transversal to the jet. This would be vital to study the formation of an instability as early as possible.

7. Conclusions and outlook

The extragalactic γ-ray sky is dominated by blazars, due to their strongly beamed jet emission. However, there is a growing number of other types of AGNs that are detected at γ-ray energies as well. Although these sources still represent a minority, they indicate that γ-ray emission is a fundamental characteristic of AGNs with relativistic jets. Commonly, the γ-ray emission from most AGNs is explained due to inverse-Compton scattering of photons internal or external to the AGN with the particles of the relativistic jet. Hence, detailed knowledge of the physical parameters of these jets is essential in understanding their formation, evolution and connection to the multi-wavelength emission. In particular, the non-blazar population of γ-ray loud AGNs are excellent to study the differences and similarities in the low- and high-energy emission processes with respect to blazars.

Radio observations are well suited to directly gain insight into the relativistic jet as the emission from these AGNs is dominated by synchrotron radiation from the jet in this frequency regime. Observations with mas-resolution or better that are made possible by VLBI are capable of resolving jets in AGNs down to sub-pc scales, measure the speed of the jet, the viewing angle and estimate the Doppler factor of the beamed emission. With increasing frequency, it is also possible to observe emission that stems from regions closer to the central supermassive black hole where the jets are formed. Radio interferometry on arcsec-scales is vital to measure the large-scale extent of the source, assess the dominance of the compact emission and study the evolution of the AGN and its host galaxy. Flux density monitoring in particular at high frequencies yields valuable insight into the variability and radio spectrum of AGNs. Using a large variety of radio astronomical instruments, I illustrate in this thesis the diverse characteristics of the γ-ray-population of AGNs that do not belong to the class of blazars in the radio regime in detail on three sources: IC 310 (Chapt. 4), PKS 2004−447 (Chapt. 5), and 3C 111 (Chapt. 6).

IC 310 is a low-luminosity radio galaxy that is detected up to the TeV energy range and exhibits a single-sided jet on pc-scales with a dominant compact VLBI core which are characteristics shared with blazars. The quasi-simultaneous and long-term VLBI observations at cm-wavelengths presented in this study confirm this morphology and reveal a mildly relativistic, faint jet that is well aligned from a few pc to hundreds of kpc. The subluminal motion is consistent with other TeV-detected radio galaxies and some blazars and coincides with a lack of strong flux density variability. This is in stark contrast to the extreme variability at TeV energies on scales of a day and down to a few minutes. These results provide further evidence that variability in the TeV regime of IC 310 is not directly related to the radio jet. Measurements of the core shift imply a distance to the black hole slightly smaller than values expected for blazars. The core shift also indicates that high magnetic fields at least of the order of 10^3G are present in the vicinity of

the central black hole where the jet is formed which is consistent with blazars, but also known from the LINER NGC 1052 (Appendix A). Further high-sensitivity monitoring of the pc-scale jet is necessary to put tighter constraints on the jet evolution due to the faintness of the jet. VLBI observations with increased frequency sampling will be able to determine the core shift with a higher accuracy in order to better estimate the distance to the black hole and the magnetic field strength of the jet.

There is a growing number of AGNs belonging to the class of RL-NLS1 that are observed in the γ-ray regime (γ-NLS1). Their detection challenges the understanding of γ-ray-loud AGNs as they have different properties than blazars and radio galaxies such as a lower black hole mass coupled with a high accretion rate, but they also share characteristics with blazars such as a relativistically beamed jets and a double-humped SED. The only representative currently known in the southern hemisphere is PKS 2004−447, which is at the lower end of the radio-luminosity distribution of γ-NLS1s. Within the framework of the TANAMI programme, high-angular resolution imaging observations are presented in this study that reveal an extended single-sided jet out to about ~ 150 pc (projected) that is in equipartition and terminates in a hot-spot like emission region. An archival VLBA observation uncovered additional diffuse emission on the opposite side of the jet which could be related to the counter-jet leading to a total size of ~ 530 kpc. Lower-resolution observations show that the large-scale extent of the source is below 11 kpc (projected), but the majority of the emission stems from the jet. The compactness of PKS 2004−447 is consistent with other RL-NLS1 and in contrast to radio galaxies such as IC 310 and 3C 111. The first long-term multi-frequency flux density monitoring exhibits a turnover below 1 GHz and another steep spectrum at higher frequencies. This confirms the previously suggested association of PKS 2004−447 with CSS/GPS sources. While this is not unusual for the RL-NLS1-population, it is currently unique among γ-NLS1s. CSS/GPS sources are even more elusive among γ-ray loud AGNs. As a result, PKS 2004−447 shares characteristics with very different types of AGNs similar to the general population of RL-NLS1s, which is highly intriguing as both, CSS/GPS and RL-NLS1 sources, are considered to be young AGNs. The ongoing monitoring of PKS 2004−447 by TANAMI will enable us to the study structural changes of the jet over time and with respect to the high-energy emission.

3C 111 was the first FR II radio galaxy detected in the γ-ray regime and only two other FR IIs have been detected so far by *Fermi*-LAT. Its faint γ-ray emission is variable challenging its detection. However, it is a very strong radio emitter with a complex single-sided jet that exhibits superluminal speeds on pc-scales. In addition, 3C 111 displays radio outbursts up to six times the nominal level, in stark contrast to IC 310. The spatially resolved impact of one of these strong flares on the pc-scale jet is studied for the first time with three VLBI observations in the 3 mm-regime starting shortly after the peak of the flare in combination with single-dish flux-density monitoring. The high-fidelity of the images resolve the jet on projected scales down to ~ 0.04 pc and suggest that multiple components emerged over the complex evolution of the flare. The most distinct feature is a bend-like instability that is tentatively associated with the peak of the radio outburst. It is well resolved spatially, grows over time and merges into a

large diffuse feature, while the jet remains collimated otherwise. At least three of these large radio outbursts are known with intermediate outbursts occurring in-between which suggest that they are recurring. Hence, a future major outburst is to be expected and will provide an excellent case to study the radio-to-γ-ray connection in an FR II galaxy.

The γ-ray loudness is studied as a general parameter to compare the radio-to-γ-ray emission with other AGNs in the MOJAVE and TANAMI sample (Sect. 3.2 and 3.3). For both samples, the recently released 3FGL catalogue was used which represents an update with respect to previous studies. However, the comparison is limited by the low number of radio galaxies and γ-NLS1s. IC 310 and 3C 111 occupy the low-luminosity end in both energy regimes as do the other radio galaxies, but their γ-ray loudness differs by more than an order of magnitude which currently sets the range for the radio galaxies. The γ-ray loudness of the radio galaxies is not unusually low compared to blazars. A slightly smaller range in γ-ray loudness is observed for γ-NLS1, but at a higher value than most of the radio galaxies. The γ-NLS1 also cover a larger range of luminosities from the BL Lac- to the quasar-dominated luminosities. In the TANAMI sample, the γ-ray loudness distribution is generally shifted slightly upwards, which could be a result of the bias of TANAMI towards the brightest radio and γ-ray sources. The sample of radio galaxies and γ-NLS1s would benefit greatly from improved data processing by *Fermi*-LAT in the lower energy regime which is now available (Pass-8), possibly leading to the detection of more source which would be vital for a statistical analysis.

For most AGNs the γ-ray emission is considered to be strongly linked to the jets, which makes the study of their evolution as early as possible in the formation process a key factor. This can be done best with VLBI at mm-wavelengths. The availability of ALMA for observations with the GMVA at 3 mm provide a significant boost in sensitivity and resolution along the north-south direction (e.g., Fish et al. 2013; Tilanus et al. 2014). In addition, the EHT consortium paves the way for VLBI at 1.3 mm, though for the moment these efforts are generally focused on Sgr-A* and M 87 to observe the shadow around the black hole caused by the last photon ring (e.g., Doeleman et al. 2008, 2012; Fish et al. 2014; Lu et al. 2014). The observations of other AGNs will also benefit from this progress in VLBI. One example from the three sources prominently discussed in this work is 3C 111. Increased resolution in north-south direction at 3 mm would be excellent to probe the evolution of an instability such as the one observed after the outburst as early as possible in order to model it. 1.3 mm observations can shed light on the substructure observed upstream of the jet at 3 mm. ALMA also significantly improves the capability of mm-VLBI arrays to observe sources in the southern sky. This makes it possible to study the closest AGN, Centaurus A, for example at the highest angular resolution and thereby on the smallest scales[1]. Moreover, mm-wavelength are best suited for correlations with the high-energy flares to probe the origin of the γ-ray emission. In order to tightly constrain the size and location of the jet-formation region with respect to the black hole, an AGN with its jets orientated close to the plane of the sky would be best suited and this is the case in NGC 1052.

[1]For Centaurus A, 1 mas correspond to 0.018 pc (Müller et al. 2011). Hence, a resolution of 50μas at 3 mm probe scales of about 1 mpc or 170 R_S.

The large-scale radio emission is also vital to understand the evolution of an AGN and the dependence on the pc-scale jet. Radio observations at low frequencies of the order of hundreds of MHz are best suited for these purposes as they are most sensitive to the oldest particle population of the jet which puts constraints on the size, power and age of the AGN. LOFAR, for example, is an excellent instruments for these kinds of studies. Due to its VLBI capabilities, it offers a resolution down to about $1''$ and that is of particular importance for RL-NLS1, because of their small large-scale extent compared to radio galaxies. This allows their place to be explored in the evolution of AGNs in greater detail and search for differences in the γ-ray-loud and -quiet population in context of the pc-scale jet. For the future, one of the most prominent new radio facilities will be the SKA operating at the low and intermediate frequencies (Aharonian et al. 2013), but there are also developments at higher frequencies such as the next generation VLA (Carilli et al. 2015) bridging the gap to ALMA. The technological evolution of astronomical instruments have always furthered our understanding of the physical processes in AGNs and will continue to provide the means for new, exciting discoveries.

A. The mm-VLBI view of the two-sided jet system of NGC 1052

As discussed in the previous chapters a common characteristic of γ-ray-loud AGNs is a relatively small angle of the jet to the line of sight that leads to significant Doppler boosting of the radio emission making these jets appear one-sided. The studies of IC 310 (Chapt. 4) and 3C 111 (Chapt. 6) are excellent examples on how difficult it is to infer the location of the black hole and the origin of the jet in one-sided jet systems. This issue can be solved to some extent if the jet has a larger angle to the line of sight, so that the jet and counter jet are observable. In addition, the source should be as close as possible in order to probe the smallest spatial scales and it should show significant radio emission. However, not many sources fit these criteria. One that does, is NGC 1052 which will be introduced in the following. This chapter presents a summary of results from a GMVA observation in 2004 which will be presented in Baczko et al. (2016) and it highlights specific contributions of mine.

A.1. Zooming into NGC 1052

NGC 1052 is located at a redshift of $z \approx 0.005$ according to measurements listed in *NASA/IPAC Extragalctic Database*[1] (NED) which corresponds to a luminosity distance of about 20 Mpc. At this distance 1 mas corresponds to about 0.10 pc. The mass of the central supermassive black hole has been measured by Woo & Urry (2002) to be $\sim 10^{8.2}\,M_\odot$ based on stellar velocity dispersion. NGC 1052 is a classical LINER (Heckman 1980)[2] hosted in an elliptical galaxy that shows indication of a merger event about 1 Gyr ago (van Gorkom et al. 1986).

On kpc scales, NGC 1052 exhibits a two-sided jet system about 3 kpc in extent (Wrobel 1984; Jones et al. 1984; Kadler et al. 2004a) as shown in the top panel of Fig. A.1. The position angle of the jets are well aligned with the morphology of the host galaxy and two ionization cones. In addition, the position of radio features in the jet coincides with bright optical knots (Pogge et al. 2000; Kadler et al. 2003). At X-ray energies, *Chandra* images have revealed a bright central nucleus dominating above 3 keV, compact features that are prominent between 1–3 keV and extended emission in particular between 0.1–1 keV (Kadler et al. 2004a; Böck 2012). The nucleus and extended emission coincide positionally with the large scale radio emission. The X-ray spectrum is not dominated by jet-like simple power law. Based on near-infrared observations, Fernández-Ontiveros

[1] http://ned.ipac.caltech.edu/

[2] See Kauffmann (2009) for a commentary on the impact of this paper.

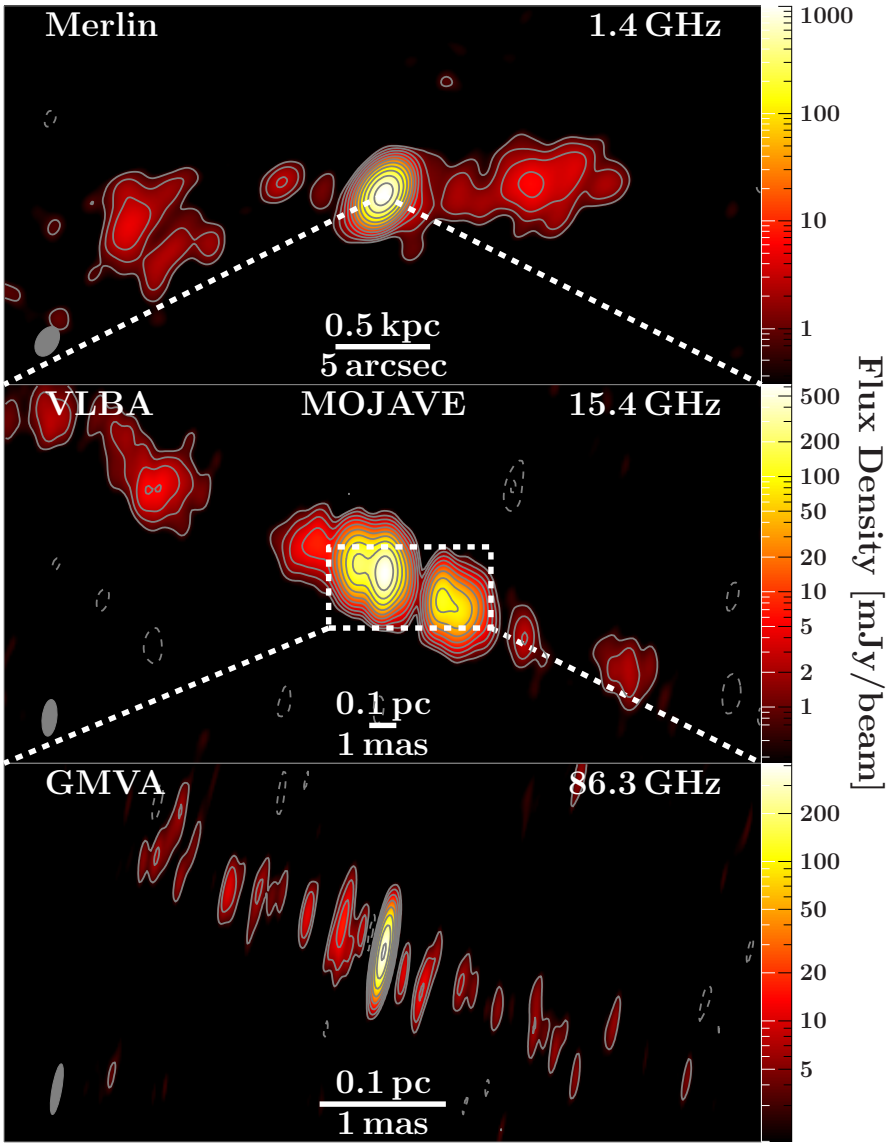

Figure A.1.: The radio morphology of NGC 1052. Top panel: Merlin image at 1.4 GHz of the kpc scale (Kadler et al. 2004a). Middle panel: 15 GHz VLBA naturally weighted image from the MOJAVE programme (Lister et al. 2013). Note, the emission gap in the central region due to the torus. Bottom panel: Uniformly weighted GMVA image at 86 GHz revealing the central region as the origin of both jets (Baczko et al. 2016). The lowest contour line starts at three times the noise level of each image, i.e., 0.22 mJy beam^{-1} (top panel), 0.23 mJy beam^{-1} (middle panel), 0.99 mJy beam^{-1} (bottom panel), and increase logarithmically by a factor of two.

et al. (2011) reports star formation activity either in a minimum or in the final stages contained within in compact young stellar clusters in the central kpc. The star formation activity was interpreted as a result of the merger.

One of the most striking features of NGC 1052 is well visible in VLBI images: The morphology shows a gap in the brightness distribution at cm-wavelengths which has been explained by free-free absorption from a circumnuclear torus with a column density between $10^{22}\,\mathrm{cm}^{-2}$–$10^{24}\,\mathrm{cm}^{-2}$. Hence, the central region where the two jets emanate from is not observable (Kameno et al. 2001; Vermeulen et al. 2003; Kadler et al. 2004b; Sawada-Satoh et al. 2008). However, due to the frequency dependence of free-free absorption (see Subsect. 2.3.1), the strength of absorption by the torus decreases with increasing frequency which leads to a decrease of the size of the emission gap. The middle panel in Fig. A.1 shows a 15.4 GHz VLBA image from the MOJAVE programme[3] in which the emission gap is still visible. At lower frequencies the gap is much more pronounced.

The first mm-VLBI obseration at 86 GHz of NGC 1052 was performed with the *Co-ordinated mm-VLBI Array* (CMVA), the predecessor of the GMVA, in 2002 (Lee et al. 2008). However, due to the short observing time and the low declination of the source, only a bright compact feature was detected. In 2004, a full-length GMVA observation of NGC 1052 was performed at 86 GHz Baczko et al. (2016). It provides the first clear detection of the two jets at this frequency at a resolution of $0.354\,\mathrm{mas} \times 0.057\,\mathrm{mas}$ for uniform weighting. Moreover, the two jets extend from a single compact, bright feature that is identified as the origin of both jets. In this case the feature does not represent the VLBI core as observed in single-sided jets. Instead the VLBI cores are located within the central region. The size of the compact feature in direction of the jets is estimated to be below $30\,\mu$as which corresponds to about $100\,R_\mathrm{S}$. Hence, both jets are formed within a distance of $\sim 50\,R_\mathrm{S}$ from the SMBH assuming the jets are symmetric. In order to determine the jet position angle of the jet, I analyse the distribution of the CLEAN-components along north-eastern (NE) and the south-western (SW) jets. The flux weighted mean yields $\phi_\mathrm{NE,mean} = (64 \pm 12)^\circ$ and $\phi_\mathrm{SW,mean} = (-120 \pm 13)^\circ$ where the error corresponds to the weighted standard deviation. The median values of the position angle are not significantly different with $\phi_\mathrm{NE,median} \approx 66^\circ$ and $\phi_\mathrm{SW,median} \approx 118^\circ$. These values are consistent with low-frequency VLBI measurements (Kadler et al. 2004a; Böck 2012).

As discussed in Baczko et al. (2016), the core dominates the total flux density and the surface brightness of the jet drops strongly from the core to the first jet-related feature. Hence, it is possible to assume that the majority of the synchrotron cooling occurs within the core. By estimating the size of the core region and assuming a jet veolcity of $\sim 0.5c$, Baczko et al. (2016) are able to estimate the corresponding magnetic field strength. A back extrapolation to a distance of $1\,R_\mathrm{S}$ yielded a magnetic fields between $\sim 360\,\mathrm{G}$ and $\sim 7 \times 10^4\,\mathrm{G}$ depending on the size of the central component and whether a purely toroidal field or a poloidal field dominate close to the SMBH.

The size of the central feature is an important quantity which is why it is necessary to assess whether projection effects are important at this frequency. Therefore, I estimate

[3] http://www.physics.purdue.edu/astro/MOJAVE/sourcepages/0238-084.shtml

the angle of the jet to the line of sight.

A.2. The viewing angle of NGC 1052 at 86 GHz

Contrary to sources with one-sided jets as discussed in the previous chapters, the flux of both the jet and counter jet can be measured in case of NGC 1052. However, given the brightness distribution as seen in the bottom panel in Fig. A.1, both jets are referred to based on their orientation with respect to the north-south axis, i.e. $S_{\rm E}$ and $S_{\rm W}$ for the flux density in the eastern and western jet, respectively. To measure the flux densities, the CLEAN-components in range of $0.1\,{\rm mas} \lesssim |{\rm Relative\ RA}| \lesssim 2.0\,{\rm mas}$ are summed up on both sides of the core. This yields $S_{\rm E} \approx 0.105\,{\rm Jy}$ and $S_{\rm W} \approx 0.074\,{\rm Jy}$ and this corresponds to a ratio of $R = 1.4 \pm 0.3$ adopting an uncertainty of the amplitudes of 15%.

Figure A.2 shows $\theta_{\rm LOS}$ and β for the calculated ratio. Baczko (2015) performed a re-analysis of 43 GHz observations with VLBA covering between 2005 and 2009, previously presented in Böck (2012). The new analysis revealed the brightest feature at 43 GHz to be the centre from which both jets extend and at times a slightly asymmetric jet morphology similar to Kadler et al. (2004b). The study determined $\beta_{\rm app}$ in both jets and the range of values is used in Fig. A.2 as these are closest in frequency and time to the 86 GHz observation. However, for comparison the Figure also shows $\beta_{\rm app}$ measured by Vermeulen et al. (2003) at 43 GHz and the median value of $\beta_{\rm app}$ from the MOJAVE programme at 15 GHz (Lister et al. 2013). The former is consistent with range of $\beta_{\rm app}$ by Baczko (2015), while the median value from MOJAVE is only slightly lower, though the maximum value extends up to an apparent speed of $\sim 0.41c$.

The grey shaded area in Fig. A.2 highlights the allowed parameter range by combining the range of R at 86 GHz and $\beta_{\rm app}$ at 43 GHz (Baczko 2015). This yields[4] $67^\circ \lesssim \theta_{\rm LOS} \lesssim 89^\circ$ and $0.22^\circ \lesssim \beta \lesssim 0.65^\circ$. Due to the large viewing angle, projection effects can be neglected and Doppler boosting is minimal, i.e., $\beta_{\rm app}$ corresponds roughly to β. While the lower limit is consistent with the lower frequency studies of Vermeulen et al. (2003) and Kadler et al. (2004b), the upper limit at 86 GHz lies above the upper limit by Kadler et al. (2004b). This could be a sign of small curvature, an asymmetry in the jet system or the difficulty in ascertaining the size of the absorption region at lower frequencies.

It is intriguing to compare NGC 1052 with Centaurus A, where both jets can also be detected (Müller et al. 2014b, see also Fig. 3.6 in Subsect. 3.3.3). Since the jet angle is significantly smaller, the range of $\beta_{\rm app}$ which overlaps with the lower end of NGC 1052 results in values of β similar to NGC 1052. The observations of Centaurus A were performed at 8.4 GHz, but the source is roughly a factor of five closer to Earth. In terms of linear scale, this means $1\,{\rm mas} \approx 0.018\,{\rm pc}$. However, the black hole mass of Centaurus A is $5.5 \times 10^7 M_\odot$ (Neumayer 2010) and thus, it is smaller by a similar factor. Hence, in terms of Schwarzschild radii the measured $\beta_{\rm app}$ at 8.4 GHz still probe the jet at a distance further away from the black hole. In addition, for the given range of viewing angles the projected linear scale is about a factor of 1.4–4.8 below the de-projected scale.

[4] Note as in Chapt. 4, the parameter range is not rectangular, thus the minimum allowed value for β does not correspond to the minimum allowed value of $\theta_{\rm los}$.

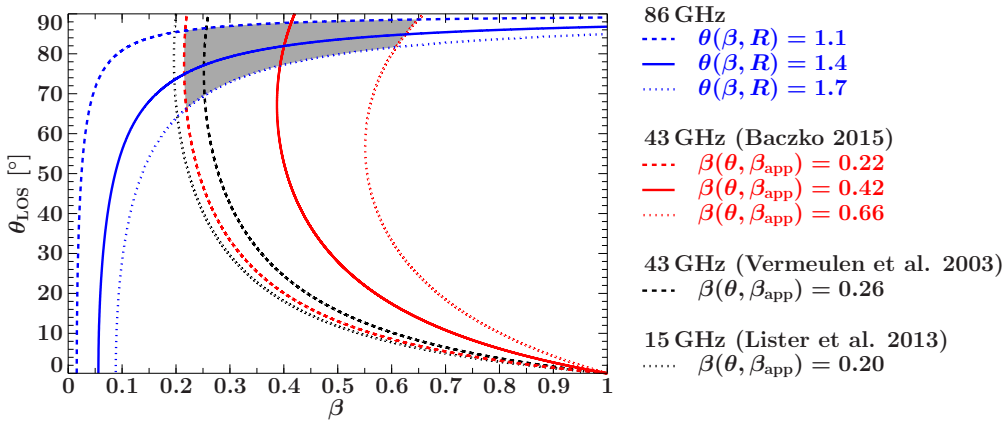

Figure A.2.: θ_{LOS} vs. β for NGC 1052. Blue lines: the flux density ratio R of the jets at 86 GHz is used to calculate θ_{LOS} for given β. Red lines: β_{app} from (Baczko 2015) yields β for a given θ_{LOS}. For simplicity the subscript of θ was dropped in the legend. The grey shaded region shows the highlights the allowed parameter range for θ_{LOS} and β. For comparison, β_{app} from Vermeulen et al. (2003) at 43 GHz (dashed, black line) and the median value of β_{app} from Lister et al. (2013) (MOJAVE programme) at 15 GHz (dotted, black line) are included.

The situation is slightly different in case of M 87. Its black hole mass is about an order of magnitude higher than for NGC 1052 ($6 \times 10^9 M_\odot$, Gebhardt & Thomas 2009) and the distance is slightly smaller ($\sim$ 16.7 Mpc, Jordán et al. 2005). Hence, it is possible to probe smaller linear scales in M 87 than in NGC 1052. In addition, the strength of the radio emission permits the observation of M 87 even up to 230 GHz (Doeleman et al. 2012). However, the viewing angle is smaller in M 87 compared to NGC 1052 ranging between 15° and 45° (Ly et al. 2007; Acciari et al. 2009) and thus intrinsic distances in the jet of M 87 are a factor of about 1.4–3.8 larger than in projection.

A.3. Outlook

The GMVA has evolved significantly since the observation of NGC 1052 in 2004. The increased bandwidth yield a notable enhancement of the sensitivity. Therefore, a new proposal for a GMVA observation of NGC 1052 was submitted and got accepted (PI: R. Schulz). The goal of the project was to study the jet emission in greater detail due to the improved sensitivity and probe the jet-to-counter jet symmetry, an essential part of the unification of AGNs. To this purpose a 43 GHz observation with the VLBA stations that participated in the GMVA campaign was conducted alternately to 86 GHz measurements when calibration scans were made by the Effelsberg telescope. This would enable a spectral index analysis of the jet and the central region based on simultaneous observations. The analysis of the data is still ongoing and will be presented elsewhere. However, it is already evident that technical difficulties lead to the loss of several stations. Therefore, the desired image fidelity required to meet all of the science goals is not reached.

As a result, a new and extended observing project of which I am a part of, has been proposed (PI: A.-K. Baczko). It utilizes the newly available capability of using ALMA in combination with the GMVA as well as Space-VLBI observations at lower frequency. Both observing campaigns are designed to resolve the jet down to the central region transversely and learn more about the jet formation in NGC 1052close to the SMBH.

B. Additional fits to the radio spectrum of PKS 2004−447

In the following two basic models are applied to the average radio spectrum of PKS 2004−447, which was determined based on the weighted average and weighted variance of data taken at the same frequency. The goal is to perform a tentative fit to the radio spectrum to constrain the turnover frequency. Following e.g., O'Dea (1998) and Kameno et al. (2003), commonly used models to describe the radio spectrum of CSS and GPS sources are synchrotron self-absorption (SSA) and free-free absorption (FFA).

Based on Kameno et al. (2003) the following definitions of an FFA and SSA spectrum, respectively, are used,

$$S_{\nu,\mathrm{FFA}} = S_{0,\mathrm{FFA}}\nu^{\alpha}\exp\left(-\tau_{\mathrm{FFA}}\nu^{-2.1}\right) \tag{B.0.1}$$

$$S_{\nu,\mathrm{SSA}} = S_{0,\mathrm{SSA}}\nu^{2.5}\left[1-\exp\left(-\tau_{\mathrm{SSA}}\nu^{\alpha-2.5}\right)\right] \tag{B.0.2}$$

To simplify the fit given the data sampling in the low frequencies, the spectral index α was fixed to the median value of $\alpha_{\mathrm{median}} = -0.72$ from Subsect. 5.4.1. While the fit converged on a best value for the two remaining parameters S_0 and τ in both models, the calculated errors did not converge for the parameter $S_{0,\mathrm{SSA}}$. However, due to the limited sampling at the lowest frequencies a physical interpretation of the differences in the FFA and SSA fit is not reasonable.

In conclusion, both fits indicate a turnover in the averaged radio spectrum of PKS 2004−447 below 1 GHz consistent with a CSS-like source (e.g., O'Dea 1998).

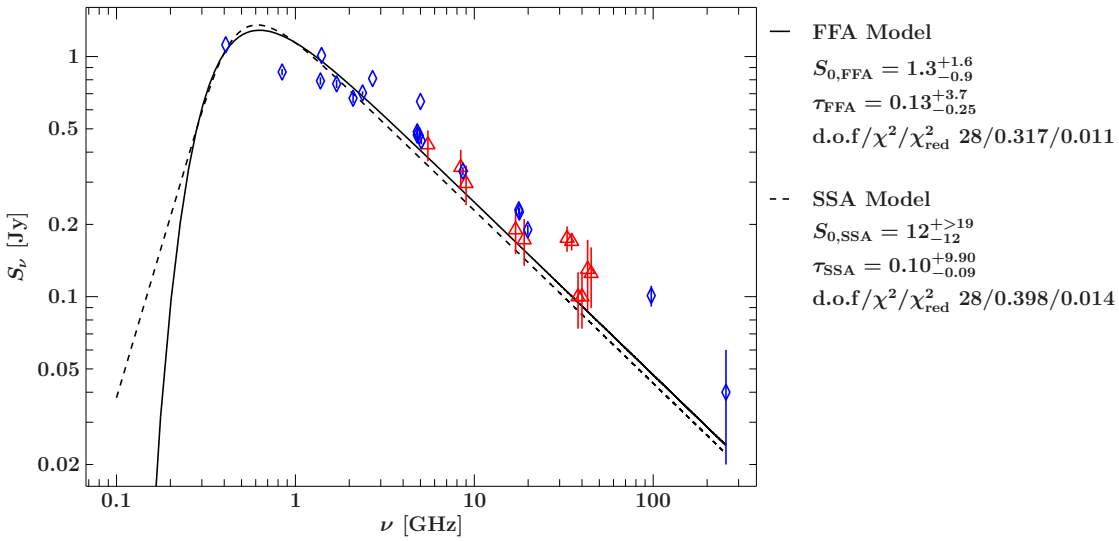

Figure B.1.: Average spectrum based on Fig. 5.4. The blue diamonds indicate single frequency measurements, while the red data indicates weighted averaged measurements based on multiple observations at the same frequency. The uncertainties of the latter are based on the weighted variance. The spectral index was fixed to its median value from Subsect. 5.4.1.

C. MOJAVE observations of 1H 0323+342

1H 0323+342 is the closest γ-NLS1 currently known at a redshift of $z = 0.0629$ (Zhou et al. 2007). Its classification as a RL-NLS1 was determined by the study of Zhou et al. (2007) that also reported blazar-like features such as a flat radio spectrum and one-sided jet morphology. 1H 0323+342 was among the first γ-NLS1s to be detected by *Fermi*-LAT in the γ-ray-regime. A detailed analysis of the flaring activity by Paliya et al. (2014) revealed both, γ-ray flares with possibly increased low-energy activity and high low-energy activity with no γ-ray flares.

Due to its nearby location compared to the other γ-NLS1s, it is currently the only one in which the host galaxy can be studied in detail. Zhou et al. (2007) proposed that the host galaxy shows a structure in the form of a one-armed spiral galaxy. Antón et al. (2008) suggested a ring-like structure, which was confirmed by León Tavares et al. (2014). The latter study concluded that the morphology of the host galaxy is strongly affected by activity from the AGN. This is in stark contrast to the common model that jet-dominated AGNs are exclusively hosted in elliptical galaxies.

The pc-scale structure was analysed in greater detail by Wajima et al. (2014) in combination with single-dish observations. The study found variability consistent with a variability brightness temperatures above 10^{11} K as well as VLBI core brightness temperatures at 8.4 GHz above 5×10^{10} K. It is suggested that the jet is at least moderately Doppler boosted. As shown in Table 5.5, the mean (median) core brightness temperature at 15 GHz goes even as high as $\sim 7 \times 10^{11}$ ($\sim 6.2 \times 10^{11}$ K). The kpc-scale structure consists of bright a core and two-sided extended emission Antón et al. (2008). Using the same data, Doi et al. (2012) determined that the projected large scale extend of 1H 0323+342 is about ~ 50 kpc.

Eight eight MOJAVE[1] observations between 2010-10-15 and 2013-07-08 and F-GAMMA single-dish monitoring observations of 1H 0323+342 are analysed in the study of Furhmann et al. (2016, RAA submitted) to which I contributed in the analysis and discussion of the MOJAVE data. The kinematic analysis of the MOJAVE observations reveal a broad distribution of apparent speeds between $\sim 0.9\,c$ and $6.9\,c$. The MOJAVE images reveal a straight single-sided jet at a position angle of $\sim 124°$ extending from a bright and dominating compact core. The VLBI flux density accounts for most of the single-dish flux density, but not all. This suggests extended flux that is resolved out by the VLBI data. An estimate of the upper limit on the viewing angle of the jet from the jet-to-counter jet ratio using three times the noise level as a limit of the counter jet yields $\lesssim 30°$. The

[1] http://www.physics.purdue.edu/astro/MOJAVE/sourcepages/0321+340.shtml

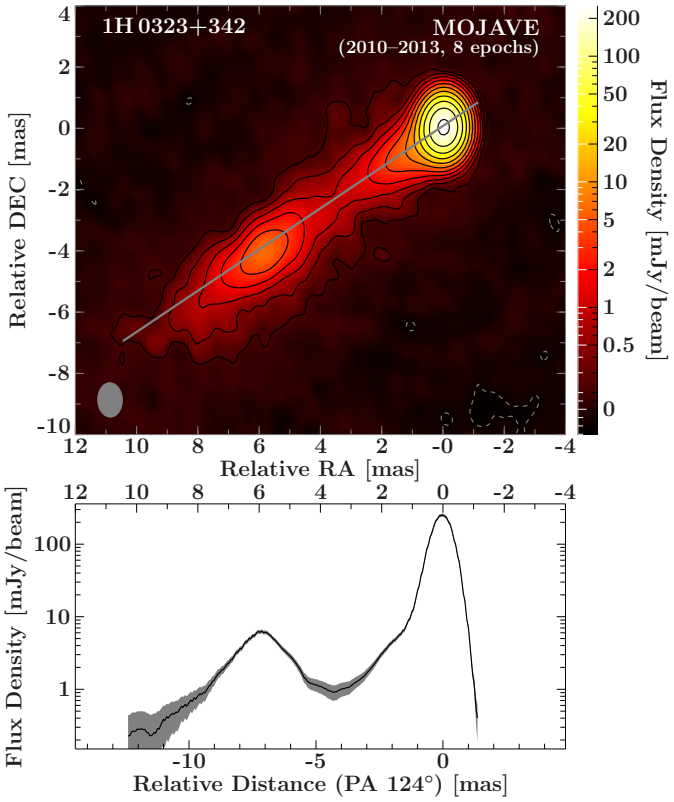

Figure C.1: Top panel: Mean stacked image of 1H 0323+342 based on the naturally weighted MOJAVE images between 2010-10-15 and 2013-07-08 as provided by the MOJAVE programme. The images were convolved with the enclosing beam of 1.12 mas × 0.80 mas, PA 1.8° (grey ellipse) prior to stacking. The contour lines starts at three times the noise level of the stacked image (0.07 mJy beam^{-1}) and increase logarithmically with a factor of two. Bottom panel: Brightness distribution along the position angle of the jet of ∼ 124 Furhmann et al. (2016, RAA submitted). The shaded region corresponds to the uncertainty of the MOJAVE amplitude calibration and accounts for the noise level.

maximum apparent speed results in a critical angle of ∼ 8°.

Figure C.1 shows the mean stacked image of the MOJAVE observations and the brightness distribution along the position angle of the jet that I produced based on the naturally weighted images provided by the MOJAVE programme. Downstream from the core, an extended feature of increased brightness is visible that is connected with the core region by fainter emission, but this connection is not always detected in the individual VLBI images. However, the extended feature is observed only with slight variations in all of the images. The fastest component in Furhmann et al. (2016, RAA submitted) moves through the gap region, which probably causes this region to be visible in the stacked image. The components of the extended region are up to a factor of ∼ 4 slower than the fastest components. This could be a sign of intrinsic differences in the jet in this region compared to the upstream jet or it could be related to the origin of the fastest component.

D. Model fit components of IC 310 and 3C 111

Table D.1 and Table D.2 list the parameters of the elliptical and circular Gaussian components fitted to the MOJAVE and EVN observations (see Sect. 4.2). The columns in the table contain the following information

Column 1: ID of the component. In case of the MOJAVE observations, these represent the components that are associated and tracked in the kinematic analysis. In case of the EVN observations the core and the components used for the core shift measurements are highlighted.

Column 2: Flux density of the component.

Column 3, 4: Polar coordinates of the components with respect to the origin of the map, i.e. distance d and position angle ϕ. The latter is oriented from the north to the east for positive values.

Column 5,6: Polar coordinates of the components with respect to Core in each epoch.

Column 7,8: Major and minor axis of the component. Note, only the core is an elliptical Gaussian distribution. Limits for the size were calculated following Kovalev et al. (2005).

Column 9: Logarithmic value of the brightness temperature of the component. In case an upper limit is given by the major or minor axis of the component

Table D.1.: Parameters of the modelfit components of IC 310 of the MOJAVE observations

ID	S_ν	d	ϕ	$d_{\rm shift}$	$\phi_{\rm shift}$	$a_{\rm maj}$	$a_{\rm min}$	$\log T_{\rm b}$
	[mJy]	[mas]	[°]	[mas]	[°]	[mas]	[mas]	[K]
(1)	(2)	(3)	(4)	(5)	(6)	(7)	(8)	(9)
Core	96.6	0.01	-49.4	0.00	0.0	0.32	0.10	10.20
J4	11.3	1.07	-139.3	1.07	-139.7	0.46	0.46	8.46
J3	4.5	3.84	-140.1	3.84	-140.2	2.06	2.06	6.75
	2.0	8.95	-135.0	8.95	-135.0	1.11	1.11	6.93
2012-09-27 (2012.74)								
Core	81.0	0.03	13.5	0.00	0.0	0.30	0.09	10.20
J5	8.2	0.64	-133.1	0.66	-134.4	0.28	0.28	8.75
J4	4.7	1.52	-140.2	1.54	-140.6	0.42	0.42	8.15

Table D.1 continued

ID	S_ν [mJy]	d [mas]	ϕ [°]	$d_{\rm shift}$ [mas]	$\phi_{\rm shift}$ [°]	$a_{\rm maj}$ [mas]	$a_{\rm min}$ [mas]	$\log T_{\rm b}$ [K]
(1)	(2)	(3)	(4)	(5)	(6)	(7)	(8)	(9)
J3	1.3	4.86	-142.6	4.89	-142.8	<0.49	<0.32	>7.62
2012-12-10 (2012.94)								
Core	78.5	0.06	-115.0	0.00	0.0	0.36	0.10	10.07
J5	11.8	0.99	-139.2	0.93	-140.6	0.47	0.47	8.44
J4	3.6	2.26	-139.2	2.21	-139.8	0.74	0.74	7.54
J3	4.5	5.27	-139.1	5.22	-139.4	1.68	1.68	6.92
J2	2.0	8.99	-140.7	8.94	-140.9	1.38	1.38	6.74
2013-05-05 (2013.34)								
Core	79.0	0.02	-129.7	0.00	0.0	0.35	0.11	10.03
J5	13.7	0.86	-139.0	0.85	-139.2	0.44	0.44	8.57
J4	5.7	1.73	-145.5	1.72	-145.7	0.98	0.98	7.50
J3	3.0	4.94	-138.3	4.92	-138.4	1.05	1.05	7.16
J2	3.4	7.85	-139.0	7.84	-139.0	1.18	1.18	7.11
2013-08-12 (2013.61)								
Core	109.9	0.21	-139.7	0.00	0.0	0.59	0.22	9.66
2013-12-15 (2013.95)								
Core	72.3	0.01	90.6	0.00	0.0	0.17	0.03	10.86
J6	14.5	0.46	-127.8	0.46	-127.3	0.20	0.20	9.27
J5	11.4	1.02	-139.8	1.03	-139.6	0.40	0.40	8.58
J4	3.3	2.25	-139.0	2.25	-138.9	0.73	0.73	7.52
J3	3.0	4.04	-141.2	4.04	-141.1	1.93	1.93	6.63
J2	2.7	7.74	-140.2	7.75	-140.1	1.57	1.57	6.76
2014-05-12 (2014.36)								
Core	68.5	0.02	53.0	0.00	0.0	<0.04	<0.02	>10.88
J7	15.2	0.41	-122.2	0.43	-122.5	0.22	0.22	9.24
J6	7.9	0.99	-137.5	1.01	-137.2	0.33	0.33	8.58
J5	5.7	1.64	-141.6	1.66	-141.4	0.55	0.55	7.99
J4	2.3	2.47	-139.8	2.50	-139.6	0.43	0.43	7.83
J3	2.2	4.98	-138.6	5.00	-138.6	0.79	0.79	7.28
J2	2.5	8.25	-142.3	8.28	-142.3	1.20	1.20	6.96
2015-07-20 (2015.55)								
Core	66.5	0.03	49.7	0.00	0.0	0.14	0.03	10.97
	11.1	0.33	-119.2	0.36	-120.0	<0.08	<0.06	>10.11
J7	9.4	0.66	-126.4	0.68	-126.5	0.30	0.30	8.73
J6	6.3	1.26	-139.9	1.29	-139.7	0.34	0.34	8.46
J5	3.0	1.95	-135.2	1.98	-135.1	0.52	0.52	7.76
J4	2.5	3.08	-140.2	3.11	-140.1	0.93	0.93	7.18
J3	1.1	5.32	-137.9	5.35	-137.9	0.57	0.57	7.24

Table D.1 continued

ID	S_ν	d	ϕ	$d_{\rm shift}$	$\phi_{\rm shift}$	$a_{\rm maj}$	$a_{\rm min}$	$\log T_{\rm b}$
	[mJy]	[mas]	[°]	[mas]	[°]	[mas]	[mas]	[K]
(1)	(2)	(3)	(4)	(5)	(6)	(7)	(8)	(9)
J2	3.0	8.85	-142.1	8.88	-142.1	1.22	1.22	7.03

Table D.2.: Parameters of the modelfit components of IC 310 of the EVN observations

ID	S_ν	d	ϕ	$d_{\rm shift}$	$\phi_{\rm shift}$	$a_{\rm maj}$	$a_{\rm min}$	$\log T_{\rm b}$
	[mJy]	[mas]	[°]	[mas]	[°]	[mas]	[mas]	[K]
(1)	(2)	(3)	(4)	(5)	(6)	(7)	(8)	(9)
Core	82.8	0.30	5.6	0.00	0.0	2.63	1.14	10.10
	6.7	4.43	-131.7	4.65	-134.2	<1.10	<0.28	>9.99
	4.9	8.48	-144.7	8.73	-145.7	2.43	2.43	8.58
$C1_{1.7}$	4.1	19.87	-127.2	20.07	-127.8	4.50	4.50	7.96
	2.0	32.55	-133.0	32.77	-133.3	5.81	5.81	7.43
	0.5	48.87	-132.2	49.09	-132.4	<5.59	<1.44	>6.89
	1.7	62.76	-139.2	63.00	-139.3	13.03	13.03	6.65
	1.3	94.54	-140.3	94.78	-140.4	8.75	8.75	6.87
	1.0	119.56	-139.3	119.81	-139.3	24.16	24.16	5.89
5.0 GHz, 2012-10-29 (2012.83)								
Core	81.3	0.13	4.7	0.00	0.0	0.78	0.43	10.09
	11.5	1.00	-124.9	1.09	-130.2	0.40	0.40	9.56
	4.4	2.50	-147.1	2.62	-148.4	1.39	1.39	8.06
	4.7	4.83	-139.7	4.94	-140.6	1.25	1.25	8.18
$C2_{5.0}$	4.9	8.12	-138.8	8.22	-139.4	2.24	2.24	7.69
	1.1	18.22	-130.0	18.31	-130.3	2.36	2.36	6.99
$C1_{5.0}$	1.6	22.28	-130.2	22.37	-130.4	2.09	2.09	7.26
	0.4	30.18	-127.9	30.27	-128.1	<1.92	<0.48	>6.82
8.4 GHz, 2012-11-01 (2012.83)								
Core	78.1	0.04	6.6	0.00	0.0	0.45	0.15	10.31
	13.6	0.76	-131.7	0.79	-133.6	<0.14	<0.04	>10.60
	4.8	1.63	-144.6	1.66	-145.3	0.41	0.41	8.70
	2.5	2.79	-147.2	2.83	-147.5	1.06	1.06	7.59
	3.0	5.00	-137.9	5.03	-138.2	1.19	1.19	7.56
$C2_{8.4}$	2.6	8.29	-137.0	8.32	-137.1	1.38	1.38	7.38
	0.5	11.94	-134.9	11.97	-135.0	<0.83	<0.24	>7.32
22.2 GHz, 2012-11-07 (2012.85)								
Core	107.0	0.00	14.5	0.00	0.0	<0.06	<0.02	>11.26

Table D.3 lists the parameters of the circular Gaussian components fitted to the three GMVA observations (see Sect. 6.2). The columns in the table contain the following information

Column 1: ID of the component that are associated and tracked in the kinematic analysis.

Column 2: Flux density of the component in Jy.

Column 3, 4: Polar coordinates of the components with respect to the origin of the map, i.e. distance d and position angle ϕ. The latter is oriented from the north to the east for positive values.

Column 5,6: Polar coordinates of the components with respect to C1 in each epoch.

Column 7: FWHM of the component.

Column 8: Logarithmic value of the brightness temperature of the component.

Table D.3.: Parameters of the model fit components of the GMVA images

ID	S_ν	d	ϕ	$d_{\rm shift}$	$\phi_{\rm shift}$	$a_{\rm maj}$	$\log T_{\rm b}$
	[Jy]	[mas]	[°]	[mas]	[°]	[mas]	[K]
(1)	(2)	(3)	(4)	(5)	(6)	(7)	(9)
2007-10-15 (2007.79)							
C1	1.51	0.070	-128.6	0.000	0.0	0.044	11.14
C2	2.47	0.015	-138.1	0.056	54.0	0.037	11.50
C2	1.80	0.039	42.9	0.109	48.4	0.046	11.18
J3	1.87	0.089	67.6	0.158	60.5	0.081	10.70
J2	1.77	0.256	75.8	0.321	70.6	0.067	10.84
J2	1.09	0.359	85.7	0.419	80.2	0.074	10.54
J1	1.53	0.590	76.8	0.655	74.2	0.120	10.27
2008-05-11 (2008.36)							
C1	0.47	0.104	-117.9	0.000	0.0	0.049	10.54
C2	1.16	0.003	-145.9	0.101	62.9	0.049	10.94
J5	0.55	0.089	59.4	0.193	60.8	0.089	10.08
	0.33	0.357	59.9	0.460	60.4	0.150	9.41
J4	0.26	0.516	57.4	0.619	58.2	0.059	10.12
J3	0.88	0.778	64.9	0.881	64.5	0.152	9.82
J2	0.52	1.003	77.6	1.103	76.2	0.197	9.37
J1	0.14	1.297	67.4	1.400	67.0	0.250	8.61
	0.06	4.108	65.9	4.211	65.8	0.166	8.60
2008-10-14 (2008.78)							

Table D.3 continued

ID	S_ν	d	ϕ	d_{shift}	ϕ_{shift}	a_{maj}	$\log T_{\mathrm{b}}$
	[Jy]	[mas]	[°]	[mas]	[°]	[mas]	[K]
(1)	(2)	(3)	(4)	(5)	(6)	(7)	(9)
C1	0.66	0.101	-117.1	0.000	0.0	0.039	10.88
C2	0.74	0.030	-142.4	0.075	72.6	0.037	10.98
C2	1.44	0.009	33.6	0.109	60.6	0.024	11.65
	0.38	0.059	53.5	0.159	59.5	0.061	10.26
	0.11	0.385	57.1	0.485	58.3	0.148	8.96
J5	0.10	0.680	59.4	0.781	59.8	0.107	9.18
J4	0.06	1.099	64.8	1.200	64.6	0.082	9.19
J3	0.10	1.418	63.8	1.520	63.8	0.110	9.14
J2	0.17	1.509	76.5	1.608	75.7	0.306	8.51
J1	0.05	1.750	65.4	1.851	65.2	0.201	8.31
	0.06	4.739	66.1	4.840	66.0	0.496	7.60

Bibliography

Aartsen, M. G., Abbasi, R., Abdou, Y., et al. 2013, Physical Review Letters, 111, 021103

Aartsen, M. G., Ackermann, M., Adams, J., et al. 2014, Physical Review Letters, 113, 101101

Abdo, A. A., Ackermann, M., Agudo, I., et al. 2010a, ApJ, 716, 30

Abdo, A. A., Ackermann, M., Ajello, M., et al. 2010b, ApJ, 715, 429

Abdo, A. A., Ackermann, M., Ajello, M., et al. 2010c, ApJS, 188, 405

Abdo, A. A., Ackermann, M., Ajello, M., et al. 2011, ApJ, 730, 101

Abdo, A. A., Ackermann, M., Ajello, M., et al. 2010d, ApJ, 719, 1433

Abdo, A. A., Ackermann, M., Ajello, M., et al. 2010e, Science, 328, 725

Abdo, A. A., Ackermann, M., Ajello, M., et al. 2009a, ApJ, 699, 976

Abdo, A. A., Ackermann, M., Ajello, M., et al. 2009b, ApJ, 707, L142

Abramowicz, M. A. & Fragile, P. C. 2013, Living Reviews in Relativity, 16

Abramowski, A., Acero, F., Aharonian, F., et al. 2013, Phys. Rev. D, 88, 102003

Abramowski, A., Acero, F., Aharonian, F., et al. 2012, ApJ, 746, 151

Acciari, V. A., Aliu, E., Arlen, T., et al. 2009, Science, 325, 444

Acero, F., Ackermann, M., Ajello, M., et al. 2015, ApJS, 218, 23

Acero, F., Donato, D., Ojha, R., et al. 2013, ApJ, 779, 133

Ackermann, M., Ajello, M., Allafort, A., et al. 2011, ApJ, 741, 30

Ackermann, M., Ajello, M., Atwood, W. B., et al. 2015, ApJ, 810, 14

Agudo, I., Gómez, J. L., Casadio, C., Cawthorne, T. V., & Roca-Sogorb, M. 2012, ApJ, 752, 92

Agudo, I., Jorstad, S. G., Marscher, A. P., et al. 2011, ApJ, 726, L13

Aharonian, F., Akhperjanian, A. G., Anton, G., et al. 2009a, ApJ, 696, L150

Aharonian, F., Akhperjanian, A. G., Anton, G., et al. 2009b, ApJ, 695, L40

Aharonian, F., Akhperjanian, A. G., Aye, K.-M., et al. 2005a, A&A, 430, 865

Aharonian, F., Akhperjanian, A. G., Bazer-Bachi, A. R., et al. 2005b, A&A, 442, 895

Aharonian, F., Arshakian, T. G., Allen, B., et al. 2013, ArXiv e-prints, 1301.4124

Ajello, M., Alexander, D. M., Greiner, J., et al. 2012, ApJ, 749, 21

Alef, W., Preuss, E., Kellermann, K. I., & Gabuzda, D. 1998, in ASPC, Vol. 144, IAU Colloq. 164: Radio Emission from Galactic and Extragalactic Compact Sources, ed. J. A. Zensus, G. B. Taylor, & J. M. Wrobel, 129

Aleksić, J., Ansoldi, S., Antonelli, L. A., et al. 2014a, A&A, 564, A5

Aleksić, J., Ansoldi, S., Antonelli, L. A., et al. 2014b, Science, 346, 1080

Aleksić, J., Antonelli, L. A., Antoranz, P., et al. 2013, A&A, 556, A67

Aleksić, J., Antonelli, L. A., Antoranz, P., et al. 2014c, A&A, 563, A91

Aleksić, J., Antonelli, L. A., Antoranz, P., et al. 2010, ApJ, 723, L207

An, T., Wu, F., Yang, J., et al. 2012, ApJS, 198, 5

Anderson, J. M., Ulvestad, J. S., & Ho, L. C. 2004, ApJ, 603, 42

Angelakis, E., Fuhrmann, L., Marchili, N., et al. 2015, A&A, 575, A55

Angelakis, E., Fuhrmann, L., Nestoras, I., et al. 2012, Journal of Physics Conference Series, 372, 012007

ANTARES Collaboration, Adrián-Martínez, S., Albert, A., et al. 2015, A&A, 576, L8

Antón, S., Browne, I. W. A., & Marchã, M. J. 2008, A&A, 490, 583

Antonucci, R. 1993, ARA&A, 31, 473
Atwood, W. B., Abdo, A. A., Ackermann, M., et al. 2009, ApJ, 697, 1071
Baczko, A. K. 2015, MSc thesis, Multi-Epoch Millimeter VLBI Observations of the Twin-Jet System in NGC 1052, Friedrich-Alexander-Universität Erlangen-Nürnberg, Erlangen, Germany
Baczko, A.-K., Schulz, R., Kadler, M., et al. 2016, A&A in press., arXiv e-prints 1605.07100
Baldi, R. D., Capetti, A., Robinson, A., Laor, A., & Behar, E. 2016, MNRAS, 458, L69
Bardeen, J. M., Press, W. H., & Teukolsky, S. A. 1972, ApJ, 178, 347
Baumgartner, W. H., Tueller, J., Markwardt, C. B., et al. 2013, ApJS, 207, 19
Beckmann, V. & Shrader, C. R. 2012, Active Galactic Nuclei (Wiley-VCH Verlag GmbH)
Bernardi, M., Alonso, M. V., da Costa, L. N., et al. 2002, AJ, 123, 2990
Berton, M., Foschini, L., Ciroi, S., et al. 2015, A&A, 578, A28
Bicknell, G. V., Dopita, M. A., & O'Dea, C. P. O. 1997, ApJ, 485, 112
Bird, A. J., Bazzano, A., Bassani, L., et al. 2010, ApJS, 186, 1
Biretta, J. A., Sparks, W. B., & Macchetto, F. 1999, ApJ, 520, 621
Biteau, J. & Williams, D. A. 2015, ApJ, 812, 60
Blandford, R. D. & Königl, A. 1979, ApJ, 232, 34
Blandford, R. D. & Payne, D. G. 1982, MNRAS, 199, 883
Blandford, R. D. & Znajek, R. L. 1977, MNRAS, 179, 433
Błażejowski, M., Sikora, M., Moderski, R., & Madejski, G. M. 2000, ApJ, 545, 107
Bloom, S. D. & Marscher, A. P. 1996, ApJ, 461, 657
Böck, M. 2012, PhD thesis, Friedrich-Alexander-Universität Erlangen-Nürnberg, Erlangen, Germany
Böck, M., Kadler, M., Müller, C., et al. 2016, A&A, 590, A40
Boettcher, M. 2010, ArXiv e-prints, 1006.5048
Boettcher, M., Harris, D. E., & Krawczynski, H. 2012, Relativistic Jets from Active Galactic Nuclei (Wiley-VCH Verlag GmbH)
Böttcher, M., Reimer, A., Sweeney, K., & Prakash, A. 2013, ApJ, 768, 54
Boutelier, T., Henri, G., & Petrucci, P.-O. 2008, MNRAS, 390, L73
Bridle, A. H. & Perley, R. A. 1984, ARA&A, 22, 319
Brown, R. L. 1987, in Spectroscopy of Astrophysical Plasmas, ed. A. Dalgarno & D. Layzer, 35–58
Burke-Spolaor, S., Ekers, R. D., Massardi, M., et al. 2009, MNRAS, 395, 504
Caccianiga, A., Antón, S., Ballo, L., et al. 2014, MNRAS, 441, 172
Caccianiga, A., Antón, S., Ballo, L., et al. 2015, MNRAS, 451, 1795
Calderone, G., Ghisellini, G., Colpi, M., & Dotti, M. 2013, MNRAS, 431, 210
Carilli, C. L., Carlstrom, J. E., & Holdaway, M. A. 1999, in Astronomical Society of the Pacific Conference Series, Vol. 180, Synthesis Imaging in Radio Astronomy II, ed. G. B. Taylor, C. L. Carilli, & R. A. Perley, 565
Carilli, C. L., McKinnon, M., Ott, J., et al. 2015, ArXiv e-prints, 1510.06438
Casadio, C., Gómez, J. L., Grandi, P., et al. 2015a, ApJ, 808, 162
Casadio, C., Gómez, J. L., Jorstad, S. G., et al. 2015b, ApJ, 813, 51
Chatterjee, R., Marscher, A. P., Jorstad, S. G., et al. 2011, ApJ, 734, 43
Chen, Y. Y., Zhang, X., Zhang, H. J., & Yu, X. L. 2015, MNRAS, 451, 4193
Chhetri, R., Ekers, R. D., Jones, P. A., & Ricci, R. 2013, MNRAS, 434, 956
Chodorowski, M. J. 2005, American Journal of Physics, 73, 639
Cohen, M. H., Lister, M. L., Homan, D. C., et al. 2007, ApJ, 658, 232

Condon, J. J., Cotton, W. D., & Broderick, J. J. 2002, AJ, 124, 675
Condon, J. J., Cotton, W. D., Greisen, E. W., et al. 1998, AJ, 115, 1693
Cornwell, T. J. & Evans, K. F. 1985, A&A, 143, 77
Cornwell, T. J. & Wilkinson, P. N. 1981, MNRAS, 196, 1067
Cotton, W. D. 1995, in Astronomical Society of the Pacific Conference Series, Vol. 82, Very Long Baseline Interferometry and the VLBA, ed. J. A. Zensus, P. J. Diamond, & P. J. Napier, 189
Cusumano, G., La Parola, V., Segreto, A., et al. 2010a, A&A, 524, A64
Cusumano, G., La Parola, V., Segreto, A., et al. 2010b, A&A, 510, A48
Dallacasa, D., Fanti, C., Giacintucci, S., et al. 2002a, A&A, 389, 126
Dallacasa, D., Tinti, S., Fanti, C., et al. 2002b, A&A, 389, 115
Daly, R. A. & Marscher, A. P. 1988, ApJ, 334, 539
D'Ammando, F., Larsson, J., Orienti, M., et al. 2014, MNRAS, 438, 3521
D'Ammando, F., Orienti, M., Doi, A., et al. 2013a, MNRAS, 433, 952
D'Ammando, F., Orienti, M., Finke, J., et al. 2013b, MNRAS, 436, 191
D'Ammando, F., Orienti, M., Finke, J., et al. 2012, MNRAS, 426, 317
D'Ammando, F., Orienti, M., Larsson, J., & Giroletti, M. 2015, MNRAS, 452, 520
de Gasperin, F., Orrú, E., Murgia, M., et al. 2012, A&A, 547, A56
D'Elia, V., Perri, M., Puccetti, S., et al. 2013, A&A, 551, A142
Deller, A. T., Brisken, W. F., Phillips, C. J., et al. 2011, PASP, 123, 275
Deller, A. T., Tingay, S. J., Bailes, M., & West, C. 2007, PASP, 119, 318
Dermer, C. D. & Schlickeiser, R. 1993, ApJ, 416, 458
Dermer, C. D., Schlickeiser, R., & Mastichiadis, A. 1992, A&A, 256, L27
Di Matteo, T., Springel, V., & Hernquist, L. 2005, Nature, 433, 604
Dixon, R. S. 1970, ApJS, 20, 1
Doeleman, S. S., Fish, V. L., Schenck, D. E., et al. 2012, Science, 338, 355
Doeleman, S. S., Weintroub, J., Rogers, A. E. E., et al. 2008, Nature, 455, 78
Doi, A., Nagai, H., Asada, K., et al. 2006, PASJ, 58, 829
Doi, A., Nagira, H., Kawakatu, N., et al. 2012, ApJ, 760, 41
Drinkwater, M. J., Webster, R. L., Francis, P. J., et al. 1997, MNRAS, 284, 85
Dunn, R. J. H., Allen, S. W., Taylor, G. B., et al. 2010, MNRAS, 404, 180
Ellingson, S. W., Clarke, T. E., Cohen, A., et al. 2009, IEEE Proceedings, 97, 1421
Elvis, M., Plummer, D., Schachter, J., & Fabbiano, G. 1992, ApJS, 80, 257
Erickson, W. C. 1999, in Astronomical Society of the Pacific Conference Series, Vol. 180, Synthesis Imaging in Radio Astronomy II, ed. G. B. Taylor, C. L. Carilli, & R. A. Perley, 601
Evans, P. A., Osborne, J. P., Beardmore, A. P., et al. 2014, ApJS, 210, 8
Fabian, A. C. 2012, ARA&A, 50, 455
Falcke, H. & Biermann, P. L. 1995, A&A, 293
Fanaroff, B. L. & Riley, J. M. 1974, MNRAS, 167, 31P
Fanti, C., Fanti, R., Zanichelli, A., Dallacasa, D., & Stanghellini, C. 2011, A&A, 528, A110
Fanti, C., Pozzi, F., Dallacasa, D., et al. 2001, A&A, 369, 380
Feain, I. J., Cornwell, T. J., Ekers, R. D., et al. 2011, ApJ, 740, 17
Fernández-Ontiveros, J. A., López-Sanjuan, C., Montes, M., Prieto, M. A., & Acosta-Pulido, J. A. 2011, MNRAS, 411, L21
Finke, J. D. 2013, ApJ, 763, 134

Fish, V., Alef, W., Anderson, J., et al. 2013, ArXiv e-prints, 1309.3519
Fish, V. L., Johnson, M. D., Lu, R.-S., et al. 2014, ApJ, 795, 134
Fomalont, E., van Kempen, T., Kneissl, R., et al. 2014, The Messenger, 155, 19
Fomalont, E. B. 1999, in Astronomical Society of the Pacific Conference Series, Vol. 180, Synthesis Imaging in Radio Astronomy II, ed. G. B. Taylor, C. L. Carilli, & R. A. Perley, 301
Foschini, L. 2011, in Narrow-Line Seyfert 1 Galaxies and their Place in the Universe, PoS, id. 24
Foschini, L., Angelakis, E., Fuhrmann, L., et al. 2012, A&A, 548, A106
Foschini, L., Berton, M., Caccianiga, A., et al. 2015, A&A, 575, A13
Fossati, G., Maraschi, L., Celotti, A., Comastri, A., & Ghisellini, G. 1998, MNRAS, 299, 433
Freedman, W. L., Madore, B. F., Gibson, B. K., et al. 2001, ApJ, 553, 47
Fromm, C. M., Perucho, M., Mimica, P., & Ros, E. 2016, A&A, 588, A101
Fromm, C. M., Perucho, M., Ros, E., et al. 2011, A&A, 531, A95
Fromm, C. M., Perucho, M., Ros, E., Savolainen, T., & Zensus, J. A. 2015, A&A, 576, A43
Fromm, C. M., Ros, E., Perucho, M., et al. 2013, A&A, 551, A32
Fuhrmann, L., Larsson, S., Chiang, J., et al. 2014, MNRAS, 441, 1899
Furhmann, L., Karamanavis, V., Komossa, S., et al. 2016, RAA submitted
Gallo, L. C., Edwards, P. G., Ferrero, E., et al. 2006, MNRAS, 370, 245
Gebhardt, K. & Thomas, J. 2009, ApJ, 700, 1690
Georganopoulos, M. & Kazanas, D. 2003, ApJ, 594, L27
Georganopoulos, M., Perlman, E. S., Kazanas, D., & McEnery, J. 2006, ApJ, 653, L5
Ghisellini, G., Celotti, A., Fossati, G., Maraschi, L., & Comastri, A. 1998, MNRAS, 301, 451
Ghisellini, G., Maraschi, L., & Tavecchio, F. 2009, MNRAS, 396, L105
Ghisellini, G., Padovani, P., Celotti, A., & Maraschi, L. 1993, ApJ, 407, 65
Ghisellini, G. & Tavecchio, F. 2008, MNRAS, 387, 1669
Ghisellini, G., Tavecchio, F., & Chiaberge, M. 2005, A&A, 432, 401
Giannios, D., Uzdensky, D. A., & Begelman, M. C. 2009, MNRAS, 395, L29
Giommi, P., Capalbi, M., Fiocchi, M., et al. 2002, in Blazar Astrophysics with BeppoSAX and Other Observatories, ed. P. Giommi, E. Massaro, & G. Palumbo, 63
Giommi, P., Polenta, G., Lähteenmäki, A., et al. 2012, A&A, 541, A160
Giroletti, M., Giovannini, G., Feretti, L., et al. 2004a, ApJ, 600, 127
Giroletti, M., Giovannini, G., Taylor, G. B., & Falomo, R. 2004b, ApJ, 613, 752
Gisler, G. R. & Miley, G. K. 1979, A&A, 76, 109
Glawion, D. 2014, PhD thesis, Julius-Maximilians-Universität Würzburg, Würzburg, Germany
Gómez, J. L., Lobanov, A. P., Bruni, G., et al. 2016, ApJ, 817, 96
Gómez, J. L., Martí, J. M., Marscher, A. P., Ibáñez, J. M., & Alberdi, A. 1997, ApJ, 482, L33
Gomez, J. L., Marti, J. M. A., Marscher, A. P., Ibanez, J. M. A., & Marcaide, J. M. 1995, ApJ, 449, L19
Götz, M. M. A., Alef, W., Preuss, E., & Kellermann, K. I. 1987, A&A, 176, 171
Grandi, P., Torresi, E., & Stanghellini, C. 2012, ApJ, 751, L3
Gregory, P. C., Scott, W. K., Douglas, K., & Condon, J. J. 1996, ApJS, 103, 427
Greisen, E. W. 2003, Information Handling in Astronomy - Historical Vistas, 285, 109

Griffith, M. R. & Wright, A. E. 1994, VizieR Online Data Catalog, 8027, 0
Großberger, C. 2014, PhD thesis, Friedrich-Alexander-Universität Erlangen-Nürnberg, Erlangen, Germany
Grupe, D. 2004, AJ, 127, 1799
Gu, M., Chen, Y., Komossa, S., et al. 2015, ApJS, 221, 3
Guainazzi, M., Oosterbroek, T., Antonelli, L. A., & Matt, G. 2000, A&A, 364, L80
Hada, K., Doi, A., Kino, M., et al. 2011, Nature, 477, 185
Hada, K., Giroletti, M., Kino, M., et al. 2015, ArXiv e-prints, 1502.05177
Hada, K., Kino, M., Doi, A., et al. 2016, ApJ, 817, 131
Hardcastle, M. J. & Krause, M. G. H. 2013, MNRAS, 430, 174
Hardcastle, M. J., Worrall, D. M., Kraft, R. P., et al. 2003, ApJ, 593, 169
Hardee, P. E. 2006, in Astronomical Society of the Pacific Conference Series, Vol. 350, Blazar Variability Workshop II: Entering the GLAST Era, ed. H. R. Miller, K. Marshall, J. R. Webb, & M. F. Aller, 205
Harris, D. E., Massaro, F., Cheung, C. C., et al. 2011, ApJ, 743, 177
Harris, G. L. H., Rejkuba, M., & Harris, W. E. 2010, PASA, 27, 457
Hartman, R. C., Bertsch, D. L., Bloom, S. D., et al. 1999, ApJS, 123, 79
Healey, S. E., Romani, R. W., Taylor, G. B., et al. 2007, ApJS, 171, 61
Heckman, T. M. 1980, A&A, 87, 152
Heckman, T. M. & Best, P. N. 2014, ARA&A, 52, 589
Henri, G. & Saugé, L. 2006, ApJ, 640, 185
H.E.S.S. Collaboration, Abramowski, A., Acero, F., et al. 2012, A&A, 539, A149
H.E.S.S. Collaboration, Abramowski, A., Acero, F., et al. 2010, A&A, 520, A83
Hirotani, K. 2005, ApJ, 619, 73
Ho, L. C. 2008, ARA&A, 46, 475
Ho, P. T. P., Moran, J. M., & Lo, K. Y. 2004, ApJ, 616, L1
Hodgson, J. A. 2014, PhD thesis, Universität zu Köln, Köln, Germany
Hogan, B. S., Lister, M. L., Kharb, P., Marshall, H. L., & Cooper, N. J. 2011, ApJ, 730, 92
Högbom, J. A. 1974, A&AS, 15, 417
Holder, J. 2012, Astroparticle Physics, 39, 61
Homan, D. C., Lister, M. L., Kovalev, Y. Y., et al. 2015, ApJ, 798, 134
Houck, J. C. & Denicola, L. A. 2000, in Astronomical Society of the Pacific Conference Series, Vol. 216, Astronomical Data Analysis Software and Systems IX, ed. N. Manset, C. Veillet, & D. Crabtree, 591
Hovatta, T., Aller, M. F., Aller, H. D., et al. 2014, AJ, 147, 143
Hovatta, T., Lister, M. L., Aller, M. F., et al. 2012, AJ, 144, 105
Hovatta, T., Nieppola, E., Tornikoski, M., et al. 2008, A&A, 485, 51
Hovatta, T., Valtaoja, E., Tornikoski, M., & Lähteenmäki, A. 2009, A&A, 494, 527
IceCube Collaboration. 2013, Science, 342, 1
Impey, C. 1996, AJ, 112, 2667
Jansky, K. G. 1933, Nature, 132, 66
Johnston, S., Bailes, M., Bartel, N., et al. 2007, PASA, 24, 174
Jones, D. L., Wrobel, J. M., & Shaffer, D. B. 1984, ApJ, 276, 480
Jordán, A., Côté, P., Blakeslee, J. P., et al. 2005, ApJ, 634, 1002
Jorstad, S. G., Marscher, A. P., Lister, M. L., et al. 2005, AJ, 130, 1418
Jorstad, S. G., Marscher, A. P., Mattox, J. R., et al. 2001a, ApJ, 556, 738

Jorstad, S. G., Marscher, A. P., Mattox, J. R., et al. 2001b, ApJS, 134, 181
Kadler, M. 2005, PhD thesis, Rheinischen Friedrich-Wilhelms-Universität Bonn, Bonn, Germany
Kadler, M., Eisenacher, D., Ros, E., et al. 2012, A&A, 538, L1
Kadler, M., Kerp, J., Ros, E., et al. 2004a, A&A, 420, 467
Kadler, M., Krauß, F., Mannheim, K., et al. 2016, Nature Physics, 12, 807
Kadler, M., Ojha, R., & TANAMI Collaboration. 2015, Astronomische Nachrichten, 336, 499
Kadler, M., Ros, E., Kerp, J., et al. 2003, New A Rev., 47, 569
Kadler, M., Ros, E., Lobanov, A. P., Falcke, H., & Zensus, J. A. 2004b, A&A, 426, 481
Kadler, M., Ros, E., Perucho, M., et al. 2008, ApJ, 680, 867
Kameno, S., Inoue, M., Wajima, K., Sawada-Satoh, S., & Shen, Z.-Q. 2003, PASA, 20, 213
Kameno, S., Sawada-Satoh, S., Inoue, M., Shen, Z.-Q., & Wajima, K. 2001, PASJ, 53, 169
Karamanavis, V. 2015, PhD thesis, Universität zu Köln, Köln, Germany
Karamanavis, V., Fuhrmann, L., Krichbaum, T. P., et al. 2016, A&A, 586, A60
Kauffmann, G. 2009, A&A, 500, 201
Kellermann, K. I. 2002, PASA, 19, 77
Kellermann, K. I., Lister, M. L., Homan, D. C., et al. 2004, ApJ, 609, 539
Kellermann, K. I. & Pauliny-Toth, I. I. K. 1969, ApJ, 155, L71
Kellermann, K. I., Sramek, R., Schmidt, M., Shaffer, D. B., & Green, R. 1989, AJ, 98, 1195
Khachikian, E. Y. & Weedman, D. W. 1974, ApJ, 192, 581
Kharb, P., Gabuzda, D., Alef, W., Preuss, E., & Shastri, P. 2003, New A Rev., 47, 621
Kharb, P., Lister, M. L., & Cooper, N. J. 2010, ApJ, 710, 764
Komossa, S., Voges, W., Xu, D., et al. 2006, AJ, 132, 531
Komossa, S., Xu, D., Fuhrmann, L., et al. 2015, A&A, 574, A121
Königl, A. 1981, ApJ, 243, 700
Kovalev, Y. Y., Aller, H. D., Aller, M. F., et al. 2009, ApJ, 696, L17
Kovalev, Y. Y., Kellermann, K. I., Lister, M. L., et al. 2005, AJ, 130, 2473
Kovalev, Y. Y., Lister, M. L., Homan, D. C., & Kellermann, K. I. 2007, ApJ, 668, L27
Kovalev, Y. Y., Lobanov, A. P., Pushkarev, A. B., & Zensus, J. A. 2008, A&A, 483, 759
Kraft, R. P., Forman, W. R., Jones, C., et al. 2002, ApJ, 569, 54
Krauß, F., Kadler, M., Mannheim, K., et al. 2014, A&A, 566, L7
Krauß, F., Müller, C., Kadler, M., et al. 2013, ArXiv e-prints, 1301.5198
Krauß, F., Wilms, J., Kadler, M., et al. 2016, A&A, 591, A130
Kreikenbohm, A., Schulz, R., Kadler, M., et al. 2016, A&A, 585, A91
Krichbaum, T. P., Bach, U., Graham, D. A., et al. 2008, ArXiv e-prints, 0812.4211
Krolik, J. H. 1999, Active galactic nuclei : from the central black hole to the galactic environment (Princeton University Press)
Kuehr, H., Witzel, A., Pauliny-Toth, I. I. K., & Nauber, U. 1981, A&AS, 45, 367
Kunert-Bajraszewska, M., Gawroński, M. P., Labiano, A., & Siemiginowska, A. 2010, MNRAS, 408, 2261
Lähteenmäki, A. & Valtaoja, E. 1999, ApJ, 521, 493
Lähteenmäki, A. & Valtaoja, E. 2003, ApJ, 590, 95
Lal, D. V. & Rao, A. P. 2005, in Astronomical Society of the Pacific Conference Series, Vol. 345, From Clark Lake to the Long Wavelength Array: Bill Erickson's Radio

Science, ed. N. Kassim, M. Perez, W. Junor, & P. Henning, 294
Laor, A. 2000, ApJ, 543, L111
Lawrence, A. 1987, PASP, 99, 309
Lee, S.-S., Lobanov, A. P., Krichbaum, T. P., et al. 2008, AJ, 136, 159
Lee, S.-S., Petrov, L., Byun, D.-Y., et al. 2014, AJ, 147, 77
León Tavares, J., Kotilainen, J., Chavushyan, V., et al. 2014, ApJ, 795, 58
León-Tavares, J., Valtaoja, E., Tornikoski, M., Lähteenmäki, A., & Nieppola, E. 2011, A&A, 532, A146
Levinson, A., Laor, A., & Vermeulen, R. C. 1995, ApJ, 448, 589
Lewis, K. T., Eracleous, M., Gliozzi, M., Sambruna, R. M., & Mushotzky, R. F. 2005, ApJ, 622, 816
Li, F., Cornwell, T. J., & de Hoog, F. 2011, A&A, 528, A31
Li, Z.-Y., Chiueh, T., & Begelman, M. C. 1992, ApJ, 394, 459
Lico, R., Giroletti, M., Orienti, M., et al. 2012, A&A, 545, A117
Linfield, R. & Perley, R. 1984, ApJ, 279, 60
Lister, M. L., Aller, M., Aller, H., et al. 2011, ApJ, 742, 27
Lister, M. L., Aller, M. F., Aller, H. D., et al. 2013, AJ, 146, 120
Lister, M. L., Aller, M. F., Aller, H. D., et al. 2015, ApJ, 810, L9
Lister, M. L., Cohen, M. H., Homan, D. C., et al. 2009a, AJ, 138, 1874
Lister, M. L. & Homan, D. C. 2005, AJ, 130, 1389
Lister, M. L., Homan, D. C., Kadler, M., et al. 2009b, ApJ, 696, L22
Lobanov, A. 2015, A&A, 574, A84
Lobanov, A. P. 1998, A&A, 330, 79
Lobanov, A. P. 2005, ArXiv e-prints, astro-ph/0503225
Lobanov, A. P. & Zensus, J. A. 2001, Science, 294, 128
Longair, M. S. 2011, High Energy Astrophysics (Cambridge University Press)
Lovell, J. E. J., McCallum, J. N., Reid, P. B., et al. 2013, Journal of Geodesy, 87, 527
Lu, R.-S., Broderick, A. E., Baron, F., et al. 2014, ApJ, 788, 120
Ly, C., Walker, R. C., & Junor, W. 2007, ApJ, 660, 200
Mack, K.-H., Feretti, L., Giovannini, G., & Klein, U. 1993, A&A, 280, 63
Mankuzhiyil, N., Ansoldi, S., Persic, M., & Tavecchio, F. 2011, ApJ, 733, 14
Mannheim, K. 1993, A&A, 269, 67
Mannheim, K. 1995, Astroparticle Physics, 3, 295
Mannheim, K. & Biermann, P. L. 1989, A&A, 221, 211
Maraschi, L., Ghisellini, G., & Celotti, A. 1992, ApJ, 397, L5
Markowitz, A. G., Krumpe, M., & Nikutta, R. 2014, MNRAS, 439, 1403
Marscher, A. P. 2006, in American Institute of Physics Conference Series, Vol. 856, Relativistic Jets: The Common Physics of AGN, Microquasars, and Gamma-Ray Bursts, ed. P. A. Hughes & J. N. Bregman, 1–22
Marscher, A. P. 2009, ArXiv e-prints 0909.2576
Marscher, A. P. & Gear, W. K. 1985, ApJ, 298, 114
Marscher, A. P., Jorstad, S. G., Gómez, J.-L., et al. 2002, Nature, 417, 625
Marscher, A. P., Jorstad, S. G., Larionov, V. M., et al. 2010, ApJ, 710, L126
Marshall, H. L., Schwartz, D. A., Lovell, J. E. J., et al. 2005, ApJS, 156, 13
Marti-Vidal, I., Conway, J., Lindqvist, M., et al. 2014, in Proceedings of the 12th European VLBI Network Symposium and Users Meeting (EVN 2014). 7-10 October 2014. Cagliari, Italy, id. 34

Martí-Vidal, I., Pérez-Torres, M. A., & Lobanov, A. P. 2012, A&A, 541, A135
Martí-Vidal, I., Vlemmings, W. H. T., Muller, S., & Casey, S. 2014, A&A, 563, A136
Massardi, M., Burke-Spolaor, S. G., Murphy, T., et al. 2013, MNRAS, 436, 2915
Massardi, M., Ekers, R. D., Murphy, T., et al. 2011, MNRAS, 412, 318
Massaro, F., D'Abrusco, R., Giroletti, M., et al. 2013a, ApJS, 207, 4
Massaro, F., D'Abrusco, R., Paggi, A., et al. 2013b, ApJS, 206, 13
Massaro, F., Thompson, D. J., & Ferrara, E. C. 2016, A&A Rev., 24, 2
Mauch, T., Murphy, T., Buttery, H. J., et al. 2003, MNRAS, 342, 1117
Mauch, T., Murphy, T., Buttery, H. J., et al. 2013, VizieR Online Data Catalog, 8081, 0
Max-Moerbeck, W., Hovatta, T., Richards, J. L., et al. 2014, MNRAS, 445, 428
McCready, L. L., Pawsey, J. L., & Payne-Scott, R. 1947, Proceedings of the Royal Society of London Series A, 190, 357
McKinney, J. C., Tchekhovskoy, A., & Blandford, R. D. 2012, MNRAS, 423, 3083
McKinney, J. C., Tchekhovskoy, A., & Blandford, R. D. 2013, Science, 339, 49
McMullin, J. P., Waters, B., Schiebel, D., Young, W., & Golap, K. 2007, in Astronomical Society of the Pacific Conference Series, Vol. 376, Astronomical Data Analysis Software and Systems XVI, ed. R. A. Shaw, F. Hill, & D. J. Bell, 127
McNamara, B. R. & Nulsen, P. E. J. 2007, ARA&A, 45, 117
Meier, D. L. 2002, New A Rev., 46, 247
Meyer, E. T., Fossati, G., Georganopoulos, M., & Lister, M. L. 2011, ApJ, 740, 98
Meyer, E. T., Fossati, G., Georganopoulos, M., & Lister, M. L. 2012, ApJ, 752, L4
Miley, G. K. 1973, A&A, 26, 413
Miller, J. S. & Hawley, S. A. 1977, ApJ, 212, L47
Moellenbrock, G. A., Fujisawa, K., Preston, R. A., et al. 1996, AJ, 111, 2174
Morganti, R., Tadhunter, C. N., & Oosterloo, T. A. 2005, A&A, 444, L9
Mościbrodzka, M., Falcke, H., Shiokawa, H., & Gammie, C. F. 2014, A&A, 570, A7
Moshir, M. & et al. 1990, in IRAS Faint Source Catalogue, version 2.0 (1990), 0
Müller, C. 2014, PhD thesis, Friedrich-Alexander-Universität Erlangen-Nürnberg, Erlangen, Germany
Müller, C., Kadler, M., Ojha, R., et al. 2014a, A&A, 562, A4
Müller, C., Kadler, M., Ojha, R., et al. 2014b, A&A, 569, A115
Müller, C., Kadler, M., Ojha, R., et al. 2011, A&A, 530, L11
Murphy, T., Sadler, E. M., Ekers, R. D., et al. 2010, MNRAS, 402, 2403
Nalewajko, K., Begelman, M. C., & Sikora, M. 2014, ApJ, 789, 161
Nan, R., Li, D., Jin, C., et al. 2011, International Journal of Modern Physics D, 20, 989
Napier, P. J. 1994, in IAU Symposium, Vol. 158, Very High Angular Resolution Imaging, ed. J. G. Robertson & W. J. Tango, 117
Narayan, R., Mahadevan, R., Grindlay, J. E., Popham, R. G., & Gammie, C. 1998, ApJ, 492, 554
Neeser, M. J., Eales, S. A., Law-Green, J. D., Leahy, J. P., & Rawlings, S. 1995, ApJ, 451, 76
Neronov, A., Semikoz, D., & Vovk, I. 2010, A&A, 519, L6
Netzer, H. 2015, ARA&A, 53, 365
Neumayer, N. 2010, PASA, 27, 449
Nityananda, R. 2009, in Astronomical Society of the Pacific Conference Series, Vol. 407, The Low-Frequency Radio Universe, ed. D. J. Saikia, D. A. Green, Y. Gupta, & T. Venturi, 389
Nolan, P. L., Abdo, A. A., Ackermann, M., et al. 2012, ApJS, 199, 31

O'Dea, C. P. 1998, PASP, 110, 493
O'Dea, C. P. & Baum, S. A. 1997, AJ, 113, 148
Ojha, R., Kadler, M., Böck, M., et al. 2010, A&A, 519, A45
Oke, J. B. & Gunn, J. E. 1974, ApJ, 189, L5
Orienti, M., D'Ammando, F., Larsson, J., et al. 2015, MNRAS, 453, 4037
Oshlack, A. Y. K. N., Webster, R. L., & Whiting, M. T. 2001, ApJ, 558, 578
Osterbrock, D. E. 1977, ApJ, 215, 733
Osterbrock, D. E. 1999, ApJ, 525, 337
Osterbrock, D. E. & Pogge, R. W. 1985, ApJ, 297, 166
O'Sullivan, S. P. & Gabuzda, D. C. 2009, MNRAS, 400, 26
Owen, F. N., Ledlow, M. J., & Keel, W. C. 1996, AJ, 111, 53
Padovani, P. 2007, Ap&SS, 309, 63
Padovani, P. & Giommi, P. 1995, ApJ, 444, 567
Paliya, V. S., Sahayanathan, S., Parker, M. L., et al. 2014, ApJ, 789, 143
Paliya, V. S., Stalin, C. S., Shukla, A., & Sahayanathan, S. 2013, ApJ, 768, 52
Perley, R. A., Chandler, C. J., Butler, B. J., & Wrobel, J. M. 2011, ApJ, 739, L1
Perucho, M. 2012, International Journal of Modern Physics Conference Series, 8, 241
Perucho, M. 2013, in European Physical Journal Web of Conferences, Vol. 61, European Physical Journal Web of Conferences, 02002
Perucho, M. & Martí, J. M. 2007, MNRAS, 382, 526
Perucho, M., Martí-Vidal, I., Lobanov, A. P., & Hardee, P. E. 2012, A&A, 545, A65
Piccinotti, G., Mushotzky, R. F., Boldt, E. A., et al. 1982, ApJ, 253, 485
Piner, B. G. & Edwards, P. G. 2004, ApJ, 600, 115
Piner, B. G., Mahmud, M., Fey, A. L., & Gospodinova, K. 2007, AJ, 133, 2357
Piner, B. G., Pant, N., & Edwards, P. G. 2008, ApJ, 678, 64
Piner, B. G., Pant, N., & Edwards, P. G. 2010, ApJ, 723, 1150
Piner, B. G., Pushkarev, A. B., Kovalev, Y. Y., et al. 2012, ApJ, 758, 84
Pittori, C., Verrecchia, F., Chen, A. W., et al. 2009, A&A, 506, 1563
Planck Collaboration, Ade, P. A. R., Aghanim, N., et al. 2014, A&A, 571, A28
Planck Collaboration, Ade, P. A. R., Aghanim, N., et al. 2011, A&A, 536, A7
Pogge, R. W., Maoz, D., Ho, L. C., & Eracleous, M. 2000, ApJ, 532, 323
Prestage, R. M., Constantikes, K. T., Hunter, T. R., et al. 2009, IEEE Proceedings, 97, 1382
Preston, R. A., Jauncey, D. L., Meier, D. L., et al. 1989, AJ, 98, 1
Preuss, E., Alef, W., & Kellermann, K. I. 1988, in IAU Symposium, Vol. 129, The Impact of VLBI on Astrophysics and Geophysics, ed. M. J. Reid & J. M. Moran, 105
Pushkarev, A. B., Hovatta, T., Kovalev, Y. Y., et al. 2012, A&A, 545, A113
Pushkarev, A. B. & Kovalev, Y. Y. 2012, A&A, 544, A34
Pushkarev, A. B., Kovalev, Y. Y., Lister, M. L., & Savolainen, T. 2009, A&A, 507, L33
Ramakrishnan, V., Hovatta, T., Nieppola, E., et al. 2015, MNRAS, 452, 1280
Randall, K. E., Hopkins, A. M., Norris, R. P., & Edwards, P. G. 2011, MNRAS, 416, 1135
Rani, B., Lott, B., Krichbaum, T. P., Fuhrmann, L., & Zensus, J. A. 2013, A&A, 557, A71
Readhead, A. C. S. 1994, ApJ, 426, 51
Reber, G. 1988, JRASC, 82, 93
Rector, T. A., Stocke, J. T., & Perlman, E. S. 1999, ApJ, 516, 145
Rees, M. J. 1966, Nature, 211, 468

Reich, W., Steppe, H., Schlickeiser, R., et al. 1993, A&A, 273, 65
Richards, J. L., Hovatta, T., Max-Moerbeck, W., et al. 2014, MNRAS, 438, 3058
Richards, J. L. & Lister, M. L. 2015, ApJ, 800, L8
Richards, J. L., Max-Moerbeck, W., Pavlidou, V., et al. 2011, ApJS, 194, 29
Rigby, E. E., Best, P. N., Brookes, M. H., et al. 2011, MNRAS, 416, 1900
Rybicki, G. B. & Lightman, A. P. 1979, Radiative processes in astrophysics (New York, Wiley-Interscience)
Ryle, M. & Windram, M. D. 1968, MNRAS, 138, 1
Sambruna, R. M., Gambill, J. K., Maraschi, L., et al. 2004, ApJ, 608, 698
Sato, K., Furusho, T., Yamasaki, N. Y., et al. 2005, PASJ, 57, 743
Sault, R. J., Teuben, P. J., & Wright, M. C. H. 1995, in Astronomical Society of the Pacific Conference Series, Vol. 77, Astronomical Data Analysis Software and Systems IV, ed. R. A. Shaw, H. E. Payne, & J. J. E. Hayes, 433
Savolainen, T., Wiik, K., Valtaoja, E., Jorstad, S. G., & Marscher, A. P. 2002, A&A, 394, 851
Sawada-Satoh, S., Kameno, S., Nakamura, K., et al. 2008, ApJ, 680, 191
Saxton, R. D., Read, A. M., Esquej, P., et al. 2008, A&A, 480, 611
Schinzel, F. K., Lobanov, A. P., Taylor, G. B., et al. 2012, A&A, 537, A70
Schinzel, F. K., Petrov, L., Taylor, G. B., et al. 2015, ApJS, 217, 4
Schmidt, M. 1963, Nature, 197, 1040
Schmidt, M. & Green, R. F. 1983, ApJ, 269, 352
Schulz, R., Kadler, M., Ros, E., et al. 2014, in Proceedings of the 12th European VLBI Network Symposium and Users Meeting (EVN 2014). 7-10 October 2014. Cagliari, Italy, id. 109
Schulz, R., Kadler, M., Ros, E., et al. 2013, ArXiv e-prints, 1301.6582
Schulz, R., Kreikenbohm, A., Kadler, M., et al. 2016, A&A, 588, A146
Schulz, R. F. 2012, MSc thesis, A Study of the Active Galaxy 3C111 with mm-VLBI, Julius-Maximilians-Universität Würzburg, Würzburg, Germany
Schwab, F. R. & Cotton, W. D. 1983, AJ, 88, 688
Seyfert, C. K. 1943, ApJ, 97, 28
Shang, Z., Brotherton, M. S., Green, R. F., et al. 2005, ApJ, 619, 41
Shields, G. A. 1978, Nature, 272, 706
Shields, G. A. 1999, ArXiv e-prints astro-ph/9903401
Sijbring, D. & de Bruyn, A. G. 1998, A&A, 331, 901
Sikora, M., Begelman, M. C., & Rees, M. J. 1994, ApJ, 421, 153
Silk, J. & Rees, M. J. 1998, A&A, 331, L1
Singal, A. K. 2009, ApJ, 703, L109
Sokolovsky, K. V., Kovalev, Y. Y., Pushkarev, A. B., & Lobanov, A. P. 2011, A&A, 532, A38
Sowards-Emmerd, D., Romani, R. W., & Michelson, P. F. 2003, ApJ, 590, 109
Sowards-Emmerd, D., Romani, R. W., Michelson, P. F., & Ulvestad, J. S. 2004, ApJ, 609, 564
Stanghellini, C. 2003, PASA, 20, 118
Stecker, F. W. 2013, Phys. Rev. D, 88, 047301
Stevens, J., Edwards, P. G., Ojha, R., et al. 2012, ArXiv e-prints, 1205.2403
Sullivan, III, W. T. 1991, in Astronomical Society of the Pacific Conference Series, Vol. 19, IAU Colloq. 131: Radio Interferometry. Theory, Techniques, and Applications, ed. T. J. Cornwell & R. A. Perley, 132

Sullivan, III, W. T. 2009, Cosmic Noise: A History of Early Radio Astronomy (Cambridge University Press)
Tadhunter, C. 2008, New A Rev., 52, 227
Tavecchio, F. & Ghisellini, G. 2008, MNRAS, 385, L98
Tavecchio, F., Maraschi, L., & Ghisellini, G. 1998, ApJ, 509, 608
Tavecchio, F., Maraschi, L., Sambruna, R. M., & Urry, C. M. 2000, ApJ, 544, L23
Taylor, G. B., Carilli, C. L., & Perley, R. A., eds. 1999, Astronomical Society of the Pacific Conference Series, Vol. 180, Synthesis Imaging in Radio Astronomy II
Taylor, J. H. & Cordes, J. M. 1993, ApJ, 411, 674
Tchekhovskoy, A. & McKinney, J. C. 2012, MNRAS, 423, L55
Tchekhovskoy, A., McKinney, J. C., & Narayan, R. 2012, Journal of Physics Conference Series, 372, 012040
Tchekhovskoy, A., Narayan, R., & McKinney, J. C. 2010, ApJ, 711, 50
Tchekhovskoy, A., Narayan, R., & McKinney, J. C. 2011, MNRAS, 418, L79
Thompson, A. R., Moran, J. M., & Swenson, Jr., G. W. 2001, Interferometry and Synthesis in Radio Astronomy, 2nd Edition (New York : Wiley)
Tilanus, R. P. J., Krichbaum, T. P., Zensus, J. A., et al. 2014, ArXiv e-prints, 1406.4650
Tingay, S. J., Goeke, R., Bowman, J. D., et al. 2013, PASA, 30, e007
Trippe, S., Krips, M., Piétu, V., et al. 2011, A&A, 533, A97
Tzioumis, A. K., Tingay, S. J., Stansby, B., et al. 2010, AJ, 140, 1506
Ueda, Y., Akiyama, M., Ohta, K., & Miyaji, T. 2003, ApJ, 598, 886
Urry, C. M. & Padovani, P. 1995, PASP, 107, 803
Valtaoja, E., Lähteenmäki, A., Teräsranta, H., & Lainela, M. 1999, ApJS, 120, 95
van Gorkom, J. H., Knapp, G. R., Raimond, E., Faber, S. M., & Gallagher, J. S. 1986, AJ, 91, 791
van Haarlem, M. P., Wise, M. W., Gunst, A. W., et al. 2013, A&A, 556, A2
Vaughan, S., Edelson, R., Warwick, R. S., & Uttley, P. 2003, MNRAS, 345, 1271
Venturi, T. 2010, in 10th European VLBI Network Symposium and EVN Users Meeting: VLBI and the New Generation of Radio Arrays, 1
Vermeulen, R. C., Ogle, P. M., Tran, H. D., et al. 1995, ApJ, 452, L5
Vermeulen, R. C., Ros, E., Kellermann, K. I., et al. 2003, A&A, 401, 113
Véron-Cetty, M.-P. & Véron, P. 2010, A&A, 518, A10
Verrecchia, F., in't Zand, J. J. M., Giommi, P., et al. 2007, A&A, 472, 705
Voges, W., Aschenbach, B., Boller, T., et al. 1999, A&A, 349, 389
von Montigny, C., Bertsch, D. L., Chiang, J., et al. 1995, A&A, 299, 680
Wajima, K., Fujisawa, K., Hayashida, M., et al. 2014, ApJ, 781, 75
Wakely, S. P. & Horan, D. 2008, International Cosmic Ray Conference, 3, 1341
Walker, R. C. 1989, in NATO Advanced Science Institutes (ASI) Series C, Vol. 283, NATO Advanced Science Institutes (ASI) Series C, ed. M. Felli & R. E. Spencer, 163–182
Warwick, R. S., Marshall, N., Fraser, G. W., et al. 1981, MNRAS, 197, 865
Wayth, R. B., Lenc, E., Bell, M. E., et al. 2015, PASA, 32, 25
Wenger, S., Magnor, M., Pihlström, Y., Bhatnagar, S., & Rau, U. 2010, PASP, 122, 1367
White, R. L. & Becker, R. H. 1992, ApJS, 79, 331
Wielebinski, R., Junkes, N., & Grahl, B. H. 2011, Journal of Astronomical History and Heritage, 14, 3
Wilkes, B. J. 2004, in Multiwavelength AGN Surveys, ed. R. Mújica & R. Maiolino, 262–274

Wilkinson, P. N., Polatidis, A. G., Readhead, A. C. S., Xu, W., & Pearson, T. J. 1994, ApJ, 432, L87
Wills, B. J. 1975, ApJ, 202, L59
Wilson, T. L. 2011, ArXiv e-prints, 1111.1183
Wilson, W. E., Ferris, R. H., Axtens, P., et al. 2011, MNRAS, 416, 832
Woo, J.-H. & Urry, C. M. 2002, ApJ, 579, 530
Wootten, A. & Thompson, A. R. 2009, IEEE Proceedings, 97, 1463
Wright, A. & Otrupcek, R. 1990, Australia Telescope National Facility
Wright, A. E., Griffith, M. R., Burke, B. F., & Ekers, R. D. 1994, ApJS, 91, 111
Wright, E. L., Chen, X., Odegard, N., et al. 2009, ApJS, 180, 283
Wright, E. L., Eisenhardt, P. R. M., Mainzer, A. K., et al. 2010, AJ, 140, 1868
Wrobel, J. M. 1984, ApJ, 284, 531
Yao, S., Yuan, W., Zhou, H., et al. 2015, MNRAS, 454, L16
Yuan, W., Zhou, H. Y., Komossa, S., et al. 2008, ApJ, 685, 801
Zensus, J. A. 1997, ARA&A, 35, 607
Zhou, H., Wang, T., Yuan, W., et al. 2006, ApJS, 166, 128
Zhou, H., Wang, T., Yuan, W., et al. 2007, ApJ, 658, L13
Zhou, H.-Y., Wang, T.-G., Dong, X.-B., Zhou, Y.-Y., & Li, C. 2003, ApJ, 584, 147

List of Figures

1.1. The Milky Way at different wavalengths . . . 6
1.2. Composite image of Centaurus A . . . 7

2.1. Schematic of an AGN . . . 13
2.2. SEDs of 3C 279 and PKS 2155−304 . . . 17
2.3. 3LAC γ-ray photon index and luminosity . . . 19
2.4. Schematic of jet launching . . . 21
2.5. Superluminal Motion . . . 23
2.6. Apparent velocity depending on the inclination angle of the jet . . . 24
2.7. Images of different radio telescopes . . . 26

3.1. Multiwavelength light curves of CTA 102 . . . 38
3.2. Radio luminosity and redshift distribution of the MOJAVE sample . . . 40
3.3. γ-ray and radio luminosity distribution of the MOJAVE sample . . . 41
3.4. Instrumental Coverage of TANAMI . . . 43
3.5. The TANAMI array . . . 44
3.6. Inclination angle and intrinsic speed of Centaurus A . . . 47
3.7. Radio spectral index diagram of TANAMI sources . . . 48
3.8. γ-ray and radio luminosity distribution of the TANAMI sample . . . 51

4.1. NVSS image at 1.4 GHz of IC 310 . . . 54
4.2. Radio spectrum of IC 310 . . . 58
4.3. EVN images of IC 310 . . . 59
4.4. Stacked image of the MOJAVE observations of IC 310 . . . 60
4.5. Time evolution of the MOJAVE images . . . 62
4.6. Distance of components with time . . . 63
4.7. Spectral index maps of IC 310 . . . 66
4.8. Viewing angle of IC 310versus intrinsic speed . . . 67
4.9. β_{app}-distribution with the luminosity of the MOJAVE sample . . . 71

5.1. PKS 2004−447lightcurve and spectrum . . . 77
5.2. TANAMI images of PKS 2004−447 . . . 80
5.3. VLBA and VLA images of PKS 2004−447 . . . 81
5.4. PKS 2004−447ATCA and archival spectrum . . . 83

6.1. 3C 111light curve at 86 GHz . . . 96
6.2. GMVA images and (u, v)-coverage of 3C 111 . . . 98
6.3. Time evolution of the GMVA observations . . . 100

6.4. Distance over time of the kinematic components and the mm-wavelength light curve . . . 102
6.5. Coordinate system for the analysis of the bend in 3C 111 . . . 104
6.6. Rotated positions of the jet components in 3C 111 . . . 105
6.7. Amplitude A_0 of the instability with respect to x_0 . . . 106

A.1. Radio morphology of NGC 1052 . . . 116
A.2. θ_{LOS} vs. β for NGC 1052 . . . 119

B.1. PKS 2004−447ATCA and archival spectrum with fits . . . 122

C.1. Stacked image of 1H 0323+342 . . . 124

List of Tables

3.1. The TANAMI sample 45
3.2. Fractional polarization of the TANAMI sample from AT20G observations 48
3.3. The TANAMI array 50

4.1. EVN and MOJAVE observations and image parameters 57
4.2. Position angle measurements from EVN and MOJAVE 61
4.3. Velocity, speed and ejection time of IC 310at 15 GHz 64
4.4. Jet parameters of IC 310 68
4.5. Estimates of the magnetic field strengths of IC 310 70

5.1. Summary of interferometric observations of PKS 2004−447 75
5.2. Spectral indices of PKS 2004−447 78
5.3. Variability index between 5.5 GHz and 19 GHz for PKS 2004−447 79
5.4. Parameters of core component of PKS 2004−447 81
5.5. Properties of γ-NLS1 90

6.1. Image properties of th GMVA observations of 3C 111 96
6.2. Velocity, speed and ejection time of 3C 111 at 86 GHz 101

D.1. Parameters of the modelfit components of IC 310 of the MOJAVE observations 125
D.2. Parameters of the modelfit components of IC 310 of the EVN observations 127

Acknowledgement

First of all, my sincere thanks go to my supervisors Prof. Dr. Matthias Kadler at Würzburg University and Prof. Dr. Jörn Wilms at Remeis Observatory Bamberg (Erlangen-Nürnberg University), who offered me the opportunity to do my PhD in their groups, to present my work at various conferences and workshops and to explore what it means for me to be a scientist beyond pure research. Their support and advice have been a key stone since my Master thesis. I have learned so much from them over the past years. It has been an immense pleasure for me to be part of their groups.

I want to express my sincere thanks to Prof. Dr. Eduardo Ros (Max-Planck-Institut für Radioastronomie) for his wonderful help, great advice and support. My additional thanks for performing the a-priori calibration of the VLBA and VLA data of PKS 2004−447 and patiently answering all my questions.

I am also very grateful having the pleasure to work with Dr. Roopesh Ojha (NASA Goddard Space Flight Center). Thank you very much for the time I spend at Goddard and for performing the challenging and time consuming a-priori calibration of the TANAMI data. Moreover, my visit to Goddard would not have been possible without my host, Dr. Neil Gehrels. I want to thank my colleagues from the *Fermi*-LAT collaboration for the wonderful work and cooperation.

It has been a great pleasure to collaborate with Prof. Dr. Manel Perucho. His theoretical knowledge on AGN has been invaluable, boosting my understanding of the inner workings of AGNs.

Special thanks go to Prof. Dr. Gilles Henri and Dr. Pierre-Olivier Petrucci at the Institut de Planétologie et d'Astrophysique de Grenoble for hosting me at the institute many times during my PhD. Our discussions on the physics of AGNs have always been highly insightful.

I also want to thank Prof. Dr. Karl Mannheim (Würzburg University) for his support and advice since my first days during my Bachelor thesis when I started working in the Chair of Astronomy.

My thanks go to Dr. Phil Edwards and Dr. Jamie Stevens at the Commonwealth Scientific and Industrial Research Organisation for providing the important ATCA data on PKS 2004−447. Thanks also Jamie, for your patience and time answering all my questions on the interpretation and calibration of the ATCA data.

In addition, I want to thank Dr. Thomas Krichbaum (MPIfR) who taught me a lot about radio astronomy and especially the particularities of mm-VLBI.

This work would not have been possible without the people providing and maintaining the IT-infrastructure at both institutes. My thanks to you, dear admins. I have learned a lot from you: Aleksander Paravac, Fritz-Walter Schwarm, Dr. Ingo Kreykenbohm, Dr. Thomas Dauser, Matthias Kühnel, Alexander Kappes, and Jonas Trüstedt.

The wonderful time that I had professionally and personally during my PhD and already before would not have been possible without the great colleagues in particular at Würzburg University and Remeis Observatory. Having two scientific homes has been one of the many delights of my scientific career so far. Many of them have also become dear friends of mine. I will most likely not be able to mention everyone, so here is a general, huge thank you to all of you. Nevertheless, there are several wonderful people whom I want to mention: it has been an immense pleasure to have shared my office with Annika Kreikenbohm and Till Steinbring. Although our *ART* office has seldom been complete with all of us being present at the same time, the joyful time we spent working together and having fun in and outside of work will never be forgotten. Many thanks also to Katharina Leiter, Marcus Langejahn, Jonas Trüstedt, Tobias Beuchert and Alexander Kappes for a great time and discussions we had in and outside the world of science. It has also been a great pleasure to work and to spent time with Dr. Cornelia Müller, who has been a corner stone for the wonderful spirit that bonds both groups. I do not want to miss to express how grateful I am for the terrific time I had with Dr. Natalia Lewandowska and Dr. Patrick Kilian, especially building models of radio telescopes until late at night. Moreover, thanks Natalia for sharing with me your fascination of radio astronomy and pulsars which has always enriched mine.

I want to thank Dr. Christoph Großberger from whom I learned a lot about programming and who provided many scripts which helped me during this work. I also enjoyed the many insightful discussions on the idiosyncrasies of radio astronomy which we shared. Thanks as well to Dr. Moritz Böck for his help and the scripts he wrote. It gives me great pleasure to work with Anne-Kathrin Baczko since her Bachelor thesis.

My visit to Goddard was also such an unforgettable time thanks to: Dr. Katja Pottschmidt who helped me a lot getting settled, showed me around and introduced me to the wonderful music of *The Chromatics*. It was great to share an office with Bryce Carpenter and work with him on TANAMI. Thanks also a lot, Bryce, for the incredible trip to the National Space and Air Museum.

Another round of thanks go to Sheetal Saxena, Dr. Daniela Dorner, Dr. Sebastian Ohlmann, Dr. Felicia Krauss, Eugenia Litzinger, Dr. Thomas Vauillaume, Thorsten Brandt, Michael Kreter, Paul Ray Burd, and Dr. Dorit Glawion.

Although I have mentioned them already, I want to explicitly thank the people who carefully read parts of the manuscripts: Annika, Till, Marcus, and Sheetal.

An important part of my life have been the friends outside the world of astronomy: In particular, I want to mention Julian Scharnagl, Madeleine Schimanski, Dr. Julia Harz, Franziska Wawrik, and Gregor Weber. Thank you so much for your friendships and the terrific time.

Last but not least, I want to thank my family from the depth of my heart, especially my parents and grandmothers for their strength, guidance, great heart, and much more than I can name here. Their support has been invaluable to me and I am proud to be their son and grandson. Many thanks also go to my parents-in-law for welcoming me into their family so warmly and supporting me ever since.

Finally, there is someone without whom I would not be where and who I am today: My lovely Katrin. I cannot thank you enough for always putting a smile on my face especially in difficult times, for being patient with the long and late hours I spent following my passion and for simply always being there for me. I have no words to express the depth of my gratitude.

Mein herzlichster Dank gilt meiner Familie, allen voran meinen Eltern und Omas für ihre Kraft, Herzlichkeit, ihre Unterstützung und Hilfe dabei meinen Weg zu finden und vieles mehr. Sie standen mir immer mit Rat und Tat bei und dies ist für mich von unschätzbarem Wert. Ich bin stolz darauf ihr Sohn und Enkel zu sein. Darüber hinaus, danke ich meinen Schwiegereltern, die mich liebevoll in ihre Familie aufgenommen und mich seitdem stets unterstützt haben.

Abschließend, möchte ich der Person danken, ohne die ich heute auch nicht hier wäre: Meine geliebte Katrin. Ich kann Dir nicht genug dafür danken, dass du stets für mich hast die Sonne scheinen lassen, besonders in schwierigen Zeiten, für deine Geduld, wenn ich mal wieder bis spät in meine Arbeit vertieft war und dafür, dass du einfach jederzeit für mich da bist. Ich finde nicht genügend Worte um meine Dankbarkeit angemessen auszudrücken.

This work was funded by Deutsche Forschungsgemeinschaft grant WI 1860/10-1.

The research leading to these results has received funding from the European Commission Seventh Framework Programme (FP/2007-2013) under grant agreement No. 283393 (RadioNet3). The European VLBI Network is a joint facility of European, Chinese, South African and other radio astronomy institutes funded by their national research councils.

This research has made use of the Interactive Spectral Interpretation System (ISIS) (Houck & Denicola 2000). This research has made use of a collection of ISIS scripts provided by the Dr. Karl Remeis observatory, Bamberg, Germany at http://www.sternwarte.uni-erlangen.de/isis/. This work has made use of data provided by the multi-wavelength monitoring program TANAMI and its participating facilities. This work has made use of data provided by the Global mm-VLBI Array. The GMVA data are correlated at the VLBI correlator of the MPIfR, Bonn, Germany. The Very Long Baseline Array (VLBA) is an instrument of the National Radio Astronomy Observatory (NRAO). NRAO is a facility of the National Science Foundation, operated by Associated Universities Inc. The Australian Long Baseline Array and the Australia Telescope Compact Array are part of the Australia Telescope National Facility which is funded by the Commonwealth of Australia for operation as a National Facility managed by CSIRO. This study makes use of 43 GHz VLBA data from the Boston University gamma-ray blazar monitoring program (http://www.bu.edu/blazars/VLBAproject.html), funded by NASA through the Fermi Guest Investigator Program. This research has made use of data from the MOJAVE database that is maintained by the MOJAVE team (Lister et al., 2009, AJ, 137, 3718). This research has made use of the NASA/IPAC Extragalactic Database (NED) which is operated by the Jet Propulsion Laboratory, California Institute of Technology, under contract with the National Aeronautics and Space Administration. This research has made use of the VizieR catalogue access tool, CDS, Strasbourg, France. This paper makes use of data from the ALMA calibrator database: https://almascience.eso.org/alma-data/calibrator-catalogue. ALMA is a partnership of ESO (representing its member states), NSF (USA) and NINS (Japan), together with NRC (Canada), NSC and ASIAA (Taiwan), and KASI (Republic of Korea), in cooperation with the Republic of Chile. The Joint ALMA Observatory is operated by ESO, AUI/NRAO and NAOJ. Part of this work is based on archival data, software or online services provided by the ASI SCIENCE DATA CENTER (ASDC).